

Interaction Between a Surface Dielectric Barrier Discharge and Transonic Airflows

THÈSE N° 4201 (2008)

PRÉSENTÉE LE 24 OCTOBRE 2008

À LA FACULTE SCIENCES ET TECHNIQUES DE L'INGÉNIEUR
LABORATOIRE DE THERMIQUE APPLIQUÉE ET DE TURBOMACHINES
PROGRAMME DOCTORAL EN ENERGIE

ÉCOLE POLYTECHNIQUE FÉDÉRALE DE LAUSANNE

POUR L'OBTENTION DU GRADE DE DOCTEUR ÈS SCIENCES

PAR

Samantha PAVÓN

ingénieur physicien diplômé EPF
de nationalité suisse et originaire d'Albeuve (FR)

acceptée sur proposition du jury:

Prof. F. Avellan, président du jury
Dr P. Ott, Prof. J. R. Thome, directeurs de thèse
Prof. J.-P. Boeuf, rapporteur
Prof. Ph. R. von Rohr, rapporteur
Prof. B. Weigand, rapporteur



ÉCOLE POLYTECHNIQUE
FÉDÉRALE DE LAUSANNE

Suisse
2008

*“Minds are like parachutes, they work
best when open”*

Sir Thomas R. Dewar

Abstract

The use of plasmas in aerodynamics has become a recent topic of interest. The potentialities of different types of plasmas are being investigated for low velocity and high velocity flow control, as well as for plasma-assisted combustion. Dielectric barrier discharges (DBDs) are good candidates since the transition of the glow or filamentary discharge to an arc is prevented by the dielectric barrier. Moreover, surface DBDs allow to ionize the gas very close to the dielectric surface and can be used to ionize the boundary layer around an object immersed in a flow. The research in flow control has basically followed two main paths: the study of DBDs in low-speed airflows and the study of volume glow or corona discharges in supersonic airflows. Until today, there has been an important technological barrier in experimental investigations with surface DBDs. Atmospheric pressure surface DBDs in air have been difficult to maintain for long operation times, typically several hours, because reactive species created in the plasma (for example atomic oxygen) generate intensive etching of the electrode and dielectric materials. Oxidation of the electrodes or reduction of the dielectric thickness will eventually lead to plasma extinction or arcing respectively. This important issue has prevented detailed studies of DBDs in extreme environment, namely in high-speed airflows.

In the present work, a solution to this technological problem has been found and is presented. Low temperature co-fireable ceramic (LTCC) technology allows, for the first time, to fully encapsulate the electrodes in a ceramic matrix and maximize the lifetime of the DBD system. Encapsulation improves the reproducibility of the experiments. Moreover, the plate can be manufactured in a curved shape. This technological advance permits, in the frame of the research presented here, to carry out a detailed experimental investigation of DBDs in high-speed flows. The goal of this experimental research is to improve the physical understanding of the interaction between a local atmospheric discharge, causing a localized weak ionization of the surrounding airflow, and the shock wave structure in transonic and supersonic flows typical for aeronautic applications. The fundamental nature of the research makes it relevant in a large domain of applications such as sonic boom alleviation, the reduction of aerodynamic losses (drag reduction) or combustion improvement.

The surface dielectric barrier discharge is first characterized without airflow in order to understand the influence of the applied electrical conditions and the structure of the DBD plate on the discharge regime its spatial distribution. Current curves and photomultiplier measurements show that the DBD comprises a filamentary and a continuous (glow- or corona-like) component. Increasing the applied voltage ramp (dU_2/dt) results in an increase in the filament generation rate and current peak amplitude. The geometry

of the electrodes has little effect on the burning voltage but plays a role in the filament generation rate. Encapsulation reduces the rate of filament production and the expansion of the plasma around the upper electrode but it generates a more uniform distribution of the plasma on the surface and as a function of time.

The behavior of the surface DBD in a high-speed air flow is first studied in a simple aerodynamic configuration: a flat DBD plate mounted on one wall of the nozzle. It is demonstrated that the DBD generated by this system can be sustained in supersonic airflows up to free stream Mach numbers of $M_\infty=1.1$. Current and time-resolved light emission measurements (photomultiplier) show that there are modifications in the discharge regime at high airflow velocity. For overall discharge, the filamentary to continuous component ratio is increased with increasing flow velocities, the plasma becomes relatively more filamentary. For individual microdischarges, the light pulse emission duration is reduced by one order of magnitude. These measurements indicate that there is a change in the breakdown mechanism and it is proposed that a transition from Townsend breakdown to streamer breakdown occurs when the airflow velocity is increased.

The inverse problem is then addressed, the effects of the DBD on the airflow, in a case where the plasma is generated on the surface of an airfoil and interacts with the shock structure in the transonic flow field around that airfoil. Although no significant effects of the surface DBD on the normal shock generated in the transonic flow have been observed with the Schlieren visualizations and far-field pressure measurements, the flow modifies the plasma characteristics in a very significant way. In addition to the effects of the flow velocity (as observed in the flat plate experiment), the significant variation of pressure on the surface of the airfoil plays an important role. Decreasing pressure increases the number of filaments and favors high current peak generation. It shows that the discharge characteristics cannot be completely controlled and that they depend on the flow field.

Keywords: surface dielectric barrier discharge, surface DBD, weakly ionized plasma, transonic flow, shock-boundary layer interaction, plasma flow control, plasma-assisted combustion, sonic boom mitigation

Version abrégée

L'utilisation des plasmas en aérodynamique est devenu un sujet d'intérêt récent. De nos jours, les potentialités des différents types de plasmas sont en étude pour le contrôle des écoulements à de faibles et hautes vitesses, mais aussi pour la combustion assistée par plasmas. Les décharges à barrière diélectrique (DBDs) représentent de bons candidats car la transition de la décharge lumineuse ou filamentaire vers une décharge de type arc est stoppée par la barrière diélectrique. De plus, les DBDs surfaciques permettent d'ioniser le gaz très proche de la surface du diélectrique et elles peuvent être utilisées pour ioniser la couche limite autour d'objets immergés dans un écoulement. La recherche en contrôle des écoulements a jusqu'à aujourd'hui suivi deux directions principales: l'étude des DBDs dans des écoulements basse vitesse et l'étude de décharges lumineuses ou couronne dans des écoulements supersoniques. Jusqu'à aujourd'hui, il a existé une importante barrière technologique aux études expérimentales des DBDs surfaciques. Les DBD surfaciques à pression atmosphérique étaient difficiles à maintenir pour de longues durées d'utilisation, typiquement plusieurs heures, car les espèces réactives créées dans le plasma (par exemple l'oxygène atomique) génèrent une ablation intensive de l'électrode ainsi que du matériaux diélectrique. L'oxydation des électrodes ou la réduction de l'épaisseur du diélectrique vont finalement mener à l'extinction du plasma ou à la formation d'arcs, respectivement. Cet important problème a empêché d'étudier en détails les DBDS dans des environnements extrêmes, notamment dans des écoulements d'air à hautes vitesses.

Dans le présent travail, une solution à ce problème technologique a été trouvée et est présentée. La technologie de lamination de céramiques à basse température (LTCC en anglais) permet, pour la première fois, d'encapsuler complètement les électrodes dans une matrice céramique et ainsi de maximiser la durée de vie du système DBD. L'encapsulation améliore ainsi la reproductibilité des expériences. De plus, la plaque peut être fabriquée avec une forme courbe. Cette avancée technologique permet, dans le cadre de la recherche présentée ici, de mener une étude expérimentale détaillée des DBDs dans des écoulements haute vitesse. Le but de cette recherche expérimentale est d'améliorer la compréhension physique de l'interaction entre une décharge locale atmosphérique, causant la faible ionisation locale de l'écoulement d'air environnant, et la structure de chocs dans des écoulements transsoniques et supersoniques typiques pour des applications aéronautiques. La nature fondamentale de la recherche la rend pertinente dans un large domaine d'applications comme l'atténuation du bang sonique, la réduction des pertes aérodynamiques (réduction de traînée) ou l'amélioration de la combustion.

La décharge à barrière diélectrique surfacique est tout d'abord caractérisée sans écoulement d'air dans le but de comprendre l'influence des conditions électriques appliquées et

de la structure de la plaque DBD sur le régime de la décharge et sur sa distribution spatiale. Les courbes de courant et les mesures avec un photomultiplicateur montrent que la DBD comprend une composante filamentaire et une composante continue (lumineuse ou couronne). Une augmentation de la rampe de tension appliquée (dU_2/dt) résulte en une augmentation du taux de génération des filaments et de l'amplitude des pics de courants. La géométrie des électrodes a peu d'effet sur le *burning voltage* mais joue un rôle dans le taux de génération de filaments. L'encapsulation réduit le taux de production de filaments et l'expansion du plasma autour de l'électrode supérieure mais génère une distribution plus uniforme du plasma sur la surface et en fonction du temps.

Le comportement de la DBD de surface dans un écoulement d'air à haute vitesse est tout d'abord étudiée dans une configuration aérodynamique simple: une plaque DBD plane montée sur une paroi de la tuyère. Il est démontré que la DBD générée par ce système peut être entretenue dans des écoulements d'air transsonique et supersonique jusqu'à des nombre de Mach de l'écoulement libre de $M_\infty=1.1$. Les mesures de courant et les mesures résolues en temps de l'émission lumineuse (photomultiplicateur) montrent que le régime de décharge est modifié à haute vitesse d'écoulement. Pour la décharge globale, le rapport de la composante filamentaire sur la composante continue augmente avec la vitesse de l'écoulement, le plasma devient plus filamentaire. Pour les microdécharges individuelles, la durée des impulsions de lumière est réduite d'un ordre de grandeur. Ces mesures indiquent un changement de mécanisme de claquage et il est proposé qu'une transition d'un claquage de type Townsend à un claquage de type streamer a lieu lorsque que la vitesse de l'écoulement est augmentée.

Le problème inverse est ensuite abordé, les effets de la DBD sur l'écoulement d'air, dans le cas où le plasma est généré sur la surface d'un profil d'aile et interagit avec la structure de chocs dans l'écoulement transsonique autour de ce profil. Bien qu'aucun effet significatif de la DBD surfacique sur le choc normal généré dans l'écoulement transsonique n'ait été observé par les visualisations Schlieren et les mesures de pressions dans le champ lointain, l'écoulement modifie les caractéristiques du plasma de manière très significative. En plus des effets dus à la vitesse de l'écoulement (comme observé dans l'expérience de la plaque plane), la variation significative de la pression à la surface du profil d'aile joue un rôle important. Une pression décroissante implique une augmentation du nombre de filaments et favorise la génération de pics de courant de grande amplitude. Ceci montre que les caractéristiques de la décharge ne peuvent pas être complètement contrôlées et qu'elles dépendent de l'écoulement.

Mots clé: décharge à barrière diélectrique surfacique, DBD surfacique, plasma faiblement ionisé, écoulement transsonique, interaction choc-couche limite, contrôle d'écoulements par plasma, combustion assistée par plasma, atténuation de bang sonique

Contents

Abstract	i
Version abrégée	iii
1 Introduction	1
1.1 Plasmas in aerodynamics	1
1.1.1 Principles	1
1.1.2 History	5
1.1.3 State of the art	6
1.2 Importance and objectives of the work	7
2 Physical background	9
2.1 Gas discharge physics	9
2.1.1 General considerations	9
2.1.2 Discharge regimes	11
2.1.3 Townsend breakdown	12
2.1.4 Streamer breakdown	14
2.1.5 Dielectric barrier discharges (DBD)	17
2.2 Compressible flows	18
2.2.1 Flow regimes	19
2.2.2 Viscous transonic flows	21
2.2.3 Sonic boom perspective	29
3 Experimental setup and diagnostics	33
3.1 DBD generation system	33
3.1.1 Flat DBD system	33
3.1.2 Electric circuit	34
3.2 Plasma diagnostics	35
3.2.1 Electrical characterization of the discharge	35
3.2.2 Time-resolved plasma light emission	36
3.2.3 Space-resolved light emission	36
3.2.4 Time- and space-resolved light emission	37
3.2.5 Optical emission spectroscopy	38
3.3 Generation of a surface plasma on an airfoil	39
3.3.1 Curved DBD system	39

3.3.2	Integration of the DBD on the surface of an airfoil	41
3.4	Transonic wind tunnels	43
3.4.1	Air supply system	43
3.4.2	Supersonic nozzle	43
3.4.3	Subsonic nozzle	45
3.5	Aerodynamic measurement techniques	46
3.5.1	Pressure measurements	46
3.5.2	Schlieren visualization method	48
4	DBD system without airflow	53
4.1	Influence of the electrical conditions	54
4.2	Influence of the DBD plate structure	59
4.2.1	Electrode geometry	59
4.2.2	Encapsulation	61
4.2.3	Dielectric properties	68
4.3	Summary	69
5	Effects of high-speed airflows on a flat surface DBD	71
5.1	Aerodynamic configuration	71
5.2	Burning voltage	73
5.3	Overall discharge regime	76
5.4	Microdischarge properties	78
5.5	Geometrical effects	80
5.6	Note on the reproducibility	82
5.7	Optical emission spectroscopy	83
5.8	Summary	86
6	Plasma-transonic flow interaction around an airfoil	89
6.1	Properties of the transonic flow	89
6.2	Effect of the DBD on the transonic flow	94
6.2.1	Shock structure	95
6.2.2	Far-field pressure gradient across the shock	100
6.2.3	Unsteady shock properties	101
6.3	Effect of the flow on the DBD	104
6.3.1	Discharge operation	104
6.3.2	Discharge regimes	107
6.3.3	Spatial discharge distribution	111
6.4	Summary	116
7	Conclusions	119
A	Theoretical complements on compressible fluids	123
A.1	Definitions	123
A.2	Rankine-Hugoniot relations	123
A.3	Turbulent compressible Navier-Stokes equations	124

B	NACA3506 coordinates	127
C	Complements on experimental results	129
D	Modeling	139
D.1	Description of the aerodynamic numerical model	139
D.2	Forced physical property changes on the blade surface	142
D.2.1	Modification of the viscosity	143
D.2.2	Modification of the turbulence level	145
D.2.3	Modifications of the surface geometry	147
D.2.4	Addition of ion wind	148
D.3	Summary	149
E	List of symbols	151
	Bibliography	155
	Remerciements	163
	Curriculum Vitae	165

Chapter 1

Introduction

1.1 Plasmas in aerodynamics

In the last few decades, the combination of plasma physics and aerodynamics has given rise to a completely new field of research. The need to understand the interaction between gas flows and plasmas has triggered the interest of physicists for aerodynamics. Reciprocally, aerodynamicists have been pushed towards plasma physics in their prospection for new flow control techniques. This collaboration has permitted the fast development of two main research areas: active airflow control using plasmas and plasma assisted ignition and combustion.

Non-thermal plasmas, which are plasmas out of thermodynamic equilibrium, have quickly turned out to be the most appropriate discharges for use in aeronautics, since they do not imply large temperature gradients in the surrounding materials, and their generation requires relatively low power input. This latter property makes them suitable for operation on board moving platforms like aircraft for example. These low power plasmas, such as glow discharges and coronas, have been extensively studied and used in very diverse plasma processing techniques, for instance material deposition or surface treatment. Because of their relatively low energy dissipation, they can alter the properties of a material surface without damaging the surface. However, it is only in the last ten years that investigations have suggested that creating weak ionization can modify aerodynamic properties of gas flows, not only at low velocities (subsonic) but also at high velocities (supersonic).

Compared to conventional control techniques, the main advantages of plasma-based flow control or combustion control devices are, in addition to their low-power consumption: their simplicity, robustness and their ability for high frequency actuation.

1.1.1 Principles

The ideal flow control device should be able to act on the airflow in the following manners: modify the laminar-turbulent transition inside the boundary layer, to prevent or to induce separation, to reduce the drag and to enhance the lift of airfoils, to stabilize or to mix airflow in order to avoid unsteadiness which generates unwanted vibrations, noise and

energy dissipation, to reduce shock strength in supersonic flows and thus sonic boom propagation.

The idea behind using plasmas for flow control is the following: in the case of most non-thermal discharges, the plasma is created by high-intensity electric fields. Free electrons are accelerated by this external field and collide with gas molecules, creating ions and additional electrons in an avalanche process. The resulting medium is made of electrons, different types of ions depending on the gas, and neutrals. Its physical properties are different from the initial completely neutral gas. Internal energy (rotational and vibrational states of the molecules) or viscosity for example are different (due to heating for example). Moreover, the trajectories and velocities of the charged particles contained in the plasma can be modified via external electric or magnetic fields. They can be used to transfer momentum to the fluid particles (neutrals) thus modifying the flow properties locally.

Volume as well as surface discharges have been used in order to study the plasma-gas flow interaction. Figure 1.1 shows an experiment of high-speed flow control (Mach=3.2) with a volume discharge. In the second image, a glow discharge is created between the tip electrode (outside the image, on the right) and the truncated cone, in the conical volume surrounding the tip. The plasma clearly modifies the structure of the shock formed in the supersonic flow around the cone.

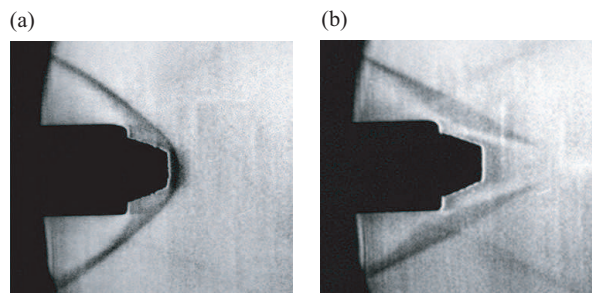


Figure 1.1: High-speed flow control experiment with a volume DC glow discharge operated in a Mach=3.2 airflow from Lebedev et al. [1]. Images are Schlieren visualizations of the flow with the discharge off (a) and the discharge on (b).

Figure 1.2 shows an example of low-speed flow control (free stream velocity is about 3 m/s) with a surface discharge. In the second image, a surface dielectric barrier discharge is generated on the airfoil, and delays the separation of the flow.

In the perspective of using plasmas for airflow control, surface plasmas are more appropriate for aeronautical applications, since they do not require an electrode sticking out of the object to ionize the gas in the volume surrounding it. Surface discharges used for aerodynamic applications are mainly corona and dielectric barrier discharges (DBD), because of their relatively simple geometry and operation. An important advantage is that they can be operated at atmospheric pressure. Figures 1.3 and 1.4 show the typical corona and DBD set-up.

The typical surface corona discharge generation system is made of two surface electrodes separated by a certain gas gap. A DC or AC high voltage (of the order of several

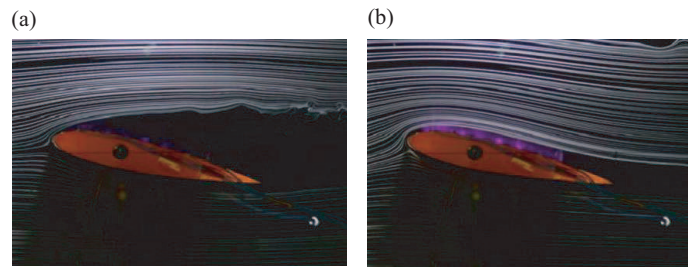


Figure 1.2: Low-speed flow control experiment with an asymmetric dielectric barrier discharge operated in a 3 m/s airflow [2]. Images are taken with the discharge off (a) and the discharge on (b).

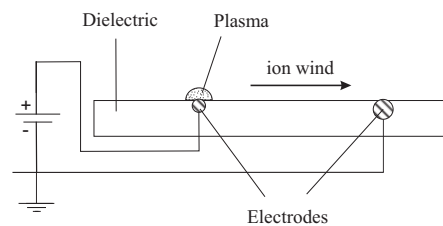


Figure 1.3: Corona discharge arrangement. If the small electrode is polarized positively and the large one negatively, the discharge is called *positive corona*. In the opposite case, the discharge is called *negative corona*.

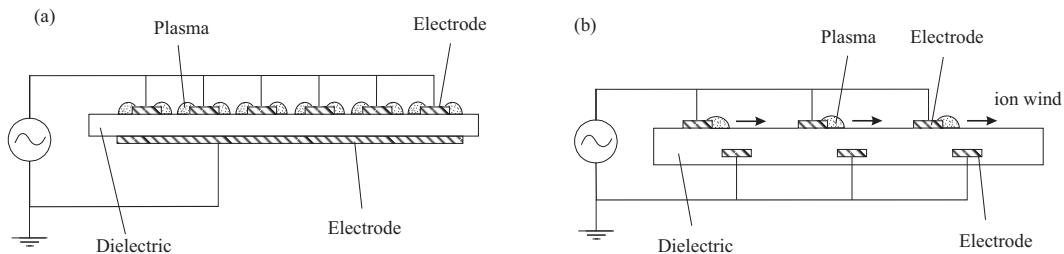


Figure 1.4: Symmetric dielectric barrier discharge (DBD) arrangement (left) and asymmetric DBD arrangement (right) for the generation of ion wind.

kV) is applied between them. The typical surface DBD system is composed of basically two electrodes separated by a dielectric. An AC voltage must be applied between the electrodes. Indeed, the charges (electrons) accumulate on the dielectric, compensating the external electric field and quenching the discharge. The polarity has thus to be inverted in order to maintain electron motion and collisions and thus maintain the discharge. The corona discharge with asymmetric electrodes and asymmetric DBD have been recognized to generate what is called *ion wind*, that is, momentum transfer from ions to the surrounding fluid. This is the aspect that has been most studied to date in subsonic air flows. However, the velocities that can be generated with today's systems are only of the order of 10 m/s. An example of velocity distribution generated by a DBD is given by

measurements from Moreau et al. in figure 1.5.

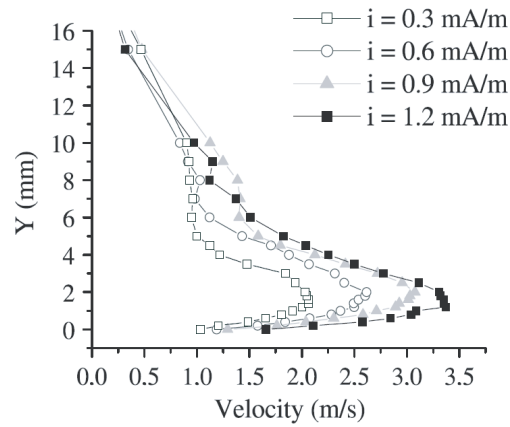


Figure 1.5: Example of measurements of the ion wind generated by a DBD, performed by Moreau et al. [3], with a glass Pitot tube.

Experimental but also theoretical studies are being carried out to find out if higher speeds could be achieved. Corona and DBD discharges give the same magnitudes of induced velocity. DBD are preferred over corona because the discharge is more stable. Indeed, the dielectric prevents the transition to an arc and the consecutive destruction of the system. Moreover, they are less sensitive than coronas to gas parameters like humidity and temperature for example. Symmetric DBD is known for generating turbulence in the gas close to the surface as shown by Opaits et al or Jukes et al. for example [4, 5]. A flow visualization by Jukes et al. is shown in figure 1.6.

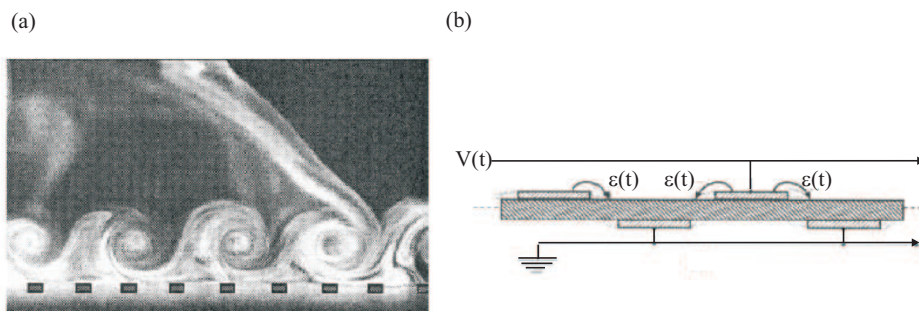


Figure 1.6: Visualization of the vortices (a) induced by successive three-electrode DBD actuators (b) from Jukes et al. [5].

In addition to flow control, DBD and corona discharge are often used in combustion experiments as well. Despite the fact that the principle of spark ignition has been used in the automobile industry for a long time, there are different applications where the use of other plasma systems might be of significant interest, for example ignition of fuel-air mixtures at moderate gas densities and high-velocity gas flows (including supersonic) or combustion enhancement at atmospheric pressure. When the electric field strength

is sufficient to cause electrical breakdown of a fuel or fuel-air mixture, plasma effects will dominate. Electron and ion temperatures can be increased and promote combustion through the formation of active species such as free radicals or the dissociation of fuel molecules into smaller, more easily combustible fragments. For combustion assistance, non-equilibrium plasmas can give a better control on the energy input into a gas. The direct energy input into gas degrees of freedom responsible for a given ignition or combustion reaction will greatly improve the ignition process. Even a relatively small fraction of atoms and radicals (10^{-5} to 10^{-3} of the total number of gas particles) can shift the equilibria in the system and initiate combustion. Moreover, if such a concentration of active particles is produced uniformly over the entire volume of gas, the combustion can be achieved in a non-detonation character. Dissociation rates could be about two orders of magnitude higher than in normal combustion [6].

1.1.2 History

Very early experiments performed during the 18th century already suggested that plasmas could generate movement of particles, that is, flows. As early as in 1709, Hauksbee reported for the first time a movement of gas induced by the repulsion of ions from a high voltage electrode. This phenomenon was first explained by Faraday in 1838. The first mathematical expression of what was then named *electric wind*, *corona wind* or *electric aura* was given in 1961 by Robinson [7].

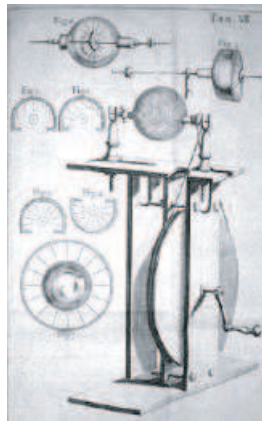


Figure 1.7: Early gas discharge experiments by Hauksbee [8].

Preliminary research on ion wind was started in the 1950s, generating a few patents in Europe and the United States. The first scientific papers were published in 1968 by Velkoff and Ketchman [9] and by Yabe [10], but the field really emerged in the middle of the 1990s. First experiments were performed with DC surface corona discharges. Then, in 1994, the group of J. R. Roth realized that the discharge they had developed for decontamination purposes could also induce a secondary airflow of several meters per second [11]. This discharge was a surface dielectric barrier discharge that they patented under the name OAUGDPTM (One Atmosphere Uniform Glow Discharge Plasma).

Dielectric barrier discharges, in their volume configuration, have been known for more than a century though. They are widely used in many different applications such as ozone generation, decontamination of gas streams and surface treatments. They have been utilized as sources for CO₂ lasers, excimer and fluorescent lamps and plasma display panels [12]. The very first experiments on dielectric barrier discharges were reported by Siemens in 1857. Thorough research with new diagnostic techniques and numerical modelling started in the 1970s.

Until very recently, the mutual interactions of plasmas and high speed flows was studied mainly in the former Soviet Union and the in the United States. There are reports from 1980s of large changes in the shock standoff distance ahead of a blunt body in ballistic tunnels, significantly reduced drag and modifications of travelling shocks in bounded weakly ionized gases. The first experiments investigating the propagation of shock waves in low pressure plasmas, where it was noted that the observations could not completely be explained by the effects of thermal gradients, were published in 1982 by Klimov et al. [13]. Progress in vehicle design and in material sciences at the beginning of the 1990s generated enthusiasm to investigate plasma mechanisms to modify high-speed external flows and reduce drag.

Finally, the application of electric fields to flames has been studied as far back as 1814 [14]. It was applied to the combustion in the 1920s [15] and was further developed for several applications in the last half of the 20th century [16].

This brief historical perspective shows that the fields of plasma flow control and plasma assisted combustion are very recent, scientifically speaking. Experiments oriented towards applications are no older than 15 years. The research as well as technical developments are nowadays in full expansion. However, technical experience and scientific understanding has still to be acquired in order to optimize plasma-flow interaction.

1.1.3 State of the art

As mentioned before, the use of surface plasmas in low speed airflows has become a recent topic of interest in the field of airflow control [3]. Recent work on the ion wind generation using asymmetric electrode DBDs can be found in [17–19]. The physics of DBDs has been studied mostly in the volume discharge configuration [20], at sub-atmospheric or atmospheric pressures, using different working gases including air. It is believed that metastable states as well as impurities etched from the dielectric surface play a key role in the behavior of the plasma [21–23]. The surface discharge configuration has been less investigated due to its complexity. Indeed, such an arrangement generates a very thin plasma layer, typically less than one millimeter, which disqualifies a certain number of standard plasma diagnostics generally used in the volume arrangement. Different geometries of the surface electrodes have been compared [24,25], but the physical properties of such plasmas are still difficult to investigate quantitatively.

For supersonic and hypersonic flow control, mostly volume discharges have been used [1,26]. A topical review can be found in [27]. Surface plasmas begin to be tested in high speed flows [28], but up to now there has been an important technological barrier hindering experimental investigations. Atmospheric pressure surface DBDs in air have

been difficult to maintain for long operation times, typically several hours, because reactive species created in the plasma (for example atomic oxygen) generate intensive etching of the electrode and dielectric materials. Oxidation of the electrodes or reduction of the dielectric thickness will eventually lead to plasma extinction or arcing respectively. This important issue has prevented detailed studies of DBDs in extreme environment, namely high-speed airflows in air.

In combustion research, various methods of acceleration of ignition have been considered, both thermal and non-equilibrium. Laser techniques present the disadvantage of requiring complex equipment. Spark ignition can be interesting for hypersonic conditions, but it imposes important restrictions on the geometry of the system. Low-temperature non-equilibrium plasmas represent an interesting alternative for initiating or supporting combustion. Different techniques have been tested, such as pulsed coronas, microwave discharge, pulsed nanosecond sparks, pulsed nanosecond DBDs and volume nanosecond glow discharges. A detailed review can be found in [6].

Physical models are still at a relatively early stage. DBDs in low-speed gas flows are starting to be studied theoretically and numerically [18, 29, 30]. This is due not only to the complexity of the physical phenomena involved in surface DBDs, but mainly to the important difference in timescales between plasma phenomena and aerodynamic phenomena. Discharge durations are of the order of several tens of nanoseconds, whereas flow perturbations are at least of the order of milliseconds typically. Moreover, the chemistry of the plasma, which becomes rather complex in the case of air where hundreds of different reactions can occur, represents an additional complexity.

1.2 Importance and objectives of the work

There are still numerous open questions in the fields of plasma flow control and plasma-assisted combustion. These areas of research being fairly recent, research has followed many different paths. Different kinds of plasmas and different velocity ranges have been combined, but detailed studies have only emerged in the last few years, basically forming two main groups: the study of DBDs in low-speed airflows and the study of volume glow or corona discharges in supersonic airflows. Surface DBDs experiments in supersonic airflows, which seem to be more realistic than volume discharges for future applications, have been briefly presented in a few papers but the short lifetime of the systems used has become a technological barrier and prevented further research in this direction.

The motivations of the present work are therefore both technical and fundamental. In order to be able to carry out the experimental study of the interaction of a surface DBD with a transonic flow, the following development phases have to be achieved:

- Find a solution to the technological barrier mentioned above, which is the short lifetime of DBD systems.
- Integrate the system on the (curved) surface of an airfoil.
- Demonstrate that a DBD can be sustained in transonic and supersonic air flows.

- Develop adapted plasma diagnostics, aerodynamic measurements techniques and analysis methods for the study plasma-flow interaction in transonic conditions.

After the completion of these phases, the following more fundamental objectives can be pursued:

- Study the DBD behavior in high-speed flows.
- Study the influence of a plasma on a high-speed flow, more specifically, the influence of a DBD on the shock structure in a transonic flow.
- Improve the physical understanding of the phenomena observed (modeling).

This research can be considered as fundamental, coupling plasma physics of non-equilibrium gas discharges and compressible fluid dynamics. The effect of the discharge on the flow but also the effect of the flow on the discharge are investigated. In the future, the present findings can be of purely theoretical interest but also of technical interest. They can be used to optimize discharge configurations and maximize plasma-flow coupling. The fundamental nature of the research will make it relevant in a large domain of applications. Important long-term applications can be pointed out:

- Sonic boom alleviation (supersonic aircraft including atmospheric re-entry vehicles).
- Reduction of aerodynamic losses, drag reduction (subsonic and supersonic aircraft, turbomachinery).
- Improvement of combustion (scramjet).

The present research has been supported by the Swiss National Science Foundation (FNS funds n° 200021-101458/1 and 200020-111879/1). The project was a collaboration involving three laboratories at EPFL:

- the Laboratoire de Thermique Appliquée et Turbomachines (LTT) of the Ecole Polytechnique Fédérale de Lausanne (EPFL) (Dr. P. Ott);
- the Centre de Recherches en Physique des Plasmas (CRPP) of EPFL (Dr. J.-L. Dorier and Dr. Ch. Hollenstein);
- the Laboratoire d'Ingénierie Numérique (LIN) of EPFL (Dr. P. Leyland).

The structure of the present manuscript is as follows. Chapter 2 introduces the theory used for the physical approach of the plasma-flow interaction. Chapter 3 describes the experimental setup as well as plasma and aerodynamic measurement techniques. Experimental results are presented and discussed in chapter 4 to 6. In Chapter 4, the DBD systems considered are characterized without airflow. In Chapter 5, the behavior of the surface DBD is studied in a high-speed flow, in a simple aerodynamic configuration (flat DBD plate mounted on a wall of the subsonic nozzle). Finally, chapter 6 presents the results of the plasma-flow interaction experiment using an airfoil.

Chapter 2

Physical background

2.1 Gas discharge physics

2.1.1 General considerations

The ionization of gases, which forms a plasma, can be achieved mainly in two ways: by adding thermal energy or by applying an external electric field.

- In the first case, when the thermal energy of the gas becomes of the same order of magnitude as the ionization energy, the electrons of the higher energy states of the atoms or molecules in the gas receive sufficient energy from the inelastic collisions with other particles of the gas to overcome binding forces in the atom. This is the process that takes place in stars, where the temperature in the core can reach millions of degrees.
- On the other hand, plasma can also be obtained using high intensity external electromagnetic field sources. In this case, free electrons are accelerated by the external electric field and collide inelastically with the molecules present in the gas, creating ions and more electrons. In addition to that, excited molecules and radicals are formed, which will react with each other and the working gas to form a very rich chemistry (depending on the complexity of the working gas).

The fundamental role that electrons play in thermal and cold plasmas has led to a classification of the different plasma states in terms of electron density n_e and electron temperature T_e , as shown in figure 2.1. Electron densities can go from 10^3 to more than 10^{20} electrons per cm^3 , whereas electron temperature can go from 10^{-2} eV to 10^5 eV¹.

An additional fundamental parameter is the degree of ionization of a plasma:

$$\alpha_i = \frac{n_e}{n_e + n_n} \quad (2.1)$$

where n_e and n_n are the densities of electrons and neutrals respectively. Plasmas are sometimes categorized by this degree of ionization in the following way:

¹1 eV \sim 11'600 K

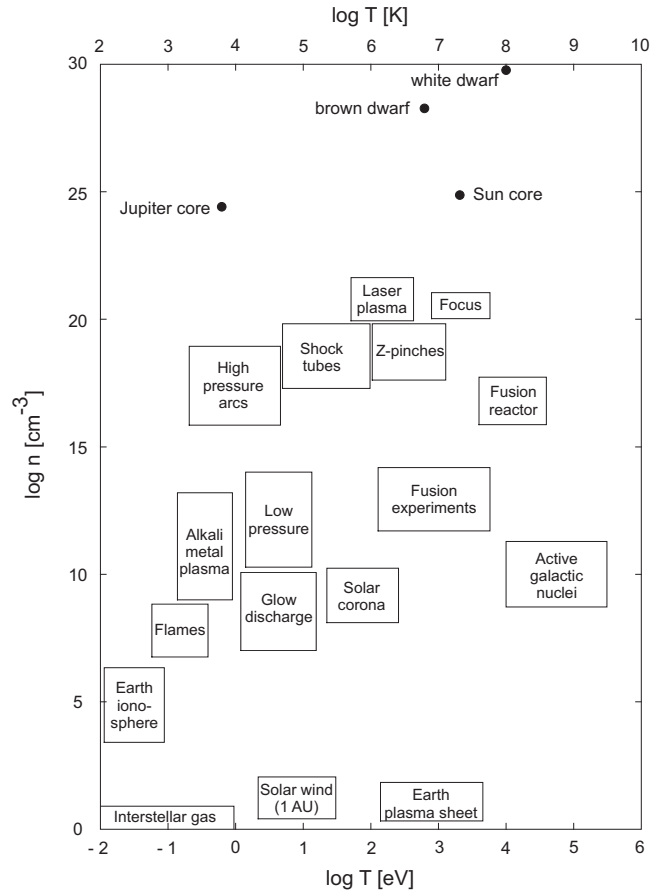


Figure 2.1: Classification of different types of plasma [31].

- $\alpha_i > 10^{-3}$: highly ionized and fully ionized plasmas, sometimes called *hot plasmas*
- $\alpha_i < 10^{-3}$: weakly ionized plasmas, sometimes called *cold plasmas*

Cold plasmas are further separated in two sub-categories according to their thermodynamic state:

- Thermal plasmas: plasmas in thermodynamic equilibrium, where the temperatures of electrons, ions and neutral species are equal: $T_e \simeq T_i \simeq T_n$. This is the case for high pressure arcs for example.
- Non-equilibrium plasmas: plasmas out of thermodynamic equilibrium, where the electron temperature is higher than the temperature of ions and neutrals $T_e > T_i \simeq T_n$. In this kind of discharge the distribution function of electrons is generally non-Maxwellian. This is the case in low-density electrical discharges.

2.1.2 Discharge regimes

The different existing gas discharge regimes can be classified according to their voltage vs. current characteristics as depicted in figure 2.2. These different conditions can be created changing for example the gas pressure, the electrode gap or the electrode configuration.

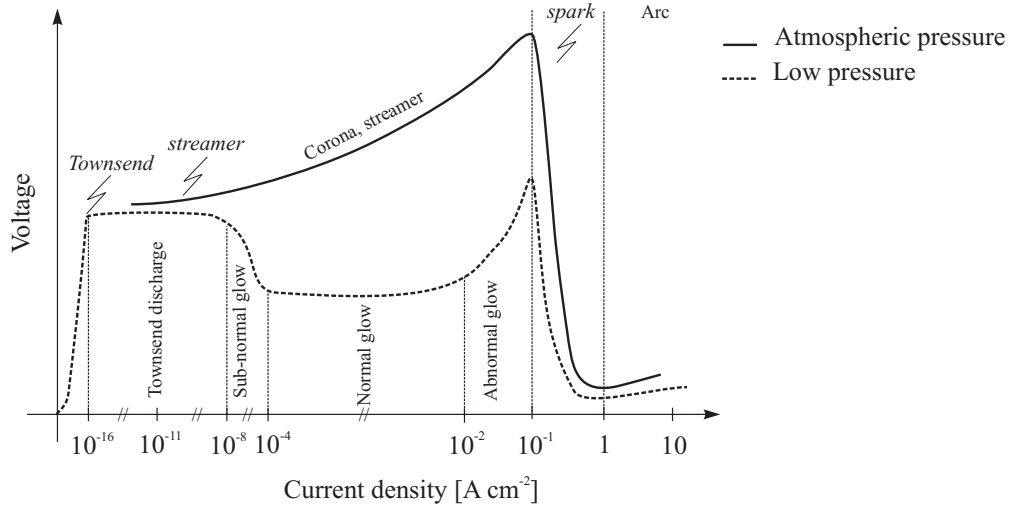


Figure 2.2: Gas discharge regimes characterized by their current density-voltage curves, adapted from [20, 32].

The upper curve corresponds to high-pressure discharges ($\sim p_{atm}$, atmospheric pressure), whereas the lower curve represents low-pressure discharges (< 1 mbar typically).

From figure 2.2, four main categories of stable or quasi-stable discharges can be distinguished:

- The dark Townsend discharge, characterized by very low current densities. The discharge is sustained by the emission of electrons via ion bombardment of the cathode (=secondary electron emission).
- The glow discharge, with low current densities. This kind of plasma is widely used in industrial applications. It is weakly ionized and out of thermal equilibrium. In most cases the discharge is sustained by secondary electron emission.
- The corona discharge and streamer discharge at atmospheric pressure. It forms usually in highly non-uniform electric fields. In these discharges electrons are produced not only by secondary emission processes but they can also be produced by photo-ionization.
- The arc discharge, carrying a very high current densities at relatively low voltages, and emitting light at high intensities. In arcs, the electron emission process is not due to ion bombardment but to thermionic emission due to the heating of the cathode. High pressure arcs are generally in thermodynamic equilibrium.

At high pressures, the discharge is usually *filamentary*², although in some very specific conditions a glow discharge can be obtained at atmospheric pressures.

In addition to these four categories, transient processes involved in the breakdown of these discharges can be recognized. Three different types can be observed:

- The Townsend breakdown
- The streamer breakdown
- The spark breakdown

These are transition mechanisms of limited lifetime which lead to the steady regimes described before. In any breakdown the *primary process* is the electron avalanche. Then *secondary processes* intervene which will determine how the discharge is sustained. Townsend and streamer breakdown are important in dielectric barrier discharges and are detailed below.

2.1.3 Townsend breakdown

Townsend breakdown generally occurs at low values of the $p \cdot d$ factor, which is the pressure multiplied by the inter-electrode gas gap.

In order to understand the breakdown mechanism, let us consider two plane electrodes separated by a gap of length d and connected to a DC power supply giving a voltage V (see figure 2.3). A uniform electric field $E = V/d$ is thus created between the electrodes. *Seed electrons* coming from external sources (cosmic rays, natural radioactivity) are accelerated by this electric field and drift to the anode, creating a low initial current. If the voltage is sufficiently high and the mean free path³ long enough, electrons have enough energy to ionize the gas by inelastic collisions, generating an avalanche and thus amplifying the current. The ionization in the avalanche can be described by the Townsend ionization coefficient α , which gives the increase in electron density per unit length

$$\alpha = \frac{1}{n_e} \frac{dn_e}{dx} \quad (2.2)$$

or

$$n_e(x) = n_{e0} e^{\alpha x} \quad (2.3)$$

This means that every seed electron generated near the cathode produces $e^{\alpha d} - 1$ positive ions in the gap, if recombination or binding to electronegative molecules is neglected. In other words, the current is multiplied by $e^{\alpha d}$.

When the voltage is further raised, all the $e^{\alpha d} - 1$ positive ions produced in the gap move back to the cathode and have enough energy to expel $\gamma[e^{\alpha d} - 1]$ electrons from the cathode

²Filamentary means composed of filaments. A filament is a generic term for a thin plasma channel. A filament can be generated by Townsend or by streamer breakdown.

³The mean free path λ_{mfp} is the distance an electron travels before colliding with a target $\lambda_{mfp} = (n_t \sigma_c)^{-1}$ where n_t is the density of targets and σ_c the collision cross section

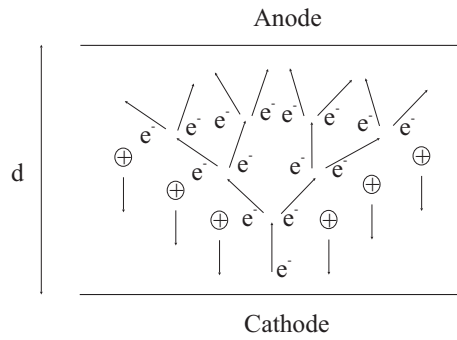


Figure 2.3: Electron multiplication in a gas gap.

in the process of secondary electron emission. γ is the probability of electron emission by the cathode under ion bombardment. It depends on the cathode material, the state of its surface, the type of gas and the reduced electric field E/n_{e0} . Secondary electron emission can be enhanced by photo-ionization, and photon⁴ or metastable⁵ bombardment. These two effects are usually included in the γ coefficient. When the voltage is high enough so that secondary emission effects take place, the current is said to be *self-sustained*, i.e. breakdown occurs. The breakdown condition is therefore:

$$\gamma[e^{\alpha d} - 1] \geq 1 \quad (2.4)$$

at a voltage $V \geq V_{br}$. The minimum breakdown voltage V_{br} condition has been described empirically by Paschen [33]. According to his law, V_{br} depends only on the $p \cdot d$ factor and the gas. So-called Paschen curves for air is shown in figure 2.4.

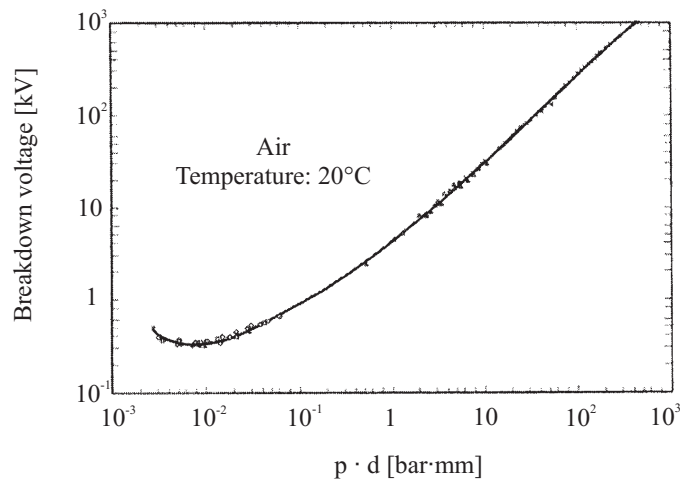


Figure 2.4: Paschen breakdown voltages for static breakdown in air (based on Dakin et al. [34]).

⁴Emission by photon bombardment is called *photoemission*.

⁵Metastables are long lifetime excited states

This curve is valid at a certain temperature T . It should be noted that humidity has an influence on breakdown voltage in air [35]. Moreover, the breakdown voltage is also dependent on the frequency of the applied voltage function [36].

Pachen curves can actually be obtained with the following relation [37]:

$$V_{br} = \frac{Bpd}{\ln(Apd) - \ln[\ln(1/\gamma) + 1]} \quad (2.5)$$

where A and B are constants depending on the type of gas. When $V > V_{br}$, a dark Townsend discharge forms first. The resistance of the circuit has to be large enough to limit the discharge current so that the positive *space charge*⁶ accumulating between the electrodes does not distort the applied electric field E . If the current rises, the electric field becomes inhomogeneous and the discharge becomes a *glow discharge*. The space charge becoming more important the voltage necessary to maintain the discharge is smaller. Indeed, a *cathode fall* is formed where positive charges grouped around the cathode induce a high intensity electric field. A quasi-neutral column forms between the electrodes. The glow discharge is *homogeneous* because the avalanches can start at different points on the cathode or the electrons can migrate on its surface. Townsend discharges can be homogeneous or display a filamentary pattern.

2.1.4 Streamer breakdown

Depending on the $p \cdot d$ factor and on the *overvoltage* $\Delta V = V - V_{br}$, as shown in figure 2.5, the breakdown is no longer a Townsend breakdown but follows another mechanism called *streamer breakdown*.

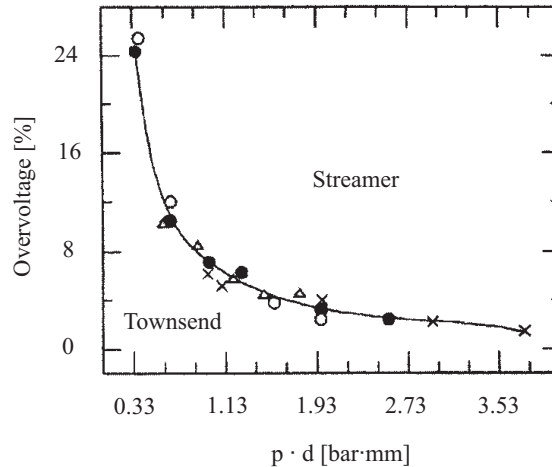


Figure 2.5: Limit between Townsend breakdown and streamer breakdown [38].

In the Townsend region, the amplification of the electron avalanche is still under a certain critical value $e^{ad} \leq N_{cr} \sim 10^{-8}$ where the space charge created by the avalanche

⁶charge accumulated at a certain position in space

does not distort the applied electric field E . This is Meek's criterion [32]. Past this limit, the accumulation of local space charges induces a completely different breakdown mechanism, the streamer breakdown. This mechanism is too fast (~ 1 ns) to be due to secondary electron emission at the cathode. It results in a thin plasma channel or filament.

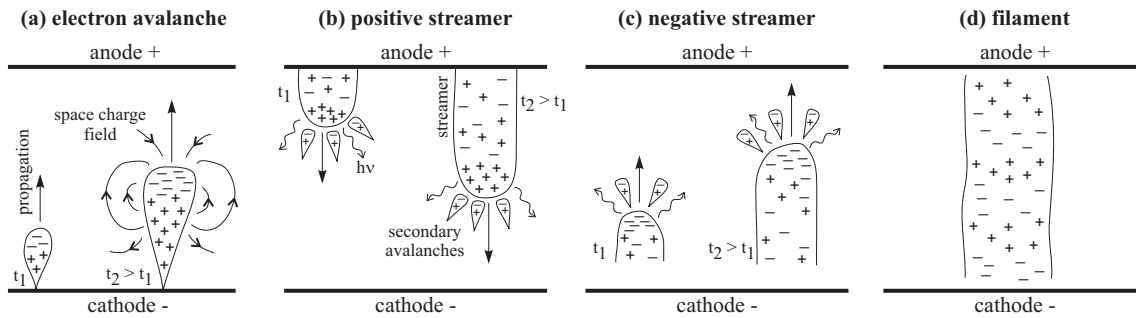


Figure 2.6: Streamer breakdown mechanism [39]. t_1 and t_2 are two different instants in the same propagation phase.

The streamer mechanism can be explained as a succession of three stages leading to the formation of a filament:

- Primary avalanche and transition to streamer (figure 2.6 (a))

A strong avalanche forms by multiplication of the primary electrons in the high electric field and grows very rapidly from the cathode to the anode. The polarization of the charges inside the avalanche, electrons at the head and ions at the tail, create an electric *space charge field* E_{sc} . This electric field increases as the avalanche propagates and amplifies. As soon as E_{sc} is equal or greater than the external electric field, $E_{sc} \geq E$ ($\Rightarrow e^{ad} \geq N_{cr}$), a weakly ionized region can be created. Indeed, in these conditions the local field is stronger than the external field and charged particles will be mostly influenced by the local field. This local ionization initiates the streamer.

- Streamer propagation (figure 2.6 (b) and (c))

Once the streamer is initiated, it propagates following a branched path due to the random nature of the propagation mechanism. The speed of this propagation can reach 10^6 m/s. The propagation can be directed towards the anode or the cathode, depending on the gap distance and voltage.

For moderate gaps and moderate voltages, the avalanche-to-streamer transition takes place only when the primary avalanche has reached the anode. The avalanche has not grown enough and the space charge field is not strong enough to create an ionized region before the avalanche has reached the anode. When the avalanche reaches the anode, only the positive charges in the tail of the avalanche are left in the gas gap. The streamer starts from there and propagates towards the cathode. This kind of streamer is called *cathode-directed* or *positive* streamer (figure 2.6 (b)). Its growth is caused by small avalanches created near the positive region that has

become the head of the streamer. These small avalanches are seeded by electrons created by photo-ionization⁷. The electrons of these avalanches are rapidly attracted into the streamer, neutralizing the streamer positive head and leaving behind them the positive ions of the small avalanches (ions move much slower than electrons). These positive charges become the new head of the extended streamer. This is how the positive streamer grows.

For large gaps or strong voltages, the space charge field of the primary avalanche is sufficiently high to create the streamer before reaching the anode. The avalanche-to-streamer transition occurs in the gap. Then, the streamer propagates towards both electrodes at the same time. If the avalanche-to-streamer transition occurs while the avalanche has not yet gone far from the cathode, the streamer grows mostly towards the anode. In this case, the streamer is called *anode-directed* or *negative* streamer (figure 2.6 (c)). The growth mechanism towards the cathode remains the same as described before, but the growth to the anode is slightly different. Here, the electrons of the primary avalanche are forming a negative streamer head. These electrons are rapidly neutralizing the positive ions of the small avalanches also initiated near the streamer head by photo-ionization and by moving electrons as shown in figure 2.6. The electrons of the small avalanches are then forming the new head of the extended streamer.

Thus, for both positive and negative streamers, the streamer is *fed* with charges created ahead of its tip by small avalanches.

- Discharge phase (figure 2.6 (d))

Once the streamer bridges the gas gap, the breakdown phase is finished and the discharge phase begins. A filament forms, which is a thin weakly ionized plasma channel. In a dielectric barrier discharge, the dielectric prevents the transition from the filament to the arc, which is a highly ionized plasma channel, and limits its lifetime to a few tens of nanoseconds.

A discharge can be composed of a multitude of filaments initiated by streamer breakdown and appearing in a random and independent way in the gas gap. If the density of primary avalanches is high, the discharge can appear homogeneous. This regime is called *streamer-coupling regime* [21]).

At atmospheric pressure, it is possible to generate a glow or Townsend discharge in certain gases, provided certain conditions are respected. In the presence of nitrogen for example, the growth of the primary avalanche can be slowed down by generating more electrons under smaller electric fields with the help of metastable states created during a preceding discharge [40]. In these conditions, the $p \cdot d$ criteria are modified.

⁷Photons come from the de-excitation of species in the volume of the discharge. For example, DBDs generate intense UV emission. Photo-ionization can also be generated artificially by an external light source.

2.1.5 Dielectric barrier discharges (DBD)

Dielectric barrier discharges can be created in very different kinds of geometries, provided there is at least one dielectric barrier (insulator) between two electrodes. They can be categorized in two main groups illustrated in figure 2.7, volume and surface discharges.

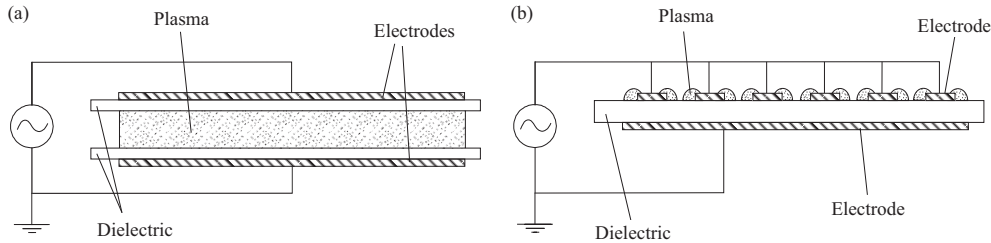


Figure 2.7: DBD set-up in the volume configuration (a) and in the surface configuration (b).

As mentioned above, volume DBDs have been mostly studied because they are technically easier to investigate than surface DBDs. Volume DBDs can be sustained in a filamentary regime, in a homogeneous regime (Townsend or glow) or in a multi-peak regime, depending mainly on the electrode configuration, voltage, pressure or working gas. It is believed that metastable states created in the gas gap play an important role in the discharge mechanisms. In the filamentary regime, a large quantity of short-duration micro-discharges form, randomly arranged in the inter-electrode gap. The current pulses are very short, a few tens of nanoseconds, and their spatial and temporal distribution is not reproducible from one discharge period to the other. The glow and the Townsend regimes display only one current peak per half-period of the voltage. It is a few microseconds long for the glow discharge and a few tens of microseconds long for the Townsend discharge. In the multi-peak regime, several current peaks appear during each half-period. They are reproducible and last about 1 microsecond [41].

Surface dielectric barrier discharges in air at atmospheric pressure exhibit a strong filamentary behavior, as shown in figure 2.8 (a). Homogeneous regions are also visible on pictures of the discharges, in addition to the filaments. The principle is shown in figure 2.8 (b). During the negative current alternance, the top electrode is the cathode. Electrons are produced at the top electrode and accelerated in the intense surface electric field. They start accumulating on the dielectric surface until the external electric field is balanced by the space charge they form. The discharge is then quenched. On the positive alternance, the dielectric becomes the cathode. Electrons are desorbed from the surface and accelerated in the opposite direction.

Typical physical characteristics of DBDs are given in table 2.1, and compared to those of classical discharge regimes.

The number density of electrons in filamentary discharges and DBDs has not been measured experimentally yet, because of the complexity induced by the spatial inhomogeneity of the discharge. Some of the values given in table 2.1 are estimations deduced from numerical simulations.

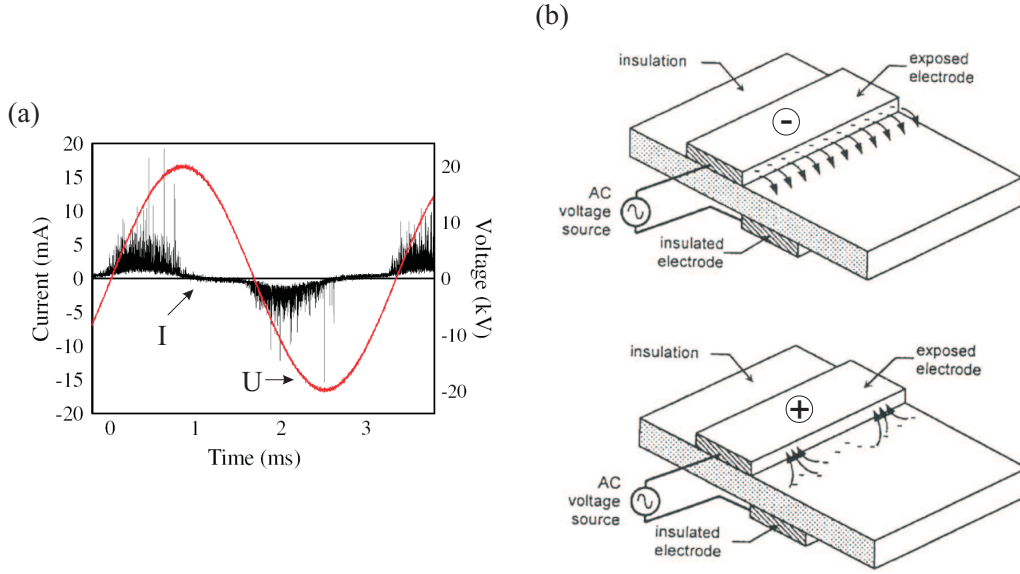


Figure 2.8: Typical current curve for a surface DBD from Moreau [3] (a) and schematic illustration of the charge movement on each voltage half-period from Enloe et al. [42] (b).

Parameter	Arc	Glow	Streamer	DBD
Pressure [bar]	up to 10-20	10^{-5} - 10^{-1}	0.1-1	10^{-3} -1
Current [A]	1 - 10^5	10^{-4} - 10^{-1}	10^{-4} - 10^{-3}	10^{-4} - 10^{-1}
Voltage	10-100 V	100-1000 V	10-100 kV	1-10 kV
E (at 1 bar)	1 - 100 V cm $^{-1}$	10 - 50 kV cm $^{-1}$	30 - 100 kV cm $^{-1}$	30 - 100 kV cm $^{-1}$
T_g [K]	3000-30000	300-600	300-400	300-600
T_e [eV]	0.5-1	1-10	1-5	1-10
n_e [cm $^{-3}$]	10^{15} - 10^{16}	10^{11} - 10^{16}	10^{11} - 10^{13}	10^{11} - 10^{14}
Spatial distribution	non-uniform	uniform	non-uniform	uniform or non-uniform

Table 2.1: Typical physical characteristics of different discharge types compared to the DBD, adapted from [6, 12].

2.2 Compressible flows

Compressibility effects on airplane aerodynamics have been important since the advent of high-speed and high-performance aircraft in the 1940s. Flow velocities higher than 0.3 of the speed of sound are associated with relatively large pressure changes and large changes in the fluid density.

The compressibility β of a fluid is defined as:

$$\beta = -\frac{1}{v} \left(\frac{\partial v}{\partial p} \right)_T \quad (2.6)$$

where v is the volume of an element of fluid which variation in volume dv is caused by a variation of the surrounding pressure dp . If the fluid element is assumed to have unit mass, v is the specific volume and the density is $\rho = 1/v$. Equation 2.7 can be written in

terms of density as:

$$\beta = -\frac{1}{\rho} \left(\frac{\partial \rho}{\partial p} \right)_T \quad (2.7)$$

Whenever the fluid experiences a change in pressure dp , the corresponding change in density will be:

$$\partial \rho = \rho \beta \partial p \quad (2.8)$$

In gases, values of β are large and moderate to strong pressure gradients lead to substantial changes in the density. At the same time, such pressure gradients create large velocity changes in the gas. Such flows are defined as *compressible flows* where ρ is a variable.

2.2.1 Flow regimes

Consider a body in a flowing gas. Depending on the upstream velocity of the flow, several different flow regimes can be defined, as depicted in figure 2.9. U_∞ is the *free-stream velocity*, i.e. the velocity far upstream of the body, where the flow is supposed to be uniform and unperturbed. If a_∞ is the speed of sound in the uniform free stream, then the free stream Mach number M_∞ is defined as the ratio U_∞/a_∞ .

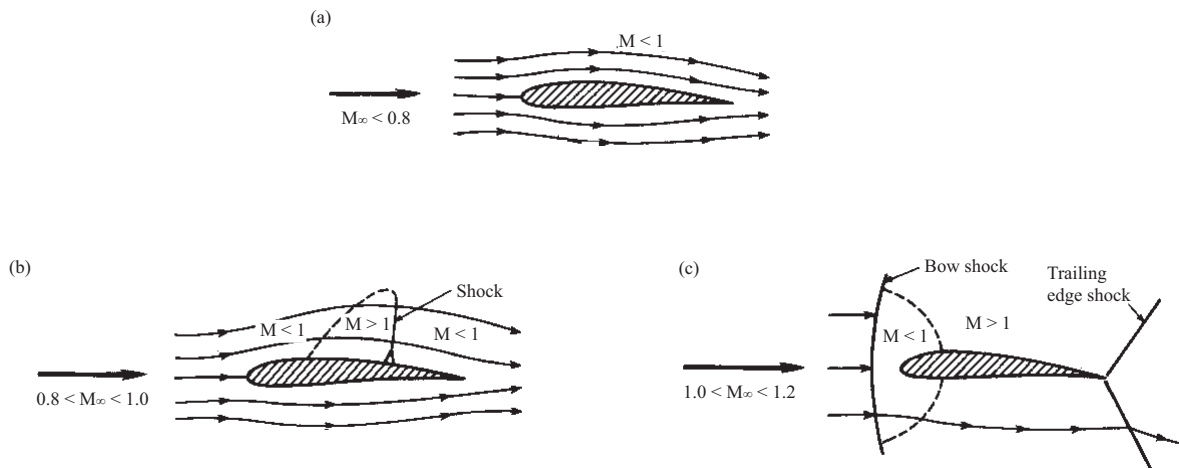


Figure 2.9: Illustration of flow regimes [43].

A flow is defined as *subsonic* (figure 2.9 (a)) when the velocity is less than the speed of sound (i.e. the local Mach number $M < 1$) at any point in the flow field. The flow is characterized by smooth streamlines and continuously varying properties. For most airfoils, this happens when $M_\infty < 0.8$, but depending on the airfoil shape, this limit can go down to $M_\infty < 0.6$.

When M_∞ remains subsonic but is sufficiently close to 1, the flow acceleration over the suction side of the airfoil may result in locally supersonic regions. Such a mixed flow is called *transonic* (figure 2.9 (b)). A pocket of locally supersonic flow is formed, which terminates with a shock wave. The flow properties are severely changed across this shock,

as is discussed below. If M_∞ is slightly above unity, the shock will move to the trailing edge of the airfoil, and a second shock, called *bow-shock*, will appear upstream of the leading edge. Passing through the part of the bow-shock that is nearly normal to the free stream, the flow becomes subsonic. However, an extensive supersonic region forms again as the flow expands over the airfoil surface, and again terminates with a trailing edge shock.

The flow is *supersonic* (figure 2.9 (c)) when $M > 1$ at any point in the flow field.

A shock wave can be seen as a discontinuity in the flow field. In reality, the transition between the two states before and after the shock is continuous, but occurs over a very short distance, typically a few molecular mean free paths. Two different kinds of shocks can be formed: *normal* shocks and *oblique* shocks. A normal shock is perpendicular to the upstream flow, and also the flow downstream of the shock is perpendicular to the shock itself. In other words, the flow is not deflected by the shock. The flow velocity behind a normal shock is always inferior to the speed of sound. Considering the flow across the shock as adiabatic, the magnitude of the pressure, temperature, velocity and density variations across the shock can be derived from the equations of continuity, momentum conservation, energy conservation and equation of state. These relations are called the Rankine-Hugoniot equations and are illustrated by the graph in figure 2.10. The detailed equations are given in appendix A.

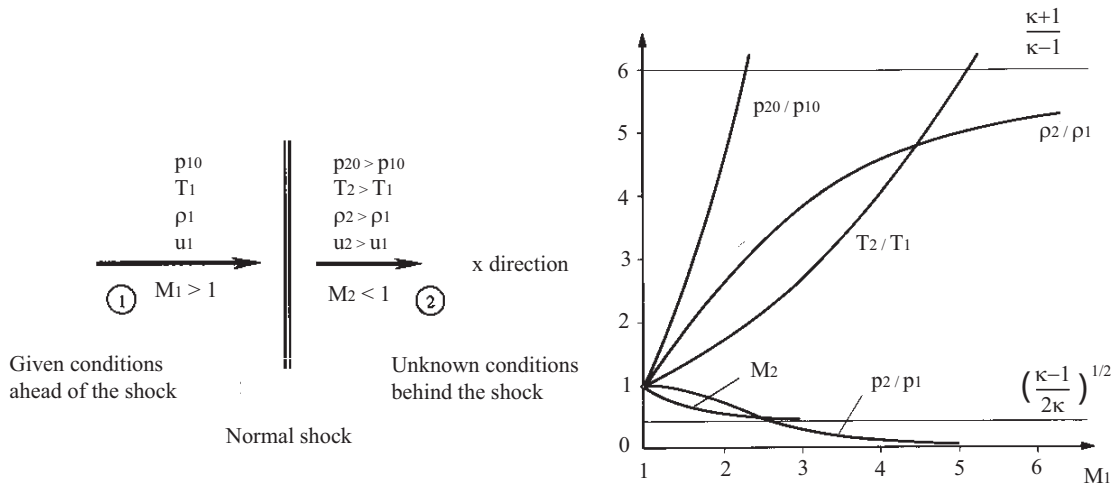


Figure 2.10: Flow property changes across a normal shock, from Rankine-Hugoniot equations [44]. p_{10} and p_{20} are the static pressures, T_1 and T_2 the temperatures, ρ_1 and ρ_2 the densities, u_1 and u_2 the velocities, p_1 and p_2 the total pressures and κ the adiabatic coefficient of the gas.

The normal shock is a particular case of the family of oblique shocks, illustrated in figure 2.11. If the supersonic flow passes a surface which is deflected upward with an angle θ , then the streamlines are deflected upward too with the same angle θ . The fluid is compressed and a compression wave, or shock is created. The shock is oblique to the direction of the impinging free stream. Across the shock wave the Mach number decreases whereas the pressure, temperature and density increase. Equations governing these property changes can be found in [43]. If $M_1 > 1$ upstream of the oblique shock,

then it can be that $1 < M_2 < M_1$ after the oblique shock (this is not the case for a normal shock).

The situation is different when the surface is deflected downwards by an angle θ . The flow streamlines are deflected downwards generating expansion waves. Behind the expansion fan, the flow is again parallel to the wall. In contrast to the discontinuities generated by a shock, the flow properties through the expansion waves change smoothly and continuously (apart from the wall streamline). Across the expansion wave, the Mach number increases whereas pressure, temperature and density decrease.

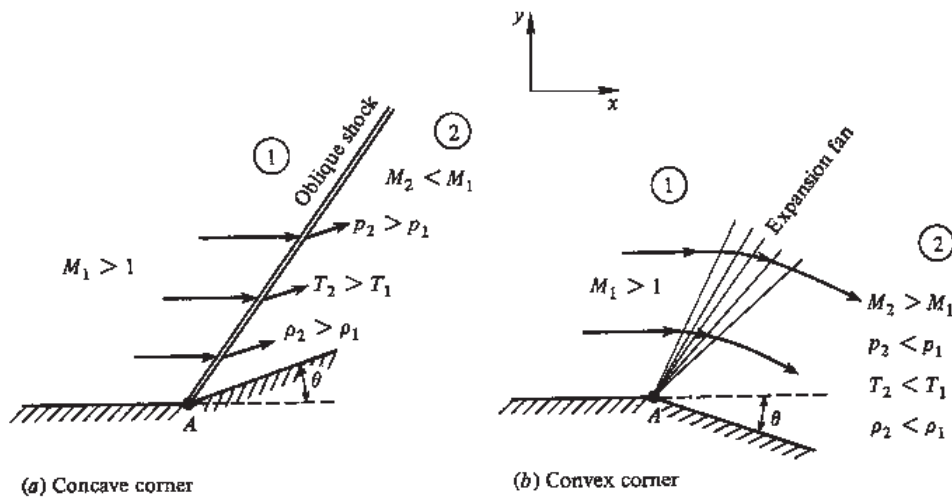


Figure 2.11: Oblique shock and expansion fan from Anderson [43].

2.2.2 Viscous transonic flows

In practice, the interaction of shock waves with solid bodies is not as simple as described above because viscosity plays an important role. Surface friction and heat transfer are entirely determined by the evolution of the boundary layers forming on the body. This evolution is very sensitive to pressure gradients generated by the surrounding flow. In particular, a boundary layer detachment is possible when the flow is slowed down by a positive pressure gradient, for example across a shock. The interaction between the boundary layer and the surrounding flow is too complex to solve mathematically, the phenomena being described by coupled non-linear partial differential equations, which type (elliptic, parabolic or hyperbolic) is different in the boundary layer and in the surrounding flow and varies with the flow velocity. Nevertheless, the most relevant phenomenological aspects of the interaction of shocks with boundary layers around test objects are summarized in the following subsections. The equations describing the motion of turbulent compressible viscous fluids are described in appendix A.

Boundary layers

The concept of boundary layer has been introduced by Prandtl in 1904 in order to obtain approximated solutions to the Navier-Stokes equations that describe the behavior of a viscous fluid around a moving body. When the Reynolds number (based on the characteristic length of the body, see appendix A) is large enough, the flow field around an object can be separated in two regions. In the external zone, the effects of viscosity are negligible compared to inertial effects and the Navier-Stokes equations are reduced to Euler equations. In the region close to the body, called boundary layer, viscosity and inertial effects are comparable. However, certain terms can be neglected which simplify the equations. An important simplification results from the fact that the variation of the static pressure normal to the surface is negligible when the longitudinal curvature radius of the surface is of the same order of magnitude or larger than the length of the body, giving $\frac{\partial p}{\partial y} = 0$.

In the reference frame of the body, the fluid has zero velocity on the surface (no slip condition) and its temperature equals that of the surface. When leaving the surface, the velocity u of the fluid increases whereas its static temperature T varies as a function of the amplitude and direction of the surface heat transfer. These two variables rapidly reach the values u_∞ and T_∞ calculated at the surface of the body with Euler equations. By convention, the external frontier of the boundary layer is reached when $u = 0.99u_\infty$, at the distance δ from the surface defined as the boundary layer thickness.

The flow in the boundary layer is rotational and the angular velocity of the rotation of particles in the fluid is defined as $\vec{\omega} = \frac{1}{2}\vec{\Delta} \times \vec{U}$. In a 2D flow, $\vec{\omega}$ is perpendicular to the x, y plane of the flow and has a single component:

$$\zeta = \frac{1}{2} \left(\frac{\partial u_x}{\partial y} - \frac{\partial u_y}{\partial x} \right) \quad (2.9)$$

In the boundary layer, $\frac{\partial u_y}{\partial x} \ll \frac{\partial u}{\partial y}$ which gives

$$\zeta \sim \frac{\partial u_x}{\partial y} \equiv \frac{\partial u}{\partial y} \quad (2.10)$$

where $u_x \equiv u$ to simplify the notation. At the surface, i.e. at $y=0$:

$$\zeta_w \sim \left(\frac{\partial u}{\partial y} \right)_w = \frac{1}{\mu} \tau_w \quad (2.11)$$

where μ is the dynamic viscosity and τ_w is the shear stress at the wall.

In a second order approximation, one can consider that the presence of the boundary layer is equivalent, for the external flow, to a thickening of the body in movement given by:

$$\delta^* = \int_0^\delta \left(1 - \frac{\rho u}{\rho_e u_e} \right) dy \quad (2.12)$$

δ^* depends on the repartition of the pressure around the body which depends itself on the *effective* shape of the body (shape + δ^*).

At Reynolds numbers around 10^5 , it is possible to obtain a laminar boundary layer. Above a certain critical Reynolds number, the flow becomes turbulent or disordered. Secondary irregular movements are superimposed on top of the main flow generating fast irregular variations of the velocity and other physical parameters of the flow. In a turbulent regime, every variable can be decomposed in a mean component and a fluctuating component as for example for the velocity:

$$u = \bar{u} + u' \quad (2.13)$$

As sketched in figure 2.12, the nature of the boundary layer has an important influence on the shape of the velocity profile.

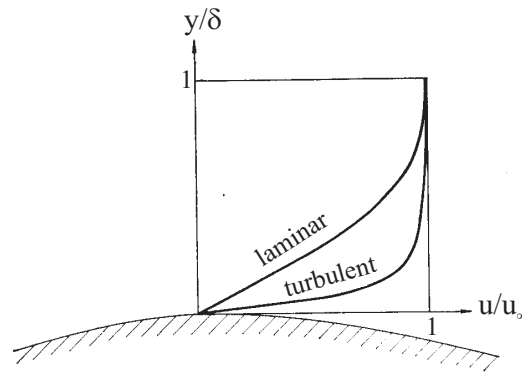


Figure 2.12: Velocity profiles in laminar and turbulent boundary layers [45].

The evolution of the boundary layer depends on the amplitude and sign of the longitudinal pressure gradient existing on the body considered. When the main flow is accelerated, the pressure gradient is negative and has a favourable effect because it counteracts the deceleration due to viscous effects on the surface and limits the thickening of the boundary layer. However, when the external flow is slowed down, the particles in the boundary layer have a low kinetic energy and do not enter easily in the zone where the pressure gradient is positive. The boundary layer then thickens and if the positive gradient is sufficiently high, it detaches from the surface generating a detachment zone where the fluid flows in the inverse direction as the external flow. The thickness of the detachment zone can be substantially higher than the thickness of the original boundary layer. The detachment phenomenon is described schematically in figure 2.13.

The separation point S can be defined as the limit separating the direct flow from the reversed flow. In a 2D flow, the skin friction coefficient c_f , the shear stress and the slope of the velocity profile are zero at S:

$$c_f = \frac{1}{\mu} \tau_w = \left(\frac{\partial u}{\partial y} \right)_w = 0 \quad (2.14)$$

The inflection of the velocity profile destabilizes the laminar boundary layer which tends to become more rapidly turbulent. The strong agitation that results gives higher kinetic energy to the particles close to the wall and retards the separation.

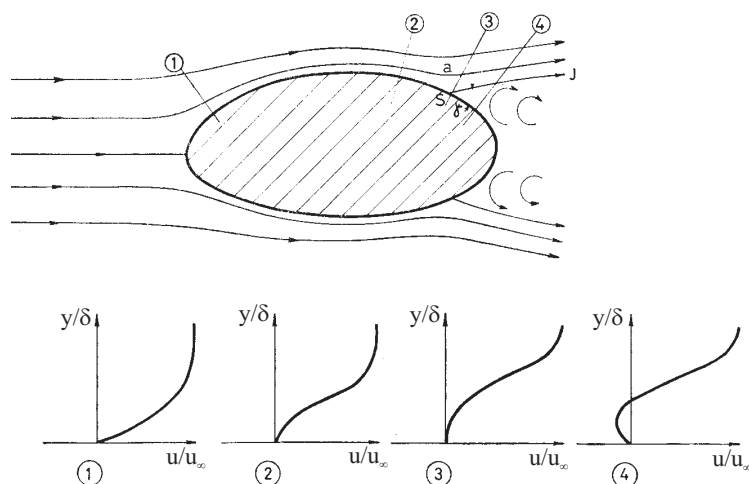


Figure 2.13: Definition of separation point [45].

There exists a strong non-linear viscous interaction between the boundary layer and the external flow. This is the case for example when a shock impinges on a solid surface where a boundary layer has formed. The interaction gives rise to a flow field which can be very different from what has been explained in the previous subsection for inviscid transonic flows, as shown in figure 2.14.

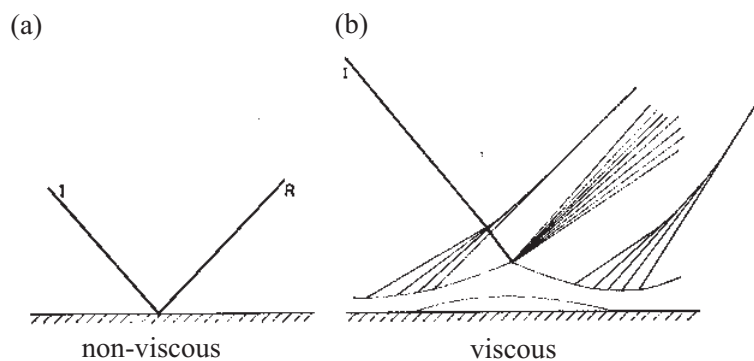


Figure 2.14: Schematics of inviscid (a) and viscous (b) shock-boundary layer interaction [45].

Interaction between a normal shock and a boundary layer

The interaction of shock waves and boundary layers is a common problem in internal and external flows. The structure of an object immersed in a high speed flow is exposed to fluctuating pressure levels and thermal loads. The maximum amplitudes of these pressure variations and thermal loads are found in the region where the shock and the boundary layer interact. These effects can have important impacts on the structural integrity of the object.

A flow submitted to an adverse pressure gradient, that is $\frac{\partial p}{\partial x} > 0$ as in a shock for example, is decelerated. In this situation, the boundary layer becomes thicker and the skin friction decreases (see appendix A). Also, the velocity profiles in the boundary layer are modified as shown in figure 2.15.

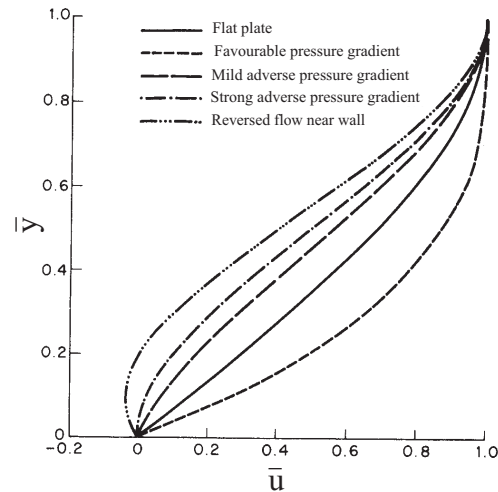


Figure 2.15: Modification of the velocity profiles in a boundary layer submitted to pressure gradients [46].

Figure 2.16 represents schematically a possible type of interaction between a boundary layer and a normal shock as can be encountered on an airfoil at transonic speeds. The boundary layer detaches upstream of the normal shock, giving rise to a compression wave or weak shock. This latter meets the normal shock in A, where a surface AS begins. This surface represents an entropy discontinuity. As discussed before, the flow direction in the separation zone is reversed compared to the main flow. Pearcey [47] observed that when the inlet Mach number is increased, a small detachment bubble appears which has no important effect on the external flow. Then, when the Mach number is further increased and is higher than a certain critical value, the bubble rapidly lengthens and significantly modifies the external flow.

The rapid pressure rise at the shock cannot be propagated upstream in the supersonic regions of the flow but it can be propagated in the subsonic region of the boundary layer. The rapid pressure rise associated with the shock becomes diffused near the base of the boundary layer and appears in the form of a progressive pressure rise starting at an appreciable distance from the upstream of the incident shock. The length of this upstream diffusion depends on the nature of the boundary layer, if it is laminar or turbulent. In a laminar boundary layer, this length can be 100δ whereas in a turbulent boundary layer it is usually only about 10δ . This is due to the fact that a laminar boundary layer is slower than a turbulent one as described in figure 2.12. As discussed before, a positive pressure gradient causes a thickening of the boundary layer and maybe a detachment. For a laminar boundary layer, a third effect appears: the transition to turbulence.

The interaction of a normal shock with a laminar boundary layer can have different

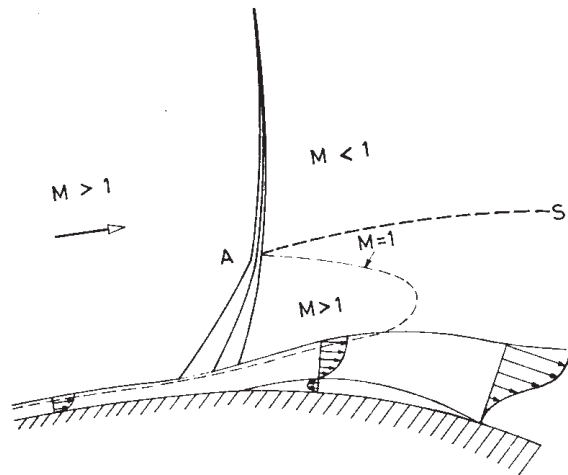


Figure 2.16: Schematics of the interaction of a normal shock with a boundary layer [45].

effects on the external flow depending on the Mach number upstream of the shock. Three typical cases are shown in figure 2.17. With an upstream Mach number just greater than unity (case (a)), the shock is relatively weak and the diffused pressure rise may simply cause a gradual thickening of the boundary layer ahead of the shock without transition or separation. Immediately behind the shock, the boundary layer tends to thin again followed by a series of expansions and compressions until the flow is completely subsonic. For upstream Mach numbers above 1.3 approximately (case (b)), the shock is much stronger. The thickening of the boundary layer is much faster and it will generally separate before reattaching. There is a high probability that the transition to turbulence will occur behind the single subsidiary shock. At still greater upstream Mach numbers (case (c)), the pressure rise at the shock can be sufficient to cause separation of the laminar boundary layer well ahead of the main shock position. This results in a sharp change in direction of the main stream flow just outside the boundary layer and be accompanied by an oblique shock. This type of shock configuration is called a lambda shock. It is unlikely that the boundary layer will reattach under these conditions. This sudden separation is associated with a sudden decrease in lift coefficient. This phenomenon is known as *shock stall*.

Because a turbulent boundary layer is much less sensitive to an adverse pressure gradient than a laminar one, separation is not likely to occur for upstream Mach numbers smaller than 1.3 approximately. Then no separation takes place, the thickening of the boundary layer ahead of the shock is fast and the compression wavelets near the base of the main shock are very localized, so that the base of the shock appears slightly diffuse, although no lambda shock structure is formed. No subsequent thinning of the boundary layer occurs behind the shock and the secondary shocks do not develop. If separation of the turbulent layer occurs ahead of the main shock, a lambda structure forms and the external flow looks much like that for a fully separated laminar boundary layer. Moreover, according to recent studies, the interaction between a plane shock wave and an isentropic

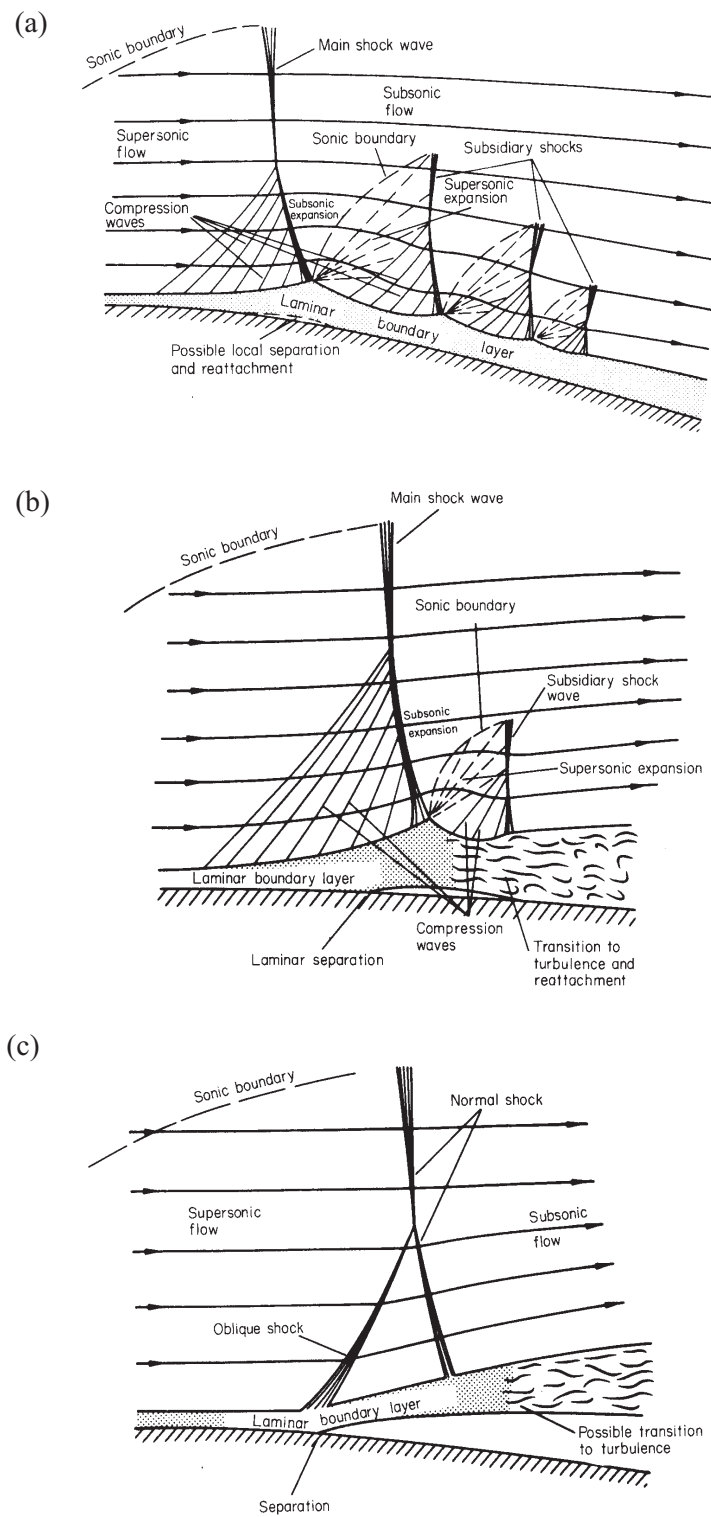


Figure 2.17: Interaction of a normal shock with a laminar boundary layer at increasing upstream Mach numbers [46].

turbulent medium present the following characteristics:

- An oscillatory motion and a deformation of the shock. The thickness of the shock is no longer constant but fluctuates with time (due to the turbulence and compressibility)
- A global increase of the turbulence intensity downstream of the shock, i.e. an amplification of the turbulent kinetic energy k and transversal⁸ vorticity components (whereas the streamwise component remains nearly constant)
- A modification of the turbulence characteristic length scales: small scales are more amplified than larger ones
- A mean flow globally in agreement with the Rankine-Hugoniot relations across the shock.

Compression ramp experiments have shown that the natural frequency of the shock system unsteadiness scales with the bursting frequency of the incoming boundary layer. This strongly suggests that the turbulence within the incoming boundary layer plays a dominant role in triggering the shock wave natural unsteadiness.

Transonic flow on a rigid airfoil

The qualitative description of the flow development around an airfoil at transonic speeds was first described by Pearcey [47]. For an airfoil, viscous effects are of primary importance in two regions: in the vicinity of the shock foot and near the trailing edge. The situation at the trailing edge is obviously strongly dependent on the previous history of the boundary-layer, which includes its interaction with the shock. Interactions entailing flow separation, which are of particular importance for practical applications, can be classified in two groups:

- *Type A flows*, where a moderately strong shock induces a local thickening of the boundary layer. As the free stream Mach number increases, the shock moves downstream and strengthens and a limit is reached where the beginning of the separation zone appears at the shock foot. The Mach number required to provoke shock-induced separation varies with surface curvature and Reynolds number. At even higher incident Mach numbers, a separation bubble forms at the shock foot and further a increase of M_∞ leads to its growth. The progressive growth of the separation bubble is characteristic for this kind of flow, where the separation point is fixed at the shock foot and the reattachment point gradually moves towards the trailing edge, as the shock becomes stronger. According to Pearcey, such a situation does not depend much on the boundary-layer thickness at the shock foot (provided it is fully turbulent).

⁸normal to the flow stream

- *Type B flows* where a very strong recompression occurs in the trailing edge region of the profile (highly loaded airfoil). The difference with Type A flows is that a second separation forms in the subsonic flow approaching the trailing edge. An increase in the upstream Mach number or in the angle of incidence results in the formation of a large separated zone extending from the shock foot. The formation of this zone can be the consequence of the merging of the bubble present at the shock foot and of the rear separated zone. This will generate the aeroelastic phenomenon called *buffeting* [48]. If the shock oscillates with large amplitudes due to the periodic variations of the boundary layer properties, *shock-induced flutter* of the airfoil can arise [48].

2.2.3 Sonic boom perspective

A sonic boom is the noise from the shock waves forming around supersonic aircraft, as heard from the ground. Sonic booms are basically weak shocks: the typical overpressure at the ground is usually up to 100 Pa. For weak shocks, non-linearities can be neglected to a first approximation, and the disturbance due to the motion of a supersonic aircraft can be approximated by a linear superposition of small disturbances (i.e. sound waves) spreading out from their successive positions at the speed of sound. In a homogeneous atmosphere, and assuming the aircraft can be considered as a point source in two dimensions, these disturbances form circular wave fronts centered at the successive positions of the aircraft, as illustrated on figure 2.18. The wave fronts overlap and form an envelope, the Mach envelope. In two dimensions the Mach envelope is a wedge, and in three-dimensions it is a cone, called the Mach cone. The Mach angle $\theta_M = \arcsin(1/M)$, where $M=U/a$ is the Mach number of the source, U being the velocity of the source and a the velocity of sound in the surrounding medium. All the sound is contained in the Mach envelope and, to a first approximation, the envelope is the location of the sonic boom.

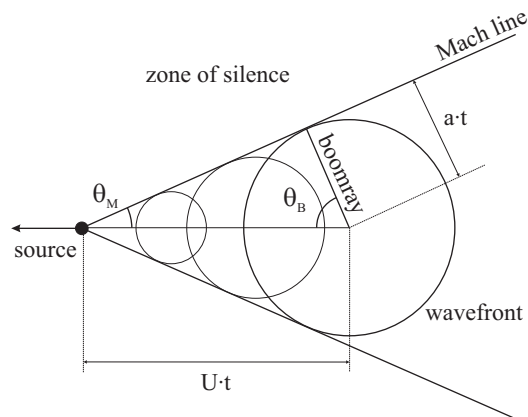


Figure 2.18: Definition of the Mach cone.

On figure 2.18 are drawn the boomrays, the rays emitted at angle $\theta_B = \arccos(1/M)$ to the direction of motion. The disturbances propagating along boomrays reinforce each

other at the observer position and are heard as a single boom (for a point source). Alternatively, the Mach envelope can be thought of as made of the tips of the boomrays, and the boom as traveling along boomrays. Tracing the boomrays is in fact the standard method to follow the path of the shock wave in sonic boom prediction methods, and constitutes the ray theory approach to sonic boom [49].

In 1946, Landau analyzed the weak shock waves from a supersonic projectile and predicted an N-wave shape for the pressure signature in the far-field (i.e. at distances large compared with the body dimensions). Soon afterwards, measurements of projectiles confirmed Landau's predictions. In 1952, Whitham explained in detail the generation of the flow pattern around a ballistic projectile and stated that sonic boom is a steady state phenomenon. It is generated continuously as the aircraft flies supersonically and not only at the moment that the aircraft breaks the sound barrier. Near the aircraft (near-field), the pressure field is directly dependent on the geometry and the aerodynamics of the vehicle. For a pointed aerofoil or axisymmetric body there are generally two shock waves, one attached to the front (bow shock) and the other attached to the tail (tail shock). An aircraft is a non-smooth body and in the near-field the shock-wave pattern contains several shock waves, corresponding to the various compressions caused by the detailed shape of the aircraft. However, away from the aircraft the shock wave pattern distorts, and in the far-field it coalesces into only a bow and a tail shock, as in the case of a simpler, smooth body. Records from flight tests substantiate this since the N-wave signatures for various aircraft of similar size and weight are essentially the same.

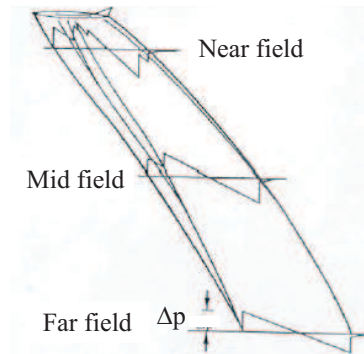


Figure 2.19: Propagation of the pressure wave in the atmosphere [50].

Figure 2.19 displays a schematic of the coalescence of the near-field shock waves, that leads to the N-wave in the far-field. At the bow shock the local pressure p increases rapidly by amount Δp above the atmospheric pressure. Δp is called the overpressure. There is a slow expansion phase between the bow shock and the tail shock until the pressure is a certain amount below the atmospheric pressure, and at the tail shock the atmospheric pressure is recovered rapidly. Generally, the overpressure and the recovery pressure are of similar size. The N-wave moves with the aircraft, it is detected once at a specific observation point on the ground. If the time difference between these two rapid compressions is small, as for a bullet, the two compressions are not separately audible

and the ear detects a single explosive sound. However, for longer bodies, or an aircraft high enough in the atmosphere, a double boom may be heard.

Whitham's theory extended to lifted non-axisymmetrical bodies predicts that the pressure is proportional to the weight W of the aircraft and also depends on the aircraft effective length L_{eff} , depicted in figure 2.20. The rear point is given by the intersection between the aircraft axis and the line parallel to the shock front attached to the nose passing by the highest point of the aircraft shape (tail).

$$p \propto \frac{W}{L_{eff}^{3/2}} \quad (2.15)$$

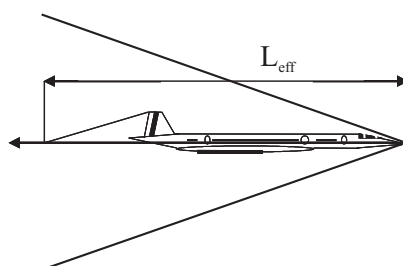


Figure 2.20: Definition of the effective length [50].

Whitham's theory also gives for the far-field

$$\Delta p \propto c(M)F_W(x) \quad (2.16)$$

which states that the overpressure is a function of the Mach number M and the Whitham function F_W . The Whitham function depends mainly on the shape of the aircraft ([51, 52]). These are very important results for sonic boom mitigation techniques based on aircraft design.

The energy of the N-wave is proportional to the overpressure integrated over time, that is, to the area delimited by the pressure signature as shown in figure 2.21.

One way to reduce the N-wave energy (and thus the noise generated by sonic booms on the ground) is to reduce the pressure amplitude of the shock waves. Equations 2.15 and 2.16 suggest that this can be done by reducing the weight of the aircraft, increasing its effective length or modifying the Whitham function by acting on the aircraft shape. Another way to reduce sonic boom energy is to prevent the coalescence of the pressure wave into a sharp N-wave as it travels to the ground. Two methods can be used:

- Act on the shape of the pressure signature by increasing the head shock and decrease the other shocks (compensate inlet and wing shocks). The near-field pressure signature should be as close as possible to the so-called optimal Whitham function and should coalesce in a somewhat flat-top ground signature
- Increase nonlinear absorption by increasing the local frequency of the pressure variation. This can be done by acting on the aircraft shape again.

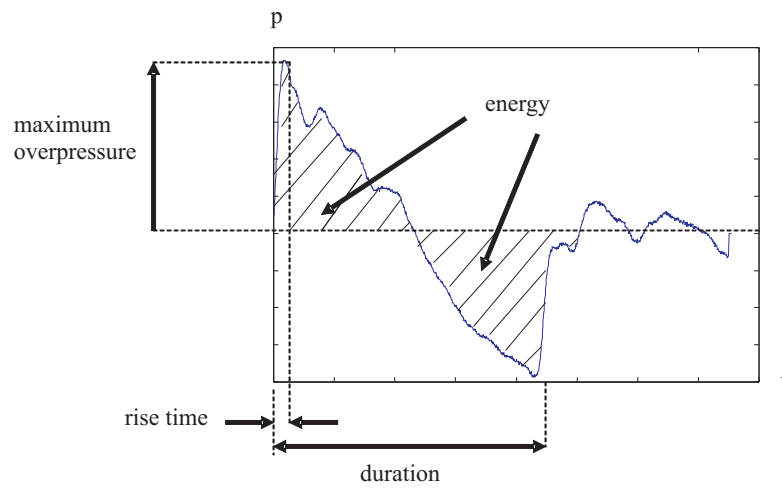


Figure 2.21: Definition of the physical parameters of sonic booms [50].

Extensive research is being carried out nowadays in the field of sonic boom shaping, trying to validate theory with both CFD simulations and experimental measurements. In addition to shape optimization methods, plasma techniques could offer new possibilities for acting on the sonic boom.

Chapter 3

Experimental setup and diagnostics

The present chapter describes the plasma set-up and plasma diagnostics, the mounting of the dielectric barrier discharge device on an airfoil, and finally the wind tunnel and aerodynamic measurement techniques.

3.1 DBD generation system

3.1.1 Flat DBD system

The typical flat DBD geometry that has been chosen in order to study the plasma-flow in a simple configuration (flat plate mounted on a lateral wall of the nozzle) is shown in figure 3.1. The dielectric consists of a 107 x 107 mm flat Al_2O_3 plate (96% purity), 0.63 mm thick. Two electrodes are printed on each side of the dielectric using a serigraphy process. A metallic paste is spread over a grid placed over the dielectric. This grid lets the paste through a mask, which allows to control the geometry and the thickness of the layer. After that, the dielectric with the metallic paste layer is heated up to 850°C to dry the solvents in the paste, leaving only the metal on the dielectric. This technique ensures a perfect contact between the electrode and the dielectric, avoiding parasitic plasmas. After firing, the electrodes are 0.015 mm thick.

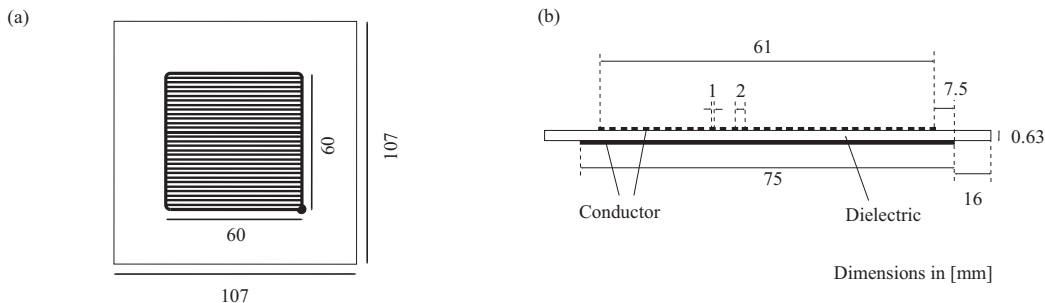


Figure 3.1: Schematic of the DBD system.

This geometry, which will be referred to as Al_2O_3 -baseline in the following chapters,

has been chosen in order to generate a plasma on a relatively large surface, and only on one of the dielectric surfaces. The top electrode is made of 31 stripes, covering a $60 \times 60 \text{ mm}^2$ area. The top electrode stripes are all connected together at each end. They are 1 mm wide and are located 2 mm apart from one another. The top electrode is made from a conducting paste containing a mixture of gold, platinum and palladium. This composition minimizes the oxidation of the electrode when it is in direct contact with the discharge, thus improving the lifetime of the DBD system. The bottom electrode, which is connected to the ground, is a $75 \times 75 \text{ mm}^2$ square. The larger area of the bottom electrode prevents the generation of plasma on the bottom side, at the edges of the bottom electrode. Since there is no discharge in contact with this electrode, a simpler material can be chosen for the conducting paste, silver for example. The capacitance of this system, without plasma, is 310 pF ¹

Several DBD plate geometries have been considered in the different experiments without and with airflow. They are described in chapter 4 and the effects of the different electrode and dielectric geometries on the discharge are discussed.

The appropriate choice of dielectric material and electrode material improves the lifetime of the DBD system of more than one order of magnitude compared to conventional systems. Systems made of polymer dielectric only last about 5 to 10 minutes before the plate is destructed by arcing through the dielectric (thinning of the dielectric due to etching). If silver is used for the electrodes (on a ceramic dielectric), the intensive oxidation of the electrode in contact with the plasma will generate a deposit on the electrode and switch off the discharge after only about 10 minutes. The DBD plate presented here can be operated for more than 20 hours (continuously). The lifetime of the system can be improve even more by encapsulating the electrodes in ceramics, as explained in section 3.3 below.

3.1.2 Electric circuit

The electric set-up for the generation of the dielectric barrier discharge is shown in figure 3.2.

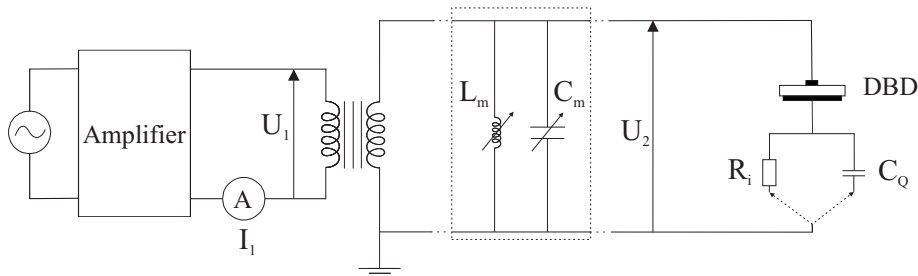


Figure 3.2: Electrical set-up of the DBD system.

The power supply consists of a low frequency power amplifier and a high voltage

¹It has been measured using an independent RLC circuit test-stand and measuring the discharge time constant.

transformer. The power amplifier is a CompactPower TITAN MAC-01. It works in a frequency range from 20 Hz to 20 kHz and gives an output power of up to 1 kV·A ($U_1 = 130$ V and $I_1 = 8$ A). The choice of the power amplifier is a key issue. It has to ensure the stability of the discharge and sustain possible high current peaks in case of arc formation. The input voltage U_1 is sinusoidal and is amplified by a high voltage transformer (from Atesys-Montoux) which has a bandwidth from 1 to 20 kHz. The mean multiplying factor is 77 and the maximum power input is 3 kV·A. In the end, the output voltage on the secondary circuit, U_2 , can reach rms values up to 10 kV.

An impedance matching circuit can be connected to the secondary circuit. Depending on the working frequency and capacitance of the DBD system, the charge of the secondary circuit is modified in order to maximize the power transfer to the DBD. The matching circuit is composed of a variable self-inductance and a variable capacitor. The self-inductance L_m can be varied in discrete steps from 0 to 600 mH, and the capacitance C_m from 0 to 44700 pF. The capacitance is varied with a set of fixed capacitors (16 x 500 pF and 16 x 2200 pF) and a continuously variable capacitor (1500 pF vacuum capacitor, Comet CV2C-1500E/35).

Depending on whether the current through the DBD or the charge is to be measured, a shunt R_i or a capacitor C_Q is connected on the secondary circuit, in series with the DBD to ground. This is further discussed in the next section.

3.2 Plasma diagnostics

3.2.1 Electrical characterization of the discharge

The voltage and current on the primary circuit, U_1 and I_1 , are measured in order to estimate the input power. On the secondary circuit, the voltage U_2 and the current I_2 through the DBD system are measured. U_2 is measured with a high-voltage probe (PMK PHV 4002, max. peak voltage: 20 kV, attenuation: x1000 and bandwidth: DC-100 MHz). The current I_2 is measured through a 50 Ω shunt, from U_{shunt} . Since $U_{shunt} \ll U_2$, this measurement does not perturb the system in a significant way (provided the shunt has minimum inductance component). It is important to point out that I_2 is the total current through the DBD system. It is a sum of a capacitive component (displacement current in the dielectric) and the plasma current (conduction current). The signals U_1 , I_1 , U_2 and I_2 are sent to a digital oscilloscope (LeCroy WaveRunner 64XI, 500 MHz bandwidth, input impedance 1M Ω) for monitoring and storage.

The power dissipated in the plasma is relatively complex to measure, because of the highly filamentary nature of the DBD discharge. Estimations have been done by integrating the product $U_2(t) \cdot I_2(t)$, giving around 10% of the injected power ($U_1(t) \cdot I_1(t)$), but the errors can be greater than 50%. Therefore, in the following sections, the power dissipated in the plasma will be discussed qualitatively with the help of Lissajous figures.

The power consumed by the DBD system P_{el} can be calculated from the charge Q_{dbd} accumulated by the DBD system and the voltage U_2 measured through the DBD system. The charge is measured by mounting an additional capacitor of known capacitance C_Q in series with the DBD (see figure 3.2). In the experiment, $C_Q=30$ nF. Measuring the

voltage U_Q through this capacitor gives the charge $Q_Q=Q_{dbd}$. The charge-voltage (Q-U) characteristic curve is called a *Lissajous figure* and is represented in figure 3.3.

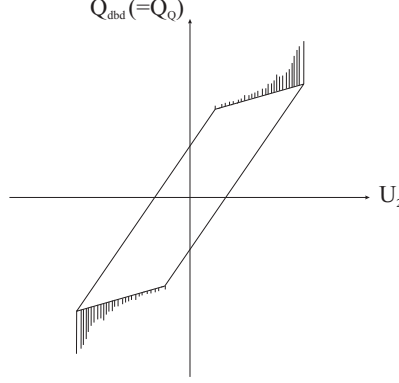


Figure 3.3: Schematic of a Lissajous figure (Q-U characteristic).

As explained in [53], the electric energy consumed per voltage period E_{el} , is equal to the area of the Q-U diagram. The power consumption P_{el} is the product of E_{el} and the frequency of the applied voltage ν :

$$P_{el} = \nu E_{el} \quad (3.1)$$

3.2.2 Time-resolved plasma light emission

The light emission from the plasma has been measured with a photomultiplier with a high time resolution². The photomultiplier tube (PMT) is a Hamamatsu H6780 (220 nm - 800 nm spectral range, 0.78 ns rise time) connected to a fast pre-amplifier Hamamatsu C6438 (DC - 50 MHz). The light is brought to the PMT by an optical fiber with a 60° angle of aperture. Since the microdischarges generated by the DBD are not fixed at a given location around the electrode stripes, they move as a function of time, it is difficult to perform PMT measurements on a single microdischarge to study the evolution of its light emission. Instead, the PMT is used to study the evolution of the discharge as a whole and the fiber is placed in front of the discharge at a distance such as to accept the light from the whole discharge surface. No focusing lens is used. The signal from the amplifier is then sent to an oscilloscope (LeCroy WaveRunner 64XI, 500 MHz bandwidth).

For the measurements with the airflow, Plexiglas or glass are used for the optical accesses and lateral windows (see figures 3.12 and 3.15). Therefore, the ultraviolet part of the spectrum is filtered out (up to about 400 nm).

3.2.3 Space-resolved light emission

The spatial distribution of the discharge is studied using CCD imaging. In the experiments with the flat DBD system mounted on one of the lateral windows of the subsonic or

²The light is integrated over the visible emission spectrum

supersonic nozzle (see figures 3.12 and 3.15), the camera can be placed relatively close to the discharge, about 10 cm. In these conditions, an 8-bit Hamamatsu C5985-10 (736 x 496 resolution, down to 0.1ms exposure times) can collect enough light and has enough dynamic range and resolution to monitor the global discharge topology. However, when the discharge is created by the LTCC plate mounted on the airfoil, the CCD camera has to be placed above the top wall, in front of the optical access. This means that the camera is at 45 cm distance away from the discharge. Moreover, the light is further attenuated by the two glass plates of the optical access and the lenses of the zooming objective placed in front of the camera. The zoom is necessary to have a high enough spatial resolution on the discharge. In this case, a more sensitive camera is used, a PCO Imaging PixelFly QE, with a 12 bit dynamic range, 1392 x 1024 pixel resolution, 5 μ s to 10 ms exposure times and transfer rates allowing for 12 frames per second on average.

3.2.4 Time- and space-resolved light emission

In order to achieve simultaneous time and space resolution for the discharge analysis, an intensified CCD camera is used. The camera is an ICCD PI-MAX from Princeton Instruments, with a 16-bit dynamic range, exposure times down to 2 ns, and a 1024x1024 pixel resolution. The intensifier integrated in the camera is a microchannel plate (MCP), which acts in a similar way as the photomultiplier. Photons emitted by the plasma first strike a photocathode and release electrons. These electrons are then attracted to the MCP input by a positive potential. The electrons are accelerated in the MCP by a high positive voltage. If they hit the channel walls, they generate additional electrons, which results in electron multiplication. When the electron exit the channels they are accelerated one last time again by a high positive voltage and end up striking the phosphor coating on the fluorescent screen causing it to release photons. Finally, these photons are detected by the CCD chip.

The MCP also acts as a fast shutter, since an inversion of the electric field sign can block the electrons in the MCP. This is called *gating*. The gate can be triggered on an external signal, for example the voltage U_2 applied to the DBD. The images can then be taken at a certain phase with respect to this reference signal, for example at the location where the current peaks appear. In order to further improve the sensitivity and signal to noise ratio, several images can be accumulated on the CCD chip. The control of the exposure times, triggered gating and image accumulation is done with the software WinSpecTM.

In order to study the discharge at its different phases with respect to the measured current, the intensified camera can be used in a triggered mode. Since the current peaks vary slightly in amplitude and position with respect to time, the camera is not triggered directly on the current signal but on the U_2 voltage sinusoid. The trigger is set at the beginning of the filamentary region, defined as t_p for the positive half-period and t_n for the negative half-period. A 10 μ s gate width is used (=exposure time of the camera). The gate definition is illustrated in figure 3.4. A delay Δt is introduced in the program defining the gate in order to shift it over the half-period.

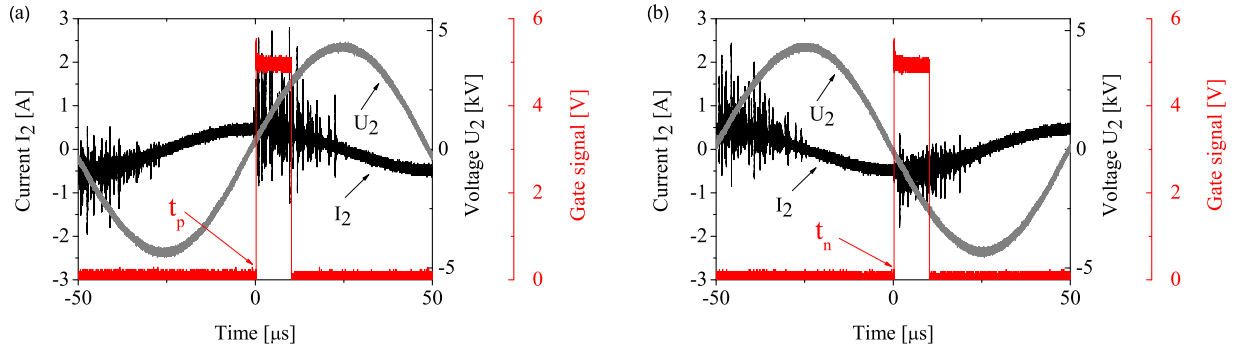


Figure 3.4: CCD camera gate definition (trigger position and exposure time= $10 \mu\text{s}$) for the positive and negative half-periods.

3.2.5 Optical emission spectroscopy

The spectral analysis of the light emitted by the plasma is performed using optical emission spectroscopy which has the advantage of being a completely non-intrusive diagnostic. The different excited species present in the plasma can then be identified and monitored.

A schematic view of the system is drawn in figure 3.5. The light emitted from the plasma is collected by an optical fiber. The fiber guides the light to the monochromator (containing the diffraction grating) coupled to the CCD detector. The monochromator is an Acton Research Corporation SpectraPro-275 with a focal length of 275 mm and an aperture ratio of $f/4$. It contains 3 different gratings with the following properties: 150 gratings/mm giving a 0.64 nm resolution and a 640 nm range, 600 gratings/mm giving a 0.15 nm resolution and a 150 nm range and finally a 1200 gratings/mm giving a 0.07 nm resolution and a 68 nm range). The CCD camera is a Princeton Instruments CCD30 EEV, with a 256x1024 pixel sensor, a Peltier cooling system (-40°C) and a 16 bit A/D converter. The spectra acquired by the CCD are sent to a computer and handled with the software WinSpecTM. The software also controls the monochromator and CCD settings.

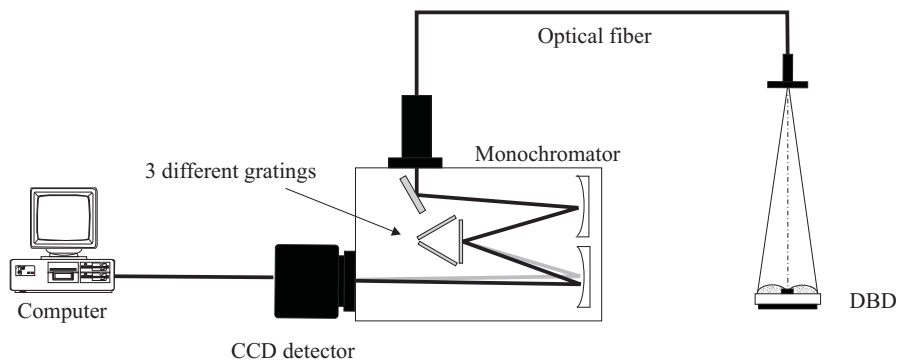


Figure 3.5: Optical emission spectroscopy set-up.

For the measurements with the airflow, Plexiglas or glass are used for the optical accesses on the top of the nozzle and lateral windows. Therefore, wavelengths up to about 390 nm are filtered out.

3.3 Generation of a surface plasma on an airfoil

3.3.1 Curved DBD system

DBDs in air are difficult to maintain for long operation times, typically several hours. Indeed, materials (dielectric and electrodes) which are directly in contact with the plasma suffer intensive chemical attack from the reactive species generated in the discharge (O_3 , O, OH for example). If the dielectric used is polymer-based, such as Kapton[®], the DBD device is easy to machine in any shape or thickness and also flexible sheets can be fabricated. However, the lifetime of such systems is very limited due to etching of the dielectric (typically about ten minutes) as shown in figure 3.6.

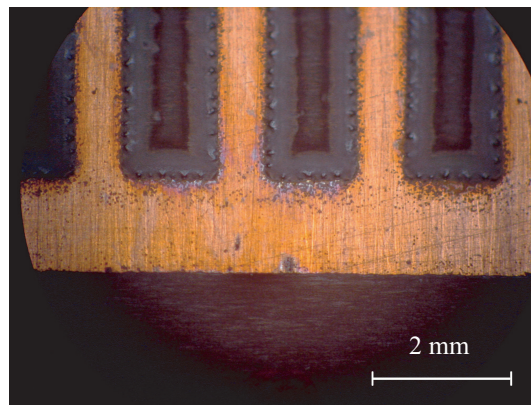


Figure 3.6: Close-up of a Kapton[®]-copper DBD system after about 7 minute use.

On the other hand, systems using massive ceramics (alumina plates, MACOR[®]) as a dielectric have longer lifetimes. However, the electrodes become the limiting factor. They are quickly oxidized by the plasma, even when covered with a dielectric paste. Moreover, machining and integration is problematic, especially on curved surfaces.

The two main questions are:

- How can the lifetime of a device generating surface plasmas be maximized?
- How can such a device be integrated on a surface of any shape and any material?

Part of the answer to the first question resides in using ceramics as dielectric supporting the electrodes. However, the problem of the electrode being in contact with the plasma remains. The use of protective layers on top of the dielectric and electrodes is not sufficient. About ten different protective layers have been tested, deposited on top

of plasma generators made of alumina (Al_2O_3) as dielectric and silver electrodes. The different protection layers tested are: SiO_2 , SiC, Teflon, Teflon-like deposited by plasma processes and about 6 dielectric pastes used in the microelectronics thick film technologies. All the tests have been unfruitful, the layers resulting either too thin, too thick, too porous or too in-homogeneous. One possible answer is to choose electrode materials less prone to oxidation when in contact with the plasma. Indeed, the use of gold or gold-platinum-palladium electrodes instead of silver or copper electrodes increases the lifetime from less than one hour to several tens of hours or more.

The idea of a protecting layer on top of the electrodes, and the problem of finding a way to curve a ceramic layer has led to the idea of using low-temperature co-fireable ceramics (LTCC) as dielectric matrix. First of all, LTCC provide a very efficient way to encapsulate electrodes inside ceramics, laminating all dielectric layers together without air trapped between them. This protects them in the most efficient manner and allows for a maximized lifetime. LTCC are thermally stable and most importantly, they have a very high dielectric strength (of the order of 3 kV for each layer of 0.1 mm after firing). Furthermore, LTCC allow to address in a very elegant way the second problem, the curvature. Indeed, once a long-lifetime system made of ceramic has been proven efficient for DBD generation, how can it be integrated on a curved surface? Ceramic is intrinsically rigid and friable. Alumina or MACOR[®] elements are not machinable in thin layers and are very delicate and breakable. Sputtered or sprayed ceramics are very porous and thick layers are needed if a DBD has to be sustained. LTCC however is prepared in thin layers (0.1 mm after firing) that are flexible before firing, so curved substrates can be covered with them. The layers can be laminated together to make thicker elements. When the LTCC is fired, most the polymer binders are evaporated. The system becomes very dense but still not as breakable as MACOR[®] for example because a certain ratio of binders stays trapped in the ceramic.

The LTCC tape used is Heraeus Heraclon HL2000 (0.2% shrinkage in the x-y plane of the layer) and conducting pastes compatible with this tape are Heraeus TC0306, TC0307 containing silver (for the bottom electrode) and TC8101 containing gold (for the top electrode). The geometry of the DBD system based on LTCC is depicted in figure 3.7. The figure shows the geometry of the top electrode, the layers before stacking and the system after stacking and curved firing.

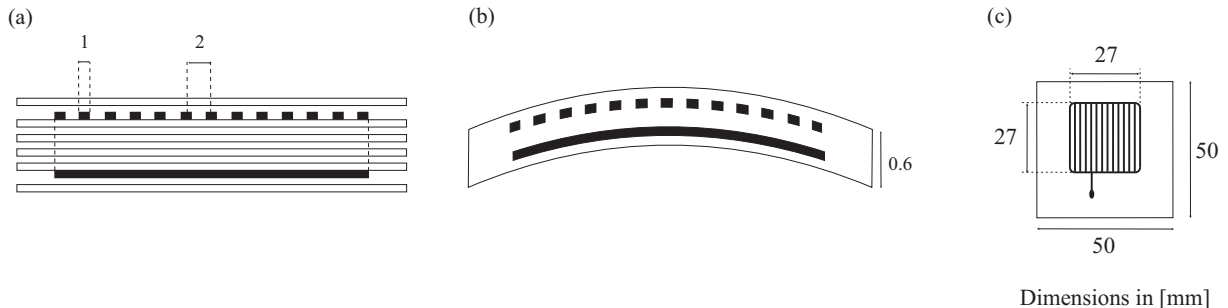


Figure 3.7: Stacking of the LTCC layers and electrodes (a), system after firing (b) and top view of the geometry of the upper electrode (c).

3.3.2 Integration of the DBD on the surface of an airfoil

For the study of the influence of the DBD on shocks, the plate is then integrated on a NACA3506 profile (coordinates are given in appendix B). This profile is a typical wing profile, also used for compressors. It has been chosen because its aerodynamic properties are well known and it has been extensively used at LTT during previous research projects. Numerical as well as experimental data are available, for example particle image velocimetry (PIV) measurements of the transonic flow around it [54]. The airfoil is made of Stavax[®] (steel alloy), in order to ensure good structural stability in transonic airflow conditions. Also temperature and chemical etching resistance is ensured when the plasma is active.

In order to give the plate the same curvature as the profile, the plate is laid on a mock-up of the suction side during firing. The mock-up is made of MACOR[®]. After firing, the system is rigid and its dimensions are adjusted using a polishing wheel. The plate is fixed with silicone on the profile and the power supply cables are connected to the electrodes. They pass through a MACOR[®] insert which insulates them from each other and from the profile body. The technical details of how this is done can be found in [55]. In order to study the influence of the plasma position with respect to the shock on the plasma-flow interaction, two configurations have been built. The first one with the DBD plate close to the leading edge and the second one with the DBD plate close to the trailing edge. A 3-D view of the parts is shown in figure 3.8 and the important dimensions are given in figure 3.9. The NACA profile and the DBD plate are 40 mm wide. The electrodes are 6.5 mm away from the lateral edges. The MACOR[®] insert is 9 mm wide. The longitudinal dimensions and positions of the DBD plate and electrode are given in figure 3.9.

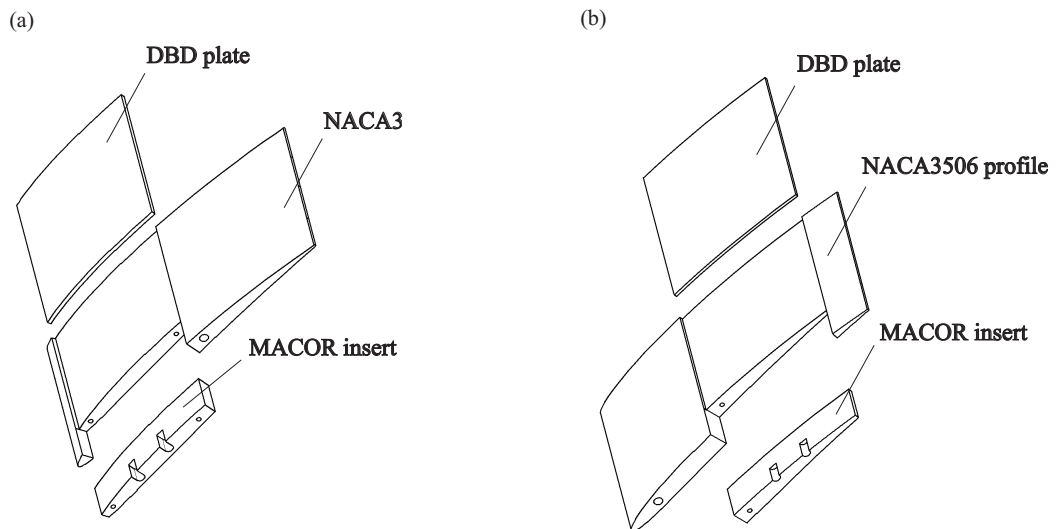


Figure 3.8: 3D view of the two profile-DBD systems considered, the plate close to the leading edge (a) and the plate close to the trailing edge (b).

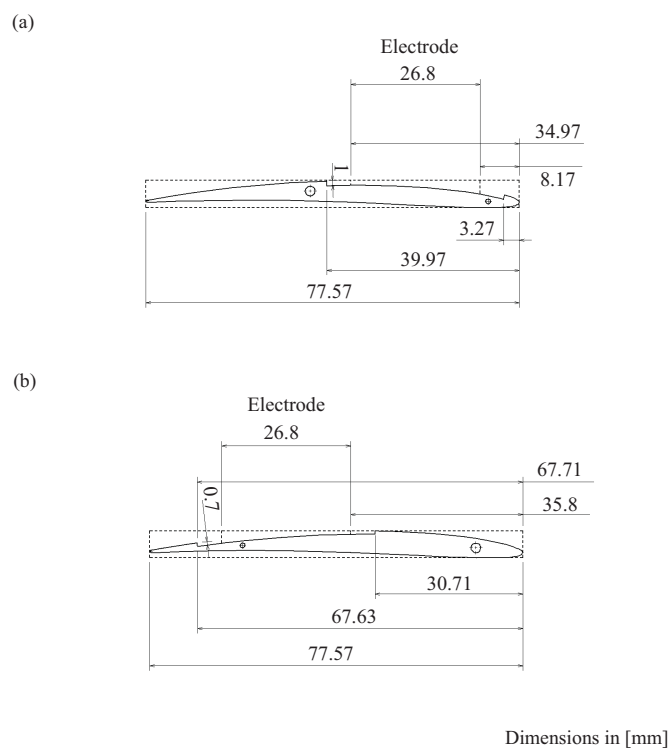


Figure 3.9: Positions of the DBD plate and electrodes with respect to the NACA profile.

Pictures of the final DBD-profile system with the plasma are shown in figure 3.10, with the plate integrated close to the leading edge and close to the trailing edge. The profiles are mounted in the nozzle between the two lateral windows made of Plexiglas (see next section). The profile is held by four metallic pins.

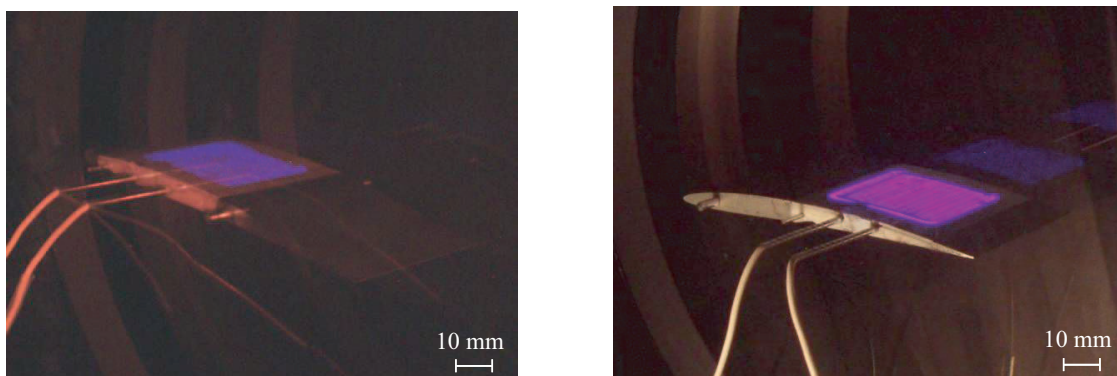


Figure 3.10: Pictures of the two configurations with the plasma generated on the suction side.

3.4 Transonic wind tunnels

3.4.1 Air supply system

The test stands at LTT are supplied with air by a radial compressor connected to a 2.4 MW electric motor. The global circuit is sketched in figure 3.11. The rotational speed of the compressor is constant. Its maximum pressure ratio is 3.5 and maximum mass flow rate is 10 kg/s. The pressure ratio is regulated by the aperture of the inlet valve of the compressor (1). The temperature of the compressed air is then cooled from 200°C down to about 20-60°C using two heat exchangers (4,5) and a bypass valve (3). The air is then injected in the different wind tunnels. On each of them one valve is placed at the inlet and another one at the outlet. The flow velocity or pressure level in the test facilities can be controlled either by the compressor pressure ratio, by the main bypass line (6), by opening an additional line (the free jet) or by throttling with the outlet valve of the test stand.

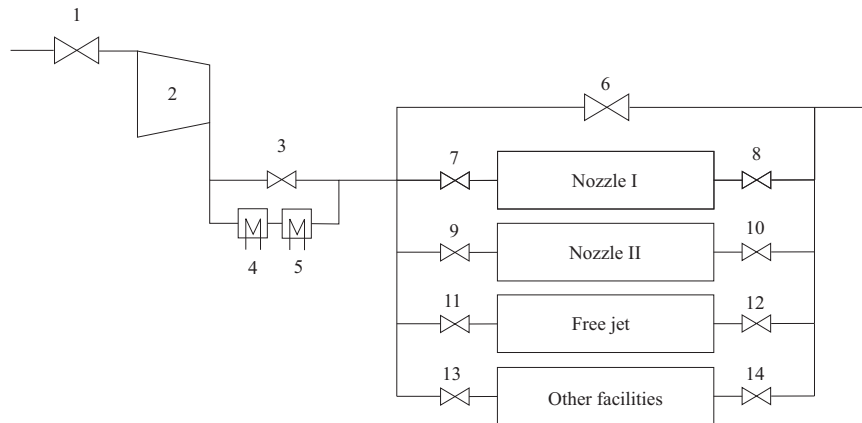


Figure 3.11: Schematic of the air supply system for the test stands.

3.4.2 Supersonic nozzle

The measurements on the flat DBD system have been carried out in the subsonic and in the supersonic nozzles. The supersonic nozzle is shown in figure 3.12. The flow coming from the air supply system passes a settling chamber where honeycomb structures calm³ the incoming flow before it enters the test section. The section is 100 mm wide (in the z direction). The upper and lower liners are made of plastic and can be adjusted using three screws in order to control the velocity distribution in the nozzle.

A lateral window has been manufactured in polyoxymethylene (POM) to mount the DBD alumina plate on the sidewall. A square insert is made on the window's inner surface, where the plate is embodied and fixed with silicone. Two holes traversing the window let the power supply cables pass from the outside of the nozzle to the DBD plate.

³Honeycomb structures break large eddies in the incoming the flow into smaller eddies.

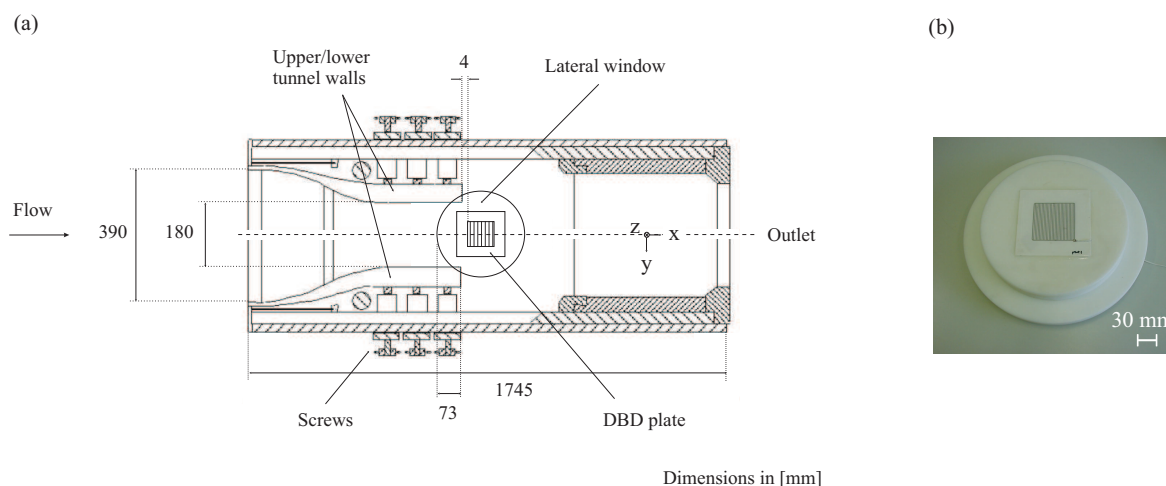


Figure 3.12: Schematic of the supersonic nozzle with the flat DBD system mounted on a lateral window (a) and picture of the window with the DBD plate (b).

The air tightness and insulation is made with silicone and Kapton[®] tape. The picture in figure 3.12 shows the system. The second lateral window on the opposite side of the nozzle is made of Plexiglas to allow for optical access to the discharge.

The positions of the upper and lower liners have been chosen such as to have a relatively uniform supersonic velocity over the discharge region. The pressure and Mach number distributions in the Laval nozzle have been calculated numerically and are shown in figures 3.13 and 3.13. The calculations have been made using Gambit as mesh generator (structured) and Fluent 6.2 as fluid solver (compressible Navier-Stokes equations using an x-y turbulence model). The mean velocity over the plasma region is about Mach=1.1.

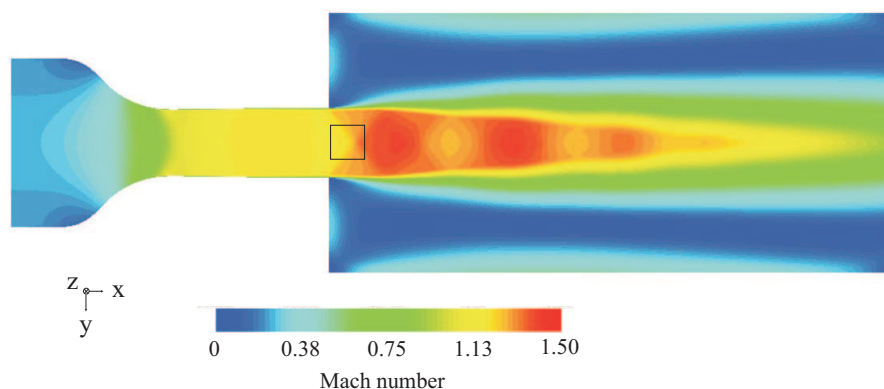


Figure 3.13: Mach number distribution in the supersonic nozzle with the position of the upper electrode (black square) [56].

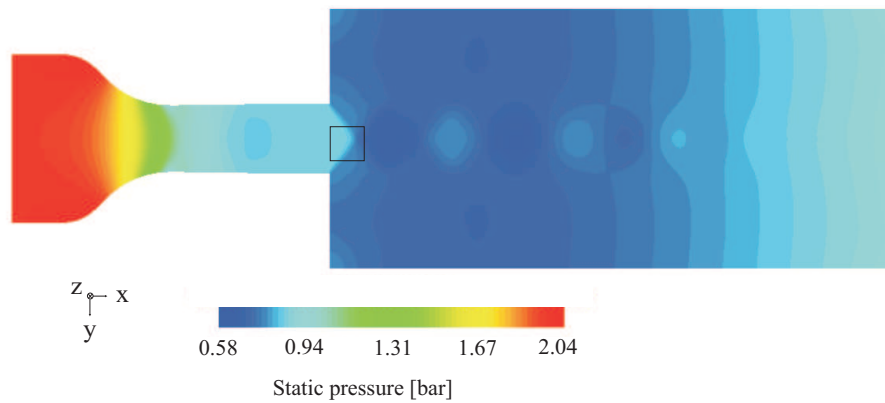


Figure 3.14: Static pressure distribution in the supersonic nozzle with the position of the upper electrode (black square) [56].

3.4.3 Subsonic nozzle

The experiments on the flat DBD system and the NACA3506 profile with the integrated DBD system have been performed in a subsonic nozzle generating flows with velocities up to $Mach=0.75$. A schematic view of the nozzle is presented in figure 3.15. The section is 40 mm wide (in the z direction). In the same way as for the supersonic nozzle, the flow is calmed in the settling chamber before entering the test section. In this nozzle the upper and lower walls, or *liners*, are parallel and guide the flow past the lateral windows where the profile is mounted. The lateral windows are made of Plexiglas in order to ensure optical access for the Schlieren visualization technique discussed in section 3.5.2. Additional optical accesses exist on the top and bottom walls, through Plexiglas plates inserted in the nozzle liners and external test stand walls. The angle of incidence of the profile can be changed by rotating the lateral windows.

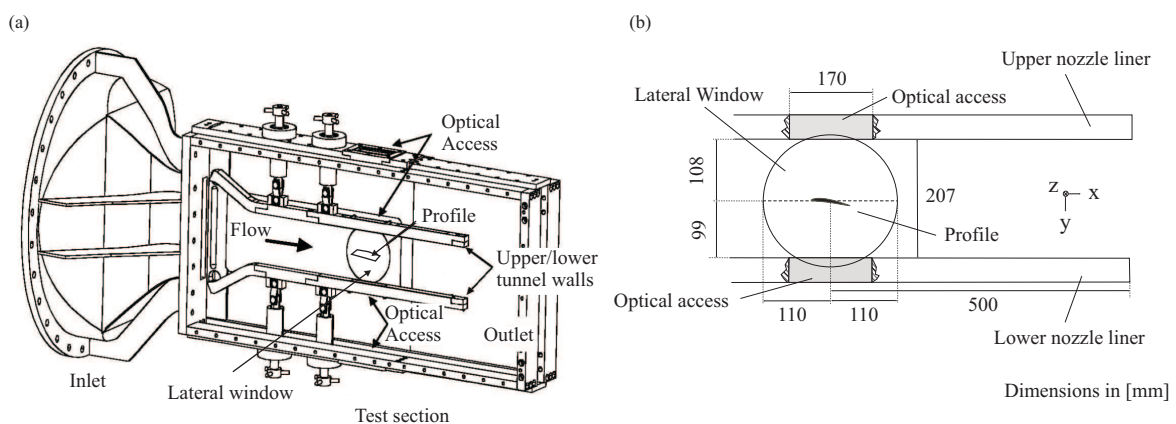


Figure 3.15: Schematic of the subsonic wind tunnel (a) with test section dimensions (b).

The pressure and Mach number distribution in the nozzle strongly depends on the characteristics of the profile as will be shown in chapter 6.

3.5 Aerodynamic measurement techniques

For the study of the flow properties, only Schlieren visualization and pressure taps on the walls of the nozzle have been used because these techniques are completely non-intrusive and avoid any interaction of the measurement technique with the flow or with the discharge. Situations *plasma on* and *plasma off* can be measured at exact same conditions and compared directly since the exact same techniques are used for both situations. Intrusive techniques to measure the velocity field, like Particle Image Velocimetry (PIV) or Laser Doppler Anemometry (LDA), require the addition of particles in the flow and could interact through electrostatic forces with the surface discharge, modifying the results. Moreover, pressure taps on the surface of the profile could provoke arcing through the holes and have effects on the measurements which would be difficult to isolate and interpret.

Schlieren images giving only qualitative information about the gas density gradient, and pressure taps giving very local pressure measurements, the Mach number and pressure distributions around and on the surface of the profile have been calculated numerically solving the Reynolds-Averaged-Navier-Stokes equations with CFD++ (finite volume method). The model, validated with Schlieren visualizations and pressure measurements, will be described in details in appendix D.

3.5.1 Pressure measurements

Pressure measurements have been used for two different purposes: the determination of the flow conditions inside the nozzle (inlet Mach number) and the study of the far-field pressure signature of the shock in the subsonic nozzle, as depicted in figure 3.16.

The pressure taps are connected to pressure sensor units via flexible tubes. A sensor unit (Scanivalve DSA 3017) consists of 16 temperature-compensated piezoresistive pressure sensors, a 16-bit A/D converter and a calibration valve. The system is controlled by a computer with a Labview program. The pressure measurements are time-averaged. The error on pressure measurements is ± 0.5 mbar.

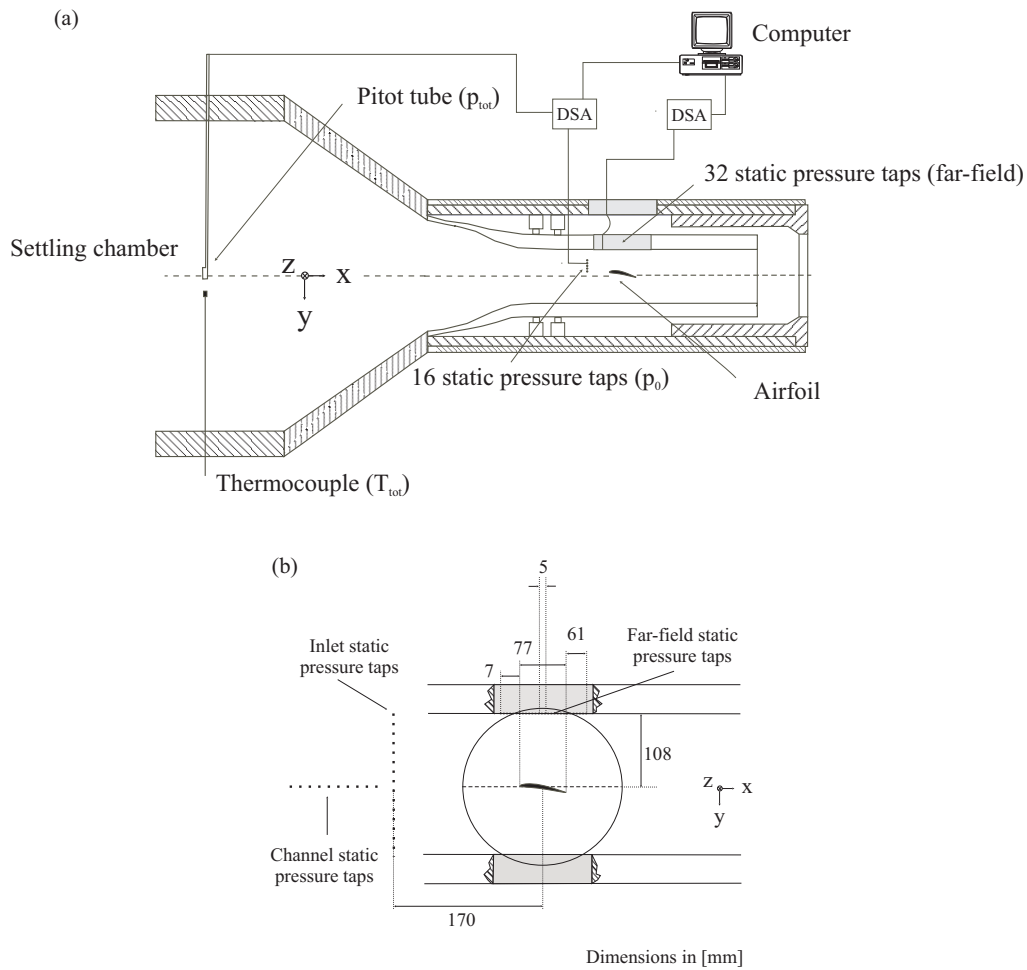


Figure 3.16: Pressure measurements for the determination of flow conditions and far-field pressure distribution on the subsonic nozzle.

Flow conditions

Flow conditions have been measured in the same way for the supersonic and the subsonic nozzle. Assuming an isentropic flow, the total pressure p_{tot} and the total temperature T_{tot} measured in the settling chamber and the static pressure p_0 measured at the desired location in the test section give the isentropic Mach number M_{is} and the velocity u at this location [43]:

$$M_{is}^2 = \frac{2}{\kappa - 1} \left[\left(\frac{p_{tot}}{p_0} \right)^{\frac{\kappa-1}{\kappa}} - 1 \right] \quad (3.2)$$

$$T = T_{tot} \left(\frac{p_{tot}}{p_0} \right)^{\frac{\kappa-1}{\kappa}} \quad (3.3)$$

$$a = \sqrt{\kappa RT} \quad (3.4)$$

$$u = M_{is}a \quad (3.5)$$

where κ is the adiabatic coefficient of the gas, a is the speed of sound, R is the specific gas constant. In the experiment, the total pressure p_{tot} is measured in the settling chamber with a Pitot probe, at the same level as the center of the test section. The total temperature T_{tot} is also measured in the settling chamber, with a PT100 platinum resistance temperature gauge. The head of the PT100 is placed close to the Pitot tube head. The variations of the total pressure and total temperature along the center line of the converging nozzle are negligible. T_{tot} is used as an indicator of the stabilization of the flow conditions.

The static pressure is measured just in front of the lateral window at several positions as shown in figure 3.16, for the supersonic and subsonic nozzles.

Far-field pressure distribution

As can be seen in figure 3.16, a field of pressure taps has been integrated in the optical access facing the suction side of the profile. These pressure taps have been installed in order to measure the pressure gradients across the shocks and by this mean gain quantitative information about the shock in addition to the qualitative measurements with the Schlieren technique described in section 3.5.2. In order to prevent disturbing effects like stagnation or eddies in the cavities of the holes, a diameter of 0.5 mm has been chosen [57]. The 32 holes are drilled 5 mm apart from each other and positioned along a line in the direction of the flow at the center of the nozzle (in the z direction), over a distance of 145 mm.

In aerodynamics, pressure distributions are often expressed in terms of the pressure coefficient c_p which is a non-dimensional quantity defined as:

$$c_{p0} = \frac{p_0 - p_{0\infty}}{p_{t\infty} - p_{0\infty}} \quad (3.6)$$

where c_{p0} is the static pressure coefficient, p_0 is the local static pressure, $p_{0\infty}$ is the static pressure in the uniform free stream and $p_{t\infty}$ is the total pressure in the uniform free stream.

3.5.2 Schlieren visualization method

Flow visualization methods can be classified in three different groups. The first one comprises the techniques by which a gas or a liquid is added to the flow being studied. If the added particles are small enough, it can be assumed that their motion is the same as the fluid. However, the visualization is indirect because the pathlines of the particles are observed and not the pathlines of the fluid itself. These techniques usually give results with sufficient precision for stationary and incompressible fluid conditions. However, the difference between the motion of the particles and the motion of the fluid might be significant in unsteady and compressible conditions, as for example in transonic flows where high density gradients appear. A second group of visualization methods, for compressible

flows, takes advantage of the direct dependency between the fluid density and the index of refraction. When light goes through a medium with a variable index of refraction, its direction changes as well as its phase. Shadowgraph and Schlieren techniques make use of the change in direction of the light beam, whereas holography methods exploit the change in phase. These methods are completely non-intrusive. The last group of visualisation techniques associates both of the methods discussed above, by injecting energy instead of particles. Thermal or electric energy is injected in order to excite fluid particles and use them as tracers. However, this technique modifies the physical properties of the flow.

The Schlieren technique, like the shadowgraph technique, is used to study density fields in transparent media. While shadowgraphs show the variation of the second derivative of the index of refraction n , Schlieren images map the first derivative of n . These methods are not only non-intrusive, but they also allow for the observation of fast transient phenomena. Therefore, they are often chosen for the investigation of shocks and flames. It is important to note that these techniques are integral, which means that the measured quantity is integrated along the path of the light beam. Their use in 3-dimensional flows is therefore not appropriate. Schlieren and shadowgraph visualizations methods give qualitative results. They can be calibrated to extract quantitative information from the results, but the process is very inaccurate and is usually not implemented.

Figure 3.17 is a sketch of the physical principle of the Schlieren method. A parallel light beam is formed with a light source S and a lens L_1 with focal length f_1 . The light then crosses the medium which deflects the light rays according to the variations of density. After re-focusing of the beam with lens L_2 , there are several focusing points corresponding to areas in the test section with different densities. A knife edge is used to cut part of the light, coming from high density or low density regions, making them appear in black in the image on the screen.

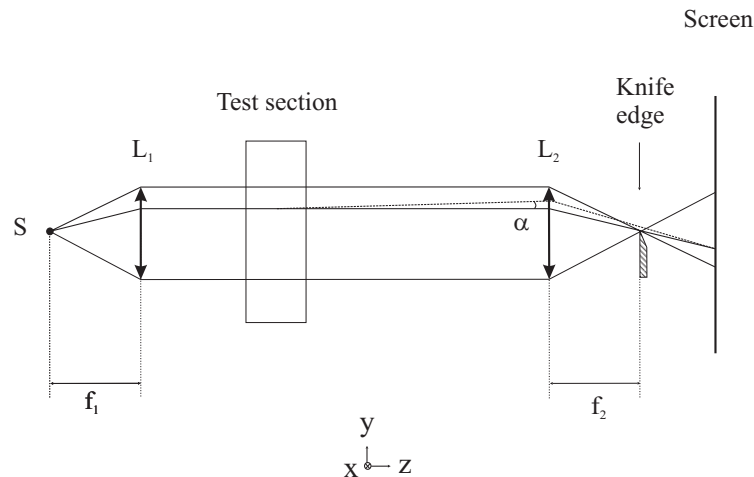


Figure 3.17: Principle of the Schlieren visualization technique.

Schlieren visualizations can be explained described in a few equations [58,59]. Gladstone-Dale equation in air gives the relation between the density and the index of refraction in the perturbed medium and the density and index of refraction at given conditions ρ_{ref}

and n_{ref} :

$$\rho = \rho_{ref} \frac{n_r - 1}{n_{ref} - 1} \quad (3.7)$$

Ray optics analysis gives the equations linking the deviation angle α_{dev} and the index of refraction:

$$\alpha_{dev} = \int_0^L \frac{\partial n_r}{\partial y} dz = \frac{n_{ref} - 1}{\rho_{ref}} \int_0^L \frac{\partial \rho}{\partial y} dz \quad (3.8)$$

Finally, the variation of intensity on the screen can be written as :

$$\frac{\Delta I}{I_K} = \pm \frac{f_2}{a_K} \frac{n_{ref} - 1}{\rho_{ref}} \int_0^L \frac{\partial \rho}{\partial y} dz \quad (3.9)$$

where I_K is the intensity on the screen resulting from a_K , which is the area not cut by the knife edge (when no disturbance is present).

The Schlieren system has been set-up around the subsonic nozzle as shown in figure 3.18. In order to reduce chromatic aberrations, two parabolic mirrors have been used instead of the two lenses. This modification in the set-up is called Z-type Schlieren due to the Z trajectory of the light beam. This system also has the advantage that mirrors are easier to manufacture in large dimensions compared to lenses. Typically a 30 cm diameter is needed to expand the beam over the lateral windows area. Moreover, space is optimized and larger focal length can be used to improve the alignment quality. However, optical off-axis aberrations are more difficult to compensate. Two plane mirrors have been added to the system in order to further fold the light beam and reduce the space needed.

All the optical elements are fixed on two optical tables, one on each side of the test section, mounted on a pneumatic bench to absorb the vibrations of the floor. The light source is a high-intensity mercury arc lamp (Linus Photonics HBO 200W). The light from the lamp is focused onto a circular pinhole diaphragm with a condenser lens. The light from the lamp is not homogeneous spatially and thus the diaphragm allows the choice of a homogeneous zone of emission from the lamp. The pinhole actually represents the light source. After the pinhole, the light beam diverges and is directed towards the first parabolic mirror (2 m focal length, 30 cm diameter) by reflection on the first plane mirror. After the first parabolic mirror, the beam becomes parallel since the source is at its focal point. The quality of the parallelism of the beam will determine the quality of the reproduction of the actual test area. Behind the test section, the beam is re-focused (after folding) by the second parabolic mirror (same characteristics as the first one). In order to minimize lateral off-axis aberrations (coma, astigmatism), the angle of reflection at the parabolic mirrors has to be minimal. The angle is the same on both mirrors, on opposite sides (Z - shape). The minimum achievable angle is the configuration presented is 12°. After the knife edge, a lens focuses the image onto a CCD detector. The focal length of the lens depends on the magnifying ratio desired. The CCD cameras used are a Nikon D1x (3008 x 1960 pixels, down to 1/16000 s exposure times) for steady images and a PCO Imaging Sensicam QE for unsteady imaging (1376 x 1040 pixels, 12 bits dynamic range, exposure times down to 0.5 μ s). The ratio of light cut by the knife edge regulates the illumination and sensitivity of the Schlieren images. The measurements are performed in the dark in order to minimize parasitic light. Also, the quality of the nozzle lateral

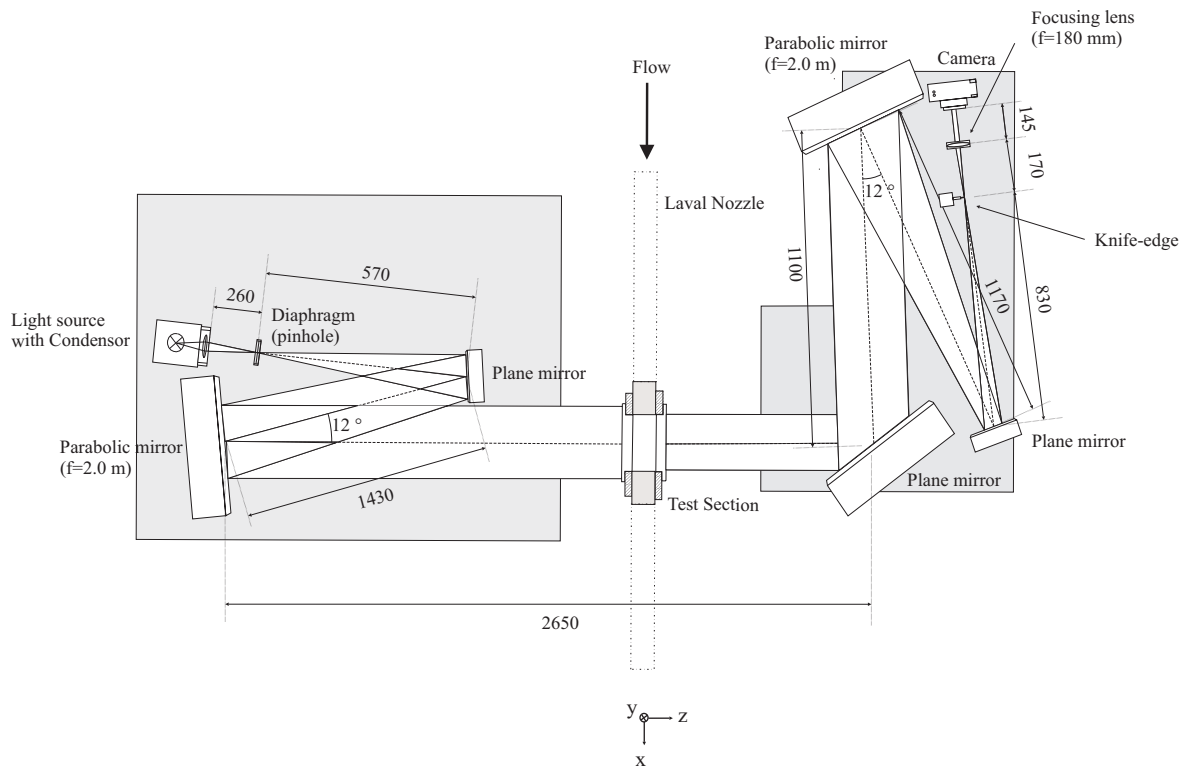


Figure 3.18: Detail of the Schlieren set-up.

windows is very important. Plexiglas has been chosen because it is less breakable than glass. Glass is easier to break around the points where strong constraints appear, as for example around the pins holding the profile in the test section. The Plexiglas has been polished at optical quality (Rugosity N1 = $\pm 0.025 \mu\text{m}$, planarity $\pm 0.005 \text{ mm}$, parallelism of surfaces $\pm 0.05 \text{ mm}$).

The Schlieren system discussed above is called *traversing*. A *reflective* Schlieren system can also be set-up, in which the second test section window would be replaced by a mirror. This set-up would allow for example to fix the test object to the mirror, and therefore avoiding pins that distort the image close to the profile. However, there are several drawbacks:

- The quality is less satisfying than in the traversing system mainly because the mirror is fixed to the nozzle wall and vibrates which perturbs the image.
- The mirror would be very close to the discharge and arcing probability would be increased in a significant way.

Chapter 4

DBD system without airflow

The objectives of the present chapter are to characterize the surface dielectric barrier discharge without airflow and to understand the influence of

- the applied electrical conditions: external circuit, voltage frequency and voltage amplitude
- the structure of the DBD plate: electrode geometry, electrode encapsulation and dielectric properties

on the following discharge properties:

- discharge regime
- spatial distribution of the discharge.

These latter will play an important role in the interaction of the plasma with a flow. In addition to that, the results presented here will help to compare the measurements that have to be performed with different DBD configurations due to technical constraints.

LTCC technology allows, for the first time, to fully encapsulate the electrodes in a ceramic matrix. It ensures their protection from the chemical attack of the reactive species created in the plasma, which increases the lifetime of the DBD system in a significant way and improves the reproducibility of the experiments. Since this DBD system is new, it is important to characterize the discharge it generates and compare it to the discharge generated by a conventional non-encapsulated DBD plate.

The first section discusses the discharge properties under different electrical conditions and the second section addresses the different DBD plate structures. The plasma is investigated using electrical as well as optical diagnostics (CCD imaging, photomultiplier measurements). Finally, the main results are summarized.

4.1 Influence of the electrical conditions

This first section discusses discharge regime and breakdown as a function of the external electrical conditions. First, a typical DBD current curve is discussed. After that, the influence of the voltage frequency and voltage amplitude are addressed. The interpretation of the observations is done with the help of the numerical model developed by Lagmich et al. and described in [60].

A typical current curve is shown in figure 4.1 (a), which is generated by the DBD system described in (b). For the present chapter and the following ones, this specific DBD system geometry will be referred to as *Al₂O₃-baseline*. The current suffers significant ringing after a peak (see zoom in appendix C), which in fact is not due to the plasma but to the external electrical circuit. A second external circuit effect is that the voltage can be slightly distorted: when the current varies, the geometry of the plasma is modified, which makes the capacitance of the DBD plate change. The impedance of the circuit then changes as well and in the end affects the voltage.

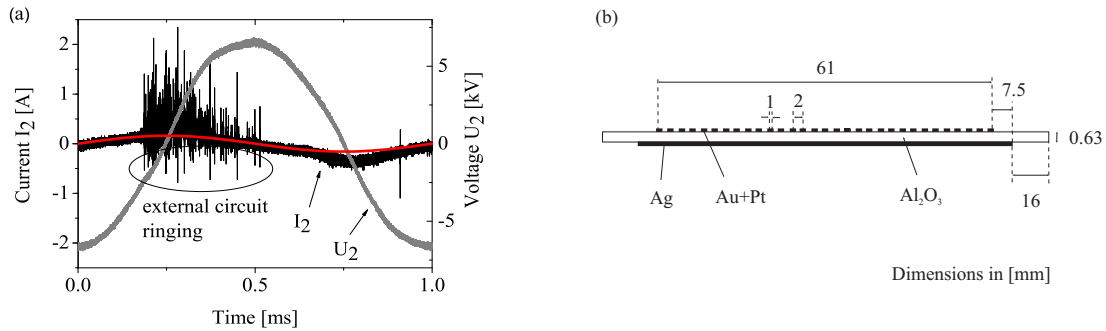


Figure 4.1: Typical current generated at applied voltage $U_2=4.2$ kV rms and 1 kHz (a) by a *Al₂O₃-baseline* geometry (b)

The current signal in figure 4.1 clearly shows that the discharge is filamentary. The microdischarge current peaks vary slightly in amplitude (about 20%) and in relative position from one period to the other, which is an indication of the unsteadiness of the filaments. The amplitude of the current peaks is about ten times larger on the positive half-period than on the negative half-period and they can reach several amperes on the positive half-period. Their duration is about 100 ns only (see appendix C), on the positive as well as on the negative half-period¹. As a consequence of the ringing due to the external circuit, the rate at which current peaks appear is rather difficult to determine in a precise manner. However, orders of magnitude can be found by counting the number of peaks appearing during a certain given time². In figure 4.1 ($U_2=4.2$ kV rms at 1 kHz), positive peaks appear at a 1 MHz rate on average and negative peaks appear at a higher

¹Note that this duration could be limited by the external circuit bandwidth

²Fast Fourier Transforms of the current give an almost continuous power spectrum, which shows that the peak generation is relatively random

rate, about 3 MHz.

After removing the capacitive current from the total current (red curve in figure 4.1), a continuous component remains which underlies the filamentary part, on both half-periods (less visible on the positive one because of the current oscillations). This implies that the plasma is not purely filamentary, but is made of a continuous glow or corona-like component and a filamentary component. This is confirmed by photomultiplier measurements of the whole discharge as shown in figure 4.2.

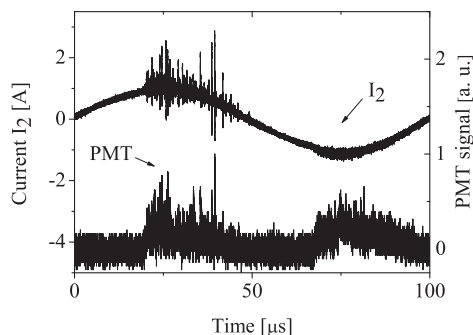


Figure 4.2: Current and the photomultiplier signal for Al_2O_3 -baseline at $U_2=2.5$ kV rms and 10 kHz.

Voltage frequency

The frequency of the applied voltage U_2 has little influence on the discharge regime. The discharge stays filamentary with an underlying glow or corona like component, from 1 kHz up to 15 kHz. An example is given in figure 4.3 (a) at 10 kHz. Nevertheless, as the frequency is increased, the peak rate increases as well. At 10 kHz, the rate of the peaks on the positive half-period is about 5 MHz and of the order of 10 MHz on the negative one (1 MHz and 3 MHz rate respectively at 1 kHz voltage frequency).

In addition to that, the frequency slightly modifies the *burning voltage*, defined here as the minimum voltage that one has to apply in order to generate the plasma uniformly around the top electrode. The burning voltage is plotted in figure 4.3 (b) as a function of the frequency of U_2 . As the frequency is increased from 1 to 15 kHz, the burning voltage diminishes from 2.3 to 1.8 kV rms, which is small but not negligible compared to the measurement errors. This is understandable, if it is assumed that the charge density does not completely vanish from one period to the other. In that case, at higher frequencies charges have less time to recombine giving higher charge build-up and allowing for lower burning voltages.

One has to be careful when talking about the effects of the applied voltage frequency. Indeed, the external circuit does interact with the DBD system in the same way for all frequencies. Even if an impedance matching circuit is added the secondary circuit properties (after the transformer) are different because the self-inductance and capacitors have been changed. Therefore, the discussion here is restricted to the qualitative effects of the voltage frequency.

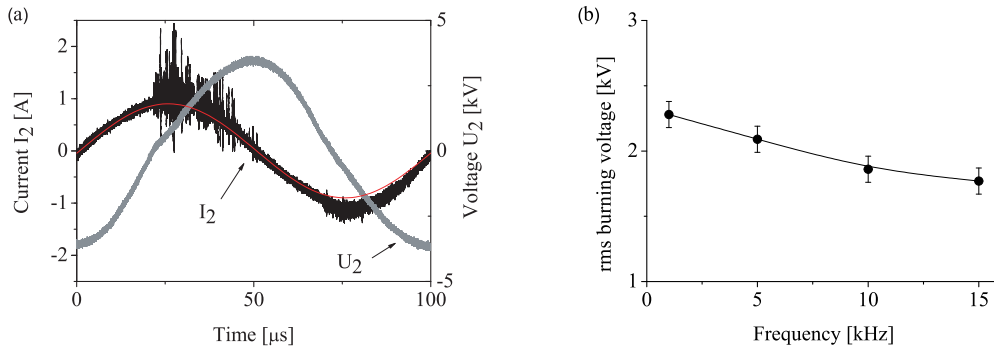


Figure 4.3: Typical current at applied voltage $U_2=2.4$ kV rms and 10 kHz (a) generated by a Al_2O_3 -baseline geometry and burning voltage as a function of applied voltage frequency (b).

Voltage amplitude

Figure 4.4 shows two current curves generated at the same voltage frequency (5 kHz) but at different voltage amplitudes. It shows that increasing the amplitude of U_2 increases the amplitude of the current peaks and the amplitude of the continuum as well. Moreover, the current peaks appear on a larger range, they start earlier regarding the voltage phase. Since the rate at which the peaks appear is found to remain constant, for these ranges of applied voltages, it means that the number of filaments slightly increases with the applied voltage. This is observable when the discharge is switched on, it does not switch on uniformly, but as the voltage is increased, a few microdischarges appear first, spread around the upper electrode and then the number of microdischarges increases and eventually the plasma forms around the whole upper electrode.

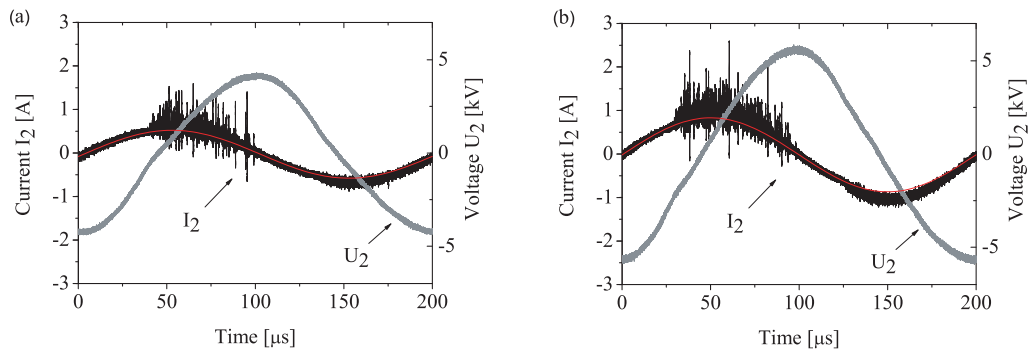


Figure 4.4: Typical current generated by a Al_2O_3 -baseline geometry at 5 kHz and applied voltage $U_2=3$ kV rms (a) and $U_2=4$ kV rms (b).

Comparison with an existing numerical model

A 2D electrical model of surface DBDs is proposed in [60] by Lagmich et al. which helps to understand the temporal evolution of the discharge on the positive and negative half-periods. The model considers a DBD in air generated at atmospheric pressure with a single upper electrode. A fluid approach has been chosen, considering the discharge collisional³. In addition to positive ions, negative ions are considered as well and are found to play an important role in the discharge physics (this is confirmed by the model of Likhanskii et al. in [61]). The only secondary process for plasma sustainment is assumed to be secondary electron emission by ion bombardment on the dielectric, photoionization effects being assumed as negligibly small. For a positive applied voltage gradient, the model predicts a development of the discharge similar to a streamer along the surface, generating a series of high current peaks as can be seen in figure 4.5 (a). Between the current peaks, low current regimes are predicted, which correspond to the formation and expansion of a positive ion cloud above the surface until space-charge sufficiently distorts the electric field that filament breakdown occurs. The current falls down to zero after each breakdown. These low current regimes resemble glow or corona regimes (they are predicted by the model of Likhanskii et al. in [61] as well). For a negative applied voltage gradient, a current of the form depicted in figure 4.5 (b) is obtained by the model. Current peaks of smaller amplitude are formed, at higher rates. The calculations show that a negative space charge forms and expands along the surface, but its expansion is not limited by breakdown as opposed to the positive case. Space charge builds up during the whole half-period, forming a continuum on the current signal underlying the current peaks.

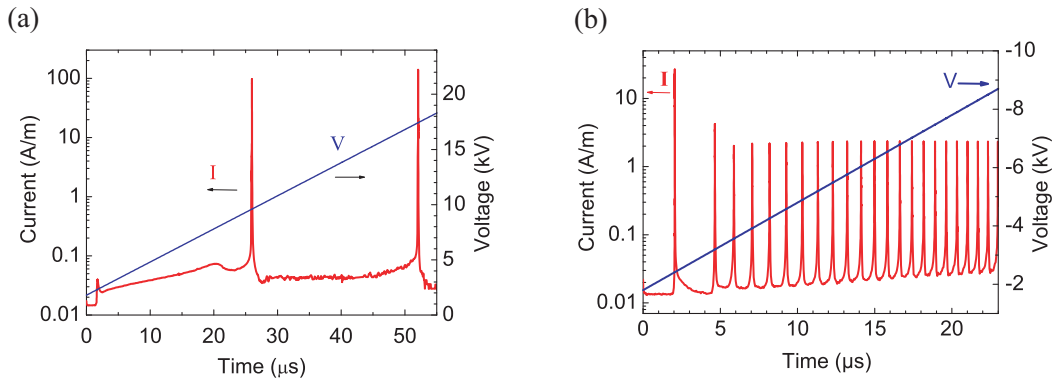


Figure 4.5: Figures adapted from Lagmich et al. [60] showing the predictions of Lagmich et al. for the current generated under a positive voltage ramp (dV/dt) (a) and negative voltage ramp (b).

Qualitatively, this model correctly reproduces the experimental current curves shown above for Al_2O_3 -baseline geometry. The current peaks with higher amplitudes on the positive half-period and higher rate on the negative half-period, as well as the continuum

³mean free path of particles $\lambda_{mfp} \ll$ characteristic dimensions of the discharge

are observed both in our experiment and in the results of the numerical model from Lagmich et al. Moreover, the model predicts higher peak amplitudes at higher voltage ramps (dV/dt). The same peak current amplification is observed in the experiments when the voltage amplitude is increased at constant voltage frequency (figure 4.4), which is equivalent to increasing the voltage ramp. In addition to that, the model predicts higher peak rates at higher voltage ramps. This is observable in the experiments when the frequency is increased (in figure 4.1 at 1 kHz, the voltage ramp is 24 V/ μ s giving 1 MHz and 3 MHz peak rates on the positive and negative half-periods, and in figure 4.3 at 10kHz, the voltage ramp is 135 V/ μ s giving 5 MHz and 10 MHz peak rates respectively)

Quantitatively, the experiments on the Al_2O_3 -*baseline* geometry and the predictions of Lagmich et al. correspond in certain aspects. In both cases the negative peaks have an amplitude about 10 times smaller than the positive peaks and they are about 2-3 times more frequent. However, the frequencies predicted by the model are about a factor 10 lower than the ones observed in the experiment presented here. This can be explained by the fact that the model is 2D and the experiments are 3D. In the experiment, several microdischarges are generated at different places in the third dimension. Depending on the repartition and diffusion of charges on the surface, the discharges might not be generated at the exact same time. This contributes to higher peak frequencies. It can also be that photoionization or photoemission, even if not dominant, contribute in the process of filament generation. In addition to that, the predicted current peak amplitude is slightly overestimated by the model (for the positive half-period, 100 A/m instead of about 30 to 60 A/m from the experiment⁴). As explained by Lagmich in [62], the intensity of the current peaks decreases when the secondary emission coefficient γ increases. Therefore, γ is probably higher in the experiment, and phenomena like photoemission or secondary emission by metastables might play a significant role.

Despite the slight quantitative divergences, the model by Lagmich et al. [60] gives good qualitative predictions of what is observed in the current curves measured with the Al_2O_3 -*baseline* geometry. This validates the hypotheses of the model that secondary emission by ion bombardment plays a leading role in the discharge dynamics and that negative ions play an essential role in the properties of the discharge forming during the negative half-period. However, it might be that other processes, even if not dominant, are contributing in a significant way.

⁴From the single-gate CCD image of Al_2O_3 -*small* (figure 4.11) and its current peaks generated during the 10 μ s gate at t_p , it can be estimated that about 100 discharges form for a single current peak. On the CCD images, the microdischarges have widths of about 0.3 mm. This gives 30 mm discharge length over the whole electrode. Current peaks having amplitudes of 1 to 2 A, the discharge generates peaks of 30 to 60 A/m

4.2 Influence of the DBD plate structure

4.2.1 Electrode geometry

The use of different electrode geometries allow to control the area where the plasma will form. However, it also has an impact on the discharge properties as is shown in the present section.

The Al_2O_3 -baseline geometry is different on the edges than in the middle of the plate as seen in figure 4.1 (longer extension of the bottom electrode on the edges). In order to better understand the effects of the edges on the discharge regime, the two set-ups shown in figure 4.6 have been studied, and their current curves are shown in the same figure. The geometry with only one stripe generates many more high current filament than the geometry with 31 stripes, on both the positive and negative half-periods. This indicates that in a Al_2O_3 -baseline geometry, the filamentary part of the plasma is mostly generated on the edges. The amplitude of the filaments seems to be strongly dependent on the space that the plasma has for expanding laterally around the electrodes. Indeed, if consecutive stripes are close to each other, their electric fields overlap, averaging out their inhomogeneities and hindering the formation of streamer-like discharges. The rate of current peaks is about the same, about 500 kHz on the positive part. It is consistent with the fact that the voltage ramp is the same and it shows that the plasma expansion does not affect the rate of filament generation.

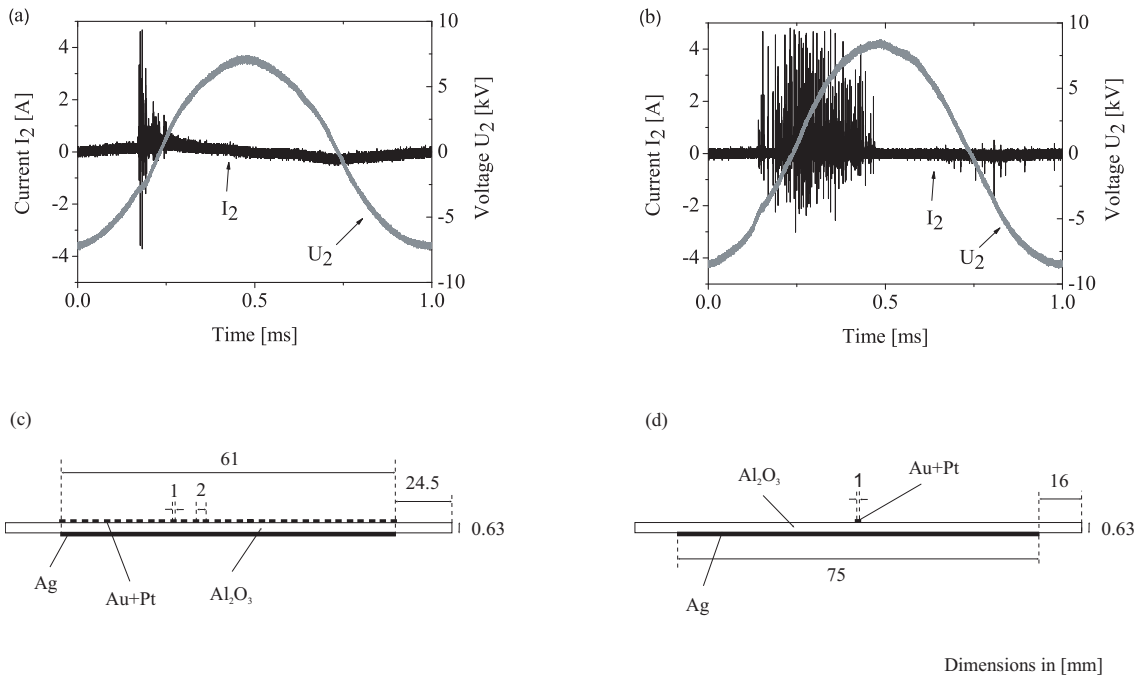


Figure 4.6: Current and voltage curves along with their respective geometries for Al_2O_3 -no-edge (a)(c) and for Al_2O_3 -line geometry (b)(d), at $U_2=4$ kV rms and 1 kHz.

Figure 4.7 (a) shows the current for an intermediate case, a Al_2O_3 -large geometry,

where stripes are 4 mm apart instead of 2 mm apart as in a Al_2O_3 -baseline geometry. The current peak rate is also about 500 kHz, but the number of high current filaments is larger than for Al_2O_3 -no-edge and smaller than for Al_2O_3 -line. This confirms the former observations that the extension around the electrodes and the number of high current filaments (or the amplitude of the filaments) are inter-dependent. Indeed, streamer behavior is favored when the $p \cdot d$ factor increases as seen in chapter 2.

If the spacing between the stripes is kept constant but the size of the overall electrode is reduced, as in Al_2O_3 -small compared to Al_2O_3 -no-edge, the current signal amplitude stays approximately the same. However, the peak rate is reduced from 500 kHz to about 300 kHz on the positive half-period. This shows that the size of the electrode slightly affects the peak rate and confirms the hypothesis mentioned previously that the total length of the upper electrode plays a role in the peak rate. This effect is difficult to point out between Al_2O_3 -no-edge and Al_2O_3 -line in figure 4.6 because of the very different peak amplitudes.

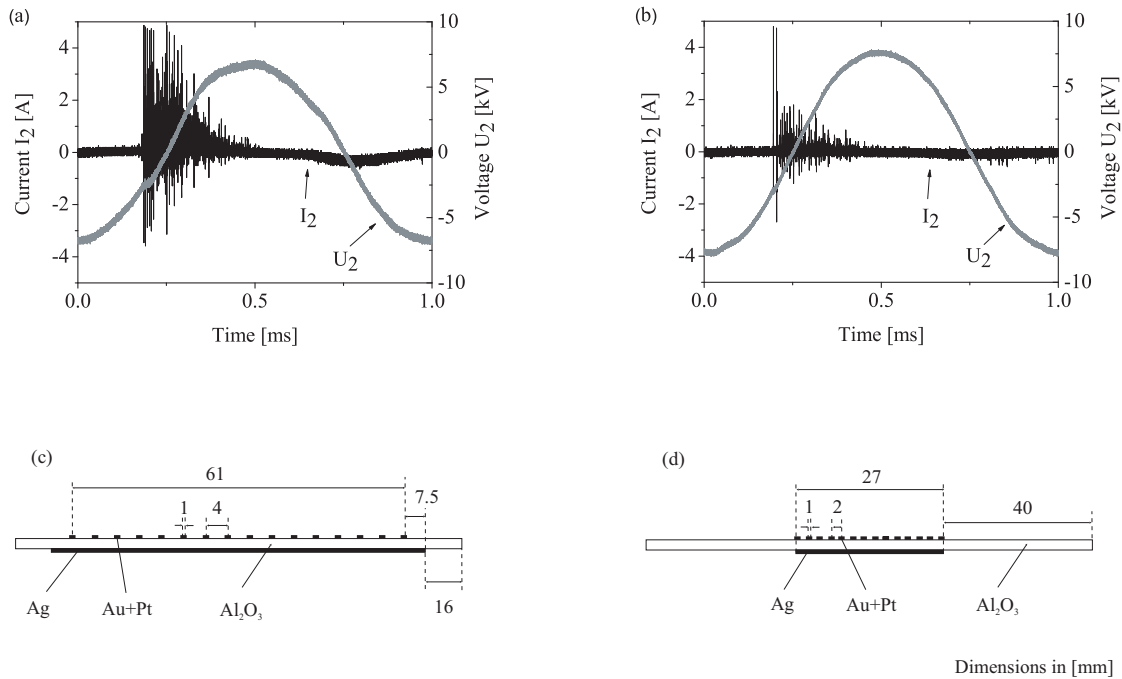


Figure 4.7: Current and voltage curves along with their respective geometries for Al_2O_3 -large geometry (a)(c) and for Al_2O_3 -small(b)(d), at $U_2=4$ kV rms and 1 kHz.

Burning voltages for the geometries described above are shown in figure 4.8. Results show that the geometry of the electrodes has not a strong influence on the burning voltage. In these cases where the electrodes are not encapsulated, the burning voltages can depend on the physical state of the electrodes, for example if they have been worn from long plasma operation times for example. In this case the burning voltage tends to increase because of the oxidation deposits that form around the electrodes which forms a small barrier (see picture in chapter 5). It is the case for the particular Al_2O_3 -baseline plate used for measurements in figure 4.8.

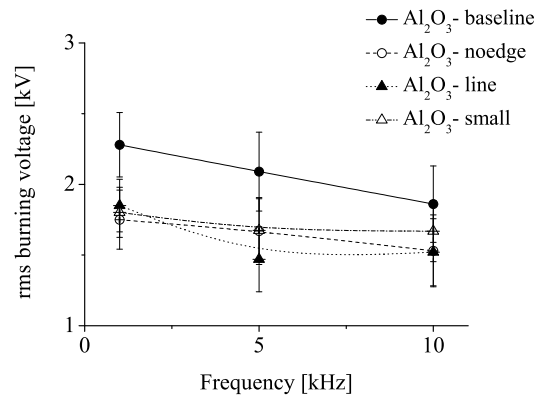


Figure 4.8: Burning voltages for different electrode geometries.

4.2.2 Encapsulation

The protection of the electrodes by encapsulation in a dielectric matrix is of primary importance to improve the lifetime of the DBD system but also to improve the reproducibility of measurements. How does this additional dielectric barrier modify the surface plasma properties (regime and spatial distribution)?

Regime

Figure 4.9 compares two DBD systems, *LTCC-not-enc* which is not encapsulated (a) and *LTCC-enc* which is encapsulated (these systems are used for the study of the plasma-flow interaction on an airfoil in chapter 6). The current curves show that the encapsulation strongly reduces the amplitude of the current peaks and their rate. For *LTCC-not-enc*, positive peaks are 0.35 A in amplitude on average, generated at a 1 MHz rate and negative peaks are about 0.15 A in amplitude at a 2 MHz rate approximately. For the encapsulated case, positive peaks are 0.05 A in amplitude on average at a 250 kHz rate and negative peaks are about 0.04 A in amplitude at about 500 kHz. These measurements show that the addition of a protecting ceramic layer (additional dielectric barrier), symmetrizes to a certain extent the properties between the positive and negative half-periods but is very costly in terms of current amplitude in the filaments and in the number of high current filaments.

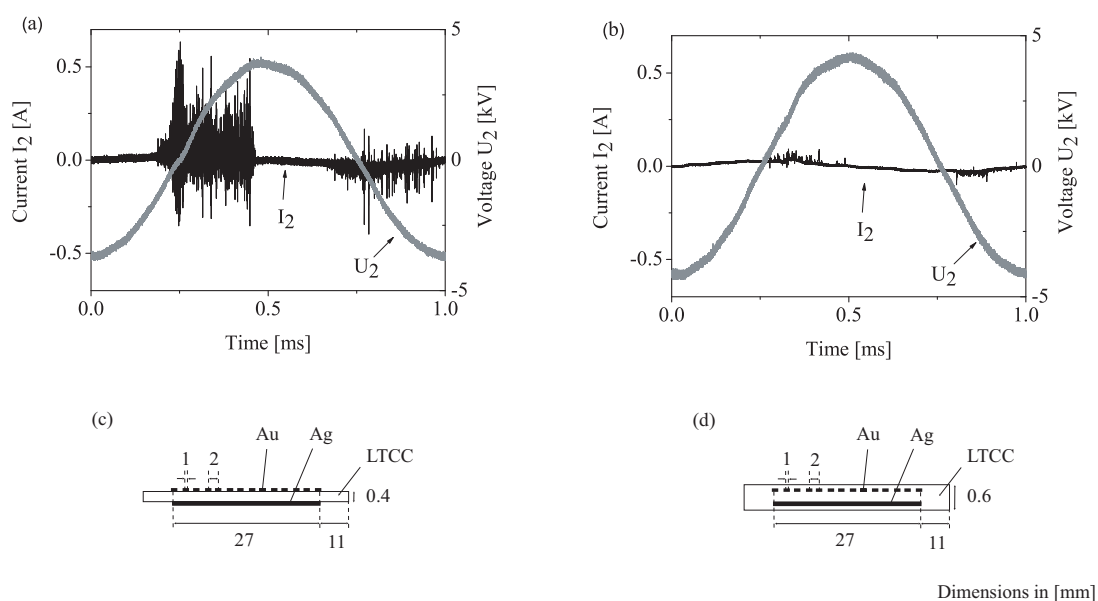


Figure 4.9: Current and voltage curves along with their respective geometries for *LTCC-not-enc* with apparent electrodes (a)(c) and for *LTCC-enc* with encapsulated electrodes (b)(d), at $U_2=3$ kV rms and 1 kHz.

At 10 kHz the encapsulation still reduces the number of peaks and their amplitude, but higher rates and current amplitudes than at 1 kHz can be obtained, as shown in figure 4.10.

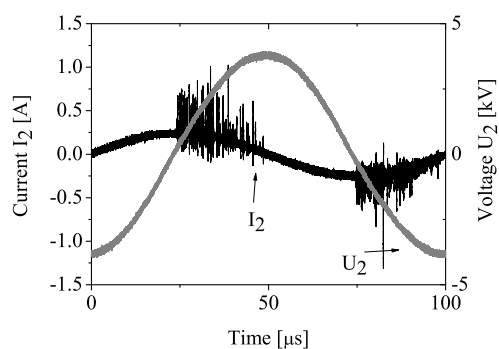


Figure 4.10: Current and voltage curves for *LTCC-enc* with encapsulated electrodes, at $U_2=3$ kV rms and 10 kHz.

The reduction of filament generation because of encapsulation is also observed on CCD images of the discharge generated by an Al_2O_3 -small geometry and an *LTCC-enc* geometry as shown in figure 4.11 (images are taken at same voltage amplitude and frequency, at time t_p which is the beginning of the positive half-period, with $10 \mu s$ exposure time). For non-encapsulated case, about 750 microdischarge spots can be counted on the surface, whereas there are only 200 spots over the same surface in the encapsulated case. These number can be divided by the number of current peaks that form in the $10 \mu s$ of exposure time (from the current in figure 4.9), giving the number of visible microdischarges per current peak. For the non-encapsulated case, this gives about 100 microdischarges per current peak, and only about 10 microdischarges per current peak in the encapsulated case. Figure 4.11 also shows that the continuous emission areas that would correspond to a corona or glow component is also reduced.

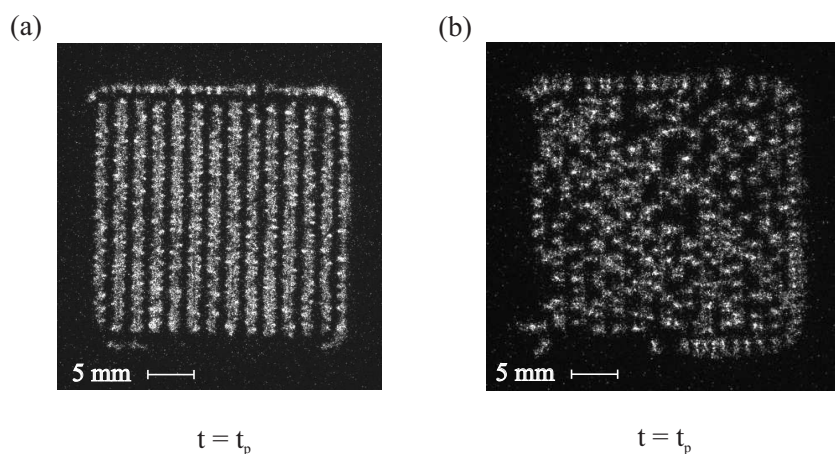


Figure 4.11: Single gate image of Al_2O_3 -small (a) *LTCC-enc* (b) at $U_2=3$ kV rms and 10 kHz, at time t_p with $10 \mu s$ exposure.

Time-resolved light emission collected with a photo-multiplier tube permits to investigate more in details the modification of the individual microdischarge properties between the non-encapsulated and encapsulated cases. Although for the negative half-period, the light peak duration is the same in Al_2O_3 -small and *LTCC-enc* and is about 50 ns, figure 4.12 shows that this is not the case for the peaks in the positive half-period. In the Al_2O_3 -small configuration, they are about 50 ns whereas they are about 150 ns for the *LTCC-enc*. In this latter case, the peaks do not display a typical intensity decay behavior, but rather seem to be formed of several overlapping peaks. It might be that the 3D statistical effects due to the repartition of charges on the surface are modified by the additional dielectric layer covering the top electrode. These overlapping peaks are not observed on the negative half-period. A detailed modeling of the encapsulated DBD configuration would be needed in order to understand these effects.

The burning voltage is also strongly affected by the addition of a dielectric layer on top of the electrodes as seen in figure 4.13. The burning voltage is doubled after the addition of a 0.1mm thick dielectric layer. The point where the current peaks start to form with respect to the voltage curve (burning condition of individual filaments) follows

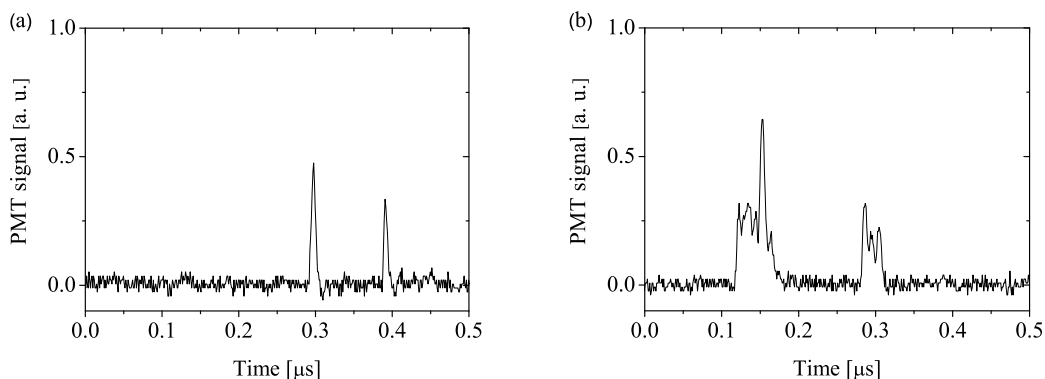


Figure 4.12: Close-up of positive PM peaks for Al_2O_3 -small at $U_2=2.5$ kV rms (a) and for $LTCC$ -enc at $U_2=3$ kV rms (b) at 10 kHz.

the same rules as can be observed in figure 4.9. The dielectric geometry is thus essential in the control of the discharge ignition.

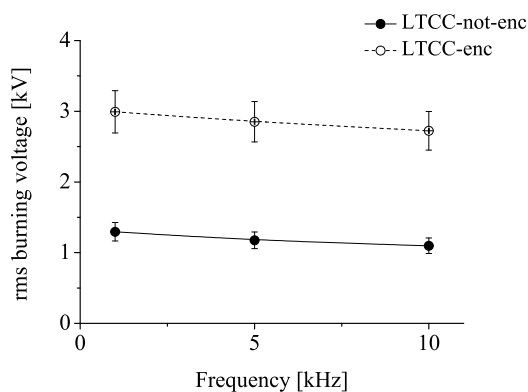


Figure 4.13: Burning voltages for non-encapsulated and encapsulated DBD plate geometries.

In addition to that, in the encapsulated geometry, the power seems to be dissipated more in the continuum component of the plasma than in the filaments, comparing to the non-encapsulated case, as shown by the Lissajous plots in figure 4.14.

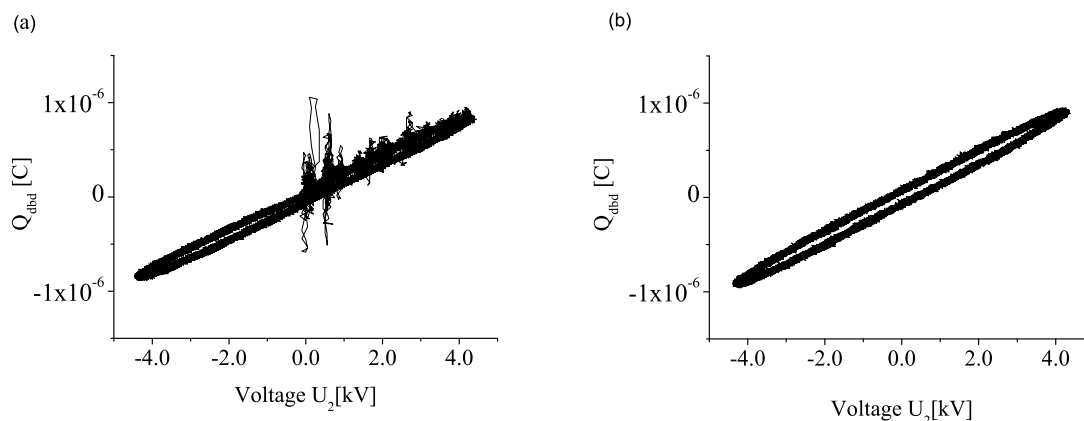


Figure 4.14: Lissajous figures for Al_2O_3 -small (a) and $LTCC$ -enc(b) at $U_2=3$ kV rms and 10 kHz.

Spatial distribution

CCD imaging shows that the discharge distribution around the electrode stripes is very much dependent on the system configuration, if it is encapsulated or not.

Time-resolved CCD images of the discharges generated by the Al_2O_3 -small (not encapsulated) and $LTCC$ -enc(encapsulated) geometries (same electrode pattern) have been acquired with the intensified gated PI-MAX camera, triggered with the voltage signal as explained in chapter 3. Results are shown in figures 4.15 and 4.17 below. Images have been taken at $10 \mu s$ exposure at the beginning of the filamentary regions on the positive and negative half periods, and with $\Delta t=10 \mu s$ and $\Delta t=20 \mu s$. At $\Delta t=30 \mu s$ and $\Delta t=40 \mu s$, when the gate is in the current region where no peaks are visible, the light emission from the plasma is negligibly small (this is valid for both geometries). In order to improve the sensitivity and signal to noise ratio, which is necessary at such a small exposure time as $10 \mu s$, images are accumulated over 400 camera gates. The images have been post-processed, normalizing the pixel intensities, in order to maximize the visibility of the discharge details. Uncorrected pixel intensities are shown in the intensity profiles in figure 4.16 and 4.18 where pixel intensities have been integrated in the direction parallel to the electrode stripes.

Figures 4.15 and 4.17 show that the discharge geometry is very different if the system is encapsulated or not. In the encapsulated case, the discharge forms on top of the electrodes as well, on both the positive and the negative half-periods. For the $LTCC$ -enc, double lines of plasma form on top of the central stripes and between the central stripes on the positive half-period. On the negative half-period, the plasma forming between the electrodes resembles the plasma forming on Al_2O_3 -small. This is better shown in the profiles of figures 4.16 and 4.18. These observations show that encapsulation of the electrodes yields a better covering of the surface by the plasma, which can be interesting for certain applications. Indeed, it allows a better distribution of the electric field and charges on the surface, namely by diffusion of charged particles on the dielectric surface.

Figure 4.16 shows that for Al_2O_3 -small, the light emission intensity decays more rapidly on the positive than on the negative half-period (which by the way indicates that different breakdown mechanisms seem to intervene in the positive and negative half-periods). On the contrary, for $LTCC$ -enc, the intensity decay rate is about the same for both half-periods. Moreover, the intensities of the positive and negative discharges are almost the same at every time step. This shows that when the electrode is encapsulated, the discharges are more symmetric from the emission intensity point of view. This symmetrization has already been observed in the current peak amplitudes.

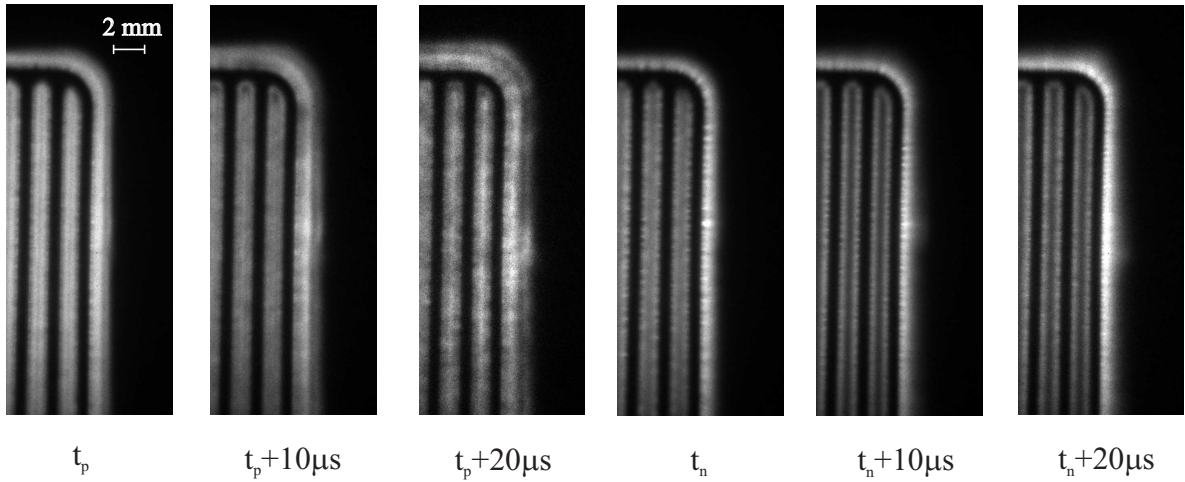


Figure 4.15: Image of Al_2O_3 -small, at $U_2=3$ kV rms and 10 kHz. Exposure time is $10 \mu s$ with different delays relative to t_p and t_n and images are accumulations of 400 camera gates.

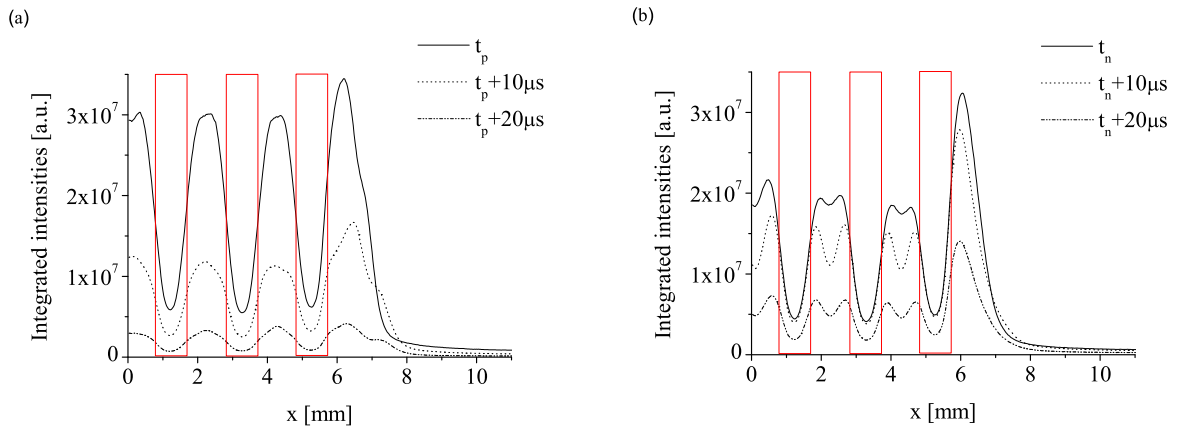


Figure 4.16: Integration of pixel intensities parallel to the electrode stripes from figure 4.15 for Al_2O_3 -small, on the positive half period (a) and on the negative half-period (b). Red squares show the positions of the electrodes stripes.

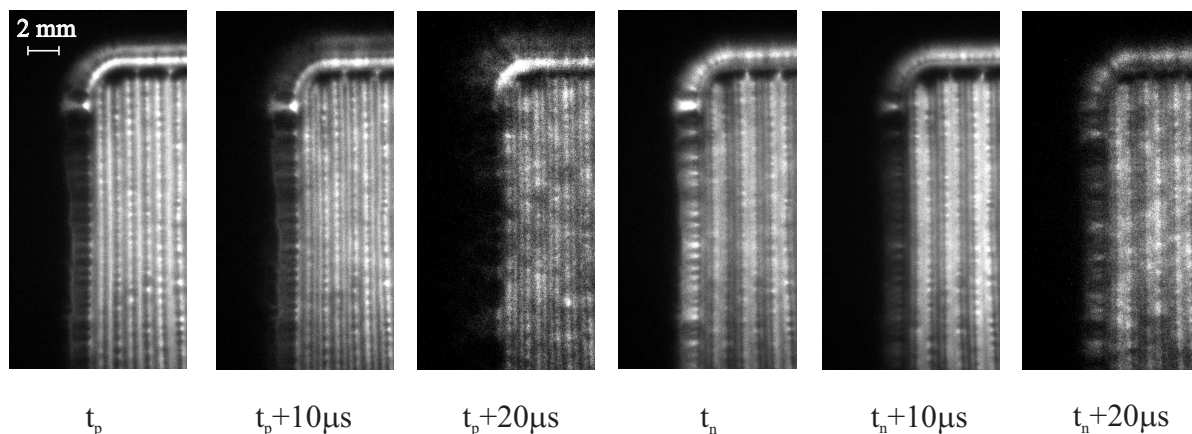


Figure 4.17: Image of *LTCC-enc*, at $U_2=3$ kV rms and 10 kHz. Exposure time is $10 \mu\text{s}$ with different delays relative to t_p and t_n and images are accumulations of 400 camera gates.

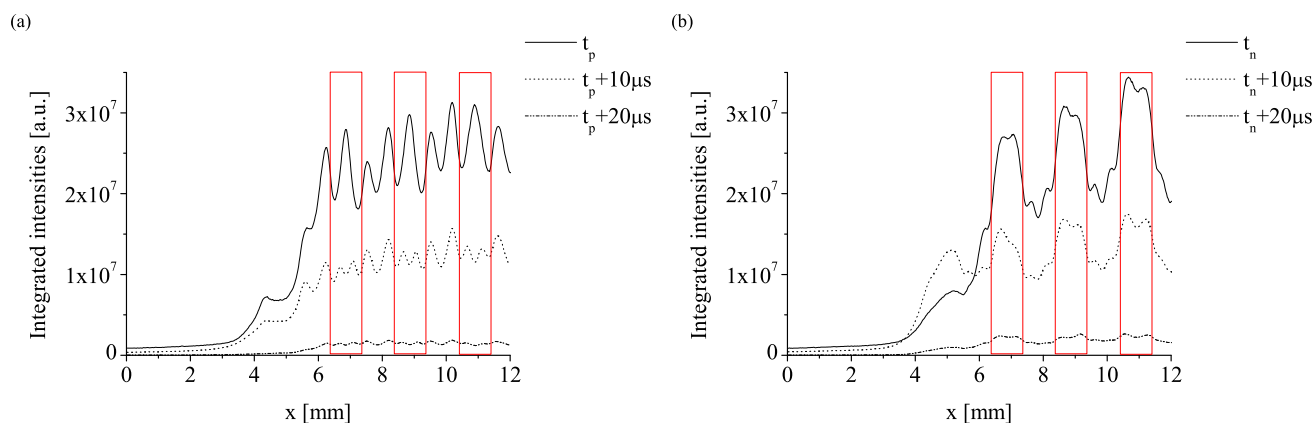


Figure 4.18: Integration of pixel intensities parallel to the electrode stripes from figure 4.17 for *LTCC-enc*, on the positive half period (a) and on the negative half-period (b). Red squares show the positions of the electrodes stripes.

In the non-encapsulated case, the plasma around the edge strip expands significantly as a function of time, as plotted in figure 4.19, whereas in the encapsulated case the plasma distribution is independent of time. The additional dielectric barrier limits the plasma expansion in a very significant way, mainly due to the significant reduction of the electric field intensity with the additional dielectric layer. For *Al₂O₃-small* the velocities of displacement of the discharge can be deduced from these measurements and are about 50 m/s for the positive discharge and about 20 m/s for the negative discharge.

The model by Lagmich et al. [60] shows that the electrons follow the expansion of the negative ion cloud. This means that the light emission, which is generated by electron excitation mostly, follows the negative ion cloud. Therefore the velocity of the plasma expansion as measured from the CCD images can be compared to the velocities found

in the model by Lagmich [62]. This model predicts a velocity of about 45 m/s for the negative ion cloud, which is in good agreement with what is observed here (a factor 2 difference). The situation is different for the positive half-period. In that case, the model shows that the electron density does not follow the positive ion density during the positive ion cloud expansion. Therefore, light emission distribution cannot be directly related to the extension positive ion cloud.

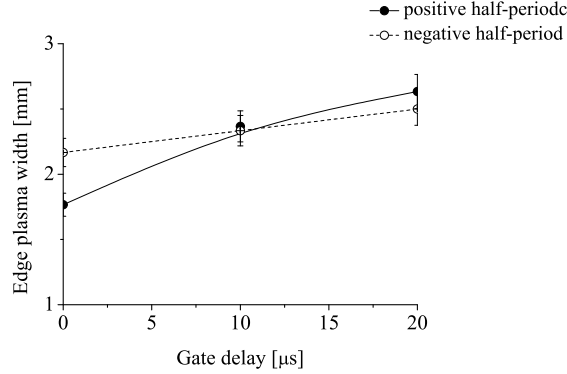


Figure 4.19: Edge plasma width as a function of the exposition gate delay, for Al_2O_3 -small at $U_2=3$ kV rms and 10 kHz.

The figures presented above show that for both the non-encapsulated and encapsulated DBD plates, the discharge appears very different on the positive and on the negatives half-periods. For Al_2O_3 -small the positive discharge extends rather homogeneously between the electrode stripes, whereas on the negative half-period, micro-discharges are clearly visible which are localized on the edges of the electrode. This fact is predicted by the model of Lagmich et al. [60] as well, which shows that negative discharges tend to form close to the cathode, whereas positive discharges expand up to the tip of the ion cloud during filament breakdown. For $LTCC$ -enc, the edge stripe has a characteristic filamentary pattern on the positive half-period, whereas it looks more like a corona on the negative half-period, emitting at higher intensities in a localized zone close to the electrode.

4.2.3 Dielectric properties

In the previous section, results from measurements on Al_2O_3 -small and $LTCC$ -enc have been compared in order to evaluate the effects of encapsulation. Although electrodes and the electrical conditions are the same, the dielectric properties slightly differ. For Al_2O_3 -small, the dielectric barrier is 0.63 mm and the permittivity of Al_2O_3 is $\epsilon_r \simeq 10$. For $LTCC$ -enc, the dielectric barrier is 0.6 mm as well (considering the electric field passes through the 0.1 mm encapsulation layer twice) but the permittivity of the LTCC material is $\epsilon_r \simeq 7.5$. Does the permittivity influence significantly the results presented above?

The model by Lagmich et al. [60] shows that the properties of the discharge depend on the behavior of the positive ion cloud on the positive half-period and on the behavior

of the negative ion cloud on the negative half-period. The model shows that the dielectric constant acts on the expansion of the positive ion cloud in the positive half-period in the way shown in figure 4.20 (η_V is the voltage ramp and w the thickness of the dielectric). As can be seen in the figure, a variation of ϵ_r between 7.5 and 10 results in a variation within 10% of the positive ion cloud extension. The model also shows that the expansion of the negative ion cloud in the negative half-period is independent of the dielectric permittivity (it only depends on the voltage amplitude in the relation $L \simeq 0.4U_{peak}$). Although the positive ion cloud expansion cannot be directly related to the light emission from the discharge, it shows that the physical conditions do not vary to a large extent and it can be said that it is consistent to compare the *Al₂O₃-small* and *LTCC-enc* geometries as has been done above.

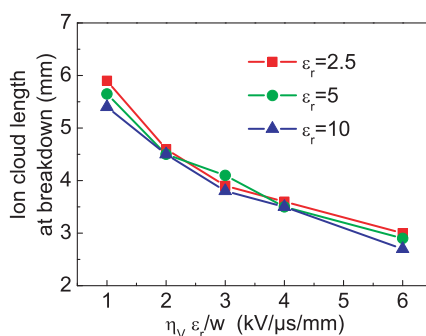


Figure 4.20: Model predictions for the extension of the positive ion cloud from the model by Lagmich et al. [60].

4.3 Summary

Current curves and photomultiplier measurements show that there is a filamentary and a glow- or corona-like component in the plasma. Results show that an increase in the applied voltage amplitude or applied voltage frequency, in other words an increase in the voltage ramp (dU_2/dt), results in:

- an increase in the filament rate
- an increase in the current peak amplitude
- thus eventually the power dissipated in the discharge (power input from the plasma in the surrounding air)

Moreover, increasing the frequency slightly reduces the burning voltage. These observations have been confirmed qualitatively by the model developed by Lagmich et al. [60], which suggests that the dominant phenomenon sustaining this kind of discharge is secondary electron emission by ion bombardment of the dielectric. The quantitative differences between this model and the experiments presented here come from the fact that

3D effects intervene in the experiment and other phenomena (photoemission and bombardment of the dielectric by metastables for example) contribute to the coefficient of secondary emission in a non-negligible way.

For the experiments on plasma-flow interaction for the airfoil case, the above results lead to the choice of a high frequency. However, the frequency should not be increased too much because the arcs are ignited at lower voltages for higher frequencies. This leads to the choice of 10 kHz as working frequency. The maximal voltage amplitude will be applied before arcs start to form with metallic parts around the DBD plate.

As shown by the measurements, the geometry of the electrodes has little effect on the burning voltage but it plays a role in the filament generation rate:

- the longer the effective length of the electrode, the more filaments are generated
- the further the electrode stripes are located, the higher the long filament generation rate (due to a higher p-d factor)

For the following technical reasons, the DBD system mounted on the airfoil has to be encapsulated:

- maximal lifetime and robustness of the system
- reproducibility of the experiment
- reduction of arcing probability with the surrounding metallic parts.

Results show that the drawbacks of encapsulation are that it increases the burning voltage, reduces the rate of filament production and the expansion of the plasma around the upper electrode. These disadvantages could be compensated by other means, for example by modifying the voltage waveform (see the calculation by Likhanskii et al. [61]). The advantages of encapsulation is that it results in a more uniform distribution of the plasma on the surface and in time (symmetrization between the positive and negative half-periods) and thus of the energy injection in the flow. The hypotheses presented here to explain the experimental results could be validated by a numerical model including a dielectric layer encapsulating the top electrode.

Chapter 5

Effects of high-speed airflows on a flat surface DBD

The objective of this chapter is to study the behavior of a surface DBD in a high-speed air flow, in a simple aerodynamic configuration, before using it on an airfoil (more complex aerodynamics) to study plasma-flow interaction.

A detailed experimental study of the effects of the high-speed flow on the discharge generated by a flat DBD system mounted on the wall of the subsonic or supersonic nozzles is presented. Thanks to the long lifetime of the flat DBD plate developed here (see chapter 3), these investigations are now possible. Moreover, it is demonstrated that the DBD generated by this system can be sustained in transonic and supersonic airflows, up to free stream Mach numbers of $M_\infty=1.1$. Some of these results have been presented in Pavon et al. [63].

The first section details the aerodynamics properties of the experiment. The following sections investigate the effects of the flow on the discharge burning voltage, the overall discharge regime and the microdischarge characteristics. The plasma is characterized electrically as well as optically (CCD imaging, photomultiplier tube measurements, optical emission spectroscopy) at different airflow velocities. Several plasma excitation frequencies and voltages are investigated. Also, geometrical effects and optical emission spectroscopy measurements are discussed. Finally, the main conclusions are summarized.

5.1 Aerodynamic configuration

The experiment consists of a flat DBD system (Al_2O_3 -*baseline*) inserted in a lateral window of one of the lateral walls of the nozzles (grazing, no steps). In the present chapter, M_∞ designates the free stream Mach number (outside the boundary layer) at position x_c along the longitudinal axis of the nozzle which corresponds to the middle of the discharge area (see figure 5.1). Measurements with free stream Mach numbers $M_\infty=0$ up to $M_\infty=0.7$ have been conducted in the subsonic nozzle, and measurements at $M_\infty=1.1$ have been performed in the supersonic nozzle. The aerodynamic configuration is simpler than on an airfoil because pressure gradients can be avoided. In the subsonic nozzle, the pressure gradients are negligible in the test section. In the supersonic nozzle, the DBD

can be placed in a region of homogeneous velocity and pressure distribution over most of the discharge area as shown in chapter 3.

As the flow enters the nozzle, boundary layers form on every of its walls, including the lateral wall where the DBD is mounted. Is the discharge completely inside the wall boundary layer and what is the velocity at the discharge location compared to the free stream velocity? The thickness of the boundary layer at the location of the plate along the x axis can be evaluated analytically using Blasius theory for boundary layers developing over flat plates (see Ryhming [44] for example). The boundary layer is assumed to start at x_0 , corresponding to the end of the nozzle convergent as shown in figure 5.1, develop laminarily up to the transition point x_t , and develop turbulently from this point on.

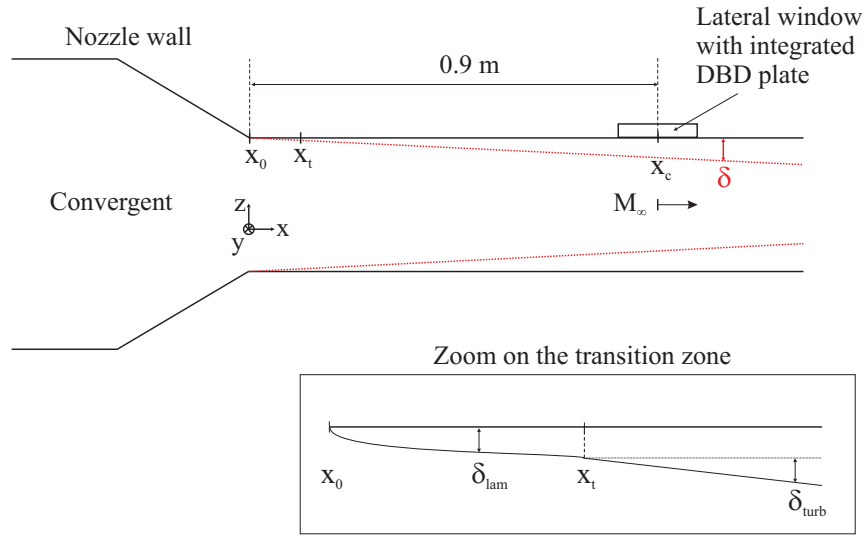


Figure 5.1: Schematics of the boundary layer development inside the nozzle, seen from top, and zoom on the transition point.

The transition point corresponds to the location where the Reynolds number reaches the critical value of $Re_t = 5 \cdot 10^5$ as given by Schlichting [64]:

$$Re_t = \frac{\rho_\infty U_\infty x_t}{\mu_\infty} = 5 \cdot 10^5 \Rightarrow x_t = \frac{\mu_\infty Re_t}{\rho_\infty U_\infty} \quad (5.1)$$

where ρ_∞ , U_∞ and μ_∞ are the free stream density, velocity, and viscosity respectively. Boundary layer theory gives the following relations for the thickness of boundary layers over flat plates:

$$\delta_{lam}(x) = \left(\frac{\mu_\infty x}{\rho_\infty U_\infty} \right)^{1/2} \quad (5.2)$$

and

$$\delta_{turb}(x) = 0.37x \left(\frac{\rho_\infty U_\infty x}{\mu_\infty} \right)^{-1/5} \quad (5.3)$$

which gives, for the total boundary layer thickness past the transition point ($x > x_t$):

$$\delta(x) = \delta_{lam}(x_t) + \delta_{turb}(x - x_t) \quad (5.4)$$

In order to calculate the velocity at a certain y position from the wall, a power law describing the velocity distributions above smooth walls can be used:

$$\frac{u}{U_\infty} = \left(\frac{y}{\delta}\right)^{1/7} \quad (5.5)$$

It is a good approximation for experiments in turbulent flows as suggested by Ryhming or Peneau [44, 65].

Considering $\rho_\infty=1.293 \text{ kg}\cdot\text{m}^{-3}$, $\mu_\infty=1.715\cdot 10^{-5} \text{ kg}\cdot\text{m}^{-1}\cdot\text{s}^{-1}$ and $x_c=0.9 \text{ m}$ (which is the location of the center of the DBD plate respective to x_0 in both the subsonic and supersonic nozzles), the boundary layer thickness is plotted in figure 5.2 as a function of the inlet Mach number $M_\infty = U_\infty/a_\infty$ ($a_\infty = \text{const.}$ because $T = \text{const.}$). The thickness of the plasma has been measured on images of the discharge taken at grazing angle and is found to be approximately $200 \mu\text{m}$. It is therefore well within the 10-15 mm thick boundary layer. The velocity at the discharge location ($y=200 \mu\text{m}$) is calculated for different M_∞ in figure 5.2 below.

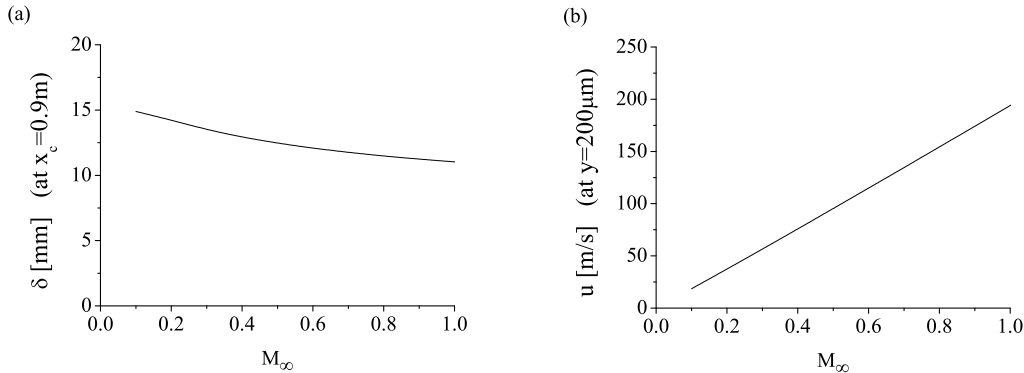


Figure 5.2: Analytical estimation of the boundary layer thickness at the DBD plate location ($x=0.9 \text{ m}$) (a) and flow velocity at the discharge location above the wall ($y=200 \mu\text{m}$) (b) for different free stream Mach numbers.

5.2 Burning voltage

The burning voltage (voltage at which the plasma ignites uniformly over the whole electrode surface) is a parameter that becomes important for applications. It is intended to minimize it in order to downsize the power supply, and be able to embark the system on flying platform for example. Burning voltages are measured on the Al_2O_3 -baseline geometry (see chapter 4, section 4.1) at different free stream Mach numbers M_∞ in the subsonic

nozzle for different voltage frequencies. Two flow directions are investigated, perpendicular and parallel to the top electrode stripes, in order to determine if the orientation of the flow with respect to the microdischarge has an importance.

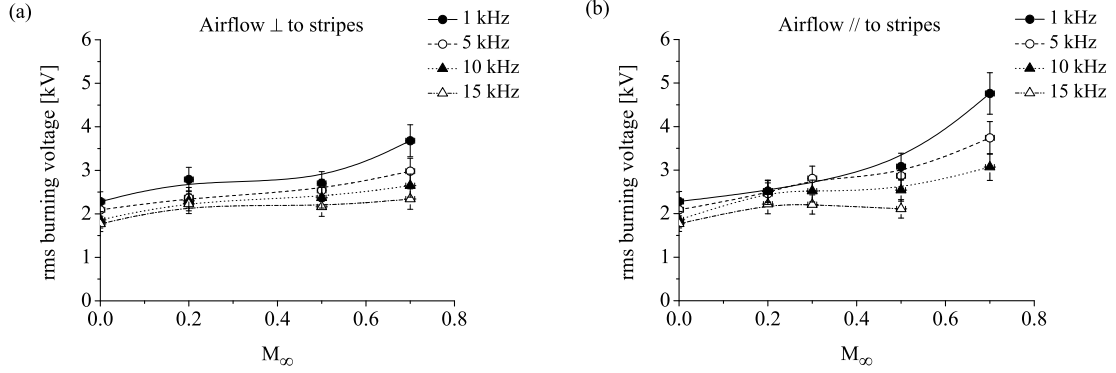


Figure 5.3: Discharge burning voltages for Al_2O_3 -baseline with an airflow perpendicular \perp (a) and parallel \parallel (b) to the electrode stripes.

The results in figure 5.3 show that the burning voltage increases significantly with the airflow velocity, specially when the electrode stripes are parallel to the air flow.

A possible cause of the increase of the burning voltage can be the variation of static pressure in the nozzle with the flow conditions. At $M_\infty=0$, the static pressure is 1 bar at the location of the discharge and at $M_\infty=0.7$ it rises up to 1.4 bar (in the subsonic nozzle). In this case, the Paschen curve for air (see chapter 2) predicts an increase in the breakdown voltage of about 40%. However, the variation of static pressure does not explain the fact that the burning voltage depends on the flow direction. The flow velocity, i.e. the fact that the working gas has non-zero momentum, must play a role in the generation of the discharge.

Even though the thermal velocity of ions is much smaller than the thermal velocity of electrons¹, the transfer of momentum to ions can still modify the expansion properties of the positive and negative ion clouds and thus influence the electrical characteristics of the discharge as suggested by Lagmich [62]. In order to understand these neutral-ion interaction in details and evaluate the impact on the measured current, the discharge should be modeled in geometrical conditions similar to the experiment presented here (with discharges extending both upstream and downstream of the external flow).

Finally, the burning voltage can also be increased due to the depletion of metastable states by the flow. This hypothesis is supported by optical emission spectroscopy measurements on the discharge as explained below.

¹ $v_{ti} \simeq$ velocity of sound ~ 300 m/s $\ll v_{te} \sim 10^6$ m/s (from the temperature of electrons $T_e \sim 1-10$ eV given by Kogelschatz in [20], section 2.4.2).

Figure 5.4 shows an optical spectrum of the emission from the DBD without air flow. The main features that can be recognized are the N_2 second positive system, corresponding to the $C^3\Pi_u \rightarrow B^3\Pi_b$ transition in the region from 300 to 500 nm, and the N_2 first positive system corresponding to the $B^3\Pi_b \rightarrow A^3\Sigma_u^+$ transition in the region from 600 to 900 nm. This suggests that the $A^3\Sigma_u^+$ metastable state, which has the longest lifetime (of the order of 10^{-2} s as given by Makabe et al. [66]), is the dominant excited species in the plasma and plays a role in the discharge dynamics. The optical emission spectra at different flow conditions are shown in section 5.7.

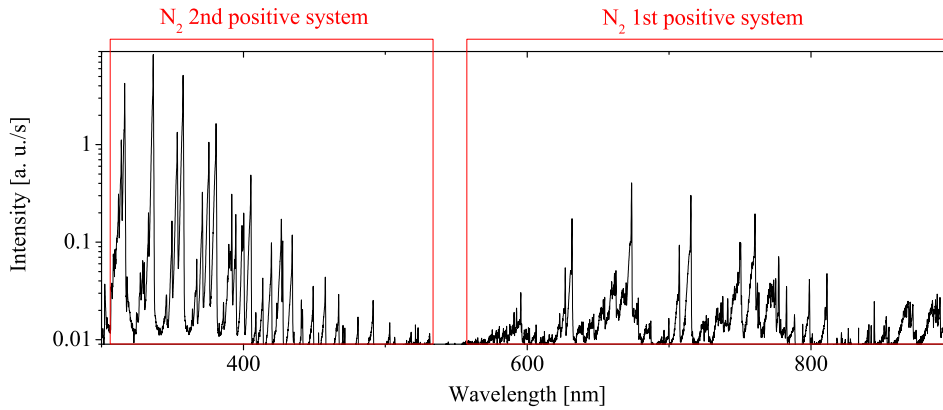


Figure 5.4: Emission spectrum from a plasma generated by a type Al_2O_3 -baseline geometry, at $U_2=2.5$ kV rms and 10 kHz.

The lifetime of $A^3\Sigma_u^+$ (10^{-2} s) is longer than the half-period of the voltage applied to the DBD ($3.3 \cdot 10^{-5}$ s at 15 kHz to $5 \cdot 10^{-4}$ s at 1 kHz). Therefore, at zero gas flow, the metastable state generated at a given time is available to the discharge generated at the following voltage half-period (since discharges form on both the positive and negative half-periods). In this way, metastables constitute a reservoir of energy in the plasma. The situation is different when the gas has a certain velocity. In this case, the metastables move at a velocity equal to the neutral molecules velocity (airflow velocity), due to momentum exchange, and are carried away from the discharge. For example, at a free stream Mach number $M_\infty=0.7$ in the nozzle, the velocity at the discharge height above the wall is about 125 m/s (figure 5.2). At this velocity, the metastable fly a distance of 63 mm during half a voltage period at 1 kHz and 4.2 mm at 15 kHz. At 1 kHz, they have the time (during one half-period) to cross the whole upper electrode area (60 mm) and be completely evacuated from the overall discharge region. In other words, metastables are purged out of the discharge during a single voltage period, thus reducing the internal energy and requiring a higher voltage for uniform ignition. At 15 kHz, metastables have the time to leave the local microdischarge region but could be re-used by discharges formed further downstream on the surface. Therefore, the effect of burning voltage increase is less significant at higher frequencies.

The metastables also contribute to the coefficient of secondary electron emission γ , through the bombardment of the dielectric. If metastables are depleted, this results in a reduction of γ . Lagmich [62] predicts that when γ decreases, the filaments start at higher voltage values, which is consistent with what is observed here.

Figure 5.3 shows that the orientation of the conducting stripes with respect to the airflow is also important. When the flow is parallel to the stripes, the burning voltage doubles, at 1 kHz frequency and $M_\infty=0.7$ for example, whereas it is only multiplied by 1.4 if the flow is perpendicular to the stripes. Indeed, when the airflow is parallel to the stripes, it is actually perpendicular to the microdischarge channels and the metastables move perpendicularly to the microdischarge channels. The removal of metastables from the channels is then more efficient than in the other case when they move parallel to the channels, and the burning voltage becomes higher.

5.3 Overall discharge regime

The flow modifies the discharge regime of the DBD, both its filamentary and continuous components. This is the case on the positive and negative half-periods.

The modification of the filamentary component can be observed by looking at the current curves. Figure 5.5 compares the DBD current signals without airflow and at $M_\infty=0.7$. The voltage at which the filaments start is increased, in a similar way as what is observed for the burning voltage.

On the positive half period, the amplitude of current peaks is slightly reduced. This cannot be explained by the reduction of γ (due to the reduction of metastable bombardment). Indeed, Lagmich et al. [60] predicts higher amplitudes for the current peaks when γ is smaller. On the other hand, at $M_\infty=0.7$, the amplitude of current peaks is significantly increased on the negative half-period of the current signal.

In addition to that, the rate at which the filaments are created does not significantly change with the flow conditions, as can be observed in figure 5.6. This gives an indication that the modification of γ and the charge distribution on the surface (positive and negative ion cloud distributions) should not be dominant effects. The reduction of the discharge region (in time) and the constant filament generation rate with increasing flow velocity means that the number of filaments is reduced as the flow velocity increases, for both half-periods.

The unsteady nature of the filamentary part of the discharge can be observed with the naked eye, microdischarge light emission varying in amplitude and position on a slow time scale (>30 ms). Filaments are much less mobile on the electrodes at high airflow velocities, they remain within a high electric field region, at the microscopic irregularities of the strip electrodes.

The continuous component of the discharge is best observed with a photomultiplier tube, generating the signals in figure 5.7 for the case without airflow and at $M_\infty=0.7$. Without flow, the photomultiplier tube detects a continuous emission underlying light pulses from the filamentary microdischarges which corresponds to the glow or corona like component of the plasma. At $M_\infty=0.7$, this continuous emission becomes negligible compared to the filamentary component. With increasing velocity, the filamentary component

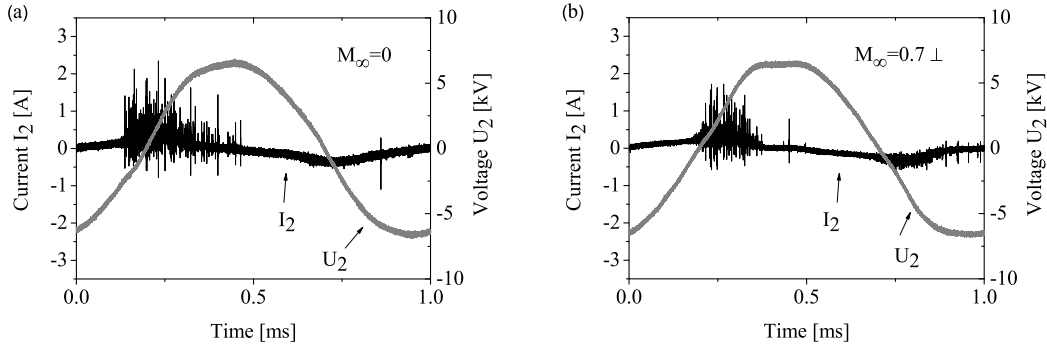


Figure 5.5: Current and voltage signals generated by Al_2O_3 -baseline for a free stream Mach number $M_\infty=0$ (a) and $M_\infty=0.7$ perpendicular \perp to the electrode stripes (b), at frequency 1 kHz and $U_2=4.8$ kV rms.

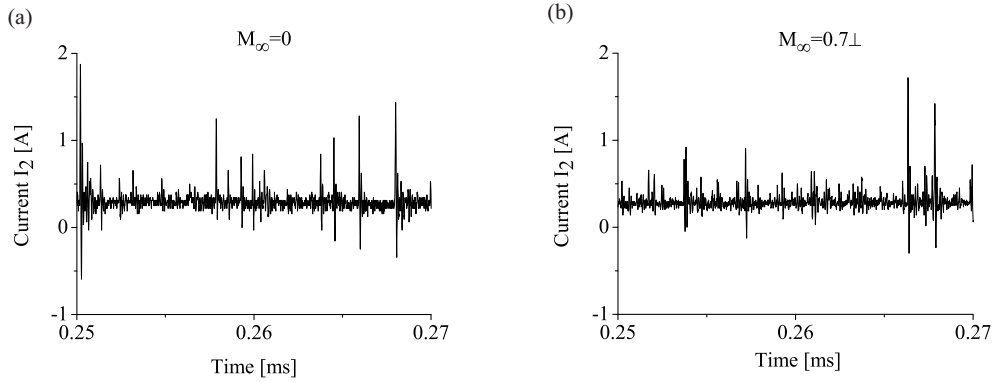


Figure 5.6: Current signal on the positive half-period generated by Al_2O_3 -baseline for a free stream Mach number $M_\infty=0$ (a) and $M_\infty=0.7$ perpendicular \perp to the electrode stripes (b), at frequency 1 kHz and $U_2=4.8$ kV rms.

of the discharge becomes more and more dominant.

The reduction of the glow component is also clearly visible on CCD images of the discharge, as shown in figure 5.8 without airflow and at $M_\infty=0.7$ with the flow direction perpendicular and parallel to the electrode stripes. At high speeds, filaments become more apparent, but actually the diffuse component does not completely disappear.

Since the discharge duration of the glow component ($3.3 \cdot 10^{-5}$ s at 15 kHz to $5 \cdot 10^{-4}$ s at 1 kHz) is of the same order of magnitude as the transit time of a molecule over the plate ($5 \cdot 10^{-4}$ s at $M_\infty=0.7$), the glow is considerably affected by the airflow. As explained by Gherardi et al. [21], N_2 metastables accumulate from one period to the other (if the period is smaller than the lifetime of the metastable), constituting a source of energy for low energy collisions. The airflow, by blowing the metastables, reduces the available internal energy and the plasma can then only develop where the electric field and the

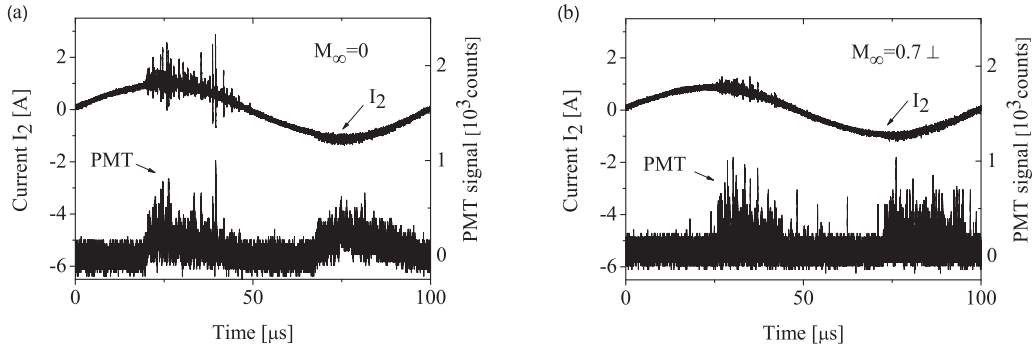


Figure 5.7: Current and photomultiplier signals generated by Al_2O_3 -baseline for a free stream Mach number $M_\infty=0$ (a) and $M_\infty=0.7$ perpendicular \perp to the electrode stripes (b), at frequency 10 kHz and $U_2=2.5$ kV rms.

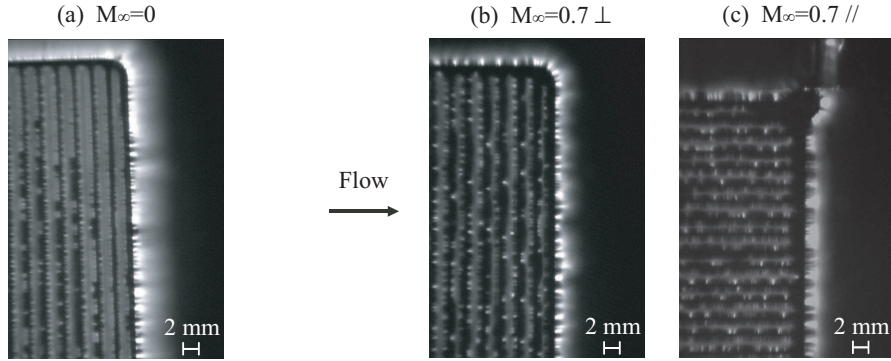


Figure 5.8: CCD images of the discharge of Al_2O_3 -baseline at frequency 1 kHz and $U_2=4.8$ kV rms and exposure time 0.2 s, at $M_\infty=0$ (a) and $M_\infty=0.7$ perpendicular \perp (b) and parallel (c) to the electrode stripes.

electron density is high enough. Localized microdischarges form: the plasma becomes more filamentary.

5.4 Microdischarge properties

Photomultiplier measurements in figure 5.9 show the light peaks emitted during the positive half-period, resolved in time, in the case without airflow and at $M_\infty=0.7$. This figure highlights the most significant effect of the airflow on the plasma: the reduction by one order of magnitude of the light pulse duration emitted by the individual microdischarges. The mean duration τ drops from 500 ns down to about 50 ns when the airflow speed increases from $M_\infty=0$ to $M_\infty=0.7$. This abrupt change suggests a transition between two breakdown mechanisms. Results for intermediate free stream Mach numbers and other frequencies are plotted in figure 5.10 for the flow perpendicular and parallel to the elec-

trode stripes. The duration of their light emission drops very quickly already at relatively low airflow speeds. The same phenomenon is observed on the negative half-period. It has been checked that the applied voltage and frequency have little influence on the transition observed.

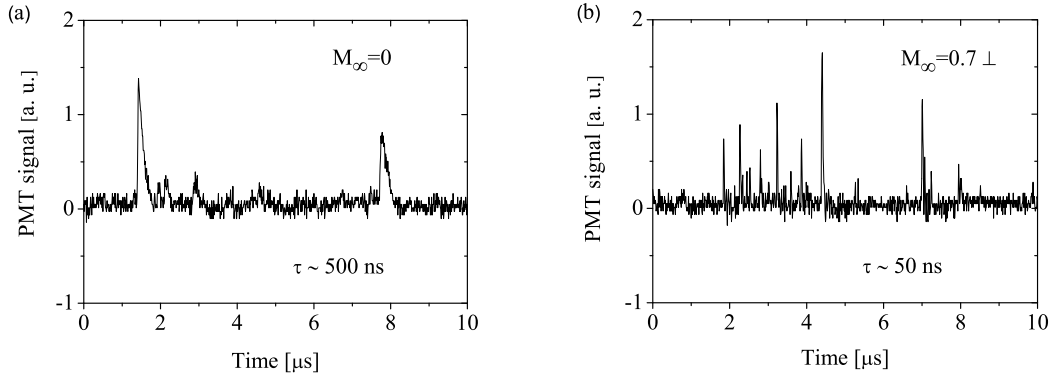


Figure 5.9: Photomultiplier signal for Al_2O_3 -baseline with a free stream Mach number $M_\infty=0$ (a) and $M_\infty=0.7$ perpendicular \perp to the electrode stripes (b), at frequency 1 kHz and $U_2=4.8$ kV rms.

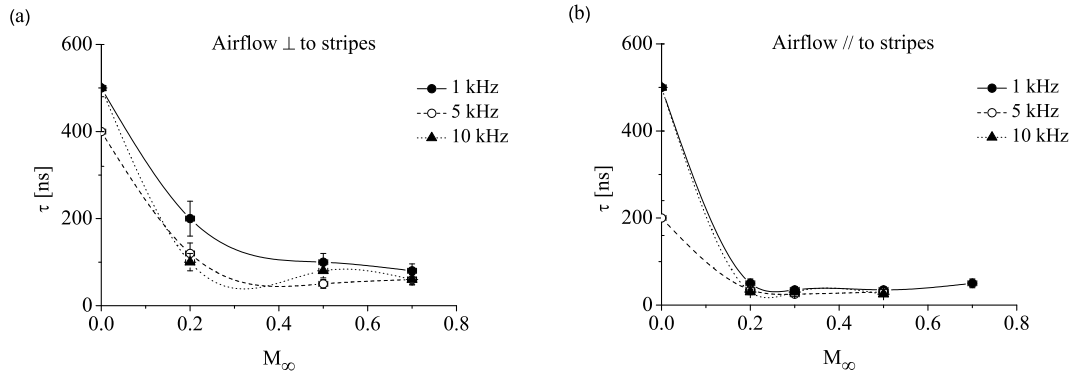


Figure 5.10: Mean microdischarge light pulse duration τ for Al_2O_3 -baseline as a function on the free stream Mach number M_∞ with the flow perpendicular \perp (a) and parallel $//$ (b) to the electrode stripes.

At low speeds ($M_\infty < 0.3$), the filament duration is very sensitive to the flow conditions. On the contrary, at high speeds ($0.3 < M_\infty < 0.7$), the filament duration is almost independent of the flow conditions². This indicates that the filament generation mechanism at low speeds depends on the distribution neutrals and metastables and thus must be

²The duration of the microdischarges reaches a plateau at about 30-50 ns, higher than the 10 ns resolution of the photomultiplier.

a secondary emission driven mechanism, like a Townsend breakdown (this is confirmed by the model of Lagmich et al. [60] without flow). On the other hand, at higher speeds, the discharge becomes independent of the behaviour of neutrals or metastables. As reported Gherardi et al. [21], when the working gas velocity is increased in a DBD system, photoionization or photoemission are likely to become the predominant electron production mechanisms rather than ion or metastable bombardment of the cathode. They suggest that photo-mechanisms are at the origin of streamer formation, which is a process much faster than filamentary Townsend breakdown. To summarize, it is proposed, based on figures 5.9 and 5.10, that a transition from a filamentary Townsend regime to a streamer regime occurs when the velocity of the gas flow is increased.

5.5 Geometrical effects

The variations of the spatial discharge distribution at different flow conditions can be visualized with CCD imaging. Figure 5.11 presents images of the overall discharge generated by the Al_2O_3 -*baseline* geometry mounted on the wall of the supersonic nozzle, at $M_\infty=0$, $M_\infty=0.7$ and $M_\infty=1.1$ for the same applied voltage $U_2=7$ kV rms, higher than the previous measurements.

Figure 5.11 shows that at $M_\infty=1.1$, strong emission comes from the edges in the form of long filaments. The edge filaments start to appear at $M_\infty=0.7$ and their number increases at $M_\infty=1.1$. These long, intensively emitting edge filaments are not observed at low speeds for this DBD plate geometry. These filaments have the typical shape of streamers, they stretch up to the back electrode boundaries. The difference in shape is clearly visible in comparison with the image at $M_\infty=0$, where the microdischarges remain close to the electrode. It is true that at $M_\infty=1.1$ the pressure is not completely uniform over the whole plate (as shown in figure 3.14 of chapter 3). However, filaments start to appear at $M_\infty=0.7$, where the pressure is constant over the whole plate. Therefore, these filaments are due essentially to variations of the momentum of particles in the flow.

The fact that long filaments appear on the edges can be explained by the fact that the p·d factor (pressure times the distance) is larger on the outside because d is larger. Indeed, the grounded back electrode stretches about 10 mm out of the edge stripe boundaries, instead of 1 mm around the central stripes. As explained in chapter 2, high p·d factors favour streamer regimes. This is confirmed by images of the Al_2O_3 -*line* and Al_2O_3 -*no-edge* geometries at $M_\infty=1.1$ as shown in figure 5.12. When placed in a supersonic airflow, the geometry with the single stripe displays the same long filaments as the ones at the edges in figure 5.11. In contrast, the discharge created by the Al_2O_3 -*no-edge* geometry generates no long filaments on the outer stripes.

The generation of long filaments as seen on the CCD images corresponds to the appearance of high current peaks on the negative half-period of the current signals. An example is given for the Al_2O_3 -*baseline* geometry in figure 5.13 at $M_\infty=1.1$. The light emission duration from the long filaments has been measured and is the same as the other peaks, about 50 ns.

As shown in figure 5.14, high current peaks are generated on the negative half-period by the Al_2O_3 -*line* geometry but not by the Al_2O_3 -*no-edge* geometry, in the same way as

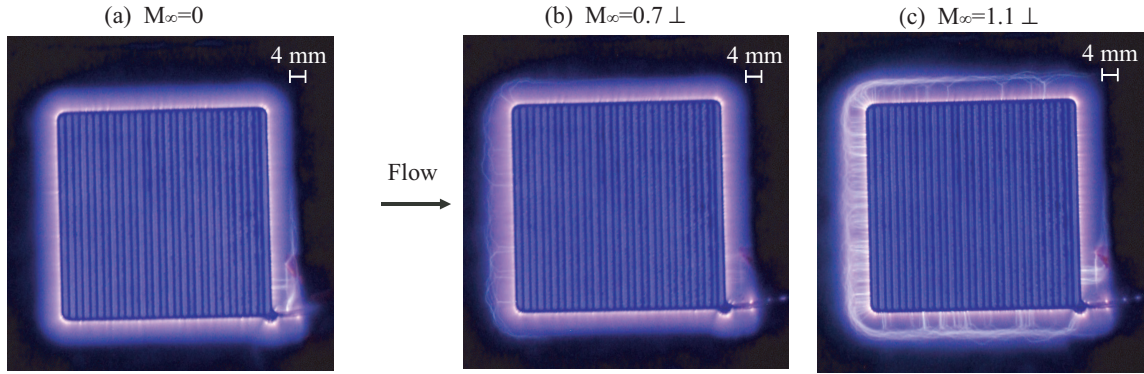


Figure 5.11: CCD images of the whole discharge area for Al_2O_3 -baseline at 1 kHz and $U_2=7$ kV rms and exposure time = 0.25 s for (a) and (b), 0.2 s for (c).

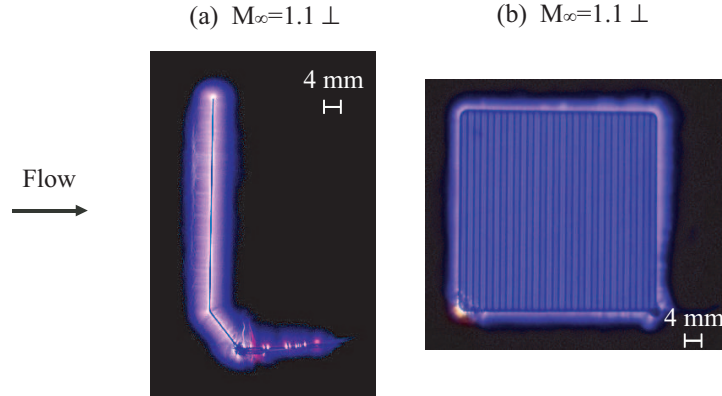


Figure 5.12: CCD images of Al_2O_3 -line and Al_2O_3 -no-edge for $M_\infty=1.1$ at 1 kHz and $U_2=6.1$ kV rms for (a), $U_2=7.4$ kV rms for (b). Exposure time is 0.25 s for (a) and 0.15 s for (b).

long filaments appear on the CCD images for the Al_2O_3 -line geometry and not for the Al_2O_3 -no-edge.

On the negative current half-period, the top electrode is the cathode: electrons are produced at the top electrode and accelerated in the intense surface electric field. They are emitted preferably at irregularities (spiky patterns) of the electrode. On the contrary, on the positive half-period, the dielectric becomes the cathode and electrons are desorbed from the dielectric surface. In this configuration, the electrons are extracted much more uniformly on the dielectric surface. This can explain why long streamers with high current amplitude are formed preferably on the negative half-period. However, in order to confirm this, a numerical model with momentum transfer from neutral particles to ions would be needed.

The reduction of the emission time for individual microdischarges as the airflow speed rises is similar for all the three geometries presented. Therefore the transition observed is

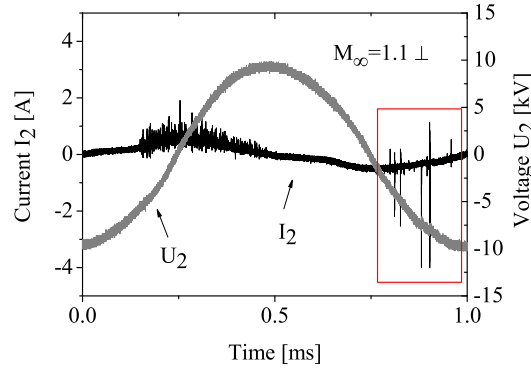


Figure 5.13: Current and voltage for Al_2O_3 -baseline for $M_\infty=1.1$ perpendicular to the electrode stripes, at 1 kHz and $U_2=7$ kV rms.

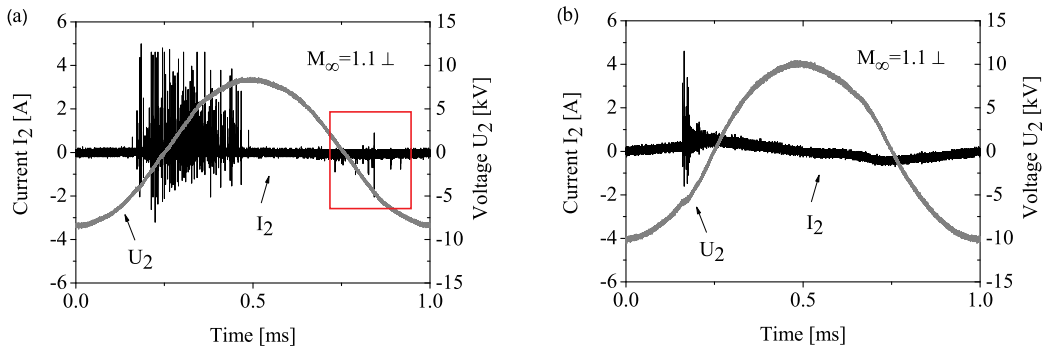


Figure 5.14: Current and voltage signals for Al_2O_3 -line and Al_2O_3 -no-edge for $M_\infty=1.1$ at 1 kHz and $U_2=6.1$ kV rms (a), and $U_2=7.4$ kV rms (b).

not related to a particular geometry.

5.6 Note on the reproducibility

The effects presented above are qualitatively reproducible. Quantitatively, the reproducibility is impaired by the attack of the electrodes by the discharge. As discussed in chapter 4, the oxidation of the electrodes generates black deposits, as shown in figure 5.15 (a), that constitute an additional dielectric barrier and increase the burning voltage. Moreover, the operation of the DBD plate in high-speed airflows generates these long filaments that cause intense ablation of electrode material and deteriorate the electrode. Long filaments then appear more easily on the edges, i.e. at lower speeds and lower voltages. Figure 5.15 (b) shows how edge stripes have been more oxidized by the discharge than central stripes.

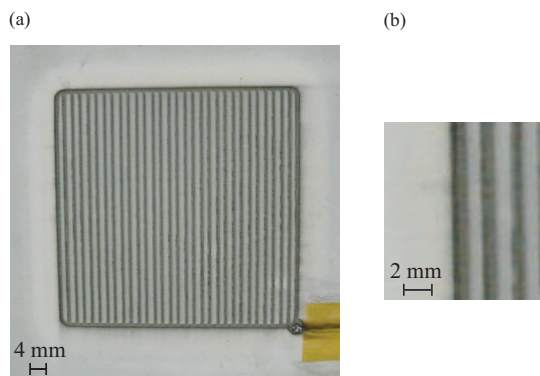


Figure 5.15: Picture of the Al_2O_3 -baseline DBD plate after about 10 hours of measurements at different airflow speeds up to $M_\infty=1.1$

As discussed in chapter 4, the reproducibility can be greatly improved by the encapsulation of the top electrode in ceramics.

5.7 Optical emission spectroscopy

The optical spectrum emitted by the surface discharge generated by a Al_2O_3 -baseline varies with the flow velocity. This is shown in figures 5.16 to 5.19 for $M_\infty=0$ and $M_\infty=0.7$. In addition to the variations in the nitrogen rotational and vibrational band systems, variations in the positive ion emission intensities are shown as well: N_2^+ bands (427.8 nm, 470.92nm, 522.83 nm) and O^+ lines (OII) (750.32 nm and 763.38 nm). Excited oxygen lines (OI) can be seen at 777.08 nm and 794.72 nm.

A portion of the N_2 first positive system is shown in figure 5.16 at $M_\infty=0$ and $M_\infty=0.7$. The measurements have been done through glass, therefore the 2nd order bands of the second positive system are cut-off, which results in a spectrum where the first positive system is easier to observe. From this figure it can be seen that when the flow velocity is increased, the vibrational and rotational band intensities diminish by about 40 to 50%. This is a necessary condition to show that the density of metastables is reduced, but it is not sufficient. The reduction of intensity is uniform, i.e. that the relative line intensities stay about the same, apart from the last band around 695 nm.

Ambrico et al. [67] stress the difficulties in measuring absolute values of the density of $A^3\Sigma_u^+$ metastables in a surface DBD.

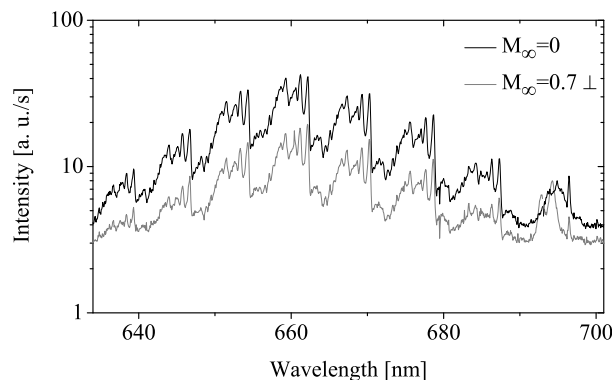


Figure 5.16: Portion of the emission spectrum from a plasma generated by a type Al_2O_3 -baseline geometry, at $U_2=2.5$ kV rms and 10 kHz, without flow and with a free stream Mach number $M_\infty=0.7$ perpendicular to the electrode stripes. Exposure time is 60 s.

Figures 5.17 and 5.18 show portions of the spectra at $M_\infty=0$ and $M_\infty=0.7$ where N_2^+ bands are identified, between the bands from the N_2 second positive system. The N_2 band intensities are reduced by 40 to 50%, as for the first positive system, but the reduction of the N_2^+ band intensities varies significantly depending on which band is considered. For example, the peak at 427.8 nm (figure 5.17) is 70% at $M_\infty=0.7$ than at zero flow, but the peaks at smaller at 470.92 nm and 522.83 nm (figure 5.18) are only about 50% smaller.

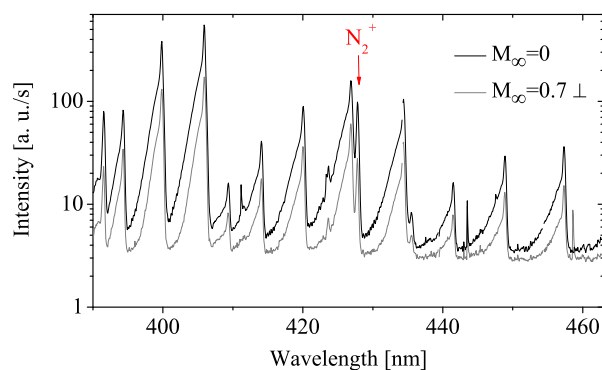


Figure 5.17: Portion of the emission spectrum from a plasma generated by a type Al_2O_3 -baseline geometry, at $U_2=2.5$ kV rms and 10 kHz, without flow and with a free stream Mach number $M_\infty=0.7$ perpendicular to the electrode stripes. Exposure time is 60 s.

The same can be observed with OI and OII lines as shown in figure 5.19. The lines at 750.32 nm (OII) and at 777.08 nm (OI) are reduced of about 70% at $M_\infty=0.7$, whereas the lines at 763.38 nm and 794.72 nm are reduced only about 50%.

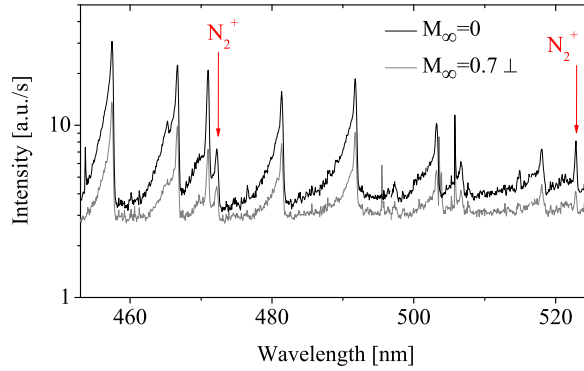


Figure 5.18: Portion of the emission spectrum from a plasma generated by a type Al_2O_3 -baseline geometry, at $U_2=2.5$ kV rms and 10 kHz, without flow and with a free stream Mach number $M_\infty=0.7$ perpendicular to the electrode stripes. Exposure time is 60 s.

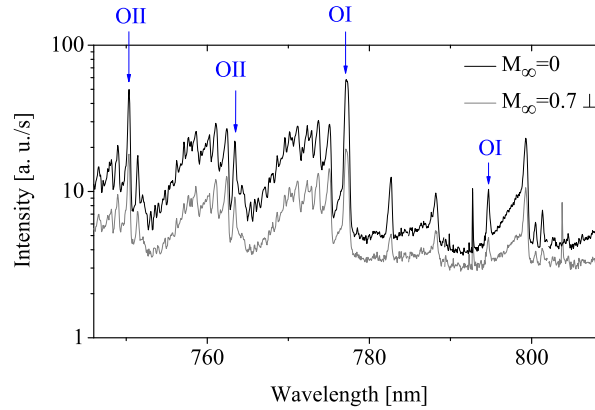


Figure 5.19: Portion of the emission spectrum from a plasma generated by a type Al_2O_3 -baseline geometry, at $U_2=2.5$ kV rms and 10 kHz, without flow and with a free stream Mach number $M_\infty=0.7$ perpendicular to the electrode stripes. Exposure time is 60 s.

The reduction of the ion band or line intensities suggests that the degree of ionization diminishes. However, the fact that the reduction of the intensity is not the same for all ion bands or line indicates that the chemistry is different without flow and with a flow at $M_\infty=0.7$. The spectra presented here are difficult to interpret further, because of the superimposed bands from different species. Atomic lines cannot be isolated (for example to integrate their intensity over the line width) because they are merged with molecular bands. Nevertheless, the results show that there seem to be effects of the flow on the reaction kinetics.

5.8 Summary

The improvement of the DBD plate lifetime has allowed to extensively study the plasma under different airflow velocity conditions. The surface dielectric barrier discharge can be sustained for several tens of hours in transonic or supersonic conditions on the wall of a nozzle. Current and time-resolved light emission measurements show that there are modifications in the discharge regime at high airflow velocity:

In the overall discharge:

- the continuous (glow or corona) component of the plasma is reduced
- the number of filaments generated in the plasma is reduced
- the filamentary to continuous component aspect is increased, the plasma is relatively more filamentary at high flow velocities.

The increase in burning voltage for increasing flow velocities is smaller when the flow velocity vector is perpendicular to the electrode stripes than when it is parallel. This leads to a perpendicular configuration for the following experiments on the airfoil.

Most importantly in individual microdischarges:

- a reduction of the light pulse emission duration by one order of magnitude is found, from 500 ns to 50 ns, when airflow velocity is increased from zero up to a free stream Mach number of 0.7.

These measurements indicate that there is a change in the breakdown mechanism. It is proposed that a transition from Townsend breakdown to streamer breakdown occurs when the airflow velocity is increased. The depletion of N_2 metastable states due to the airflow seems to be the dominant cause, reducing the internal energy and reducing the relative importance of secondary emission processes.

The discharge characteristics are also very sensitive to the electrode geometry. In a two-dimensional grid geometry as studied here, the discharge forming on the edges takes the form of long filaments corresponding to high current peaks. According to Opaitis et al. [68], highly filamentary discharge regimes seem to be the most appropriate for acting on an external gas flow. However, they are an important source of electrode wear.

In order to confirm the hypotheses that have been presented to explain the experimental results, a numerical model including the momentum transfer from neutral particles of the working gas to the ions would be needed.

Optical emission spectroscopy measurements on the discharge show that there seem to be effects of the flow on the chemical reaction kinetics of the discharge. In order to understand the contribution of the different species in the discharge and the effects of the flow on the chemistry, the spectra could be simulated with a numerical model like SPECAIR [69] for example. However, this would require a certain number of hypotheses

on the discharge properties and spectra fitting, which might give conclusions that strongly depend on these initial hypotheses. A better solution would be to set-up the same experiment in a pure gas, like argon or nitrogen, but this would require large quantities of gases. For such measurements, a closed-loop wind tunnel would be most appropriate.

Chapter 6

Plasma-transonic flow interaction around an airfoil

This chapter is devoted to the study of plasma-flow interaction in a case where the plasma is generated on the surface of an airfoil and interacts with the transonic flow field around that airfoil. The study focuses on the effects of the surface plasma on the shock structure outside the boundary layer and its far-field pressure signature which will determine the acoustic impact of the airfoil. The objective is to approach as much as possible sonic boom experiment conditions.

The versatility (curved surfaces) and robustness of the DBD system developed from LTCC technology extend the possible measurement domain in a significant way in the field of research of flow control with plasmas. The system can be operated in the extreme environments, not only in subsonic flows but now in supersonic flows as well. Their lifetime (tens of hours) now allows for extensive experimental investigations. Experiments in the case of a discharge generated on the suction side of a NACA3506 airfoil in a transonic flow is presented here.

The first section describes the aerodynamic characteristics of the transonic flow around the profile. The second section investigates the effects of the plasma on the airflow, using non-intrusive measurement techniques (Schlieren visualization and far-field static pressure measurements). In order to improve the interpretation of the results, the last section studies how the plasma is modified by the flow in the airfoil configuration. Finally, the main results are summarized.

6.1 Properties of the transonic flow

As discussed in chapter 3, the study of the interaction between the surface dielectric barrier discharge and the transonic flow is performed using a NACA3506 profile placed in a subsonic nozzle. The angle of incidence of the profile in the test section is kept constant (at $i=8^\circ$). The only flow parameter varied is the inlet Mach number M_∞ . In the present chapter, M_∞ is defined as the free stream Mach number far upstream of the airfoil, at the entrance of the test section where the inlet static pressure is measured (see figure 3.16 in chapter 3). The local isentropic Mach numbers in the flow field around the airfoil will

be denoted by M_{is} . The temperature has been set in order to avoid condensation in the main flow and is $40 \pm 10^\circ\text{C}$ in transonic conditions.

The surface of the airfoil has a certain roughness and most of all, there is surface irregularities due to the silicone paste spread on the suction side (at the interstices between the metal of the airfoil and the ceramics of the plate, where the DBD plate begins and ends). This means that the boundary layer should transition to a turbulent state at the latest at the position where the DBD plate starts¹.

The angle of incidence of the profile has been chosen in order to obtain a strong aerodynamic shock at different positions on the suction side. Consequently, different positions of the plasma with respect to the shock can be studied. The shock position on the NACA3506 as a function of the inlet Mach number M_∞ is given in figure 6.1 for different angles of incidence. It has been measured from Schlieren images at 50% cut-off.

From the results in figure 6.1 (a), an angle of incidence $i=8^\circ$ has been chosen, the range of shock positions being the largest. The red zones in the figure represent the areas where the plasma is created, in the configuration where the DBD is mounted close to the leading edge and in the second configuration where it is mounted close to the trailing edge. A raw Schlieren image at $i=8^\circ$ and $M_\infty=0.7$ is shown in figure 6.1 (b). Raw images at $M_\infty=0.65$, and 0.73 are given in appendix C.

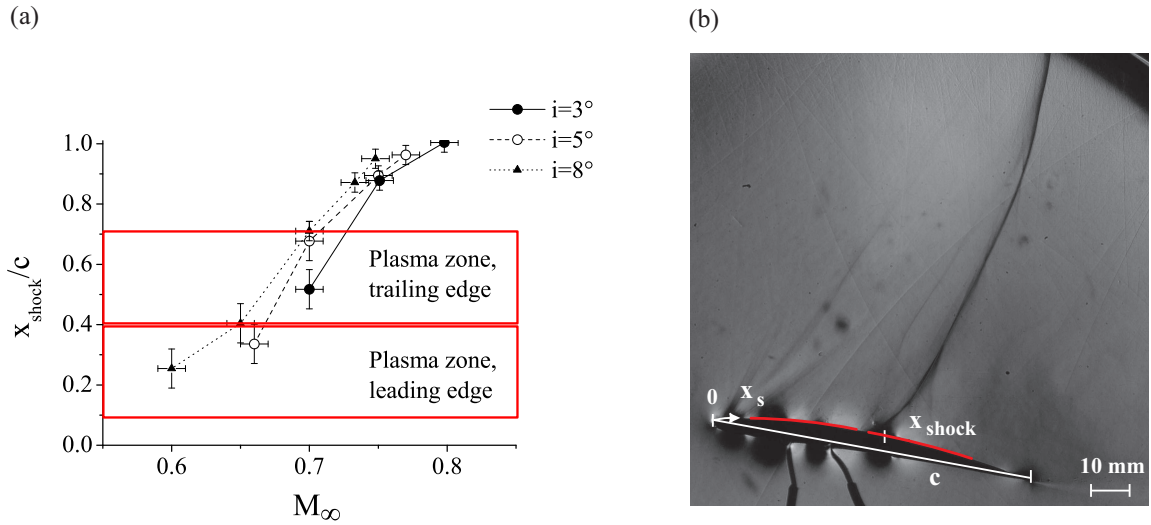


Figure 6.1: Shock position on the suction side (SS) as a function of the inlet Mach number, for different angles of incidence (a) and raw Schlieren image at $i=8^\circ$ and $M_\infty=0.7$ with the definition of dimensions (b).

¹Surface irregularities act as tripping wires.

The shocks on this NACA profile at this angle of incidence are very unstable, specially when the shock is close to the leading edge. At $M_\infty=0.65$ and $M_\infty=0.7$, the shock oscillates on a 10 mm distance which represents 13% of the profile length. This effect cannot be neglected. For $M_\infty>0.7$, the shock moves to the trailing edge and becomes stronger and more stable (lower amplitude oscillations, over about 5 mm). According to Bron [70], shock instability indicates that the boundary layer is indeed turbulent. The instability is amplified by the influence of the separation zone downstream of the shock, as well as by the aerodynamics of the nozzle. Ferrand [71] suggests that for weak shocks, acoustic propagations in a nozzle seem to become significant producing larger instabilities of the unsteady flow.

The quantitative flow field properties around the profile have been calculated numerically using a compressible and turbulent Navier-Stokes model validated with experimental measurements (see appendix D). The flow field generated by the NACA3506 at $i=8^\circ$ is depicted in figure 6.2 in terms of isentropic Mach number. The calculations have been made for three different inlet Mach numbers M_∞ displaying a shock on the suction side. In the figure it is easy to identify the supersonic pocket upstream of the shock, and to see that the boundary layer is fully separated downstream of the shock. In order for the model to correspond to experimental measurements, turbulence has to be added to the boundary layer. Consequently, shock instability also appears on the numerical calculations as in the experiments. $M_\infty=0.65$ is the condition where convergence is most difficult to obtain and where the shock oscillates most. Figure 6.2 and 6.3 present averaged solutions in order to address the steady state properties of the shock. Unsteady simulations would require a more evolved code in order to give results which are physically consistent (see Bron et al. [72] for example).

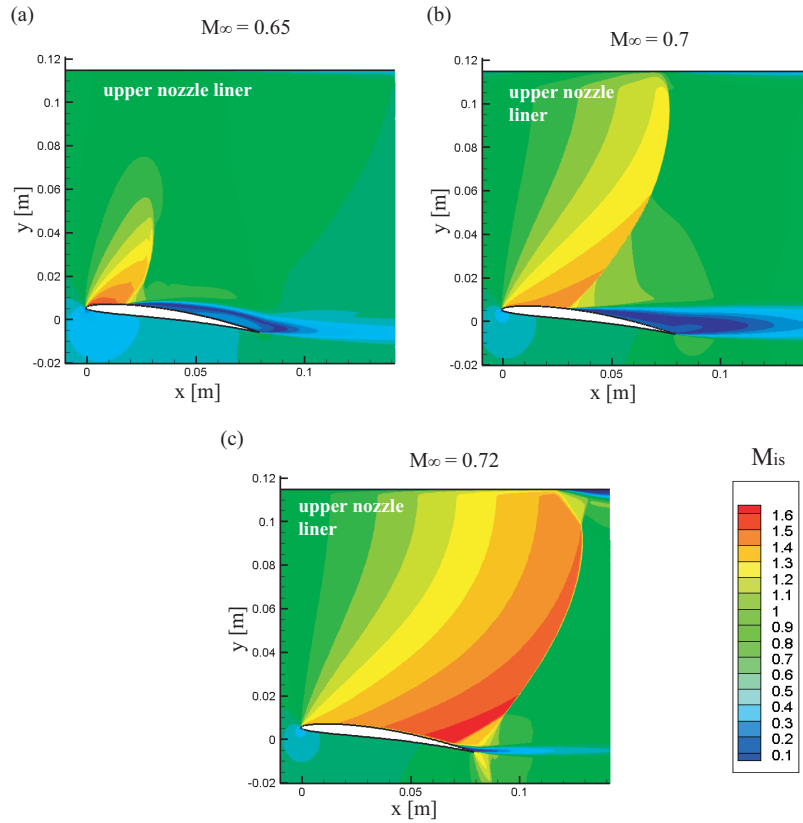


Figure 6.2: Isentropic Mach number distributions around the NACA3506 at angle of incidence $i=8^\circ$, for different inlet Mach numbers.

The distribution of static pressure has been calculated over the suction side surface, with the same model, and steady (averaged) results are shown for the same three conditions in figure 6.3. The pressure level varies in a large range, from 0.25 bar to 1.1 bar, depending on the inlet Mach number and on the position on the suction side. For conditions where $M_\infty < 0.65$ which are not shown here, there is almost no compression and the pressure is at a level close to the far-field pressure. The pressure distribution is important for the discussion of the effects of the flow on the surface plasma in section 6.3. In the experiment the shock is unsteady but according to Edwards and Squire [73], there is no significant phase shift between the shock movement and the surface pressure variations in an interaction between a normal shock and a turbulent boundary layer. Therefore the shock position is given by the highest pressure gradient in the pressure distribution and inversely.

The static pressure profiles in the far-field (p_{0FF}) are given in figure 6.4 with the corresponding c_{p0} coefficient profiles (defined in chapter 3). x_{FF} is the position on the tap array and the relative position of the leading edge (LE) and trailing edge (TE) of the profile are indicated by the dashed lines. The figures show that a significant pressure gradient is visible above $M_\infty=0.7$, when the shock extends up to the upper nozzle liner.

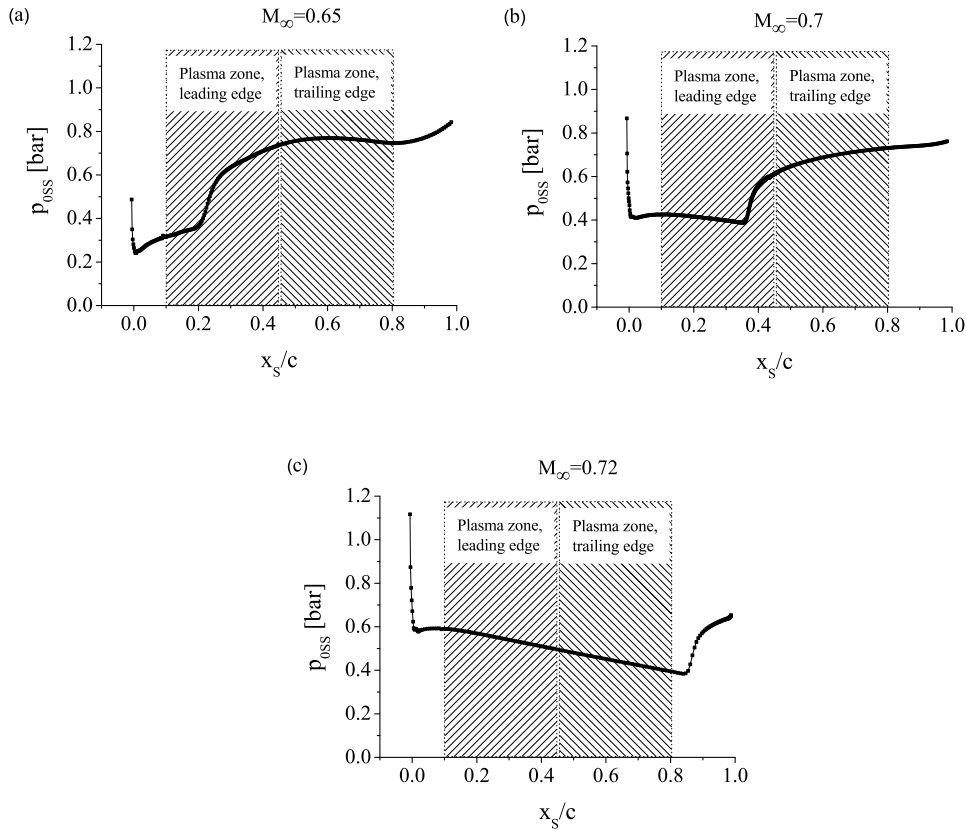


Figure 6.3: Calculated static pressure distributions on the NACA3506 suction side p_{0SS} at angle of incidence $i=8^\circ$, for different inlet Mach numbers.

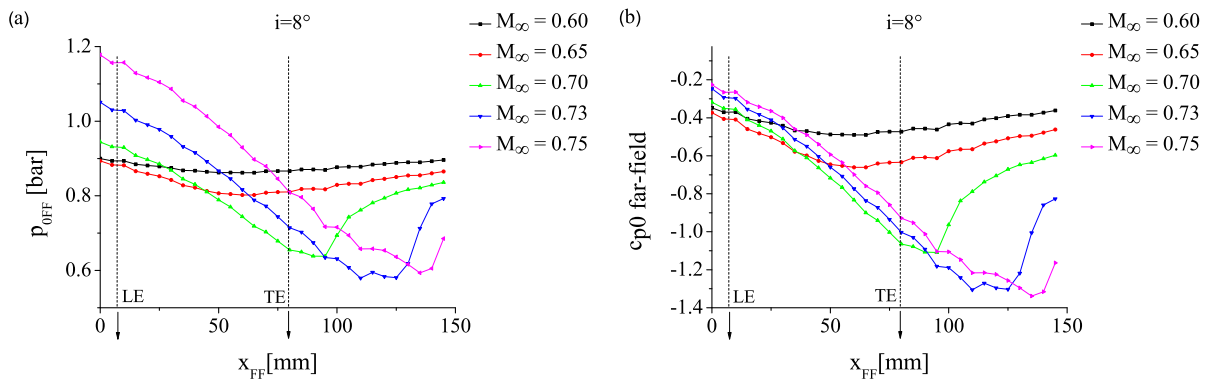


Figure 6.4: Static pressure distributions measured on the far-field pressure tap array described in chapter 3, and corresponding c_{p0} distributions.

6.2 Effect of the DBD on the transonic flow

The objective of the measurements presented in this section is to determine if a DBD created on the surface of an airfoil can have effects on the surrounding flow. Note that this is difficult to predict theoretically at the present stage of knowledge in the field of dielectric barrier discharges as well as in the field of transonic flows. The discharge can have an impact on the complex phenomena involved in shock-boundary layer interaction explained in chapter 2. It can modify the mechanical properties of the boundary layer, heating it and locally changing the viscosity for example, but also indirectly through the movement of the charged particles in the electric field transferring momentum to the boundary layer in different directions. In the type of symmetrical geometry considered here, this momentum transfer can only modify the turbulence in the boundary layer, since ions are moving between the electrode stripes in both directions with respect to the flow. Moreover, since there corona regimes seem to exist at certain phases of the discharge, as explained in chapter 4, effects similar to the ones described by Lebedev et al. [1] could be detected.

In the following subsections the results of Schlieren visualizations and far-field pressure measurements performed on the transonic flow are presented, in *plasma on* and *plasma off* conditions. The flow conditions are first set and stabilized. Only then the discharge voltage is switched on and off. This ensures a good stability of flow conditions between the measurements with and without surface discharge. Two geometrical configurations are considered: the system with the DBD plate close to the leading edge and the case with the DBD plate close to the trailing edge (see chapter 3, figure 3.10). Indeed, the shock can be affected by property changes not only upstream of the shock but also downstream of the shock. As explained by Dussauge et al. [74], when the flow downstream of a shock is subsonic as in the transonic case, feedback of the downstream flow on the upstream flow is possible. This is not only due to the reversed flow as explained in chapter 2, but also to propagating acoustic waves.

The plasma is generated by an *LTCC-enc* (see chapter 4, figure 4.9) geometry in both the leading edge and trailing edge configurations. The applied voltage amplitude U_2 has been set to the maximum possible before arcs start to form between the top electrode and the metallic airfoil (see figure 6.12 below). The applied voltage frequency is 10 kHz for all the experiments described in the present chapter. These voltages are given in section 6.3. M_∞ has been varied from 0.65 to 0.75 where distinctive shocks appear of the suction side of the NACA3506 at $i=8^\circ$. Because of the temporal instability of the shock, the measurements shown in the first two sub-sections have been time-averaged. It is the best way to make comparisons possible. In order to reduce shock instabilities, the angle of incidence could be reduced or a different airfoil profile should be chosen. However, reducing the angle of incidence reduces the range of shock positions on the suction side.

6.2.1 Shock structure

The Schlieren visualizations performed on the flow around the NACA3506 with DBD close to the leading edge have been performed with the Nikon camera with a vertical 50% knife edge at the focal point in order to display the (horizontal) density gradients across the shock. The images have been taken randomly in time with 100 μs exposure. Due to the significant variation of the shock position in the case where the plasma is off as well as in the case where the plasma is on, the results have been averaged over the set of 10 images taken for each condition.

The averaged Schlieren images without and with plasma are shown in figure 6.5 (a) and (b) respectively, for an inlet Mach number $M_\infty=0.7$. The four black circular zones along the profile are due to the pins holding the profile on the two lateral windows, and the holes through which the powering wires for the DBD electrodes are inserted. These wires are visible at the bottom of the images. The maximum voltage applicable to the DBD in these conditions is $U_2=2.2$ kV rms (before arcs start to form). The red line shows the position of the discharge which is created in the supersonic pocket upstream of the shock and in the beginning of the shock-boundary layer interaction zone. In order to quantify the shock distribution, intensity profiles across the shock are extracted, at the level indicated by the yellow line, and plotted in figure 6.5(c). The distance of the profile extraction line has been chosen in order to be just above the shock-boundary layer interaction zone since the discussion presented here focuses on the shock properties rather than the boundary layer properties.

In the conditions of figure 6.5, at $M_\infty=0.7$, averaged Schlieren images as well as the intensity profile show no fundamental difference between the cases with and without plasma. Small effects are visible but they cannot be considered as significant in comparison with the error in the measurements (due to the aerodynamic instability of the shock). Close to the upper nozzle liner, images show that the shock appears slightly more diffuse when the discharge is on. However, the spread is not wider than 2-3 mm, which is smaller than the variation in the shock position due to aerodynamic fluctuations which are ± 5 mm (see figure 6.1). Close to the suction side, the opposite effect is observed: intensity distribution show an averaged shock 2-3 mm wider when the plasma is off. It is important to remember that only 10 images have been used in figure 6.5 for the averages, which is statistically not highly representative. Raw Schlieren images given in appendix C show that the same shock structure can be reproduced without and with surface discharge.

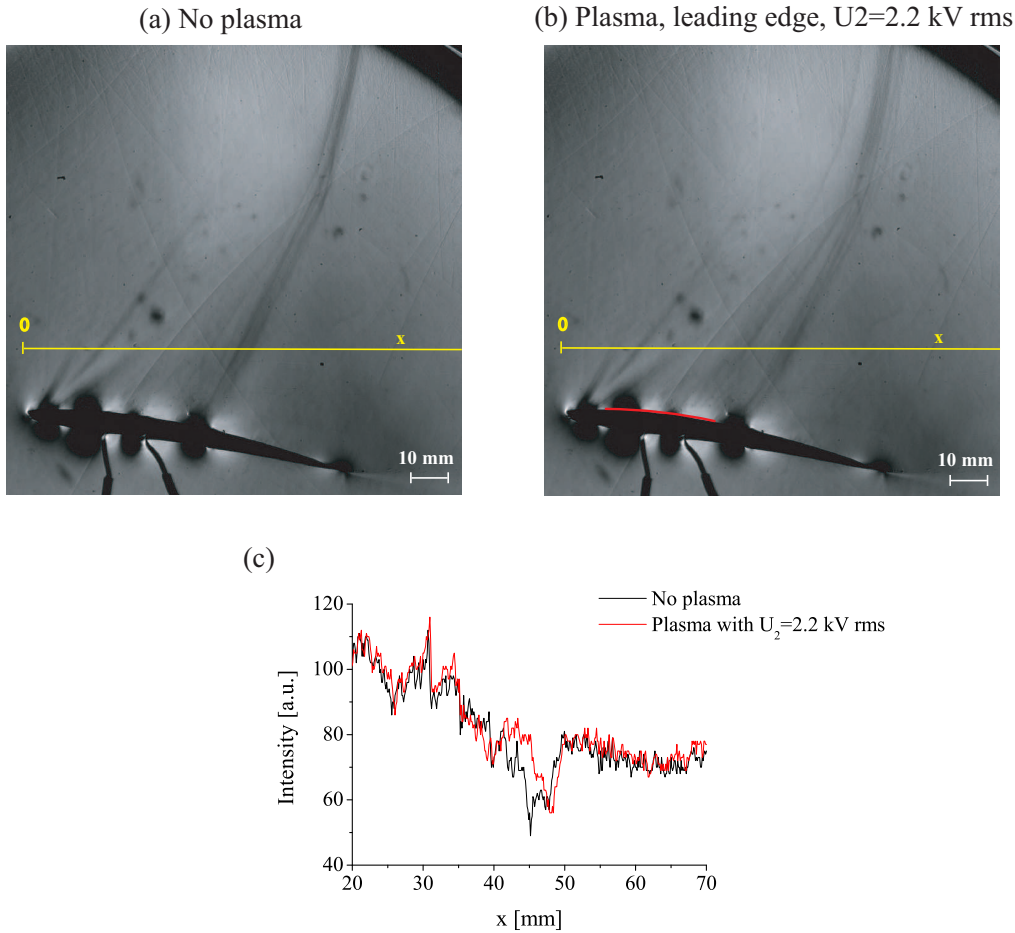


Figure 6.5: Averages of 10 Schlieren images at $M_\infty=0.7$ without plasma (a) and with a surface plasma at 10 kHz close to the leading edge (b), with intensity profiles (c) measured along the yellow lines.

Measurements have been performed at $M_\infty=0.65$ and $M_\infty=0.72$ as well for the following reasons:

- The position of the plasma relative to the shock (upstream or downstream) is different. This could have an influence on the action of the plasma on the flow.
- At different inlet Mach numbers, the shock separation mechanisms are different. At $M_\infty=0.65$, the separation is shock induced, but at $M_\infty=0.7$ and $M_\infty=0.72$, the lambda structure observable on some of the raw Schlieren images (see chapter 2) indicates that the boundary layer separates upstream of the shock foot periodically². One or the other mechanism could be easier to perturb with the plasma.
- At $M_\infty=0.65$ the pressure gradient across the shock is smaller (the shock is weaker), and could be more sensitive to the surface plasma.

²Note that the phenomenon is transient, the lambda structure is not visible on averaged images.

- At $M_\infty=0.72$, the shock is more stable and it could be easier to detect a potential effect of the discharge on the flow.

The averaged Schlieren images and corresponding intensity profiles are shown in appendix C and exhibit only small effects as well, which stay within the variations that can be attributed to the aerodynamic fluctuations or to the measurement technique errors. Even though the shock is weaker, more stable, or if the separation mechanism is different, the plasma used here does not modify the transonic flow in a significant way.

The fact that the shock structure does not exhibit significant differences without and with plasma can have several physical causes. First, as discussed in the previous section, the boundary layer is turbulent in the case without plasma already. It is thus not possible in these conditions to generate a transition from a laminar boundary layer to a turbulent one with a plasma upstream or below the shock foot for example, which could induce a significant and observable effect in the shock structure. Also, the modification of the longitudinal pressure gradients by the DBD might be too small to influence the movement of the particles in the separation zone. Moreover, the eddies generated in this separation zone (which have a strong effect on the shock properties as suggested by Dussauge et al. [74]) might be difficult to affect because they are highly energetic structures. Finally, the measurements show that the separation mechanism is different at $M_\infty=0.65$ and at $M_\infty=0.7$, but they appear to be both insensitive to the discharge.

In order to be able to apply higher voltages to the DBD, the plate has been mounted close to the trailing edge which allows for rms voltages up to 3 kV without a risk of arcing, as described in section 6.3. Moreover, at this position the plasma can be generated below the shock attachment point when $M_\infty=0.7$ and $M_\infty=0.72$. At these inlet Mach numbers, the shock is stronger and spreads up to the upper nozzle liner where the pressure gradient across it can be measured. The statistics on the images has been improved taking 100 images at 21 frames per second with the Sensicam camera. The images have been taken at an exposure time of $15 \mu\text{s}$ in order to reduce intrinsic time integration. Figure 6.6 shows averages over 100 images for $M_\infty=0.7$ as well as the intensity profile. Measurements at $M_\infty=0.65$ and $M_\infty=0.75$ are shown in appendix C. The acquisition time is approximately 5 seconds, covering several periods of the shock oscillations which are smaller than 1 s.

With the improved statistics, the results show an even closer similitude between the cases without plasma and the cases with a plasma. At $M_\infty=0.7$, the variation measured on the average intensity profiles is less than ± 1 mm and therefore negligible. Even at $U_2=3$ kV rms and even though the plasma is in the shock-boundary layer interaction zone, the plasma does not modify sufficiently the flow properties in order to observe significant differences in the density gradients from the Schlieren visualizations.

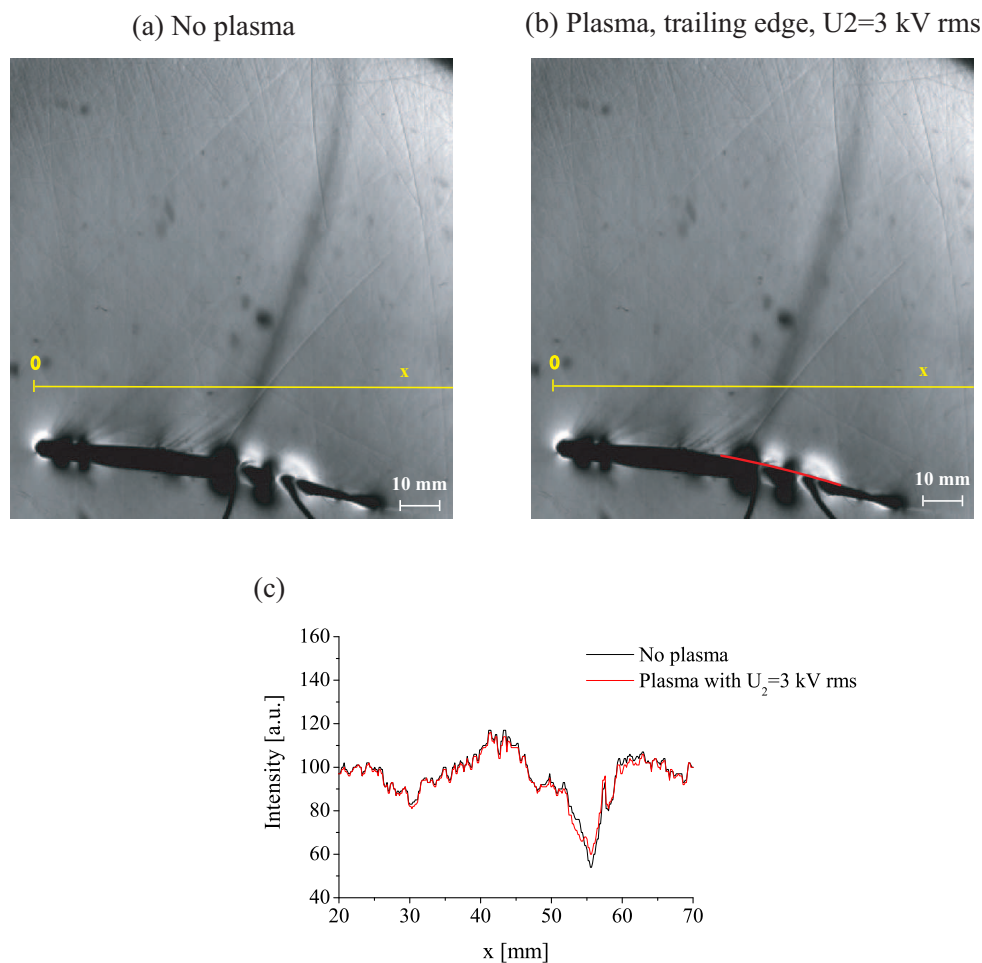


Figure 6.6: Averages of 100 Schlieren images at $M_\infty=0.7$ without plasma (a) and with a surface plasma at 10 kHz close to the trailing edge (b), with intensity profiles (c) measured along the yellow lines.

The similarity of the cases with and without plasma is further confirmed by the images shown in figure 6.7 calculated using an AND function on 10 raw images to represent the span of the shock movement.

In order to investigate the effects of the plasma on the separation zone directly, the Schlieren set-up has been modified. Instead of cutting the convergence point vertically with the knife edge, it can be cut horizontally and the Schlieren images will display the vertical density gradients. 100 raw images taken at $15 \mu\text{s}$ exposure time and 21 frames per second have been averaged in the same way as previously. Resulting pictures are shown in figure 6.8 at $M_\infty=0.7$. Unfortunately the holes for the power supply wires disturb the visualization close to the shock, but most of the detachment zone is still observable. The images and plots show that the detachment zone case with plasma is slightly larger, the detachment seems to start slightly earlier. The difference is however not significant enough to give a reliable conclusion.

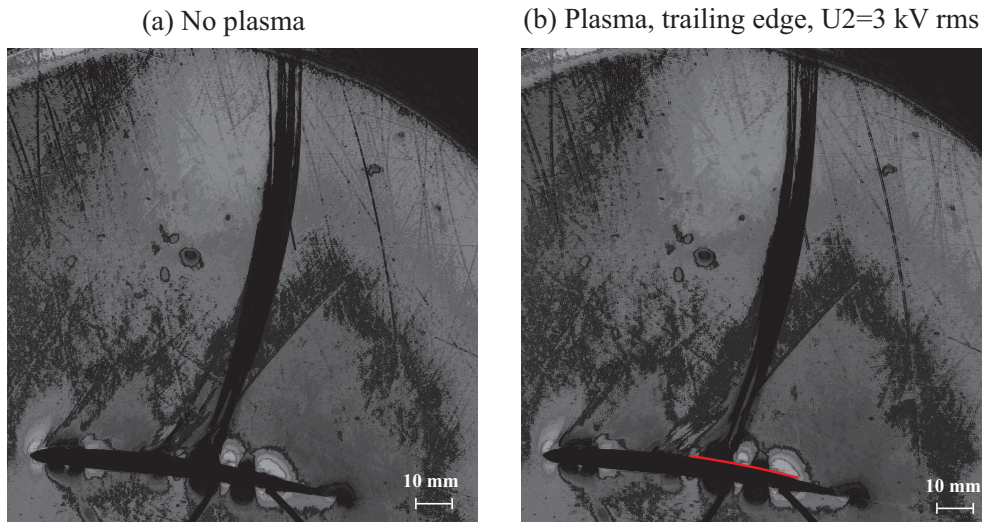


Figure 6.7: AND operation on 10 Schlieren images at $M_\infty=0.7$ without plasma (a) and with a surface plasma at 10kHz close to the trailing edge (b).

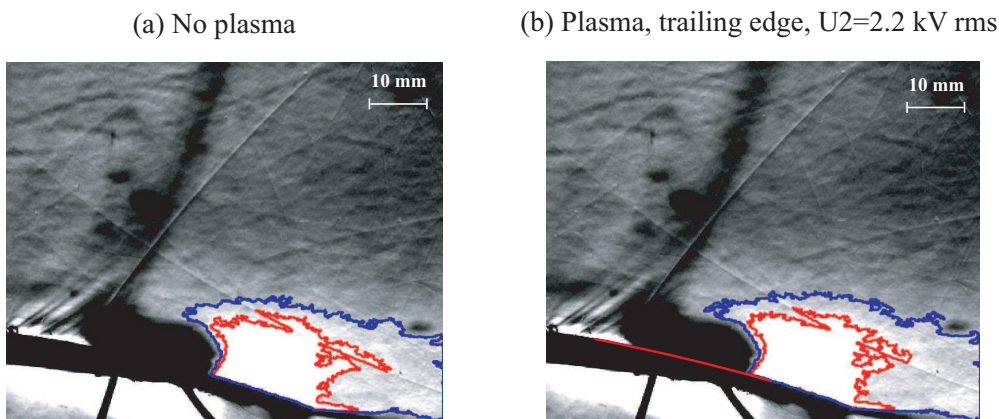


Figure 6.8: Averages of 100 Schlieren images (horizontal cut-off) with intensity contours at $M_\infty=0.7$ without plasma (a) and with a surface plasma at 10 kHz close to the trailing edge (b).

Averaged Schlieren imaging does not give conclusive results about the effects of a surface DBD discharge on the shock structure around the NACA3506 airfoil at voltages up to $U_2=3$ kV rms. Horizontal and vertical density gradients across the shock and detachment zone respectively have been observed, but the results without and with plasma are similar taking into account the variations of the bulk flow inside the nozzle. The possible physical reasons have been exposed, but it must be pointed out that the measurement technique presents a few limitations on the sensitivity of the measurements. Schlieren images have the disadvantage that they integrate the effects in the z direction along the optical axis. Therefore it might be that 3D effects in the nozzle (boundary layers forming on the lateral walls) will increase the observed shock width or its oscillation amplitude and eventually mask the effects of the discharge. Indeed, there might be a shock-induced

separation on the lateral windows as well which will perturb the shock in a considerable way as suggested by Bron et al. [72]. The lateral boundary layers are about 10 mm wide on each side as measured by Ott [75] on the same nozzle as the one used in the present project, on a 40 mm nozzle width only. This could be improved by performing focused Schlieren as described by Settles [59] in order to study only one layer in the z dimension. Moreover, Schlieren basically gives qualitative information only about the density gradients in the flow. Quantitative Schlieren can be set-up as described by Settles [59] but the implementation requires a very precise calibration and the interpretation of the results must be done very carefully. Since the objective here is to investigate what happens through the shock at a relatively long distance from the profile (in analogy to sonic boom experiments), quantitative information about the shock strength can be obtained using far-field static pressure measurements on the upper wall of the nozzle³ (see chapter 3). In order to reduce the influence of the nozzle aerodynamics on the results, the profile could be placed further away from the upper nozzle liner or even fixed to the bottom nozzle wall. However, this would prevent from measuring pressure gradients across the shock.

6.2.2 Far-field pressure gradient across the shock

Schlieren images give only qualitative information about the phenomena occurring through the shock. In order to quantify the pressure gradients through the shock, static pressures are measured on the upper nozzle liner with the field of pressure taps described in chapter 3. They are placed on a single row along the x direction parallel to the main flow direction. The pressure tap field is located relatively far from the profile in order to simulate so called *far-field* pressure measurements performed in sonic boom experiments. The upper wall is located at a distance of about 1.4 times the length of the profile chord. Far-field pressure distribution results are shown in figure 6.9 for the leading edge and trailing edge configurations at $M_\infty=0.7$. The results at $M_\infty=0.65$ and $M_\infty=0.73$ are shown in appendix C. These results show time-averaged values over 60 measurements acquired in about 6 seconds. The uncertainties due to the measurement techniques are very small because pressure transducers are very precise. The error in the position is less than 1 mm. Therefore the error bars are not visible on the plots.

The far-field pressure distributions at $M_\infty=0.7$ are plotted in figure 6.9 without and with plasma. When the plasma is generated in the supersonic pocket upstream of the shock, the pressure well is less than 1% deeper. When the plasma is generated in the shock foot region, the pressure well becomes about 2% less deep. The effects present relatively small amplitudes which are within the pressure measurement errors (from tubes linking the pressure tap to the pressure transducer, the transducer itself and the A/D converter).

The results presented in this section show that the surface plasma does not significantly affect the steady properties of the shock quantitatively either. The pressure variation in the relatively far-field across the shock remains almost the same (within 2%). This indicates that the reasons why the interaction cannot be observed are physical and not

³Pressure taps are inside the wall boundary layer, but as discussed in chapter 2, the static pressure does not vary in the direction perpendicular to the boundary layer and the measured static pressures will be the same as the static pressures across the shock.

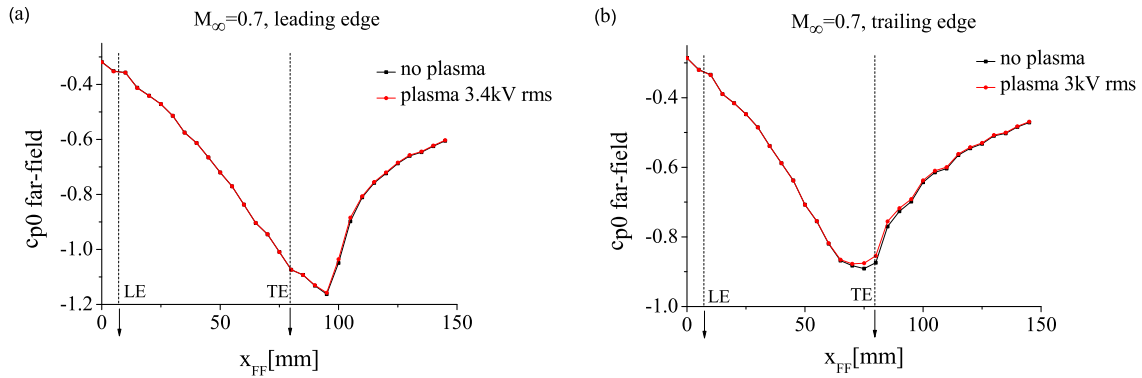


Figure 6.9: Averaged far-field pressure distributions at $M_\infty=0.7$ in the leading edge (a) and trailing edge (b) configurations, in conditions without discharge and with a discharge at 10 kHz.

due to the sensitivity of the measurement techniques.

6.2.3 Unsteady shock properties

Transient properties of the shock, which might be more sensitive to excitations created by the surface discharge, are investigated using time-resolved Schlieren measurements. The shock motion and thus the pressure distribution along the surface can be critical regarding the self-exciting oscillations of the airfoil as suggested by Ferrand et al. [76]. In turbomachinery for example, the safety and efficiency are affected by the presence of unsteady phenomena. The aerodynamic force on the blades, the efficiency of the stage, the noise generation or the energy transfers are directly dependent on unsteady flow phenomena as explained by Aubert et al. [77].

First of all, the shock oscillation frequency is measured from raw Schlieren images taken with the Sensicam camera. In a similar way as the averaged profiles have been calculated in the previous section, a reference line close to the profile is chosen to draw an intensity profile, determine the minimum and deduce the position of the shock. This is done for 100 images ($15\mu s$ exposure time at 21 frames per second) covering a time range of 5 s. The results for the trailing edge configuration are given in figure 6.10, at inlet Mach number $M_\infty=0.7$, with the results of the Fast Fourier Transform (FFT) on the displacement shown as a power spectrum. Results for $M_\infty=0.65$ and $M_\infty=0.75$ are shown in appendix C. The methodology is similar to what is usually done in transonic flow analysis, for example by Bron et al. [72].

The frequency and amplitude of the variation is comparable in the cases without and with plasma. The power spectrum is very similar in both cases as well, although the amplitude at higher frequencies for the case with plasma is usually higher. This could be an indication of the addition of turbulence in the boundary layer by the plasma, generating high frequency oscillations in the shock position. Indeed, Dupont [78] reminds that experiments show that very low frequencies are related to shock motion, medium

range frequencies are linked to separation phenomena and high frequencies are correlated to bursting properties in the incoming turbulent boundary layer. However, this hypothesis has to be confirmed with plasmas generating higher turbulence levels in the boundary layer in order to have clearer tendencies.

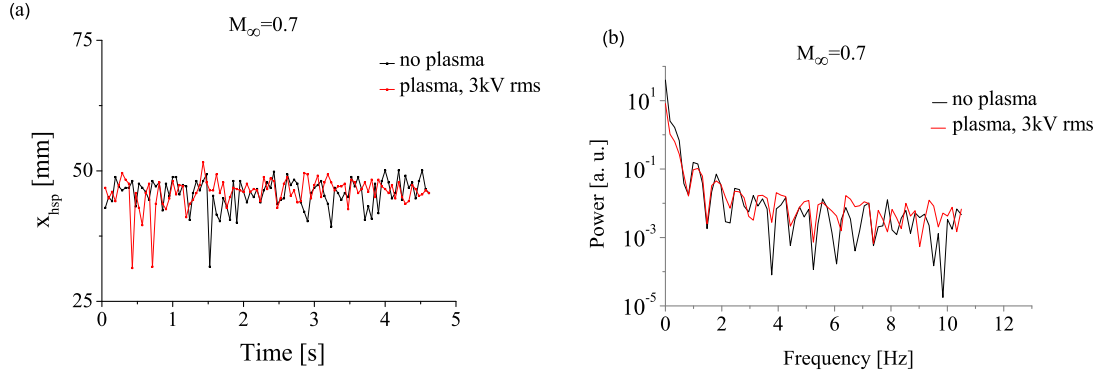


Figure 6.10: Variation of the instantaneous horizontal shock position $x_{h,sp}$ with time (a) and FFT spectrum (b), at $M_\infty=0.7$ in the trailing edge configuration, in conditions without discharge and with a discharge at 10 kHz.

In the case where the plasma is on, the shock properties could be affected differently at different moments in time with respect to the DBD voltage signal since the discharge is not continuous. Chapter 4 shows that there is almost no plasma generated between the current peak regions. Consequently, part of the Schlieren images *with plasma*, taken at those instants, correspond actually to no-plasma conditions and results are in fact averaged on conditions without and with plasma. In order to solve this problem, the Sensicam camera taking the Schlieren images has been triggered on the plasma voltage signal and voltage phase-dependent Schlieren imaging results are shown below. 100 images taken at the same voltage phase have been averaged and intensity profiles close to the airfoil have been drawn. Intensity profiles at different phases for $M_\infty=0.7$ with the plasma generated close to the trailing edge are shown below in figure 6.11. t_p and t_n are the instants at which the filamentary discharges start on the positive and negative half-periods respectively, as defined in chapter 4.

Averaged images do not bring additional information and profiles are again very similar in all cases, geometrical differences staying lower than 5 mm and being therefore small compared to the scale of aerodynamic perturbations that can be due to bulk flow around the airfoil. Moreover, measurements show the same shock instability properties at every phase of the plasma voltage.

Even though, as suggested by Andreopoulos and Muck [79], the shock unsteadiness is closely dependent on the bursting properties of the incoming boundary layer, the turbulent boundary layer already has high kinetic energy and maybe a plasma with higher ionization rate would be needed in order to significantly increase the turbulence. On the other hand, Ott et al. [80] also infer that the frequency of an excitation of the flow down-

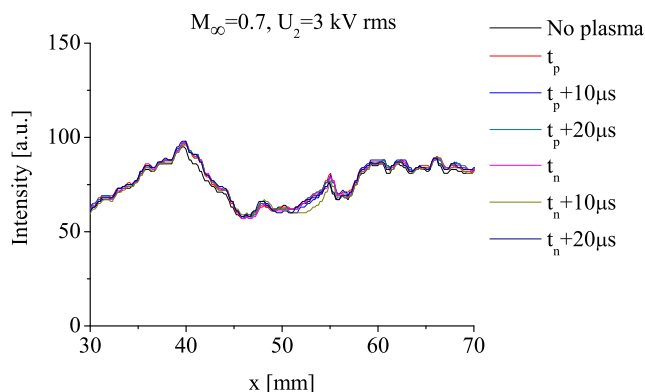


Figure 6.11: Intensity profiles at different voltages phases, from averages of Schlieren 100 images, at $M_\infty=0.7$ and in conditions without discharge and with a discharge at 10 kHz close to the trailing edge at $U_2=3$ kV rms.

stream of the shock has significant consequences on the unsteady properties of the shock, like the amplitude of the shock oscillation. However, these results have been obtained in conditions where the whole downstream bulk flow is modified and the excitation frequencies are between 0 and 180 Hz. Therefore, a variation in the frequency of the plasma voltage which would induce a variation in the frequency of plasma properties and flow perturbations might be negligible because of the difference in frequency scales (10 kHz for plasma excitation, which is 3 orders of magnitude higher than the shock oscillation frequencies).

Unsteady far-field pressure measurements have not been performed since they can be strongly affected by the pressure waves propagating upstream and downstream in the nozzle as explained by Bron et al. [72] and interpretation would be hazardous.

In order to understand why no effect of the discharge on the steady or unsteady characteristics of the shock can be observed, the behavior of the surface DBD in the flow has to be studied in more in details. Since high flow velocities and high pressure gradients are present in the transonic flow, the flow might affect the discharge in a significant way. This is confirmed by the results presented in the following section.

6.3 Effect of the flow on the DBD

As seen in chapter 5, the working gas flow velocity has a significant influence on several discharge properties in a flat plate configuration. When the plasma is generated on the surface of an airfoil in a transonic flow, the situation is different. First of all, the pressure levels change on the surface of the airfoil. Upstream of the shock, the gas is accelerated and the pressure drops. This is followed by a strong recompression and deceleration of the gas through the aerodynamic shock. Also, at some point on the surface, the boundary layer will separate. These spatially changing physical conditions will have important repercussions on the plasma operation and intrinsic properties which are discussed in this section.

6.3.1 Discharge operation

When the plasma is generated on the surface of an airfoil like the NACA3506, its operation domain in terms of voltage becomes strongly dependent on the inlet Mach number M_∞ as shown in figure 6.13. The measurements have been performed with an encapsulated LTCC plate geometry (*LTCC-enc* defined in chapter 4) placed close to the leading edge (a) and close to the trailing edge (b). The lower boundary of the operation domain is given by the burning voltage and the upper boundary is given by the highest voltage applicable before arcs start to form between the upper electrode and the metallic profile as shown in figure 6.12. These arcs are destructive in the sense that they melt the top LTCC layer and leave permanent holes in it.

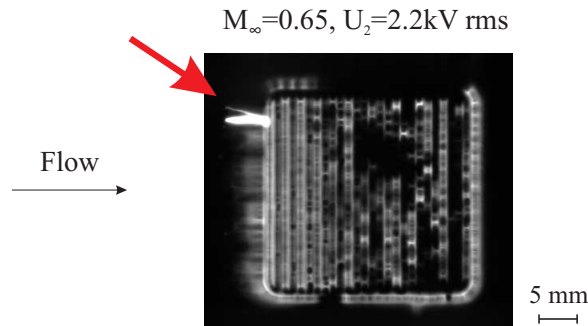


Figure 6.12: CCD image of the discharge generated by a *LTCC-enc* geometry at 10 kHz forming an arc attaching on the metallic profile. Exposure time is 40 ms.

Figure 6.13 shows that the operation domain is dependent on the position of the plate on the airfoil. In the leading edge case, for inlet Mach numbers up to $M_\infty=0.33$, the burning voltage increases M_∞ in a similar way to what has been observed on the flat plate. However, as the inlet flow velocity is further increased, a drastic change in the burning voltage behavior takes place. It decreases from $M_\infty=0.33$ to $M_\infty=0.7$, together with the maximum voltage and rises again at $M_\infty=0.72$. In the trailing edge case, the burning voltage always drops, at a higher rate when the inlet Mach numbers is higher. The maximum voltage drops as well but stabilizes at high velocities.

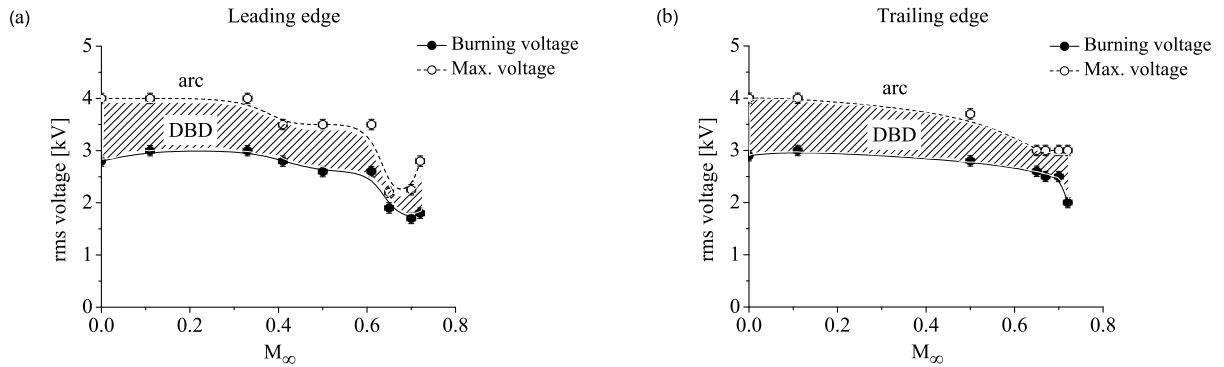


Figure 6.13: Operation domain of the discharge generated by a *LTCC-enc* geometry at 10 kHz for different inlet Mach numbers and geometrical configurations.

In order to measure more precisely the effects of the flow on the instantaneous burning voltage, individual microdischarge burning voltage has been determined from the voltage U_{2i} corresponding to the beginning of the current peak region (at $U_2 = 3$ kV rms and 10 kHz applied voltage, see definition in appendix C). These measurements are more precise since they are given by the current and not by the geometrical aspect of the overall discharge. Furthermore, the trends are more defined in the sense that they are much greater than the measurement errors. Figure 6.14 shows that the microdischarge burning voltage varies significantly on both half-periods. The burning voltages at $M_\infty = 0.65$ and $M_\infty = 0.7$ are not measurable at $U_2 = 3$ kV rms because of the formation of arcs. The curve variations are similar to the burning voltage curves (with an opposite sign on the negative starting voltage). It is difficult to understand intuitively the physical meaning of the change of sign of U_{2i} observed in figure 6.14. A numerical model of the discharge at different gas pressures would help answer this question.

For $M_\infty < 0.33$, the discharge burning voltage varies in the same way as what is observed in the flat plate experiment, which means that the effects of the flow velocity are dominant. The situation is different for $M_\infty > 0.33$. In order to understand the origin of these effects, the static pressure levels calculated from the numerical model have been averaged on surface where the plasma is created and plotted against the inlet Mach number. The results are shown in figure 6.15. They show that at $M_\infty > 0.33$ the qualitative variation of the burning voltage follows the variation of the static pressure on the surface. It is the case for the leading edge and trailing edge positions. This is in accordance with Paschen curve in air (figure 2.4 in chapter 2) predicting lower breakdown voltages at lower working pressures, in this range of pressures. These observations indicate that at $M_\infty > 0.33$, the discharge burning voltage is driven by pressure effects. Benard et al. [81] also find the voltage required to create the discharge decreases with pressure. They also observe that the positive filamentary zone starts earlier (with respect to the voltage curve) with decreasing pressure.

An even better demonstration is brought by CCD imaging of the discharge in the

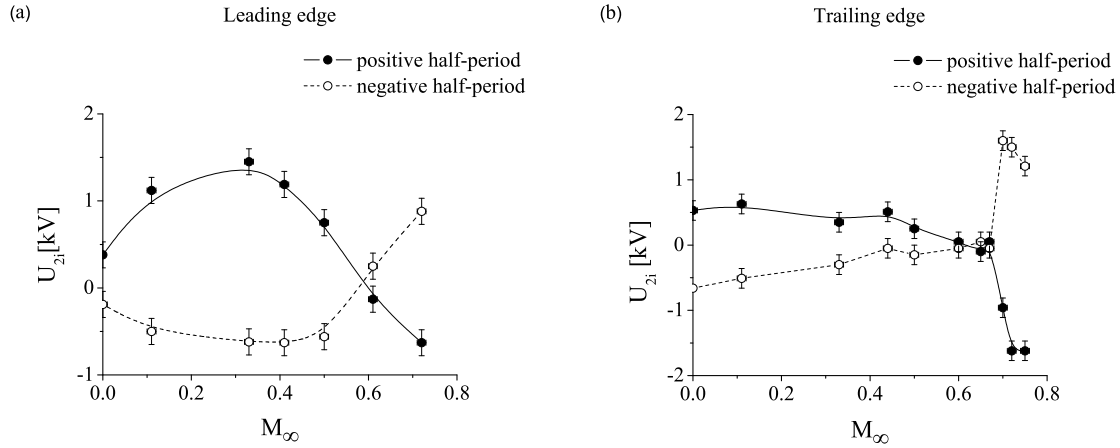


Figure 6.14: Voltage at which filaments start to form on the positive and negative half-periods for an external applied voltage $U_2=3$ kV rms at 10 kHz.

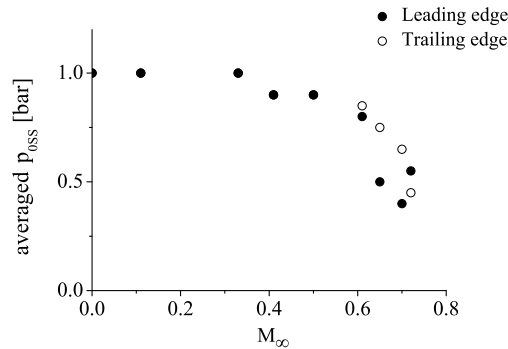


Figure 6.15: Static pressure averaged over the discharge surface, calculated with the RANS numerical model.

leading edge configuration at $M_\infty=0.65$ as seen in figure 6.16. Indeed, they show that it is possible, at a slightly lower voltage, to switch on the discharge only upstream of the shock, where the pressure is lower (figure 6.3) and the plasma easier to ignite. If the velocity effects were dominant, the plasma would not switch on upstream but downstream of the shock, where the velocity is lower.

Finally, Lissajous plots in figure 6.17 clearly show the reduction of power dissipated in the plasma between the case at $M_\infty=0$ and $M_\infty=0.7$.

Taking into account the measurement errors, single-line electrode geometries give similar results in terms of burning voltages and are therefore not shown here. This is consistent with the burning voltage measurements presented in chapter 4 leading to the conclusion that the electrode geometry has little effect on the burning voltage properties.

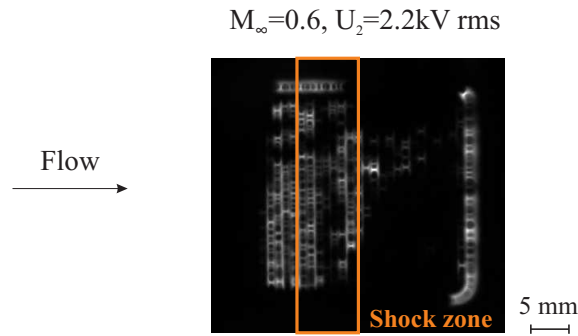


Figure 6.16: CCD image of the discharge generated close to the leading edge at 10 kHz. Exposure time is 40 ms.

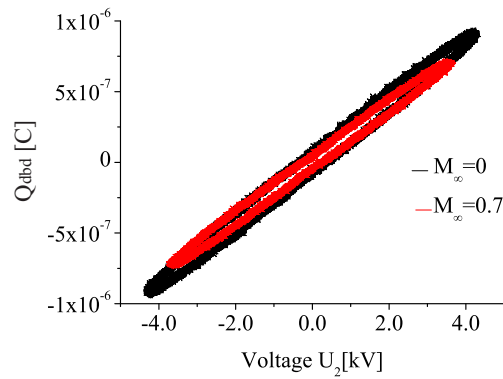


Figure 6.17: Lissajous figures at $M_\infty=0$ and $M_\infty=0.7$ at 10 kHz and $U_2=3$ kV rms.

6.3.2 Discharge regimes

The electrical characteristics of the discharge are strongly affected by the flow, as has been demonstrated on the flat plate experiment. This is the case when the DBD is mounted on the airfoil as well, as is shown in the present section.

The current and voltage curves I_2 and U_2 through the DBD have been measured for different inlet Mach numbers M_∞ in the nozzle, when the DBD is mounted close to the leading edge, and are shown in figure 6.18.

As the inlet flow velocity increases, the current peak amplitudes first diminish on both half-periods. At $M_\infty=0.65$, the amplitude of the peaks on the positive half-period starts to increase again, which is not the case on the negative half-period. At $M_\infty=0.7$, distinct high current peaks appear on the positive half-period. Note that the applied voltage U_2 is slightly lower, giving smaller overall peak amplitudes, because at higher voltages at this velocity arcs start to form (see figure 6.13). A peak with higher amplitude also appears on the negative half-period but less distinctly. The amplitude of the high current peaks drops again at $M_\infty=0.72$. The current curves show that the aerodynamic properties of the flow around the profile have an effect on the discharge regime. It is interesting to see

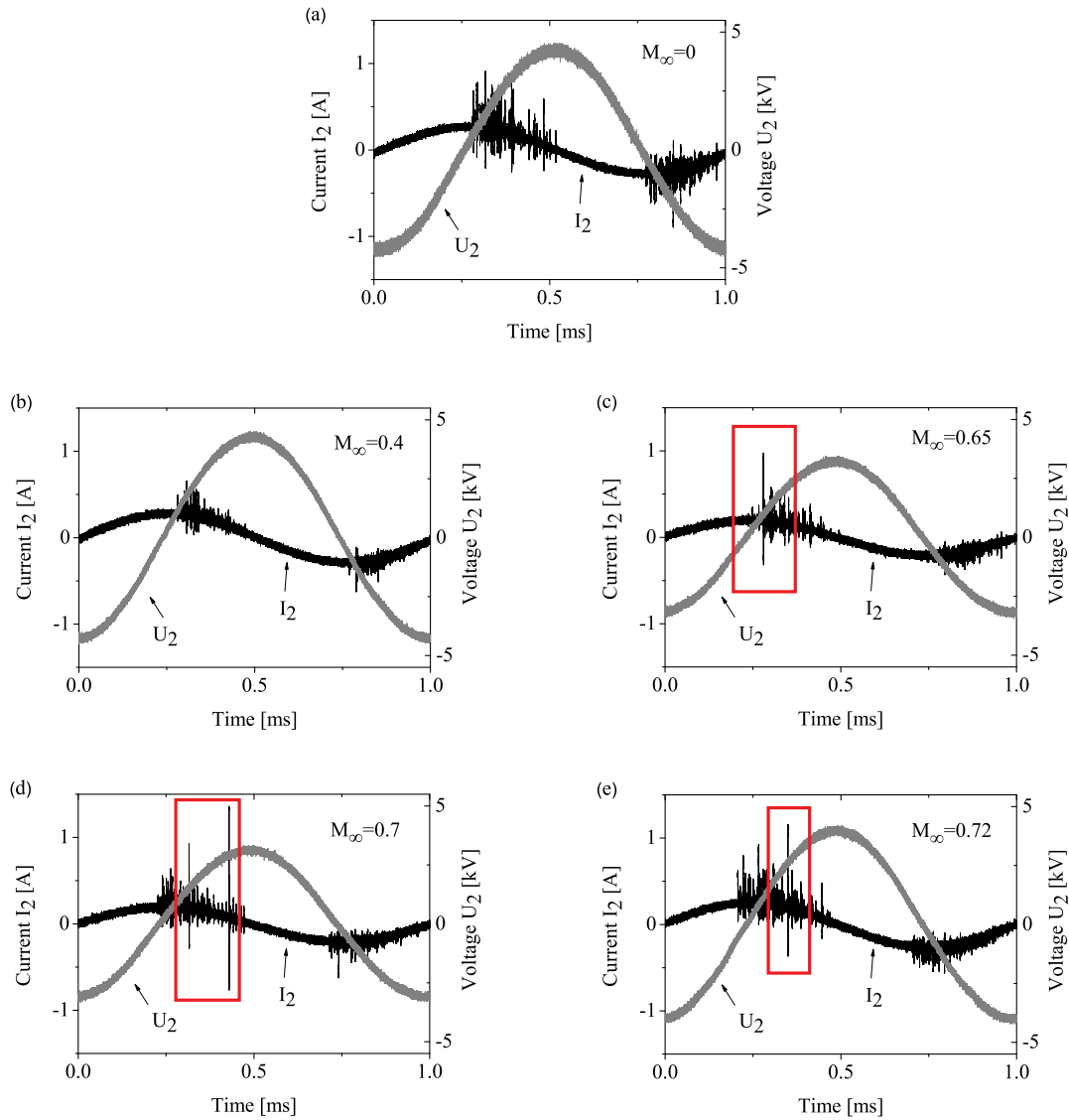


Figure 6.18: Voltage and current for the discharge generated close to the leading edge at 10 kHz (slightly variable applied voltage), at different inlet Mach number conditions.

that high current peaks appear on the positive half-period here, whereas they appeared on the negative half-period in the flat plate case. It is difficult to understand this at this stage and interpretations should be supported by a numerical model of the discharge at different pressure levels. Although the geometry is encapsulated, there is still a strong asymmetry between the positive and negative half-period currents. Moreover, the high current peak amplitude seems to follow the variations of the pressure on the surface given by figure 6.15. Benard et al. [81] have performed current measurements on a surface DBD with no gas flow but different pressure levels. They find that when the gas density is reduced due to a pressure drop, the current pulses become more intense (at constant

electric field). They think that this happens because fewer collisions between the charged particles and the surrounding neutral species occur.

Opaits et al. [68] suggest that the filamentary regime is most advantageous in order to affect a surrounding flow and that filament generation should be maximized. As suggested by the experiments of Abe [82], both positive and negative half-periods of a DBD have an equivalently essential contribution to the momentum transfer to the surrounding flow. It is thus interesting to study the variation of the number of filaments on both half-periods for different flow conditions. This is shown in figure 6.19 where light emission peaks have been measured with a photomultiplier as a function of the inlet Mach number. Up to about $M_\infty=0.33$ the number of peaks is reduced, in the same way as in the flat plate experiment discussed in chapter 5. Then the filament generation is drastically enhanced, which seems to be due to pressure effects taking over. Benard et al. [81] observe the same effects as a function of pressure. The effect is even more significant on the negative half-period because the peak frequency is higher as demonstrated in chapter 4. No significant effects of the flow on the continuous (glow or corona) component can be pointed out because it is not observable with the photomultiplier measurements. The encapsulated single-line geometry has been studied as well and gives the same qualitative results.

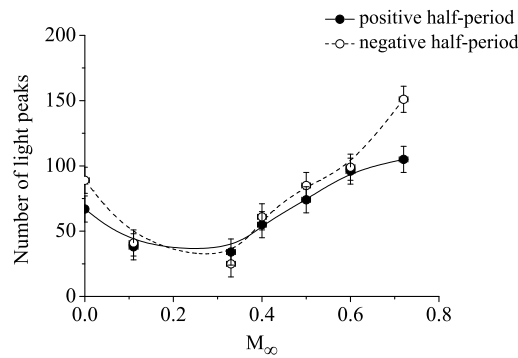


Figure 6.19: Number of peaks measured on photomultiplier measurements, for the positive and negative half-periods, for the discharge generated close to the leading edge at 10 kHz and $U_2=3$ kV rms.

In order to compare the different inlet Mach number cases at the same plasma applied voltage $U_2=3$ kV rms, the trailing edge configuration has been studied as well, and the results are presented below. Like for the burning voltage, the effects of the flow properties on the discharge are less visible in this case. The current curves are shown in figure 6.20. A high current peak appears at $M_\infty=0.4$ on the negative half-period, as in the same way as observed on the measurements on flat plate in chapter 5, but then no distinct high current peak is observed at higher inlet Mach numbers on the positive half-period. The pressure variation on the trailing edge is much smaller than close to the leading edge and the pressure might not be low enough to display the same kind of high-current peaks as in the leading edge configuration.

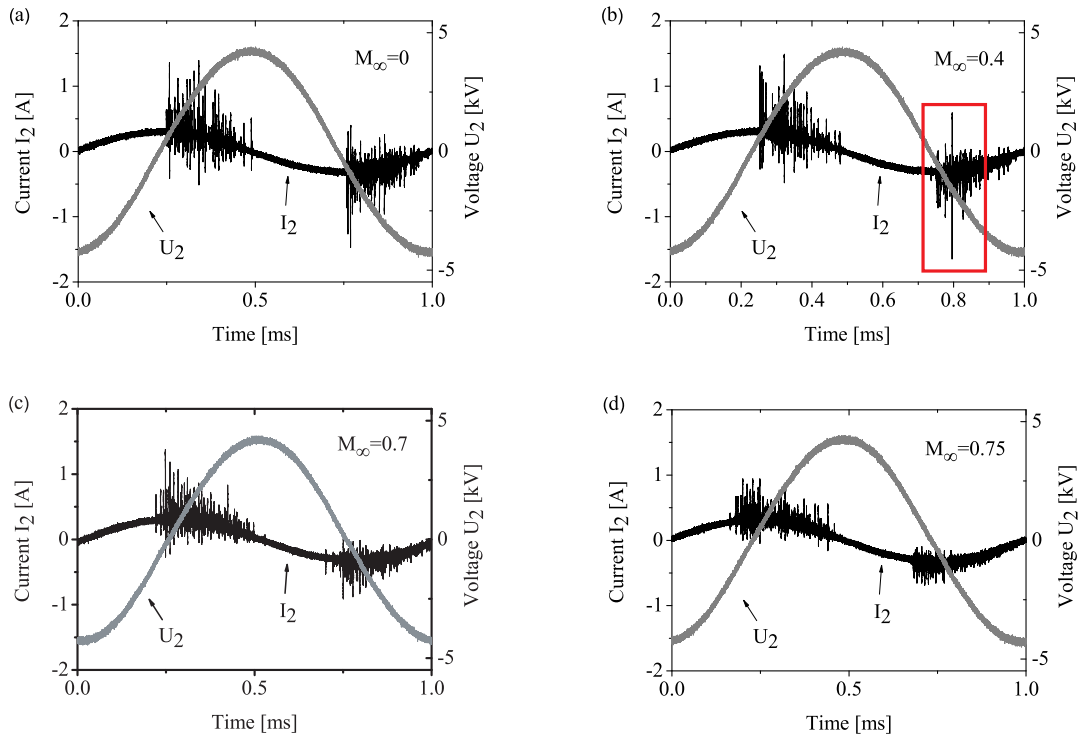


Figure 6.20: Voltage and current for the discharge generated close to the trailing edge at 10 kHz and $U_2=3$ kV rms, at different inlet Mach number conditions.

The number of light peaks measured with a photomultiplier are displayed in figure 6.21 (a). Again the filament generation is clearly favoured at higher velocities. The variations follow the pressure curve given in figure 6.15 again. The fact that the pressure dominates the other effects can be confirmed by measurement of the number of light emission peaks at the same inlet Mach number but at higher pressure levels. This will compress the air in the test section. Results are shown in figure 6.21 (b). The graph shows that for both half-periods, even a small change in pressure, from 1.3 to 1.5 bar induce a reduction of peaks generated by the DBD by almost 50%. This constitutes a good proof that pressure has a strong influence on the discharge regime and filament generation. It dominates the plasma-flow interaction on the airfoil configuration when the inlet Mach number is high enough to generate a transonic flow around it and a resulting non-homogeneous pressure distribution.

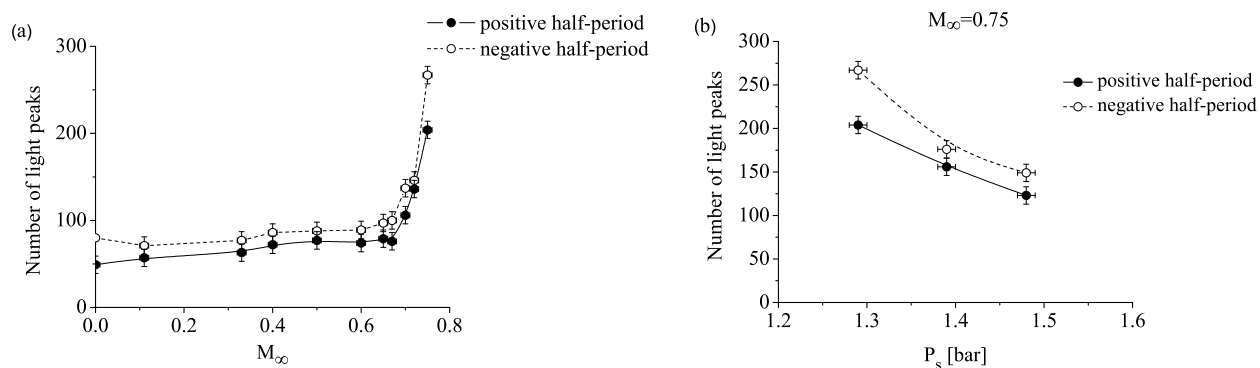


Figure 6.21: Number of peaks measured on photomultiplier measurements, for the positive and negative half-periods, for the discharge generated close to the trailing edge at 10 kHz and $U_2=3$ kV rms.

6.3.3 Spatial discharge distribution

In order to investigate the spatial properties of the discharge and the distribution of energy injection in the flow, CCD images of the plasma have been taken with the PixelFly camera mounted on top of the wind tunnel in front of the upper optical access. The images are long exposure (40-50 ms) and thus integrate the light over several positive and negative half-periods. The images taken on the leading edge configuration at different inlet Mach numbers are shown in figure 6.22. Again note that, due to different burning voltages and arcing limits at different inlet Mach numbers, not all the applied voltage U_2 are the same. It means that only the qualitative attributes of the different discharges can be compared but not the light intensity levels. The fact that the stripe closest to the trailing edge (on the right) is the most intense at $M_\infty=0$ is due to a slight misalignment of the top and bottom electrodes. The bottom electrode is slightly shifted to the right which favors the formation of the discharge on this side.

The CCD images show that from $M_\infty=0$ to $M_\infty=0.33$ the discharge becomes more sparse in the same way as observed in the flat plate experiment. However, at $M_\infty=0.65$ the plasma covers all the zone that corresponds to the supersonic pocket upstream of the shock. As the inlet flow velocity is further increased, the plasma becomes more intense on the whole electrode surface like at $M_\infty=0.7$. At $M_\infty=0.72$ the intensity of the light emission becomes actually stronger closer to the trailing edge.

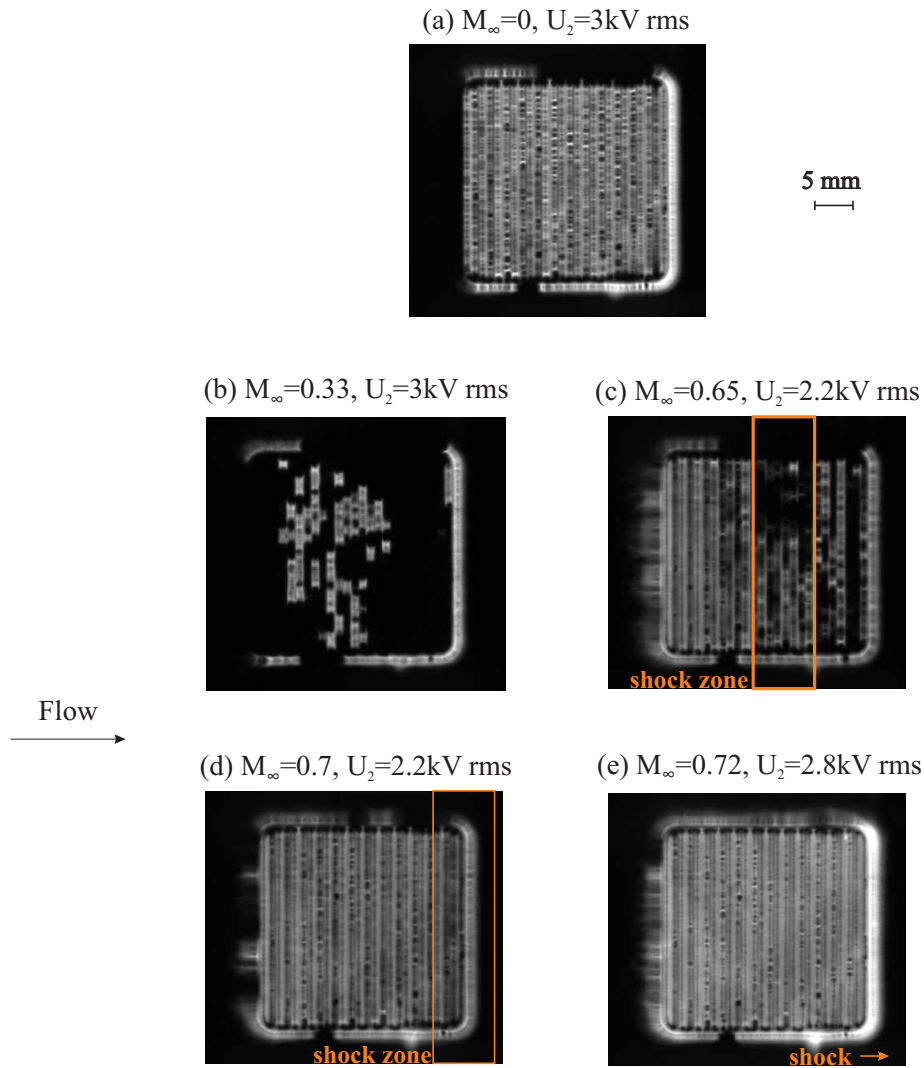


Figure 6.22: CCD images of the discharge at different inlet Mach numbers for the discharge generated close to the leading edge at 10 kHz. Exposure time is 50 ms for (a) and (b), and 40 ms for (c) to (e).

The intensity profiles calculated from the images in figure 6.22, integrated along the electrode stripes, are plotted in figure 6.23. They are compared to the pressure distribution along the suction side at the same position calculated from the numerical model. The plots show a (inverse) correlation between the pressure curves and the intensity curves at the three inlet Mach numbers considered. This is an additional confirmation that the bulk plasma distribution is dominated by pressure effects.

Images in figure 6.22 also show that long filaments start to form close to the leading edge when $M \geq 0.65$. At this inlet Mach number, the local velocity of the flow and the local pressure at the edge stripe position are minimum as shown in figure 6.24. It is therefore difficult to say at this point which of the velocity or pressure favours the appearance of long filaments (and corresponding high current peaks).

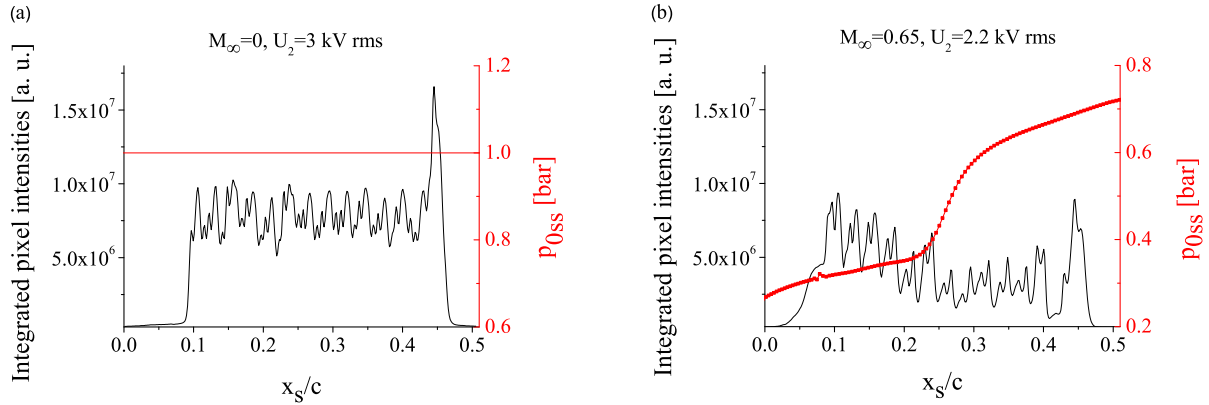


Figure 6.23: Integrated pixel intensities parallel to the electrode stripes from CCD images in figure 6.22 (at 10 kHz) and pressure distributions calculated from the numerical model.

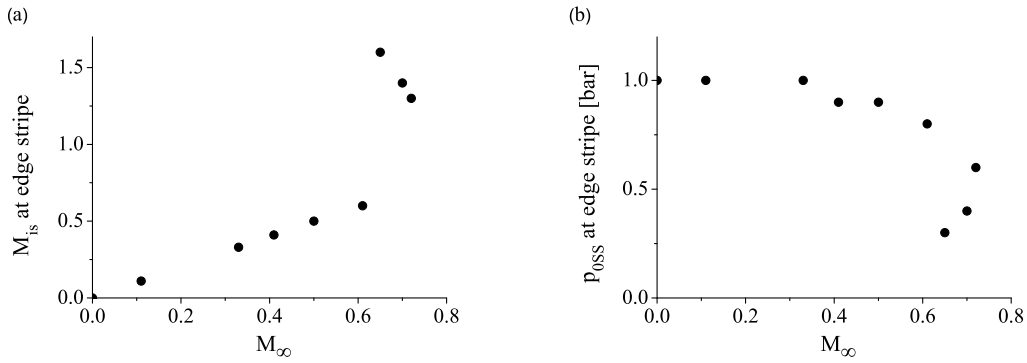


Figure 6.24: Isentropic Mach number (a) and static pressure (b) at the location of the upstream edge stripe ($200 \mu\text{m}$ above the surface) in the leading edge configuration, calculated with the RANS numerical model.

Since the applied voltages are not the same for all images in figure 6.22 for the leading edge configuration, it is difficult to draw straight conclusions. Therefore the trailing edge configuration has been considered, where all the measurements can be done at $U_2=3$ kV rms.

In the trailing edge configuration, it is found that the plasma distribution stays homogeneous on the whole electrode area (see figure C.14 in appendix C) and the intensity follows the pressure distribution as in the leading edge case.

At $M_\infty=0.7$, the structure of the positive and negative edge stripe discharges are clearly different as shown in figure 6.25. The images have been post processed in order to be able to see the full geometry of the discharge at any phase position. The true intensity levels are shown in the integrated intensity profiles in figure 6.26. On the negative half-period, at time $t_n+20\mu\text{s}$, structures that resemble long filaments appear which are not

visible on the positive half-period where the discharge rather form in a diffuse manner. The structure of the *filaments* at $t_n+20\mu\text{s}$ is however not as much defined as in the leading edge case. Also, the corresponding current signals (see figure 6.20) do not display high current peaks. It might be that the structures in figure 6.25 are dominated by pressure effects as opposed to the filaments in the leading edge case which are probably due to velocity effects as in the flat plate case.

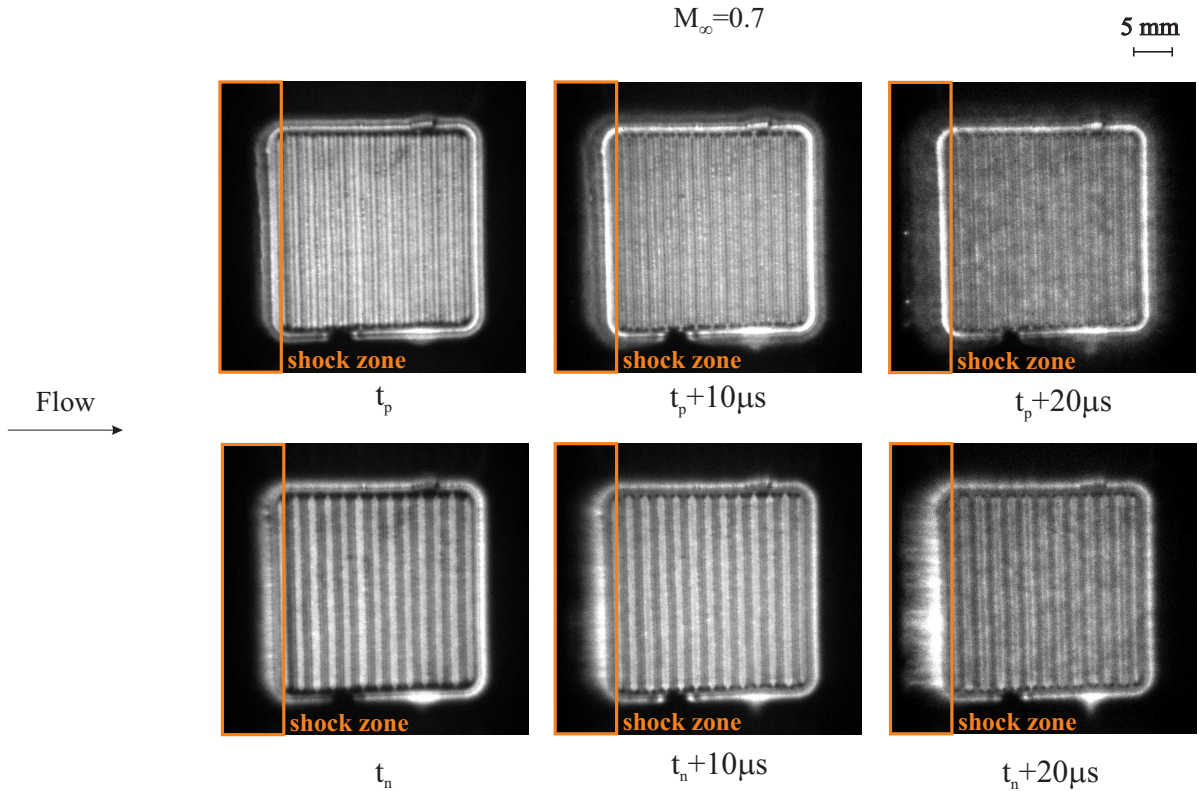


Figure 6.25: Images of the discharge triggered on the voltage signal, at different times as defined in chapter 4 for $U_2=3$ kV rms and 10 kHz in the trailing edge configuration. Exposure time is $10 \mu\text{s}$ and images are accumulations of 600 camera gates.

At $M_\infty=0.7$, the plasma significantly expands around the upstream edge stripe as shown in figure 6.25. At this inlet Mach number, the pressure at the upstream edge stripe position is actually minimum as shown in figure 6.27. The expansion of the discharge is plotted in figure 6.28 as a function of time. The expansion rate is about the same for the positive and negative half periods, which might be due to encapsulation (in chapter 4 for the non-encapsulated plate, the expansion rates are different). This discharge expansion is not observable at $M_\infty=0$ (see chapter 4). This corresponds to what is found by Benard et al. in [81], where a significant discharge expansion is observed as the pressure is decreased and the plasma length is found to extend beyond the end of the grounded electrode for a pressure of 0.2 bar.

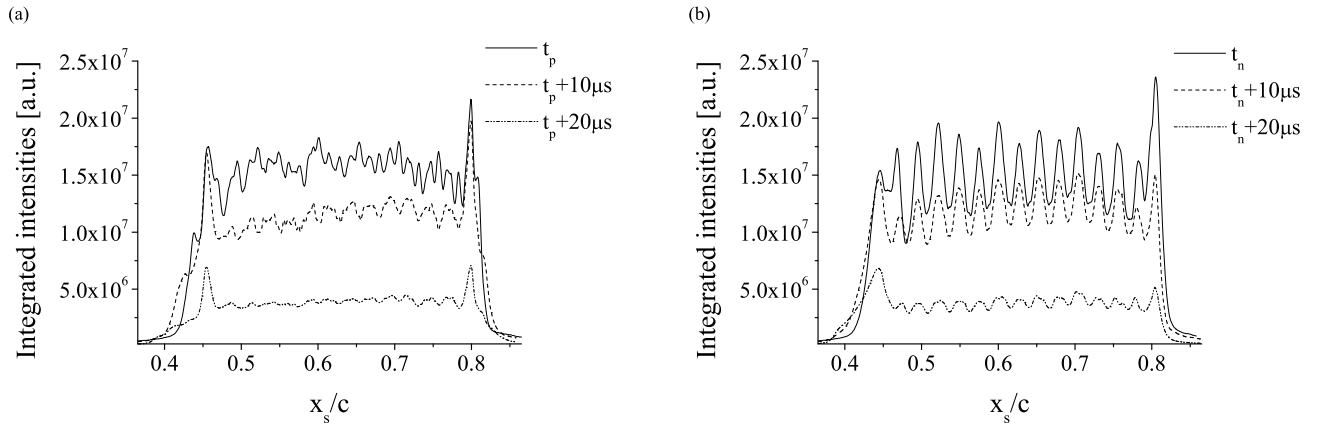


Figure 6.26: Pixel intensities integrated parallel to the electrode stripes from CCD images in figure 6.25 ($M_\infty=0.7$, $U_2=3$ kV rms at 10 kHz), for the positive half-period (a) and the negative half-period (b).

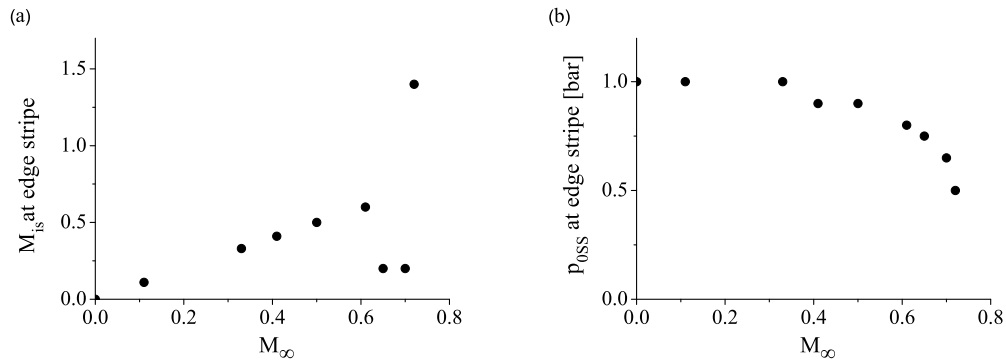


Figure 6.27: Isentropic Mach number (a) and static pressure (b) at the location of the upstream edge stripe ($200 \mu\text{m}$ above the surface) in the trailing edge configuration, calculated with the RANS numerical model.

Experiments have been conducted using an encapsulated DBD plate with a single stripe as upper electrode, in order to try to maximize the generation of long filaments creating high current peaks. However, this configuration does not generate more high current peaks and the results are very similar to the measurements done with a grid electrode.

In the papers by Gregory et al., Benard et al. and Abe et al. [81–83], the generated ion wind is studied as a function of pressure. Benard et al. [81] show that the time-averaged force produced by a DBD actuator first increases, reaches a maximum at 0.6 bars and then decreases linearly with air pressure from 0.8 to 0.2 bar. This is due to the reduction of air density at lower pressures and thus the reduction of mass flow rate.

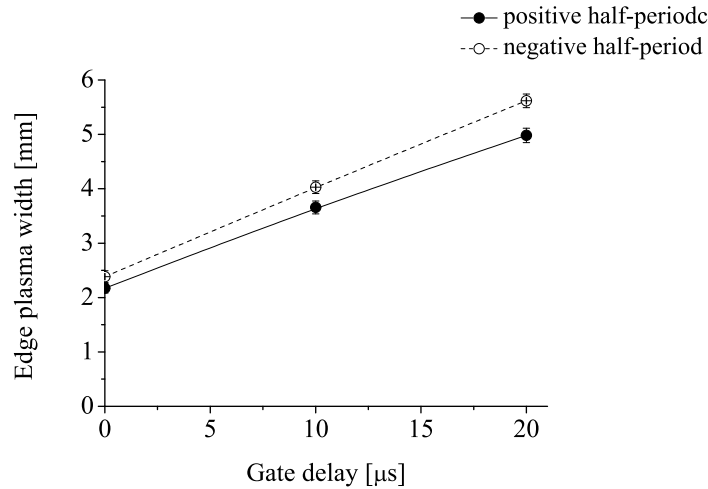


Figure 6.28: Expansion of the plasma around the left edge stripe from CCD images in figure 6.25 ($M_\infty=0.7$, $U_2=3$ kV rms at 10 kHz).

6.4 Summary

No significant effects of the surface DBD on the normal shock generated in the transonic flow have been observed in the experiments presented in this chapter. Averaged and time-resolved Schlieren visualizations and averaged pressure measurements show that the shock structure, pressure distribution across the shock and unsteady properties of the shock (shock-boundary-layer interaction) are similar in the conditions without plasma and with a plasma generated in the boundary layer.

However, the flow modifies the plasma in a very significant way. The flow modifies the discharge regime and the spatial discharge intensity distribution:

- Velocity effects similar to the ones observed in the flat plate case seem to generate high current filaments (spatially wide spread) and be positive for enhancing plasma-flow interaction.
- Decreasing pressure increases the number of filaments and favors high current peak generation.

It shows that the discharge characteristics cannot be completely controlled and that they depend on the flow field. Nevertheless, it can be sustained in high-pressure gradient flows and the effect of the flow on the filaments can be interesting in applications like plasma assisted combustion or supersonic combustion, where the plasma is used for the enhancement of chemical reactions. Moreover, the good reproducibility of the measurements (due to the robustness of the encapsulated DBD system) could make the system usable for measurements of velocities or pressures, i.e. the DBD could be used as a velocity or pressure sensor. The interpretation of the results would be improved with a numerical model at different pressure levels.

In order to increase the filament production rate and current peak intensity for flow control, the following solutions might prove efficient:

- change the DBD system to a geometry where the grounded electrode and the electrode submitted to the potential are coplanar and interlaced in a brush-type geometry
- optimize the applied voltage function as suggested by Likhanskii et al. [61]
- apply higher voltages, but in this case the NACA+DBD system would have to suffer fundamental design modifications (change profile size and material for example) in order to reduce the probability of arcing

Note that, as described in appendix D, the RANS numerical model of the flow around the NACA3506 airfoil in the subsonic nozzle has been used for two more purposes in addition to the characterization of the flow:

- Identify and model the possible physical effects of the plasma on the flow. Physical properties of the boundary layer are modified locally in a *control volume* close to the airfoil surface (corresponding to the discharge volume).
- Find orders of magnitude for the modifications of physical parameters required to induce a significant effect on the shock

This parametric study gives a physical feeling of the impact of different forced boundary layer properties on the external flow. The orders of magnitude of the modifications needed in order to affect the shock pattern have been estimated and it is shown that they are still much higher than what can be obtained to date with DBDs. The calculations help understand why, from an aerodynamical point of view, the experiments show little effect of the surface discharge on the Schlieren visualization and far-field pressure distributions. However, the hypotheses in the model are very rough and the results should be taken considered with care.

Chapter 7

Conclusions

The highly interdisciplinary subject of flow control with plasmas has started to develop in the scientific community not longer than a decade ago. The wide range of possible plasma generation systems and flow configurations have enriched the subject very quickly. The different research directions are getting structured slowly, and two main groups can be recognized:

- low-velocity flow control with surface DBDs through the generation of ion wind
- supersonic flow control using volume glow or corona discharges.

Flow control using surface DBDs could not be studied in details due to technical difficulties of sustaining a DBD for long operation times and in extreme environments.

A solution to this problem has been found in the present work, and it is proposed in the present work to use LTCC technology to fabricate long-lifetime (several tens of hours) DBD systems which can be integrated on the surface of any shape and material. It is the first time, to our knowledge, that this technological barrier has been overcome and that detailed studies of surface DBDs in transonic flows can be undertaken, with good reproducibility of the experiments (thanks to the encapsulation of the electrodes in the ceramics). Additionally, the successful demonstration of the plasma-on-airfoil system in transonic flows has led to the deposition of a patent [55]. This will help extend the impact of the research area from academics to industry. Mainly aeronautical applications have target here, but there is potential interest in plasma processing applications as well, for example in textile surface treatment. Finally, completely non-intrusive diagnostics have been implemented, which guarantee a minimum perturbation of the discharge and flow. Inversely, the perturbation of the measurements by the discharge and flow has also been minimized.

The complexity of the physics involved in non-equilibrium atmospheric discharges keeps numerous questions open. The inhomogeneity and short time phenomena occurring in (surface) DBD has made experimental and numerical studies a challenge, and the interpretation of the results has to be made carefully. On the other hand, transonic flows are also not fully understood today and shock-boundary layer interaction in this regime is still difficult to model. The knowledge in the interaction phenomena between surface DBDs and transonic flow is thus scarce. The present work presents a first detailed

experimental parametric study. An additional novel approach is to exploit the instability of the shock in a transonic regime to modify its properties with a surface discharge placed in the shock-boundary layer interaction zone.

Characterization of the surface DBD without flow has shown that the plasma is made of a filamentary and a glow- or corona-like component. An increase in the voltage ramp (dU_2/dt) results in an increase in the filament generation rate and current amplitude. These observations are qualitatively confirmed by the model developed by Lagmich et al. [60], which suggests that the dominant phenomenon sustaining this kind of discharge is secondary electron emission by ion bombardment of the dielectric. The geometry of the electrodes has little effect on the burning voltage but it plays a role in the filament generation rate: the longer the effective length of the electrode, the more filaments are generated and the further the electrode stripes are located from each other, the higher the filament generation rate (due to a higher p·d factor). In order to improve the lifetime of the DBD system, improve the reproducibility of the experiments and reduce the probability of arcing in the experiment on the airfoil, the DBD system has to be encapsulated. The negative consequences of this encapsulation on the discharge are that it reduces the rate of filament production and the expansion of the plasma around the upper electrode. The advantages of encapsulation is that it results in a more uniform distribution of the plasma on the surface and in time (symmetrization between the positive and negative half-periods) and thus of the energy injection in the flow.

The measurements on the DBD created by a flat plate system on the wall of the nozzle have evidenced the modifications in the discharge regime at high airflow velocity. In the overall discharge, the continuous (glow or corona) component of the plasma is more reduced than the number of filaments with increasing flow speeds, the plasma becomes relatively more filamentary. In individual microdischarges, the reduction of the light pulse emission duration by one order of magnitude (from 500 ns to 50 ns) when airflow velocity is increased (from $M_\infty=0$ to $M_\infty=0.7$) indicates that there is a change in the breakdown mechanism. It is proposed that a transition from Townsend breakdown to streamer breakdown occurs when the airflow velocity is increased. The depletion of N_2 metastable states due to the airflow seems to be the dominant cause, reducing the internal energy and reducing the relative importance of secondary emission processes. The discharge characteristics are also very sensitive to the electrode geometry. When the plasma has enough space to expand perpendicularly to the electrode stripe, the discharge takes the form of long filaments corresponding to high current peaks.

Although no significant effects of the surface DBD on the steady or unsteady properties of the normal shock generated in the transonic flow have been observed, either by the (averaged and time-resolved) Schlieren visualizations or by the (averaged) far-field pressure measurements, it is found that the flow modifies the plasma in a very significant way. Additional effects to those observed in the flat plate experiment have been detected, which are due to the variation of pressure on the surface of the airfoil. Decreasing pressure increases the number of filaments and favors high current peak generation. Measurements show that the discharge characteristics cannot be completely controlled and that they depend on the flow field. Nevertheless, it can be sustained in high-pressure gradient flows and the effect of the flow on the filaments can be interesting in applications like

plasma assisted combustion or supersonic combustion, where the plasma is used for the enhancement of chemical reactions. The good reproducibility of the measurements (due to the robustness of the encapsulated DBD system) could make the system usable as a diagnostic, for measurements of velocities or pressures. The DBD could be used as a velocity or pressure sensor.

As mentioned before, the subject of the interaction of surface plasmas and high speed flows is a complex and very broad subject that has not been addressed in details before. The first approach needs to be qualitative, in order to acquire a physical insight of the phenomena and chose the correct path for subsequent research. This has been done in the present work, setting the technical and physical basis.

In order to be able to improve plasma-flow interaction, the first step is to deepen the physical understanding of the DBD. The estimation of the power dissipated in the plasma can be improved by developing a measurement or analysis technique which will result in quantitative estimations of the efficiency of the DBD system and of its energy injection in the fluid. Also, this would help evaluate the contribution of the continuous and filamentary components of the discharge in the modification of the flow properties. The chemistry of the discharge in air is complex. In order to understand it and be able to model it better, it would be interesting to perform experiments in pure gases simpler than air, for example argon or nitrogen, with high-speed flow. However, this might be technically challenging. A *closed loop* wind tunnel would be the best solution.

In order to maximize the effect of the plasma on the airflow, the following directions could be followed:

- Explore other DBD electrode setups and try to maximize filament generation. For example, co-planar interlaced brush-shaped electrodes could be encapsulated in LTCC.
- Optimize the applied voltage function as suggested by the calculation of Likhanskii et al. [61]
- Concentrate on ion wind generation (see appendix D)

There is still efforts to be made in order to understand plasma-flow interaction from a theoretical point of view. Today the most advanced numerical models describing the DBD do not include a gas flow yet, and they are usually non-chemical models. As pointed out in chapters 4 to 6, experimental observations need to be supported by more advanced numerical models in order improve the interpretation of the results. Full models containing the electrical, chemical and flow descriptions are still needed, partly because the chemical and electrical timescales are much smaller than the flow timescale, which makes the problem computationally intensive.

Finally, it can be said that the initial objectives have been met, in the sense that a DBD could be sustained in a transonic flow and that the plasma-flow interaction could be studied. Moreover, direction for improving the influence of a surface plasma on a normal shock are given, based on the study of the behavior of the plasma in the flow and on an aerodynamic modelling of the experiment.

Appendix A

Theoretical complements on compressible fluids

A.1 Definitions

Reynolds number

The Reynolds number is a non-dimensional quantity representing the ratio of inertial to viscous forces:

$$Re = \frac{O(\rho u \frac{\partial u}{\partial x})}{O(\mu (\frac{\partial u}{\partial x})^2)} = \frac{\rho_\infty U_\infty L}{\mu_\infty} \quad (\text{A.1})$$

A.2 Rankine-Hugoniot relations

The ratio between the pressure downstream (2) and upstream of a normal shock (1), as well as the velocity, density and temperature ratios are given by the Rankine-Hugoniot relations expressed in the following way [44]:

$$\frac{p_2}{p_1} = 1 + \frac{2\kappa}{\kappa + 1} (M_1^2 - 1) \quad (\text{A.2})$$

$$\frac{u_2}{u_1} = \frac{\rho_1}{\rho_2} = \frac{1}{M_1^2} \left[1 + \frac{\kappa - 1}{\kappa + 1} (M_1^2 - 1) \right] \quad (\text{A.3})$$

$$\frac{T_2}{T_1} = \frac{1}{M_1^2} \left[1 + \frac{2\kappa}{\kappa + 1} (M_1^2 - 1) \right] \left[1 + \frac{\kappa - 1}{\kappa + 1} (M_1^2 - 1) \right] \quad (\text{A.4})$$

where M_1 is the Mach number upstream of the normal shock and κ is the adiabatic coefficient of the gas.

A.3 Turbulent compressible Navier-Stokes equations

The motion of compressible viscous Newtonian fluids is governed by the Navier-Stokes equations for compressible media given by equations (A.5) to (A.12) [84]. These equations are derived from the conservation laws for mass, momentum and energy, and the thermodynamic relations for perfect gases.

Mass conservation:

$$\frac{\partial \rho}{\partial t} + \nabla \cdot (\rho \vec{u}) = 0 \quad (\text{A.5})$$

where ρ is the density and \vec{u} is the velocity vector.

Momentum conservation:

$$\frac{\partial (\rho \vec{u})}{\partial t} + \nabla \cdot (\rho \vec{u} \otimes \vec{u}) = \nabla p + \nabla \cdot \bar{\bar{\tau}} \quad (\text{A.6})$$

where p is the pressure, and $\bar{\bar{\tau}}$ is the shear stress tensor. A fluid is called *Newtonian* when:

$$\bar{\bar{\tau}} = 2\mu \bar{\bar{S}} + \zeta_\mu (\nabla \cdot \vec{u}) \bar{\bar{I}} \quad (\text{A.7})$$

where $\bar{\bar{I}}$ is a unit tensor, $\bar{\bar{S}}$ is the strain tensor defined as:

$$S_{ij} = \frac{1}{2} \left(\frac{\partial u_i}{\partial x_j} + \frac{\partial u_j}{\partial x_i} \right) \quad (\text{A.8})$$

and the second viscosity ζ_μ can be expressed as a function of μ as

$$\zeta = -\frac{2}{3}\mu \quad (\text{A.9})$$

This is correct for a mono-atomic gas, and is generally used for all gases in standard CFD applications.

Energy conservation:

$$\frac{\partial (\rho E_f)}{\partial t} + \nabla \cdot (\rho \vec{u} E_f) = -\nabla \cdot (p \vec{u}) + \nabla \cdot (\bar{\bar{\tau}} \cdot \vec{u}) - \nabla \cdot \vec{q} \quad (\text{A.10})$$

The heat-flux factor \vec{q} is usually obtained from Fourier's law so that

$$\vec{q} = -\lambda \nabla T \quad (\text{A.11})$$

where λ is the thermal conductivity.

Equation of state (ideal gases):

$$p = \rho RT \quad (\text{A.12})$$

where R is the specific gas constant.

In order to account for the natural turbulent characteristics of the flow, the Navier-Stokes equations are transformed into the Reynolds-averaged Navier-Stokes equations (RANS). This is done using statistical methods and assuming that a turbulent flow can be split into a statistically steady velocity $\langle \vec{u} \rangle$ and a turbulent fluctuating part \vec{u}' so that $\vec{u} = \langle \vec{u} \rangle + \vec{u}'$. This transformation generates new unknowns, such as the Reynolds stress tensor with double correlation terms. They have to be modelled in order to close the problem. The Boussineq assumption proposes to express the Reynolds stress tensor as a linear relation between the mean strain-rate tensor $\bar{\bar{S}}$ and the turbulent viscosity μ_t . The turbulence closure problem consists in best evaluating this turbulent viscosity.

The turbulent viscosity can be obtained by the determination of two characteristic scales, a length scale and a velocity scale. These are generally determined by means of two transport equations for the turbulent properties. The velocity scale is always provided by solving a transport equation for the turbulence kinetic energy k (equation D.6). The length scale is provided by solving a transport equation for another property of the turbulence, for example the dissipation rate ϵ (equation A.15) or the turbulence frequency ω . The models are then called k - ϵ or k - ω respectively. The transport equations for the k - ϵ model are given as [84]:

Kinematic eddy viscosity:

$$\mu_t = C_\mu \rho \frac{k^2}{\epsilon} \quad (\text{A.13})$$

Turbulence kinetic energy:

$$\frac{\partial(\rho k)}{\partial t} + \nabla \cdot (\rho k \vec{u}) = \nabla \cdot \left[\left(\mu + \frac{\mu_t}{\sigma_k} \right) \nabla k \right] - \rho \epsilon + P_k \quad (\text{A.14})$$

Dissipation rate:

$$\frac{\partial(\rho \epsilon)}{\partial t} + \nabla \cdot (\rho \epsilon \vec{u}) = \nabla \cdot \left[\left(\mu + \frac{\mu_t}{\sigma_\epsilon} \right) \nabla \epsilon \right] + C_{1\epsilon} \frac{\epsilon}{k} P_k - C_{2\epsilon} \rho \frac{\epsilon^2}{k} \quad (\text{A.15})$$

where P_k is a source term representing the production of turbulent energy

$$P_k = \mu_t \bar{\bar{S}} \cdot \bar{\bar{S}} \quad (\text{A.16})$$

and C_μ , σ_k , $C_{1\epsilon}$, $C_{2\epsilon}$ and σ_ϵ are closure coefficients.

Appendix B

NACA3506 coordinates

The original NACA 3506 has a chord length of 80 mm. The trailing edge of the NACA manufactured for the experiment has been truncated to 77.6 mm, in order to avoid bending of the thin trailing edge and in order to simplify manufacturing. The coordinates of the resulting airfoil are given below:

Suction Side		Pressure Side	
x	y	x	y
0.000	0.000	0.000	0.000
0.004	0.099	0.027	-0.096
0.100	0.270	0.160	-0.240
0.348	0.537	0.464	-0.440
0.743	0.784	0.905	-0.589
1.156	0.985	1.351	-0.689
1.233	1.019	1.433	-0.704
2.534	1.493	2.799	-0.874
5.170	2.194	5.499	-0.997
7.821	2.729	8.179	-1.001
10.486	3.165	10.848	-0.947
13.158	3.527	13.509	-0.860
15.835	3.825	16.165	-0.753
18.516	4.069	18.817	-0.634
21.200	4.264	21.467	-0.509
23.885	4.414	24.115	-0.382
26.571	4.522	26.762	-0.256
29.258	4.592	29.409	-0.133
31.944	4.625	32.056	-0.017
34.630	4.622	34.703	0.093
37.316	4.586	37.351	0.193
40.000	4.518	40.000	0.282
42.683	4.418	42.650	0.361
45.364	4.288	45.302	0.426
48.044	4.129	47.956	0.479
50.721	3.941	50.612	0.518
53.397	3.724	53.270	0.542
56.070	3.480	55.930	0.552
58.741	3.208	58.592	0.547
61.410	2.909	61.257	0.526
64.075	2.583	63.925	0.489
66.738	2.229	66.595	0.438
69.398	1.848	69.268	0.370
72.055	1.440	71.945	0.288
74.709	1.005	74.624	0.190
77.359	0.542	77.307	0.077

Table B.1: Coordinates of the NACA3506 profile in non-dimensional units. The trailing edge center is at (77.333, 0.309) and the trailing edge radius is 0.2337

Appendix C

Complements on experimental results

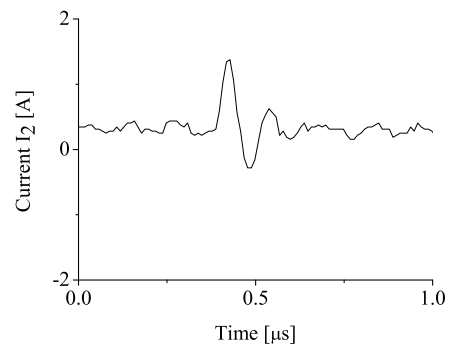


Figure C.1: Zoom on the current generated by Al_2O_3 -baseline at $U_2 = 4.2$ kV rms and 1 kHz.

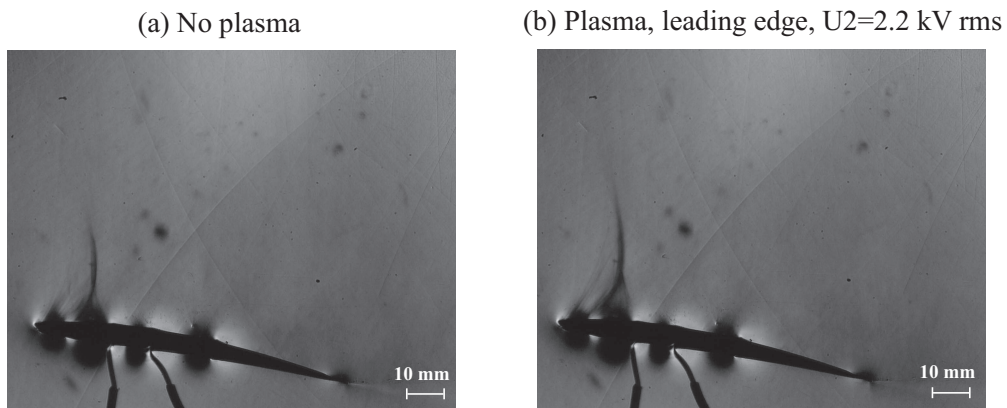


Figure C.2: Raw Schlieren images at $M_\infty=0.65$ without plasma (a) and with a surface plasma at 10 kHz close to the leading edge (b).

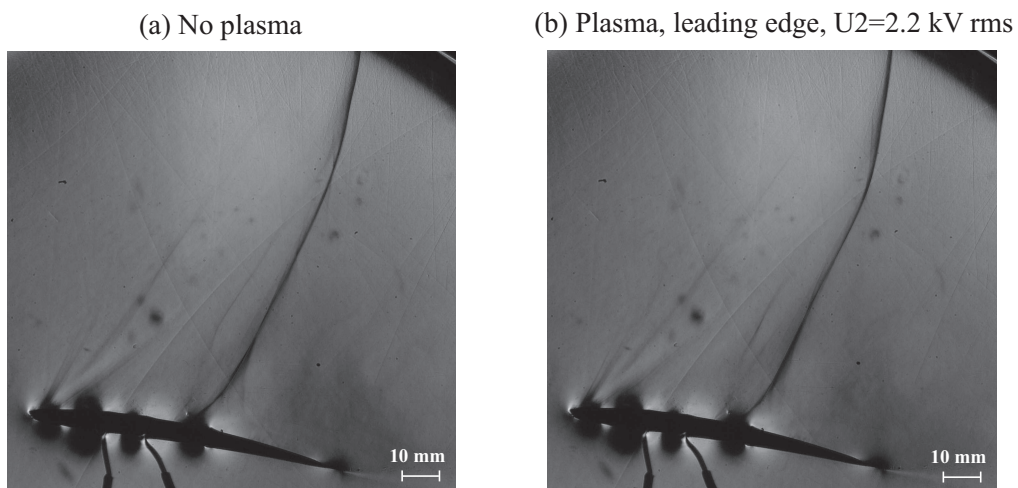


Figure C.3: Raw Schlieren images at $M_\infty=0.7$ without plasma (a) and with a surface plasma at 10 kHz close to the leading edge (b).

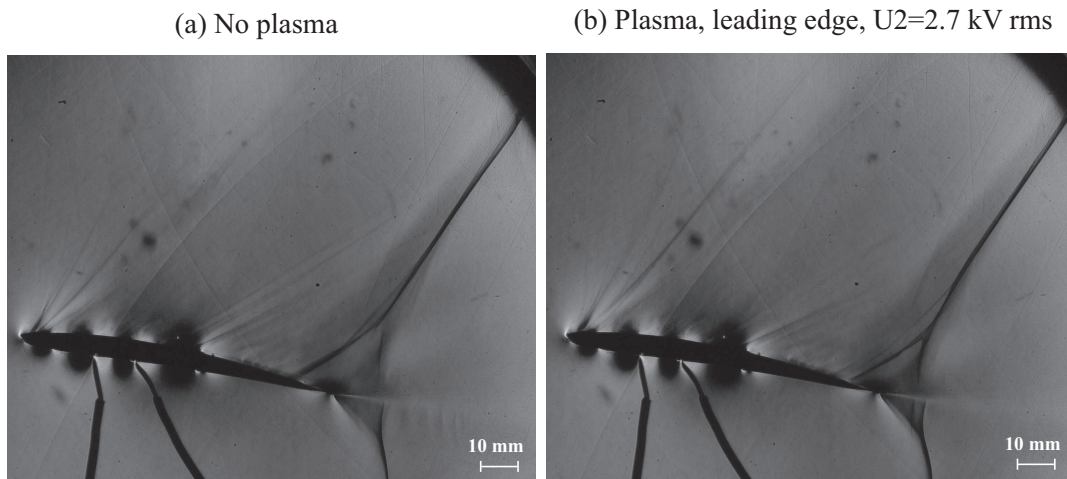


Figure C.4: Raw Schlieren images at $M_\infty=0.73$ without plasma (a) and with a surface plasma at 10 kHz close to the leading edge (b).

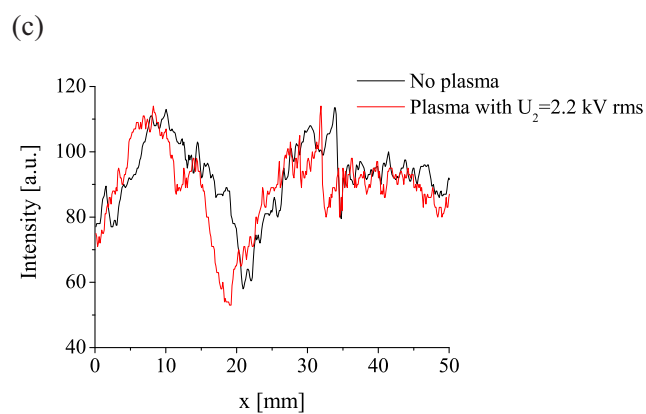
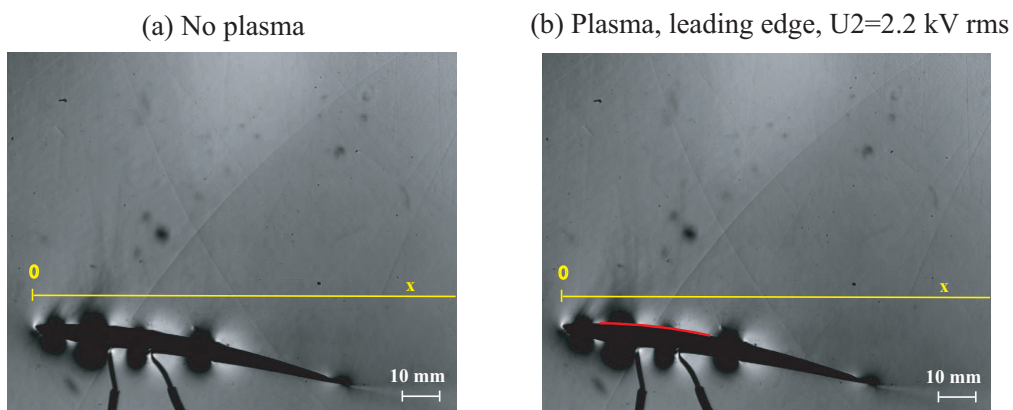


Figure C.5: Averages of 10 Schlieren images at $M_\infty=0.65$ without plasma (a) and with a surface plasma at 10 kHz close to the leading edge (b), with intensity profiles (c) measured along the yellow lines.

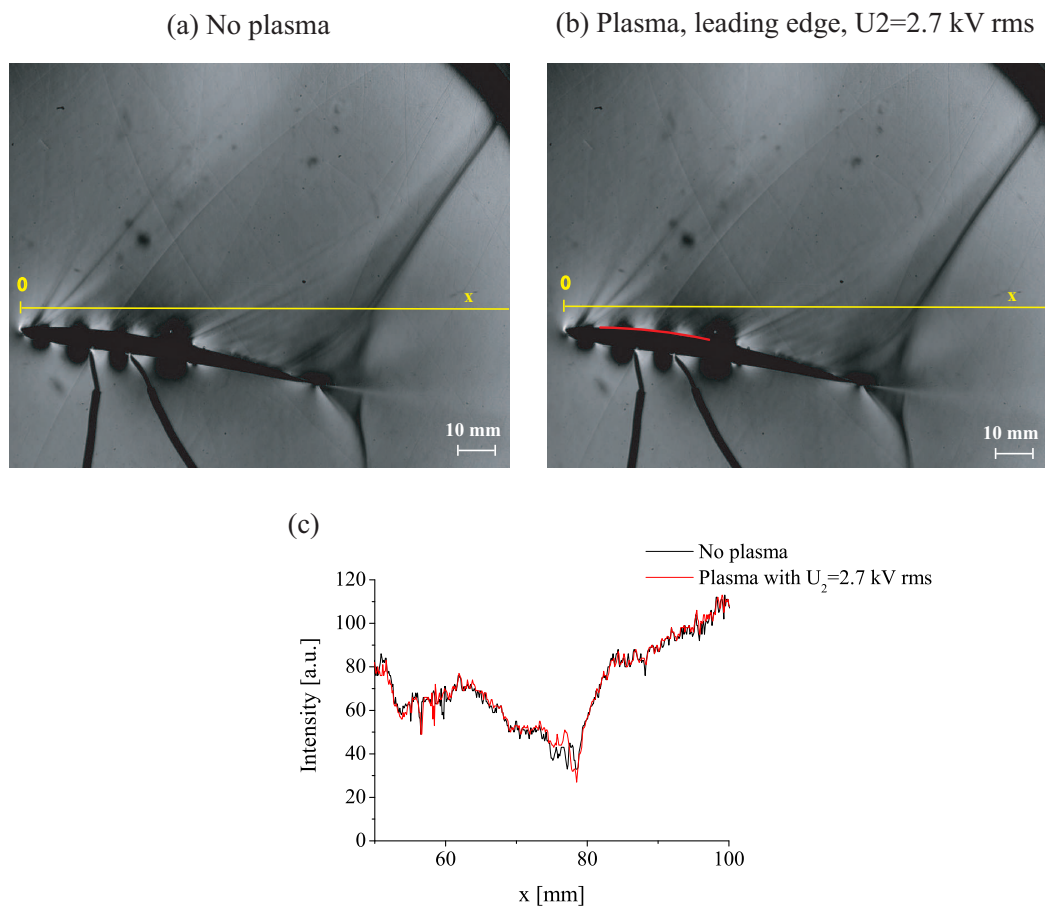


Figure C.6: Averages of 10 Schlieren images at $M_\infty=0.72$ without plasma (a) and with a surface plasma at 10 kHz close to the leading edge (b), with intensity profiles (c) measured along the yellow lines.

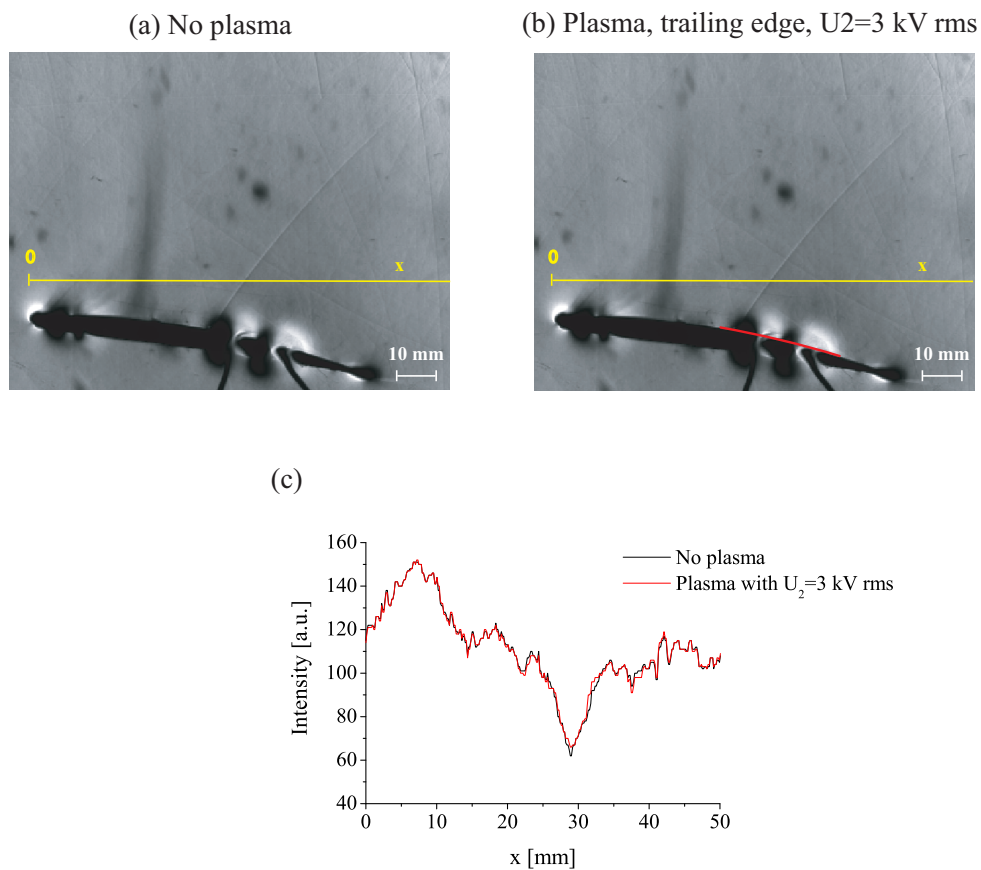


Figure C.7: Averages of 100 Schlieren images at $M_\infty=0.65$ without plasma (a) and with a surface plasma at 10 kHz close to the trailing edge (b), with intensity profiles (c) measured along the yellow lines.

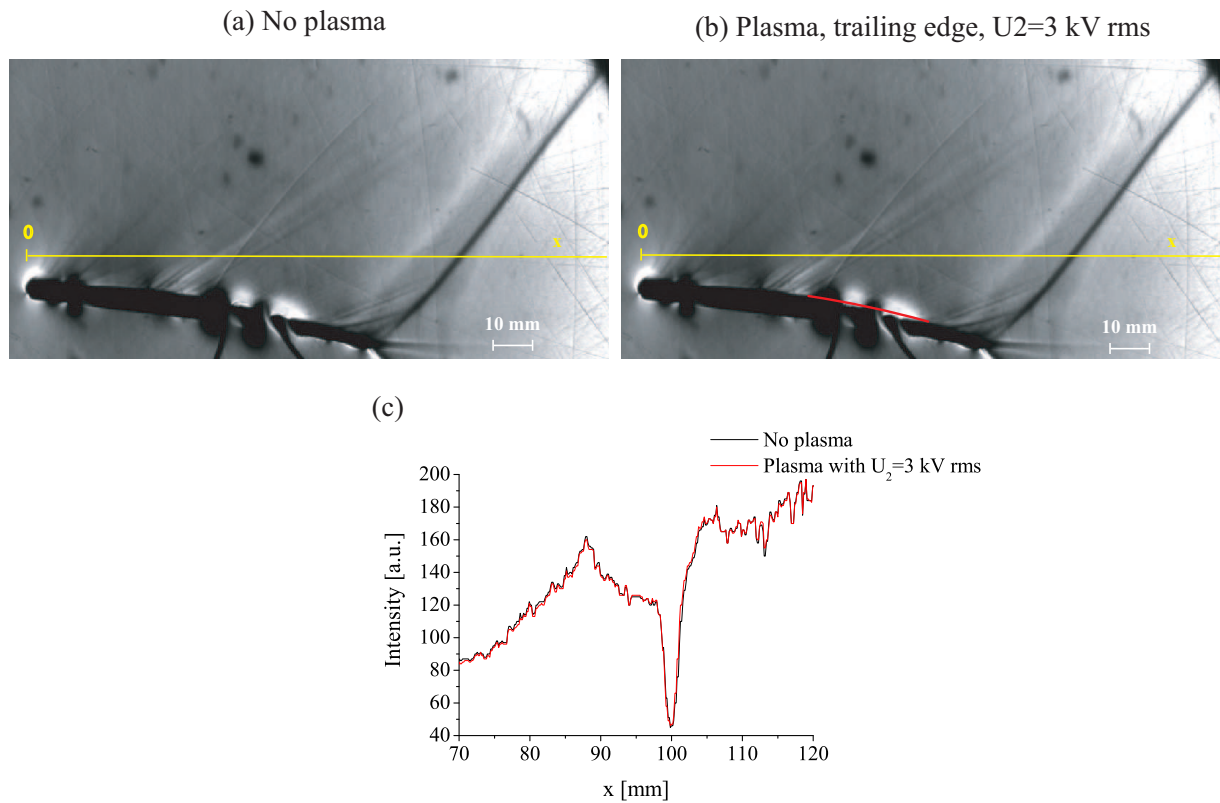


Figure C.8: Averages of 100 Schlieren images at $M_\infty=0.75$ without plasma (a) and with a surface plasma at 10 kHz close to the trailing edge (b), with intensity profiles measured along the yellow lines (c).

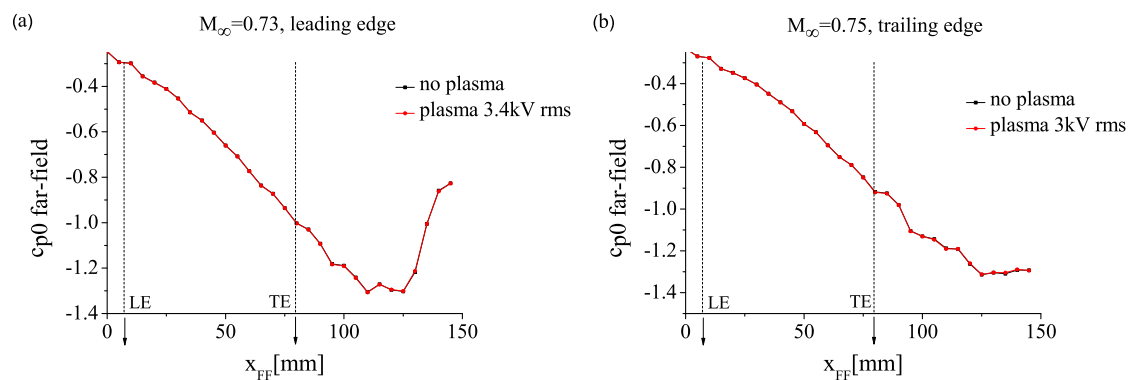


Figure C.9: Averaged far-field pressure distributions at $M_\infty=0.73$ without and with a plasma at 10 kHz close to the leading edge (a) and at $M_\infty=0.75$ without and with a plasma at 10 kHz close to the trailing edge (b).

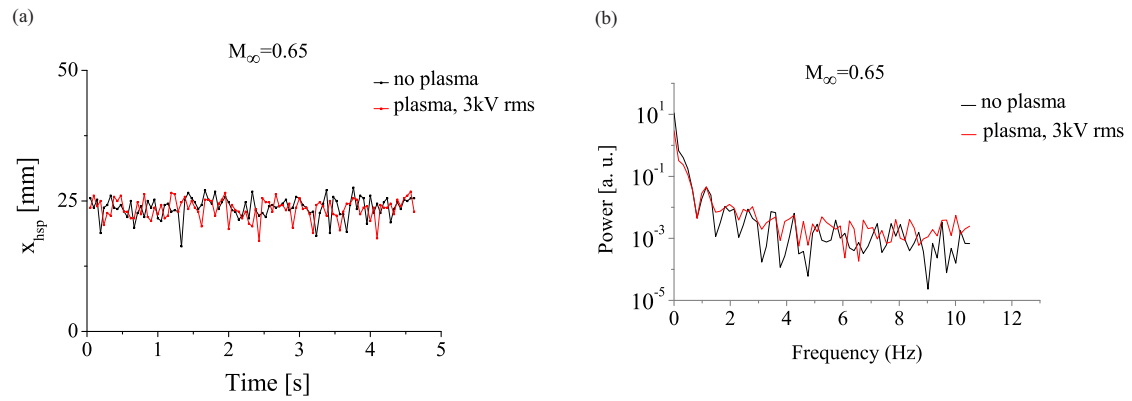


Figure C.10: Variation of the instantaneous horizontal shock position $x_{h,sp}$ with time (a) and FFT spectrum (b), at $M_\infty=0.65$ in the trailing edge configuration, in conditions without discharge and with a discharge at 10 kHz.

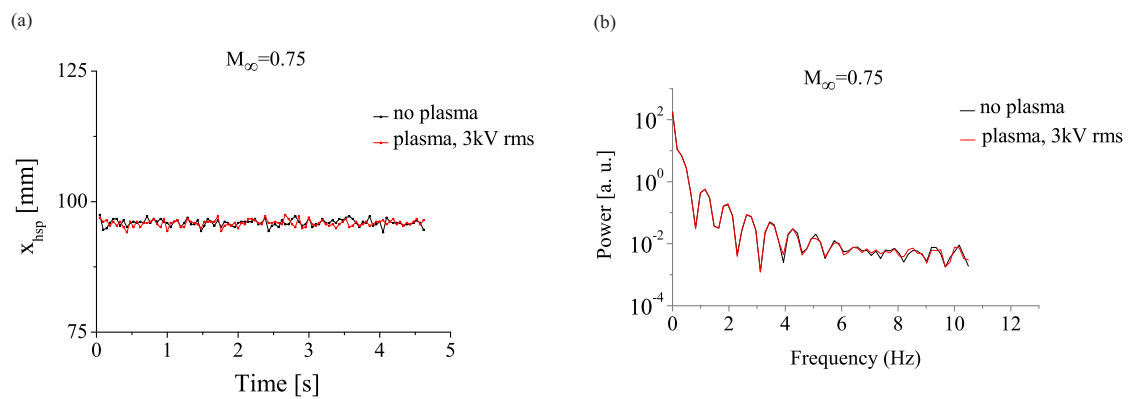


Figure C.11: Variation of the instantaneous horizontal shock position $x_{h,sp}$ with time (a) and FFT spectrum (b), at $M_\infty=0.75$ in the trailing edge configuration, in conditions without discharge and with a discharge at 10 kHz.

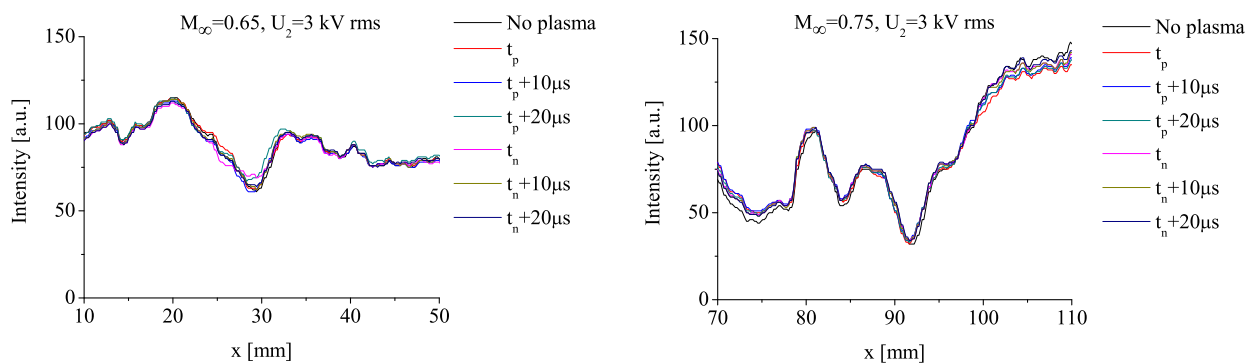


Figure C.12: Intensity profiles at different voltages phases, from averages of Schlieren 100 images, for different inlet Mach numbers and in conditions without discharge and with a discharge at 10 kHz close to the trailing edge.

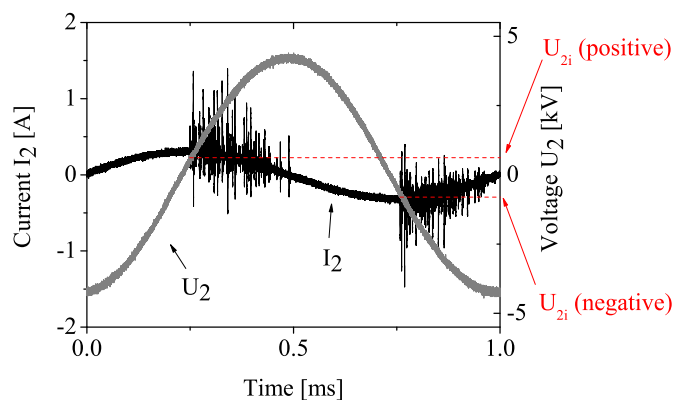


Figure C.13: Definition of the U_{2i} voltage at which filaments start to form.

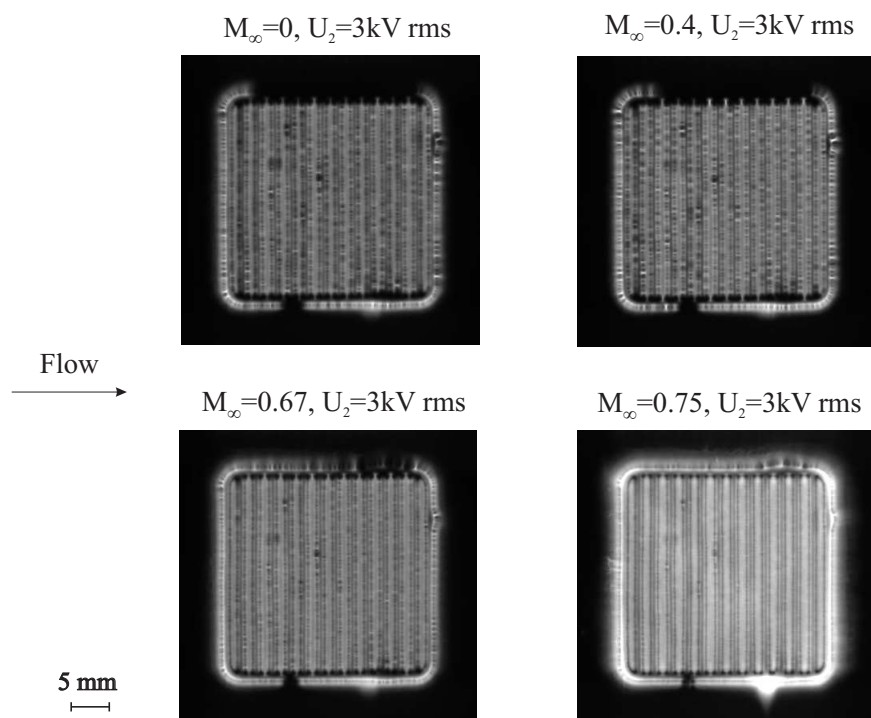


Figure C.14: CCD images of the discharge at different inlet Mach numbers for the discharge generated close to the trailing edge at 10 kHz. Exposure time is 40 ms.

Appendix D

Modeling

The Reynolds Averaged Navier-Stokes numerical model of the flow around the NACA3506 airfoil in the subsonic nozzle has been used for three purposes:

- Compute the isentropic Mach number and pressure distributions in the test section, as discussed in chapter 6. These distributions are not measured experimentally in order to stay fully non-intrusive and avoid interaction of diagnostics with the discharge.
- Identify and model the possible physical effects of the plasma on the flow. Physical properties of the boundary layer are modified locally in a *control volume* close to the airfoil surface (corresponding to the discharge volume).
- Find orders of magnitude for the modifications of physical parameters required to induce a significant effect on the shock

This parametric study is very specific to the problem of flow control with surface plasmas in high-speed flows and gives a first phenomenological insight into the subject¹. However, the model gives rough estimates and the results presented here should be interpreted carefully.

In the first section, the numerical methodology is described and the model is validated using Schlieren measurements. The second section discusses the effects on the shock of a modification of the viscosity, addition of turbulence energy, modification of the surface geometry and addition of ion wind. Finally, the main findings are summarized.

D.1 Description of the aerodynamic numerical model

The calculations have been performed using a two-dimensional approximation of the problem. Even though the geometry is almost completely 2D, boundary layers form on the nozzle lateral walls which means that the flow is actually three dimensional. In fact, previous measurements have shown that the lateral boundary layers on the subsonic nozzle are about 10 mm wide as measured by Ott [80] in the same nozzle, for a section width of

¹Such questions have not yet been addressed in the literature

only 40 mm. The 3D effects are therefore significant. However, a 3D model would add much more complexity and could mask the effects that want to be pointed out here.

The numerical computational domain of the model has been chosen as close as possible to the experimental conditions in the subsonic nozzle. The domain is shown in figure D.1 (a). The upper and lower nozzle wall positions relative to the profile in the y direction correspond exactly to the experimental case. Their length however have been slightly modified. In order to reduce the computational field and therefore the computation time, the wall lengths in the upwind direction have been reduced. Instead of starting at the inlet of the nozzle, the domain starts at the vertical static pressure measurement field (see chapter 3). This allows to cut the domain off of about 10 times the profile characteristic lengths. However, it has to be taken into account that the wall boundary layers start to form at the nozzle inlet and not at the domain inlet. Therefore, the wall boundary layers at the domain inlet are calculated analytically using the equations in chapter 5 for the development of a boundary layer over a flat plate. They are considered in the inlet pressure distribution condition. On the other hand, the domain has been extended in the downstream direction in order to avoid numerical perturbations of the outlet boundary conditions on the calculated flow field. This is very common in transonic calculations (see example from Bron et al. [72]), where numerical artifacts like shock reflections can appear if the outlet is too close to the region studied where the primary shock forms. The angle of incidence of the profile has been fixed to 8° as has been done in the experimental measurements.

The mesh has been generated with IcemCFD (version 11.0) from ANSYS [85] and the zone around the profile is shown in figure D.1 (b). A structured mesh has been chosen because the linear structures like the shock are of primary interest. The mesh is refined in the shock region and in the airfoil boundary layer region. It is refined as well at the walls generating a local mesh fine enough in order to avoid using a pre-defined *wall function* boundary condition in the solver. The total number of cells is 250'000.

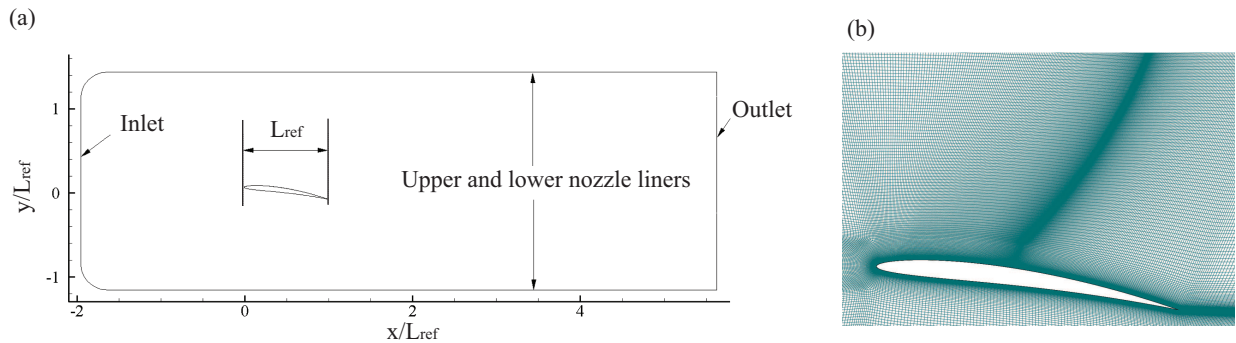


Figure D.1: Computational domain and close-up of the structured mesh close to the profile.

The Reynolds Averaged Navier-Stokes (RANS) equations (see chapter 2) are solved using CFD++ version 7.1.1 [86]. This solver uses a finite volume numerical method, which gives better results in terms of energy conservation, and a second order spatial discretization has been chosen in order to have a reasonable precision. This is the closest

to the numerical set-ups typically chosen in models used for the study of shock-boundary layer interaction (see Bron [70] for example).

The boundary conditions for the profile and the nozzle walls have been set in the same way. They are defined as adiabatic viscous walls with no-slip condition. The inlet flow boundary conditions have been set defining a pressure profile which corresponds to the static pressure measurements in the central part, and to the analytical estimations of the pressure distributions in the boundary layers close to the walls. The outlet flow boundary conditions have been set as a single back pressure value. It has been adjusted in order to have an acceptable correspondence of the calculated density gradients with the Schlieren measurements (see chapter 6).

The convergence criterion has been based on several parameters (mass, momentum, energy, turbulence) with residues of the order of 10^{-6} .

The shock-boundary layer interaction is a complex mechanism as discussed in chapter 2. The boundary layer at the profile surface thus has to be modelled very carefully in order to predict accurately the position of the separation point which determines the distribution of the entire flow field. The turbulence model giving the best concordance with experimental results is a Shear-Stress Transport (SST) model. The SST model solves the $k - \omega$ model at the walls and the $k - \epsilon$ model in the bulk flow (see appendix A). More details about this model are given by Wilcox [84]. Since turbulence is difficult to measure, the turbulence in the model usually has to be adapted for the model to match the experiments as is done by Bron et al. [72].

Figure D.2 shows a comparison between the isentropic Mach number distributions calculated with the RANS model and with an inviscid simulation (Euler) at the same conditions (but with a coarser mesh with about half the number of cells). It shows that the viscous effects on the profile play an essential role in the behavior of the flow. The boundary layer forming on the upper wall also modifies the transonic flow, in a smaller extent.

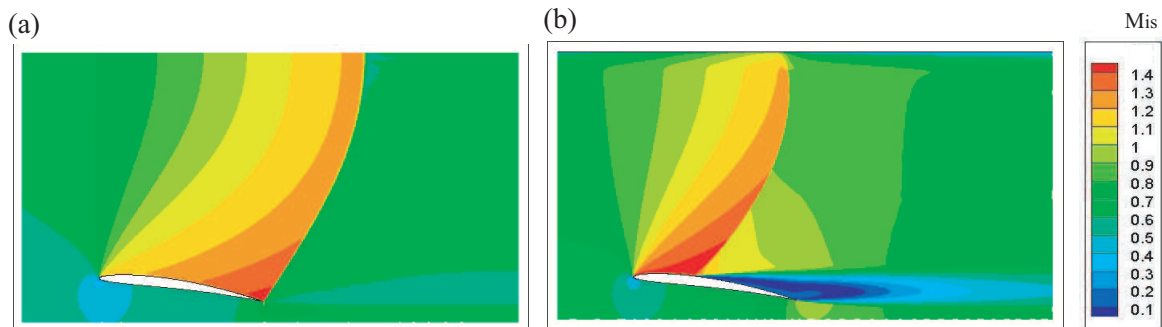


Figure D.2: Isentropic Mach number distribution around the NACA3506 at $i=8^\circ$ and $M_\infty=0.7$ with the RANS model (a) and an Euler model (b).

The numerical model can be validated with Schlieren visualizations and the far-field pressure measurements on the upper nozzle liner as shown in figure D.3. In this figure, two images are superimposed, for the case $M_\infty = 0.7$. The first one is a Schlieren image and the second one is a contour plot of the density gradient. Taking into account a ± 5

mm fluctuation of the shock position on the Schlieren images, the model predicts correctly the flow properties.

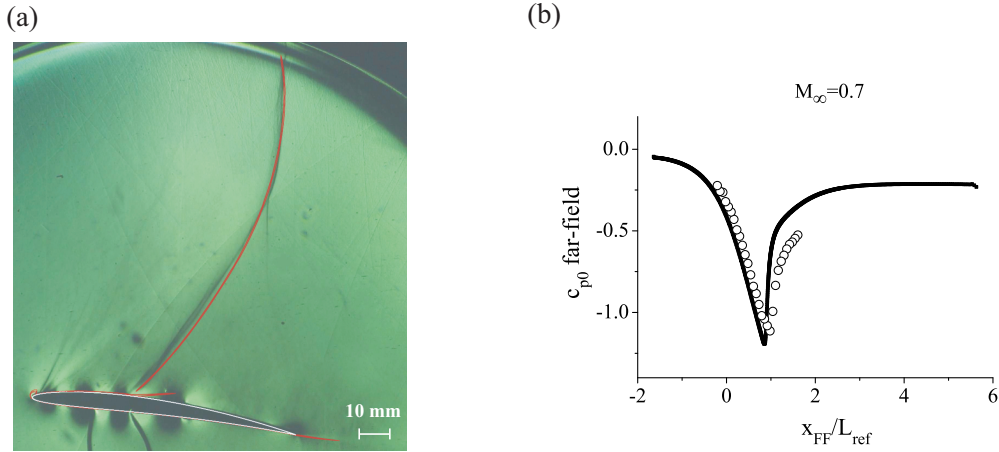


Figure D.3: Validation of the numerical model comparing the calculated density gradient with a Schlieren image and the far-field pressure distributions.

As discussed before, the turbulence model has been chosen in order to obtain the best correspondence possible with the Schlieren image. Moreover, in order to compensate for 3D effects, the pressure downstream of the profile has been manually set as has been done by Bron et al. [72]. The instability of the shock is also visible in the calculations and the results are presented with time-averaged values.

D.2 Forced physical property changes on the blade surface

In order to simulate the effects of the surface plasma on the external flow, the idea is to modify flow properties in a control volume similar to the plasma volume in the boundary layer. The mesh is divided into two cell groups: the *bulk flow* and the *control volume* corresponding to the location of the plasma on the surface. The control volume is 0.2 mm high (corresponding to the measured 200 μm of the plasma thickness) and 28 mm long. In analogy with the experiment, two configurations are studied: one where the control volume is placed close to the leading edge and one where it is placed close to the trailing edge. The first configuration is shown in figure D.4. The inlet Mach number M_∞ has been fixed to 0.7 to have a relatively long shock impinging on the upper nozzle liner (and simulate the far-field pressure variation through the shock at the wall) and to have the shock approximately in the middle of the suction side to study different relative positions of the plasma with respect to the shock. External energy or forces and physical properties have been modified in this control volume and the effects on the external airflow have been investigated. First of all, the viscosity and the turbulence level of the control volume are modified. After that, in analogy with the cone experiment by Lebedev et al. [1] where

the corona discharge deflects the incoming flow as if the plasma were a solid, the control volume has been replaced by a solid or by a series of solid steps. Finally, the effect of an addition of momentum in the boundary layer at the control volume location is investigated as a simulation of ion wind experiments. The effects of these changes are quantified in terms of the density gradient in the bulk flow, which corresponds to the physical quantity displayed by Schlieren visualizations. The far-field pressure distribution across the shock on the upper nozzle liner has also been investigated. The different conditions and the results of the calculations are presented in the following subsections. They are compared with the unperturbed case validated by the measurements. In order to summarize the effects of the different case, the lift and drag coefficients have been calculated and are presented in the last subsection.

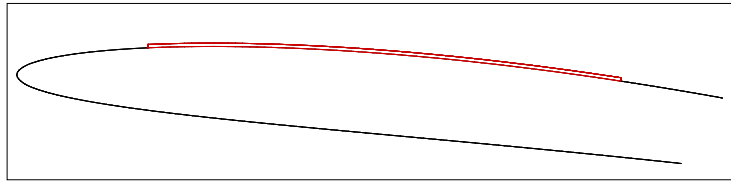


Figure D.4: Geometry of the control volume in the leading edge case.

D.2.1 Modification of the viscosity

As explained by Bron [70], the viscous effects play an important role in the pressure amplification in the shock-induced separation. The boundary layer thickening originating from the superposition of two adverse pressure gradient effects (curvature and shock discontinuity) is believed to be closely related to the observed pressure amplification. As explained by Jaumotte [45], the laminar boundary separation position and length can be estimated as a function of the Reynolds number (and thus viscosity), but in turbulent boundary layers, the effect of the Reynolds number is smaller and more difficult to observe experimentally. Jaumotte [45] also suggests that the upstream propagation of perturbations takes place in the viscous sublayer of the turbulent boundary layer.

The viscosity appears in the equations for momentum conservation and for energy conservation (appendix A) through the shear stress tensor $\bar{\tau}$ which is a function of the viscosity:

Momentum conservation:

$$\frac{\partial(\rho\vec{u})}{\partial t} + \nabla \cdot (\rho\vec{u} \otimes \vec{u}) = \nabla p + \nabla \cdot \bar{\tau} \quad (\text{D.1})$$

Energy conservation:

$$\frac{\partial(\rho E_f)}{\partial t} + \nabla \cdot (\rho\vec{u} E_f) = -\nabla \cdot (p\vec{u}) + \nabla \cdot (\bar{\tau} \cdot \vec{u}) - \nabla \cdot \vec{q} \quad (\text{D.2})$$

Shear stress tensor:

$$\bar{\tau} = 2\mu\bar{S} + \zeta_{\mu}(\nabla \cdot \bar{u})\bar{I} \quad (\text{D.3})$$

It is not exactly clear if the viscosity in the boundary layer is increased or decreased by the plasma. If the plasma heats the boundary layer, its viscosity increases according to Sutherland's law D.4 [44]:

$$\mu = \mu_{ref} \left(\frac{T}{T_{ref}} \right)^{3/2} \left(\frac{T_{ref} + S}{T + S} \right) \quad (\text{D.4})$$

with S is Sutherland's temperature equal to 110.4 K for air.

On the other hand, depending on the configuration of the electrodes, the plasma can also add momentum to the boundary layer (ion wind) and thus in a sense reduce the viscosity in a certain direction. Therefore, two cases have been considered, $\mu = 10\mu_0$ and $\mu = 0.1\mu_0$ where μ_0 is the reference viscosity of the unperturbed flow ($\mu_0 = 1.715 \cdot 10^{-5} \text{ kg m}^{-1} \text{ s}^{-1}$). The density gradient and far-field pressure distribution are shown in figure D.5 for the leading edge case where the effects are most significant.

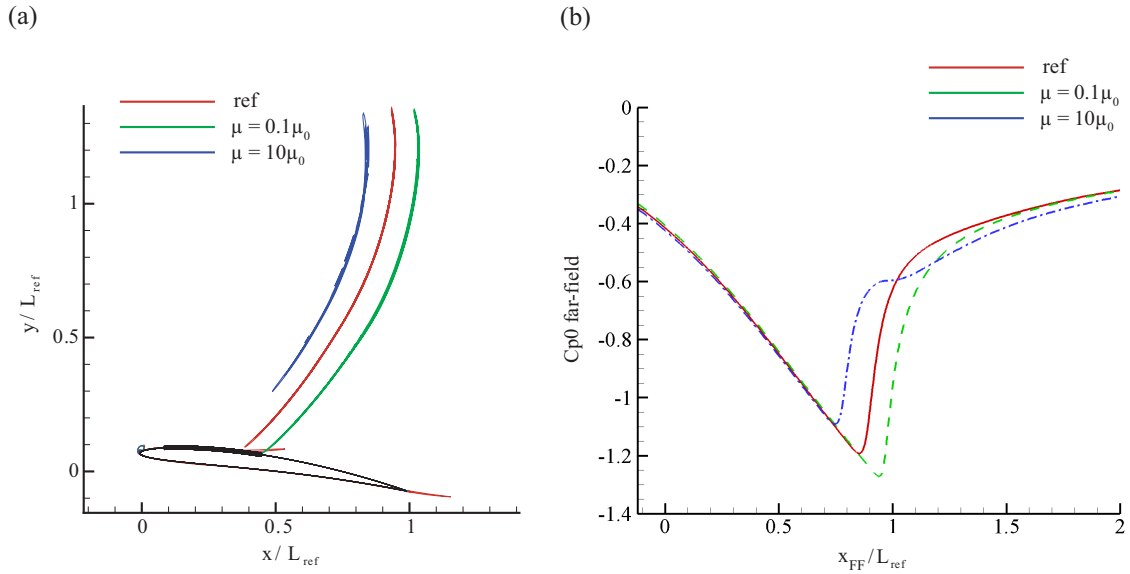


Figure D.5: Density gradient (a) and far-field pressure distribution (b) in the reference case and in the cases where the viscosity is modified close to the leading edge.

The density gradients show that increasing viscosity one order of magnitude upstream of the shock moves it by about 7 mm in the upstream direction for $\mu = 10\mu_0$. The detachment takes place closer to the leading edge, due to a thickening of the boundary layer. Indeed, when the viscosity increases, the turbulent boundary layer thickness increases according to relation D.5 from Blasius theory [44] and the detachment occurs earlier.

$$\delta_{turb}(x) = 0.37x \left(\frac{\rho U x}{\mu} \right)^{-1/5} \quad (\text{D.5})$$

This shock displacement is accompanied² by a reduction of the amplitude of the far-field pressure drop of 15% as shown in figure D.5 (a).

On the contrary, when $\mu = 0.1\mu_0$, the shock is shifted by about 7 mm in the downstream direction, due to a thinner boundary layer. Consequently, the amplitude of the far-field pressure drop simultaneously increases by 8%.

The viscosity has also been modified downstream of the shock in the separation zone. According to Bron and Dussauge et al. [70, 74], separation generates strong eddies that affect the shock in a considerable proportion and might be its source of excitation. However, the effects are negligibly small compared to the case where the viscosity is modified upstream of the shock. It seems that modifying the viscosity in the separation zone does not affect the structures in the separation zone like strong eddies and the modification should be done upstream of the separation point.

Numerical results indicate that the DBD used in the experiments does not modify significantly the viscosity of the boundary layer, at least less than one order of magnitude, otherwise a modification of the shock position would have been detected.

Is it realistic to try to modify the viscosity of air of one order of magnitude, up or down, with a non-equilibrium electrically generated plasma? In order to increase the viscosity by one order of magnitude by heating the gas, the temperature would have to be increased by two orders of magnitude according to Sutherland's law ($\mu \propto T^{1/2}$). As explained in chapter 2, non-equilibrium plasmas do not heat the gas in a significant way ($T_e > T_i \sim T_n$). Most probably such high temperatures can be reached only using thermal plasmas, like arcs for example. For applications in aeronautics this could become a technically challenging problem. The use of lasers or UHF energy sources is also considered nowadays for flow control (see Zheltovodov [87] for example). The possibilities of the reduction of viscosity through momentum injection is more difficult to evaluate. A detailed (microscopic) electro-chemical model would be needed in order to evaluate those possibilities.

D.2.2 Modification of the turbulence level

As suggested by Bron [70], the turbulence plays an essential role in shock-boundary layer interaction through the modification of particle kinetic energies and pressure levels for example. Moreover, Opaitis et al. and Jukes et al. [4, 5] for example have shown that DBDs can generate local vortex structures that could modify the turbulence level in a boundary layer.

The turbulence level can be increased by adding a source term S_K on the right hand side of the turbulent kinetic energy equation (appendix A):

$$\frac{\partial (k)}{\partial t} + \nabla \cdot (k\vec{u}) = \frac{1}{\rho}P_k - \epsilon + \nabla \cdot \left[\frac{1}{\rho} \left(\mu + \frac{\mu_t}{\sigma_k} \right) \nabla k \right] + S_K \quad (\text{D.6})$$

Practically, in CFD++, S_K is introduced as *volumetric source term* which means that S_K is introduced in each cell *volume* (2D volume). First of all, S_K has been arbitrarily

²The modifications of the far-field pressure distributions are not a direct effect of the modifications in the boundary layer but are directly correlated to the displacements of the shock.

set to 100W, which is the same order of magnitude as the electrical power input in the primary circuit of the power supply for the DBD. Then S_K has been set to one order of magnitude higher, 1000W. The density gradient and far-field pressure distribution are shown in figures D.6 for the leading edge configuration where the most significant effects can be obtained.

When the turbulence is increased upstream of the shock, the density gradients show that the shock is pushed towards the trailing edge. If $S_K=100W$ the shock is pushed only about 1 mm, and if $S_K=1000W$ the shock pushed about 3.5 mm. The momentum close to the wall is higher, which is typical for turbulent boundary layers (chapter 2), and the boundary layer becomes more resistant to the adverse pressure gradient and this effect is in fact dominant. As a consequence of the movement of the shock, the depth of the far-field pressure well is slightly higher, about 4%. However, the effect can be considered small compared to the magnitude of the power that has to be injected. Even though the detachment point is pushed towards the trailing edge, it is interesting to see that the density gradient close to the profile is actually higher for the perturbed case.

When turbulence is added downstream of the shock, the effects are not significant on the density gradient and far-field pressure. Indeed, the turbulent kinetic energy is very small compared to the energy of the eddies generated downstream of the shock.

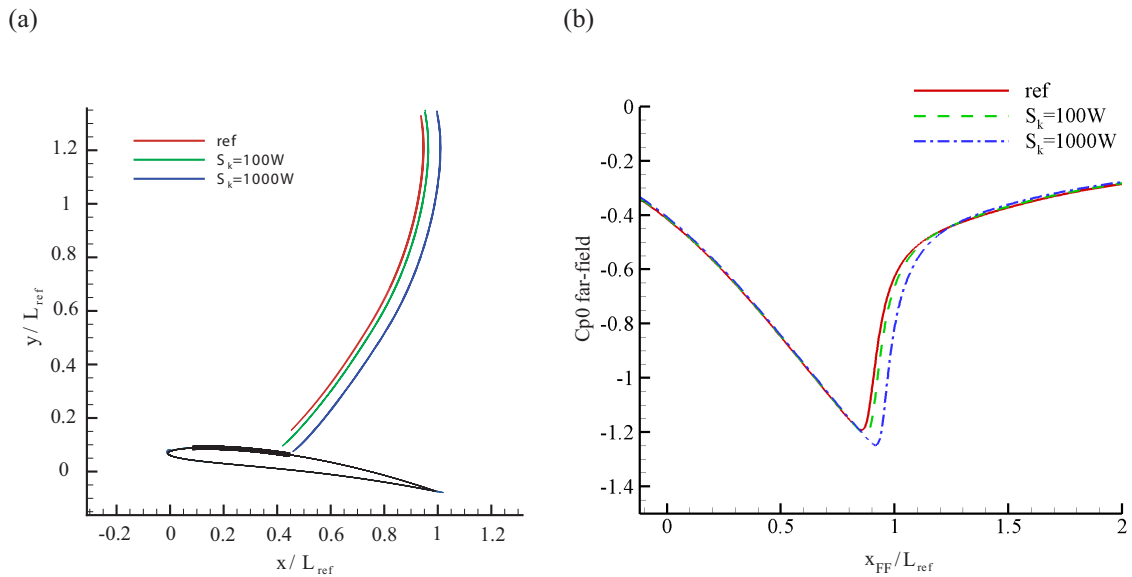


Figure D.6: Density gradient (a) and far-field pressure distribution (b) in the reference case and in the cases where the turbulence level is modified close to the leading edge.

The symmetric DBD systems can induce turbulence in the boundary layer since they create ion wind in both directions upwind and downwind (see chapter 1 and [4, 5]). However, the calculations show that the turbulent energy that needs to be injected in order to significantly affect the shock is more than 10^3W , which is high even if all the electrical input energy were converted into momentum in the boundary layer which cannot be the case. Therefore, using a DBD in a symmetric configuration to generate turbulence

through bi-directional ion wind does not seem to be an efficient way to affect the shock.

D.2.3 Modifications of the surface geometry

Vorticity can be introduced by the plasma in the boundary layer by ion wind effects as described by Opaits et al. [4] or by geometrical effects similar to the ones described by Lebedev et al. [1].

Two modified surface geometries have been considered and are presented in figure D.7. Geometry (a) is a single step, as if the plasma would represent a solid layer on the surface of the profile. Geometry (b) is more precise and consists of a series of 15 steps, 1 mm wide, which correspond to the zones where the discharge forms between the upper electrode stripes. Practically, the mesh is modified in the zone close to the profile in order to follow the contour of the new surface geometry. In CFD++, the single and multiple steps are considered in the same way as the rest of the profile surface, adiabatic viscous walls with no-slip condition. The density gradient and far-field pressure distribution are shown in figure D.8 in the leading edge case showing the strongest effects.

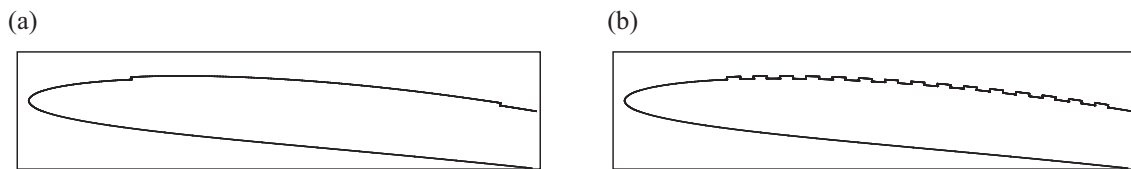


Figure D.7: Definitions of the modified surface geometries: single step case (a) and multiple step case (b).

The modification of the geometry close to the leading edge induces a displacement of the shock towards the leading edge in both the single and multiple step cases. Here the shock moves about 2 mm forward for the single step case and about 6 mm forward for the multiple step case. This effect is inverse to what is observed when adding kinetic turbulent energy to the boundary layer. Here, step geometries thicken the boundary layer and induce an earlier separation. Moreover, since the kinetic energy contained in the boundary is dissipated by the steps away from the zone close to the surface, the boundary layer becomes less resistant to adverse pressure gradients and the shock moves upstream. For the multiple step configuration, the density gradient close to the profile is reduced and the amplitude of the pressure drop in the far field is reduced by 18%.

The geometry has also been modified downstream of the shock in the separation zone. However, the effects are negligibly small compared to the case where the geometry is modified upstream of the shock.

The results show that a multiple step geometry generates a significant modification of the transonic flow when it is placed close to the leading edge. If the plasma could reproduce this effect of deflecting the flow like a solid, it would induce a significant effect on the shock.

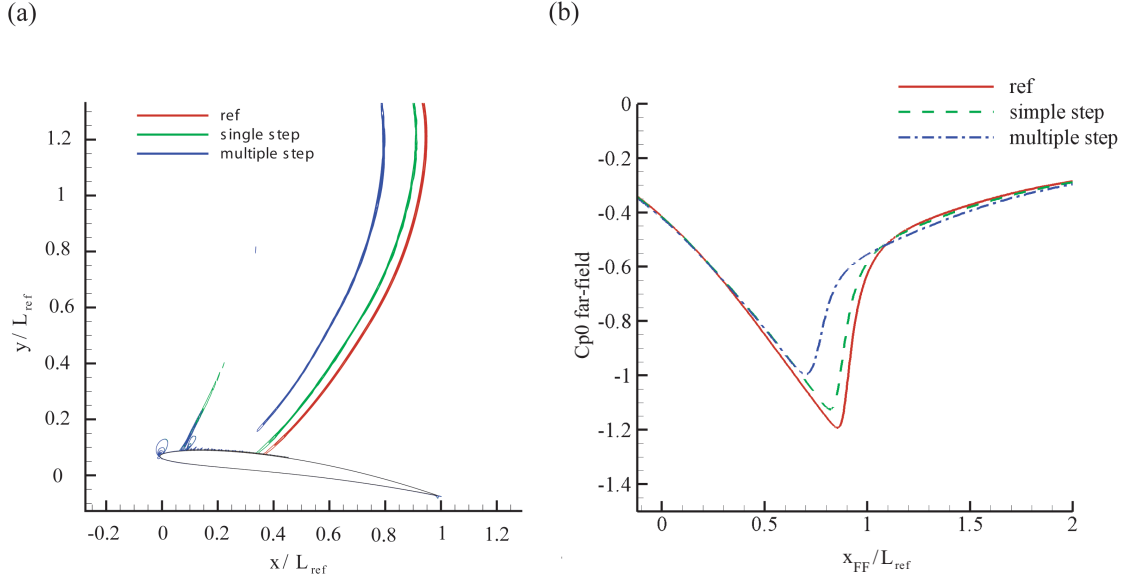


Figure D.8: Density gradient (a) and far-field pressure distribution (b) in the reference case and in the cases where the geometry is modified close to the leading edge.

D.2.4 Addition of ion wind

The ion wind is introduced in the boundary layer in the form of a force acting on the particles and generating a momentum. The average force that could be generated by a filamentary DBDs is in the range $F=5 \cdot 10^2 - 5 \cdot 10^4 \text{ N} \cdot \text{m}^{-3}$ as given by Boeuf et al. [30] (corresponding to 3 -30 m/s ion wind velocities³). For the calculations in the present section, the upper limit is used as reference $F_0= 5 \cdot 10^4 \text{ N} \cdot \text{m}^{-3}$. The force direction is chosen to be tangent to the surface in the direction of the flow. The force is introduced in the momentum conservation equation (appendix A) as an additional external force on the right hand side:

$$\frac{\partial(\vec{u})}{\partial t} + \nabla \cdot (\vec{u} \otimes \vec{u}) = \frac{1}{\rho} \nabla p + \frac{1}{\rho} \nabla \cdot \bar{\tau} + F_{ext} \quad (\text{D.7})$$

In CFD++ this is implemented as *volumetric source term*, which means that F_{ext} acts on every cell volume (as a potential force). Three cases have been considered, F_0 , $10F_0$ and $100F_0$. The density gradient and far-field pressure distribution are shown in figure D.9, in the trailing edge case where the perturbation is most effective.

The case where $F_{ext}=F_0$ is not shown because it overlaps with the unperturbed flow. The introduction of momentum moves the shock to the trailing edge when the force is at least of the order of $10F_0$. The shock drifts by about 2 mm and the depth of the far-field pressure well is increased by about 4%. This might be due to the acceleration in the part very close to the shock. At $F_{ext}=100F_0$, the shock is completely pushed towards

³Boeuf et al. [30] give the relation $u \simeq \left(\frac{2Fd}{\rho}\right)^{1/2}$ for the DBD, where d is the distance over which the force is applied, i. e. the width of the plasma sheath (non-neutral tip of the discharge)

the trailing edge by about 30 mm which is about 40% of the profile length. The depth of the far-field pressure well increases as well but only by 16%. This configuration seems therefore to be very efficient.

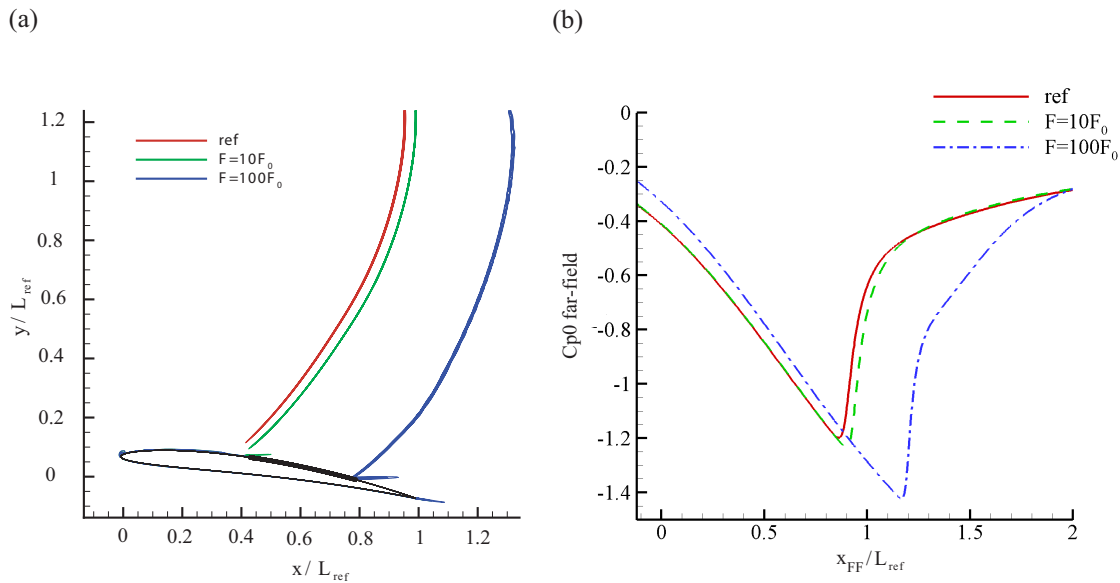


Figure D.9: Density gradient (a) and far-field pressure distribution (b) in the reference case and in the cases where ion wind is added close to the trailing edge.

According to the model, the highest reachable momentum input with today's DBD technologies is clearly not sufficient in order to efficiently affect the shock structure and properties. The momentum input needs to be multiplied by one or two orders of magnitude in order to significantly move the shock towards the trailing edge. In terms of velocity, this corresponds to values of at least to 150 m/s or 300 m/s respectively ($u \propto F^{1/2}$ [30]). At the present time it is difficult to say if this is possible with DBDs or surface coronas, but most probably the plasma generation technology will have to be drastically improved in order to reach those velocities. Maybe plasma jet technologies could be used. Also, at lower pressure levels higher velocities can be reached as well [81], which would be interesting for high-altitude flights. In order to check this, experiments with air flows at low pressure should be conducted. This is unfortunately not possible in the subsonic and supersonic nozzles presented in chapter 3 and other wind tunnels would have to be used.

D.3 Summary

The model presented in this chapter has permitted to acquire a physical feeling of the impact of different forced boundary layer properties on the external flow. The orders of magnitude of the modifications needed in order to affect the shock pattern have been estimated and it is shown that they are still much higher than what can be obtained to date with DBDs. The calculations help understand why, from an aerodynamical point of view,

the experiments show little effect of the surface discharge on the Schlieren visualization and far-field pressure distributions. However, the hypotheses are very rough and the results should be taken as such.

The model could still be refined, for example by modifying the physical properties in a series of small volumes, instead of a single continuous volume, in order to represent more precisely the areas where the plasma is generated. However, this would mainly change the quantitative effects of the control volume on shock. Here the goal is to obtain the qualitative behaviors and orders of magnitude only. Moreover, the present results should first be confirmed by a more advanced (non-commercial) code or simple experiments. As suggested by Bron [70], the numerical and experimental results might differ when the shock gets stronger due to the difficulties in the prediction of separation zone properties. Also, the interaction of shock and turbulent boundary layers is complex and not completely understood today. According to Dupont et al. [78], it may result from the superposition or coupling of several elementary problems which are still difficult to model, like:

- shock motion as a result of the action on the incoming boundary layer
- shock motion as a result of the unsteadiness of the separated zone
- production of turbulence (possibly including strong compressibility effects) by the shock
- formation of a new boundary layer downstream of the separation, characterized by vortex interactions and in some cases by low-frequency unsteadiness induced by the shock motion

Also, the model could be implemented in 3D to improve the description of the experiment (3D aerodynamic effects, non-homogeneity of the discharge in the z direction).

Appendix E

List of symbols

Symbol	Unit	Description
a_∞	m/s	free stream speed of sound
a_K	m ²	area not cut by the knife edge
c	m	length of the profile chord
c_f	s ⁻¹	skin friction coefficient
C_Q	F	capacitance used to measure the charge
C_m	F	capacitance of the matching box
c_{p0}	-	static pressure coefficient
C_μ	-	closure coefficient for the $k - \epsilon$ model
$C_{1\epsilon}$	-	closure coefficient for the $k - \epsilon$ model
$C_{2\epsilon}$	-	closure coefficient for the $k - \epsilon$ model
d	m	distance
E	V/m	electric field
E_f	J	energy in the fluid
E_{sc}	V/m	space charge field
E_{el}	J	electric energy dissipated in the discharge
f	m	focal length
F_L	N	lift force
F_D	N	drag force
F_W	-	Whitham function
i	°	angle of incidence
I_1	A	current in the primary circuit (before transformer)
I_2	A	voltage in the secondary circuit (after transformer)
\bar{I}	-	a unit tensor
ΔI	a.u.	light intensity gradient
I_K	a.u.	light intensity not cut by the knife edge
k	J	turbulence kinetic energy
L_{eff}	m	effective length of a body
L_m	H	self-inductance of the matching box
M	-	local Mach number
M_{is}	-	local isentropic Mach number
M_∞	-	free stream Mach number

Symbol	Unit	Description
n_e	cm^{-3}	density of electrons
n_{e0}	cm^{-3}	initial density of electrons (present naturally)
n_i	cm^{-3}	density of ions
n_n	cm^{-3}	density of neutral particles
n_r	-	index of refraction
n_t	cm^{-3}	density of target particles (in collisions)
N_{cr}	-	critical multiplication factor in an electron avalanche ($=10^8$)
p or p_{tot}	bar or Pa	total pressure
δp	bar or Pa	overpressure
p_0 or p_{stat}	bar	static pressure
p_{atm}	bar or Pa	atmospheric pressure ($= 1 \text{ bar} = 101300 \text{ Pa}$)
$p_{0\infty}$	bar	static pressure in the uniform free stream
p_{0FF}	bar	static pressure in the far-field
p_{0SS}	bar	static pressure on the suction side
P_{dbd}	W	electric power dissipated in the discharge
P_k	J	production of turbulent energy
\bar{q}	$\text{W} \cdot \text{m}^{-2}$	heat-flux factor
Q_{dbd}	C	charge accumulated on the DBD
Q_Q	C	charge accumulated on capacitor C_Q
R	$\text{J} \cdot \text{kg}^{-1} \text{K}^{-1}$	perfect-gas constant
R_i	Ω	shunt used to measure the current
Re	-	Reynolds number
Re_t	-	Reynolds number at laminar-turbulent transition point ($=5 \cdot 10^5$)
\bar{S}	s	strain tensor
\dot{S}_Q	J	thermal energy source term
\dot{S}_k	J	turbulence energy source term
T or T_{tot}	bar	total temperature
T_e	eV	temperature of electrons
T_i	eV or K	temperature of ions
T_n or g	K	temperature of the neutral gas
T_E	m/s	local temperature calculated with Euler's equations
t_p	s	time at which the filaments start to form on the positive half-period
t_n	s	time at which the filaments start to form on the negative half-period
Δt	s	time delay for the PI-MAX camera gate
u	m/s	local velocity
u_e	m/s	local velocity calculated with Euler's equations
\bar{u}	m/s	averaged local velocity
u'	m/s	turbulent component of the local velocity
U_∞	m/s	free stream velocity
U_1	V	voltage in the primary circuit (before transformer), in rms value if not mentioned
U_2	V	voltage in the secondary circuit (after transformer), in rms value if not mentioned
U_{2i}	V	voltage at which the filaments start to form
U_Q	V	voltage through capacitor C_L
v	m^3	unit volume
V	V	electric potential
V_{br}	V	breakdown voltage
δV	V	overvoltage
W	kg	weight of a body
x_{FF}	m	position in the far-field
x_s	m	curvilinear coordinate on the suction side
x_{hsp}	m	position of the shock on the horizontal reference line
x_{shock}	m	position of the shock on the suction side
x_t	-	position of the transition from laminar to turbulent boundary layer

Greek symbol	Unit	Description
α_{dev}	rad	deviation angle
α_i	-	degree of ionization
α	m^{-1}	Townsend ionization coefficient
β	bar^{-1}	compressibility
γ	-	coefficient of secondary electron emission
δ	m	boundary layer thickness defined where $u = 0.99u_e$
δ^*	m	variation of the shape of an object du to the boundary layer
δ_{lam}	m	thickness of the laminar boundary layer
δ_{turb}	m	thickness of the turbulent boundary layer
ϵ	m^2s^{-3}	dissipation rate
ϵ_r	F/m	electric permittivity
ζ	rad/s	component of the angular velocity
ζ_μ	$kg \cdot m^{-1} \cdot s^{-1}$	second viscosity
κ	-	adiabatic coefficient
λ	$W \cdot m^{-2} K^{-1}$	thermal conductivity
λ_{mfp}	m	mean free path
μ	$kg \cdot m^{-1} \cdot s^{-1}$	dynamic viscosity
μ_∞	$kg \cdot m^{-1} \cdot s^{-1}$	free stream viscosity
μ_i	$m^2 \cdot s^{-1} \cdot V^{-1}$	mobility of ions
μ_t	$kg \cdot m^{-1} \cdot s^{-1}$	kinematic eddy viscosity
ν	Hz	frequency of the applied voltage U_2
θ_M	rad	Mach angle
θ_B	rad	Boomray emission angle
ρ	$kg \cdot m^{-3}$	density
ρ_∞	$kg \cdot m^{-3}$	density of the uniform free stream
σ_k	-	closure coefficient for the $k - \epsilon$ model
σ_ϵ	-	closure coefficient for the $k - \epsilon$ model
σ_c	cm^{-3}	collision cross section
τ_w	$kg \cdot m^{-1} \cdot s^{-2}$	shear stress at the wall
$\bar{\tau}$	$kg \cdot m^{-1} \cdot s^{-2}$	shear stress tensor
ω	s^{-1}	turbulence frequency
$\vec{\omega}$	rad/s	angular velocity

Abbreviation	Description
a. u.	arbitrary unit
CRPP	Centre de Recherche en Physique des Plasmas
DBD	dielectric barrier discharge
FF	far field
FFT	Fast Fourier Transform
LE	leading edge
LIN	Laboratoire d'Ingénierie Numérique
LTCC	low temperature co-fireable ceramics
LTT	Laboratoire de thermique Appliquée et Turbomachines
PM or PMT	photomultiplier (tube)
POM	polyoxymethylene
RANS	Reynolds-Averaged-Navier-Stokes
SS	suction side
SST	shear stress transport
TE	trailing edge
\perp	flow perpendicular to stripes
//	flow parallel to stripes

Bibliography

- [1] V.M.Fomin, Th. Alziary de Roquefort, A.V. Lebedev, and A. I. Ivanchenko, “Supersonic flows with longitudinal glow discharge”, *Proceedings of the 3rd Workshop on Magneto-plasma Aerodynamics, Moscow (Russia)*, (2001).
- [2] J. R. Roth, R. C. M. Madhan, M. Yadav, J. Rahel, and S. Wilkinson, “Flow field measurements of paraelectric, peristaltic and combined plasma actuators based on the one atmosphere uniform glow discharge plasma (OAUGDP TM)”, *Proceedings of the 42th Aerospace Sciences Meeting and Exhibit, Reno (USA)*, (2004).
- [3] E. Moreau, “Airflow control by non-thermal plasma actuators”, *J. Phys. D: Appl. Phys.*, **40**, 605–36 (2007).
- [4] D.F. Opaitis, G. Neretti, A.V. Likhanskii, S. Zaidi, M.N. Shneider, R.B. Miles, and S.O. Macheret, “Experimental investigation of DBD plasma actuators driven by repetitive high voltage nanosecond pulses with DC or low-frequency sinusoidal bias”, *Collection of Technical Papers - 38th AIAA Plasmadynamics and Lasers Conference, Miami (USA)*, (2007).
- [5] T. N. Jukes, K. S. Choi, G. A. Jonhson, and S. J. Scott, “Turbulent drag reduction by surface plasma through spanwise flow oscillation”, *Proceedings of AIAA Meeting - San Francisco*, **2006-3693** (2006).
- [6] S. M. Starikovskaia, “Plasma assisted ignition and combustion”, *J. Phys. D: Appl. Phys.*, **39**, R265–299 (2006).
- [7] M. Robinson, “Movement of air in the electric wind of the corona discharge”, *AIEE Trans.*, **80**, 143–50 (1961).
- [8] F. Hauksbee, “Physico-mechanical experiments on various subjects - Second Edition”, *Facsimile, London*, (1719).
- [9] H. Velkoff and J.Ketchman, “Effect of an electrostatic field on boundary layer transition”, *AIAA J.*, **16**, 1381–3 (1968).
- [10] A. Yabe, Y. Mori, and K. Hijikata, *AIAA J.*, **16**, 340–5 (1978).
- [11] J. R. Roth, D. M. Sherman, and S. P. Wilkinson, “Boundary layer flow control with a one atmosphere uniform glow discharge surface plasma”, *Proceedings of the 36th Aerospace Sciences Meeting and Exhibit, Reno (USA)*, (1998).

- [12] U. Kogelschatz, “Dielectric-barrier discharges: their history, discharge physics and industrial applications”, *Plasma Chemistry and Plasma Processing*, **23**, 1–46 (2003).
- [13] A. I. Klimov, A. N. Koblov, G. I. Mishin, Y. L. Serov, and I. P. Yavor, *Sov. Tech. Phys. Lett.*, **8**, 192 (1982).
- [14] W. T. Brande, “The Bakerian Lecture: On some new electro-chemical phenomena”, *Phil. Trans. Royal Soc.*, **104**, 51–61 (1814).
- [15] G. T. Southgate, “Increasing flame temperatures by aid of the electric arc”, *Chem. Metallurgical Engr.*, **31**, 16–19 (1924).
- [16] J. Lawton and F. J. Weinberg, “Chem. Metallurgical Engr.”, *Clarendon Press*, (1969).
- [17] C. O. Porter, J. W. Baughn, T. E. McLaughlin, C. L. Enloe, and G. I. Font, “Plasma actuator force measurements”, *AIAA J.*, **45**, 1562–70 (2007).
- [18] A.V. Likhanskii, M. N. Shneider, D. F. Opaits, R. B. Miles, and S. O. Macheret, “Numerical modeling of DBD plasma actuators and the induced air flow”, *Collection of Technical Papers - 38th AIAA Plasmadynamics and Lasers Conference, Miami (USA)*, (2007).
- [19] E. Moreau, C. Louste, and G. Touchard, “Electric wind induced by sliding discharge in air at atmospheric pressure”, *J. of Electrostatics*, **66**, 107–114 (2008).
- [20] K. H. Becker, U. Kogelschatz, K. H. Schoenbach, and R. J. Baker, “Non-equilibrium Air Plasmas at Atmospheric Pressure”, *Series in Plasma Physics - Institute of Physics Publishing*, (2005).
- [21] N. Gherardi and F. Massines, “Mechanisms controlling the transition from glow silent discharge to streamer discharge in nitrogen”, *IEEE Trans. on Plasma Science*, **29**, 536–44 (2001).
- [22] F. Massines, P. Ségur, N. Gherardi, C. Khamphan, and A. Ricard, “Physics and chemistry in a glow dielectric barrier discharge at atmospheric pressure: diagnostics and modelling”, *Surface and Coatings Technology*, **174-175**, 8–14 (2003).
- [23] N. Naudé, J.-P. Cambronne, N. Gherardi, and F. Massines, “Electrical model and analysis of the transition from an atmospheric pressure Townsend discharge to a filamentary discharge”, *J. Phys. D: App. Phys.*, **38**, 530–538 (2005).
- [24] J. Engemann and D. Korzec, “Assessment of discharges for large area atmospheric pressure plasma-enhanced chemical vapor deposition (AP PECVD)”, *Thin Solid Films*, **442**, 36–9 (2003).
- [25] E. G. Finantu-Dinu, D. Korzec, M. Teaschke, and J. Engemann, “Influence of the electrode layout on performance of insulated surface discharge: electrical characterization”, *Surface and Coatings Technology*, **174-175**, 524–29 (2003).

- [26] P.-Q. Elias, B. Chanetz, S. Larigaldie, and D. Packan, “Study of the effect of glow discharges near a M=3 bow shock”, *AIAA J.*, **45**, 2237–45 (2007).
- [27] P. Bletzinger, B. N. Ganguly, D. Van Wie, and A. Garscadden, “Plasmas in high speed aerodynamics”, *J. Phys. D: Appl. Phys.*, **38**, R33–57 (2005).
- [28] S. B. Leonov, V. A. Bityurin, D. A. Yarantsev, Y. I. Isaenkov, and V. R. Soloviev, “High-speed flow control due to interaction with electrical discharges”, *Proceedings of the 13th AIAA/CIRRA International Space Planes and Hypersonics Systems and Technologies Conference, Capua (Italy)*, (2005).
- [29] K. P. Singh and S. Roy, “Simulation of an asymmetric single dielectric barrier plasma actuator”, *J. Appl. Phys.*, **98**, 1–7 (2005).
- [30] J.-P. Boeuf, Y. Lagmich, Th. Unfer, Th. Callegari, and L. C. Pitchford, “Electrohydrodynamic force in dielectric barrier discharge plasma actuators”, *J. Phys. D: Appl. Phys.*, **40**, 652–62 (2007).
- [31] D. L. Book, “Plasma Formulary”, *Naval Research Laboratory Publication*, (1990).
- [32] J. M. Meek and J. D. Craggs, “Electrical breakdown of gases”, *Clarendon Press*, (1953).
- [33] F. Paschen, “Über die zum Funkenübergang in Luft, Wasserstoff und Kohlensäure bei verschiedenen Drücken erforderliche Potentialdifferenz”, *Wied. Anal. Phys. Chem.*, **37**, 69–96 (1889).
- [34] T. W. Dakin, G. Luxa, G. Oppermann, J. Vigreux, G. Wind, and H. Winkelkemper, “Breakdown of gases in uniform fields. Paschen curves for nitrogen, air and hexafluoride”, *Electra*, **32**, 61–82 (1974).
- [35] E. T. Protasevich, “Cold non-equilibrium plasma”, *Cambridge International Science Publishing*, (2000).
- [36] E. E. Kunhardt, “Generation of large-volume, atmospheric-pressure, nonequilibrium plasmas”, *IEEE Tran. Plasma Sci.*, **28**, 189–200 (2000).
- [37] A. Fridman, A. Chirokov, and A. Gutsol, “Non-thermal atmospheric pressure discharges”, *J. Phys. D: Appl. Phys.*, **38**, R1–R24 (2005).
- [38] Yu. D. Korolev and G. A. Mesyats, “Physics of pulsed breakdown in gases”, *URO-Press*, (1998).
- [39] Y. P. Raizer, “Gas discharge physics”, *Springer-Verlag*, (1991).
- [40] F. Massines, A. Rabehi, P. Decomps, R. Ben Gadri, P. Ségur, and C. Mayoux, “Experimental and theoretical study of a glow discharge at atmospheric pressure controlled by dielectric barrier”, *J. Appl. Phys.*, **83**, 2950–57 (1998).

- [41] A. Sublet, “Caractérisation de décharges à barrière diélectriques atmosphériques et sub-atmosphériques et application à la déposition de couches d’oxyde de silicium”, *PhD Thesis - Ecole Polytechnique Fédérale de Lausanne (EPFL)*, (2007).
- [42] C. L. Enloe, T. E. McLaughlin, R. D. VanDyken, K. D. Kachner, E. J. Jumper, T. C. Corke, M. Post, and O. Haddad, “Mechanisms and responses of a single dielectric barrier plasma actuator: geometric effect”, *AIAA J.*, **42**, 595–604 (2004).
- [43] J. D. Anderson, “Modern Compressible Flow - Third Edition”, *Series in Aeronautical and Aerospace Engineering - McGraw Hill*, (2004).
- [44] I. L. Ryhming, “Dynamique des fluides - Deuxieme edition”, *Presses Polytechniques Universitaires Romandes (PPUR)*, (1991).
- [45] A. L. Jaumotte, “Chocs et ondes de choc”, *Masson*, (1973).
- [46] E. L. Houghton and P. W. Carpenter, “Aerodynamics for engineering students - Fifth edition”, *Butterworth-Heinemann*, (2003).
- [47] H. Pearcey, “Boundary-layer and flow control”, **2**, 742–75 (1955).
- [48] R. L. Bisplinghoff, H. Ashley, and R. L. Halfman, “Aeroelasticity”, *Dover Publications*, (1996).
- [49] A. D. Pierce, “Acoustics - An introduction to its physical principles and applications”, *American Institute of Physics, Acoustical Society of America*, (1994).
- [50] F. Coulouvrat, “Sonic Boom Tutorial for HISAC”, *Dassault Aviation*, (2005).
- [51] G. B. Whitham, “Linear and Non-linear Waves”, *Wiley*, (1974).
- [52] K. Kaouri, “Secondary Sonic Boom”, *PhD Thesis - University of Oxford*, (2004).
- [53] H.-E. Wagner, R. Brandenburg, K.V. Kozlov, A. Sonnenfeld, P. Michel, and J.F. Behnke, “The barrier discharge: Basic properties and applications to surface treatment”, *Vacuum*, **71**, 417–436 (2003).
- [54] A. Lehr, “Application of a Particle Image Velocimetry System to the Periodic Unsteady Flow Around an Isolated Compressor Airfoil”, *PhD Thesis - Ecole Polytechnique Fédérale de Lausanne (EPFL)*, (2002).
- [55] S. Pavon, A. Sublet, J.-L. Dorier, Ch. Hollenstein, P. Ott, and P. Leyland, “Long lifetime system for the generation of surface plasmas”, *US provisional patent n° 61027044*, (2008).
- [56] D. Charbonnier, “Modeling of the flow in the Laval I nozzle at LTT”, *LTT internal report*, (2006).

- [57] T. Arts, H. Boerrigter, J.-M. Buchlin, M. Carbonaro, G. Degrez, R. Denos, D. Fletcher, D. Olivari, M. L. Riethmuller, and R. A. Van Den Braembussche, “Measurement Techniques in Fluid Dynamics - An Introduction”, *Von Karman Institute for Fluid Dynamics*, (2001).
- [58] R. J. Goldstein, “Fluid Mechanics Measurements”, *Taylor and Francis*, (1996).
- [59] G. S. Settles, “Schlieren and Shadowgraph Techniques - Visualizing Phenomena in Transparent Media”, *Springer Verlag*, (2001).
- [60] Y. Lagmich, Th. Callegari, L. C. Pitchford, and J.-P. Boeuf, “Model description of surface dielectric barrier discharge for flow control”, *J. Phys. D: Appl. Phys.*, **41** (2008).
- [61] A. V. Likhanskii, M. N. Schneider, S. O. Macheret, and R. B. Miles, “Modeling of dielectric barrier discharge plasma actuator in air”, *J. Appl. Phys.*, **103** (2008).
- [62] Y. Lagmich, “Diagnostic et modélisation d’une décharge à barrière diélectrique pour le contrôle d’écoulement”, *PhD Thesis - Université Toulouse III - Paul Sabatier*, **41** (2008).
- [63] S. Pavon, J.-L. Dorier, Ch. Hollenstein, P. Ott, and P. Leyland, “Effects of high-speed airflows on a surface dielectric barrier discharge”, *J. Phys. D: Appl. Phys.*, **40**, 1733–1741.
- [64] K. Gersten H. Schlichting, “Boundary layer theory - 8th edition”, *Springer*, (2000).
- [65] F. Péneau, H. C. Boisson, A. Kondjoyan, and N. Djilali, “Structure of a flat plate boundary layer subjected to free-stream turbulence”, *J. of Computational Fluid Dynamics*, **18**, 175–88 (2004).
- [66] T. Makabe, H. Awai, and T. Mori, “Spectroscopic investigations of $N_2(A^3\Sigma^+_u)$ metastables in the spatial ionization growth in nitrogen”, *J. Phys. D: Appl. Phys.*, **17**, 2367–76 (1984).
- [67] P. F. Ambrico, M. Šimek, G. Dilecce, and S. De Benedictis, “On the measurement of $N_2(A^3\Sigma^+_u)$ metastable in N_2 surface dielectric barrier discharge at atmospheric pressure”, *Plasma Sources Science and Technology*, **15**, 627–34 (2006).
- [68] D.F. Opaitis, D. V. Roupasov, S. M. Starikovskaia, A.Yu. Starikovskii, I. N. Zavalov, and S. G. Saddoughi, “Plasma control of boundary layer using low-temperature non-equilibrium plasma of gas discharge”, *43rd AIAA Aerospace Sciences Meeting and Exhibit - Meeting Papers, Reno (USA)*, (2005).
- [69] C. Laux, “Radiation and non-equilibrium collisional-radiative models - In Physico-chemical models for high-enthalpy and plasma flows”, *Von Karman Institute for Fluid Dynamics - Lecture Series*, (2002).

- [70] O. Bron, “Numerical and experimental Study of the Shock-Boundary Layer Interaction in Transonic Unsteady Flow”, *PhD Thesis - Royal Institute of Technology (KTH)*, (2003).
- [71] P. Ferrand, L. Smati, and S. Aubert, “Analysis of nonlinear transonic blockage in unsteady transonic flows”, *AIAA Paper*, **97-1803** (1997).
- [72] O. Bron, P. Ferrand, and T. H. Fransson, “Unsteady Aerodynamics, Acoustics and Aeroelasticity of Turbomachines - in - Experimental and numerical study of nonlinear interactions in two-dimensional transonic nozzle flow”, *Springer*, (2006).
- [73] J. Edwards and L. Squire, “Experimental observations on an unsteady normal shock/boundary layer interaction”, *In AGARD Conference on Transonic and Supersonic Phenomena in Turbomachines*, (1986).
- [74] J.P.Dussauge, P. Dupont, and J.-F. Debiève, “Unsteadiness in shock wave boundary layer interaction with separation”, *Aerospace Science and Technology*, **10**, 85–91 (2005).
- [75] P. Ott, “Oszillierender senkrechter Verdichtungstoss in einer ebenen Düse”, *PhD Thesis - Ecole Polytechnique Fédérale de Lausanne (EPFL)*, (1992).
- [76] P. Ferrand, “Etude theorique des ecoulements instationnaires en turbomachine axiale. Application au flottement de blocage”, *PhD Thesis - Ecole Centrale de Lyon*, (1986).
- [77] S. Aubert, “Etude de schemas a haute precision pour la simulation d’écoulements transsoniques instationnaires ou visqueux. Application aux turbomachines.”, *Ecole Centrale de Lyon*, (1993).
- [78] P.Dupont, C. Haddad, J.-P. Ardissonne, and J.-F. Debiève, “Space and time organization of a shock wave/turbulent boundary layer interaction”, *Aerospace Science and Technology*, **9**, 561–72 (2005).
- [79] J. Andreopoulos and K. Muck, “Some new aspects of the shock wave/boundary layer interaction in compression ramp flows”, *J. of Fluid Mechanics*, **180** (1987).
- [80] P. Ott, A. Bölcs, and T. H. Fransson, “Experimental and Numerical Study of the Time-Dependent Pressure Response of a Shock Wave Oscillating in a Nozzle”, *Trans. of ASME*, **117**, 106–14 (1995).
- [81] N. Benard, N. Balcon, and E. Moreau, “Electric wind produced by a surface dielectric barrier discharge operating in air at different pressures: aeronautical control insights”, *J. Phys. D: Appl. Phys.*, **41** (2008).
- [82] T. Abe, Y. Takizawa, and S. Sato, “A parametric experimental study for momentum transfer by plasma actuator”, *45th AIAA Aerospace Sciences Meeting and Exhibit - Meeting Papers, Reno (USA)*, (2007).

- [83] J. W. Gregoy, C. L. Enloe, G. I. Font, and T. E. McLaughlin, “Force production mechanisms of a dielectric barrier discharge plasma actuator”, (2007).
- [84] D. C. Wilcox, “Turbulence modeling for CFD - Second edition”, *DCW Industries*, (2000).
- [85] *www.ansys.com*, .
- [86] Metacomp Inc., “CFD++ version 7.1.1 user’s manual”, .
- [87] A. A. Zheltovodov, E. A. Pimonov, and D. D. Knight, “Numerical modeling of vortex/shock wave interaction and its transformation by localized energy deposition”, *J. Appl. Phys.*, **103** (2008).

Remerciements

In this last chapter I would like to devote a few lines to the persons who have been on the road with me during this adventure of four years. This part will be written in english, french, spanish so that I can thank everybody.

Tout d'abord j'aimerais remercier mon directeur de thèse le Dr. Peter Ott, directeur du Laboratoire de Thermique Appliquée et Turbomachines, pour m'avoir permis de travailler sur ce projet hautement innovateur et multidisciplinaire. Je le remercie pour la confiance qu'il m'a accordée et pour son *oeil ingénieur*.

I would like to thank Professor François Avellan, Professor John R. Thome, Professor Jean-Pierre Boeuf, Professor Philipp Rudolf von Rohr and Professor Bernhard Weigand for being part of the jury for my thesis and for their support in the last phases of the project.

Je voudrais aussi remercier Dr. Christoph Hollenstein du CRPP et Dr. Pénélope Leyland du LIN pour leur collaboration. Un grand merci au Dr. Jean-Luc Dorier du CRPP pour m'avoir fait profiter de son expérience en physique expérimentale et pour son soutien jusqu'à la fin de la thèse. Un merci spécial au Dr. Alban Sublet pour avoir partagé avec moi son expérience des DBDs volumiques, avant de partir en voiture avec Simone.

Je remercie aussi le Service des Relations Industrielles de l'EPFL, Mme Zuber et Mr Clerc, pour avoir soutenu notre projet de brevet. Merci aussi au Dr. Gilles Zalamansky de Dassault Aviation pour son intérêt tout au long du projet.

Je voudrais aussi remercier les ingénieurs, doctorants et post-doctorants des trois laboratoires (les anciens et les nouveaux), pour les très bons échanges, les moments de détente et les rigolades (et les virées à Sat): Klaus Hubrich, Stefan Kristukat, Arrigo Berretta, Guillaume Wagner, Magnus Jonsson, Elia Colombo, Virginie Chenaux, Dominique Charbonnier, Malko Gindrat, Hannes Schmidt, Antoine Descoedres, Alban Sublet (re), Benjamin Strahm, Lukas Derendinger, Raffaello Sobbia et Matthieu Vital-Durand. Spéciale dédicace à Virginie et Elia pour leur amitié, leur bonne humeur et leur soutien moral dans toutes les situations! Merci aussi aux doctorants du LTCM et du LENI pour les discussions existentielles (ou pas) au café et à midi!

Merci à Claude Nicollier pour m'avoir permis d'être assistante pour son cours. Merci Claude de nous permettre de nous évader au delà de l'atmosphère à travers tes récits. Merci aussi à Renato Krpoun, André Noth, Yves Wiaux, Noémy Scheidegger et Virginie Chenaux (re) qui partagent avec moi cette passion de l'Espace.

Je remercie les mécaniciens et électriciens pour leur maîtrise et leur patience même dans les situations *exotiques* auxquelles je les ai confrontés. Je remercie tout spécialement

Jean-François Mion, Robert Bochy, Robert Lassueur, Christophe Zurmühle, Jean-Pierre Rougnon, Jean-Pierre Rudaz (pour les travaux d'Hercules) et Roger Mottier (qui est aussi un compatriote). Merci encore à Annick Despont pour son aide dans les tâches administratives et pour sa gentillesse. Merci aussi à Lise Von Gross, Cécile Taverney, Edith Grüther et Heidi Francelet.

Merci aux étudiants que j'ai suivis lors de leurs projets de semestre ou diplôme au LTT. Je remercie en particulier Johannes Haag pour son aide à la mise en place des méthodes de mesure aérodynamiques et Benoit Béguin pour les calculs effectués avec CFD++ que j'ai pu utiliser pour l'appendice D de cette thèse.

Gracias a toda mi familia, mis papas, Vanessa y Maël por haber creído en mí desde el principio y por todo el amor y la felicidad que me daís. Gracias por vuestra paciencia. Un abrazo a la familia en España y à Crans. Un recuerdo para los abuelos y Mimile et Louloute.

Je voudrais dire un grand merci à Karin Schombourg pour son amitié de longue date, son écoute et mon éducation culturelle;) Je prends déjà rendez-vous pour le café des vieilles physiciennes: le 15 août 2058 à la Place St-François vers 19h00 ça va pour toi Karin?

Finally, I would like to thank the friends I have met through my activities, with who I have soared the skies of Switzerland and explored the beautiful mountains of Switzerland, Chile, Nepal, Africa and Mars. I would like to dedicate a special line to my friends in skydiving, this big family from all over the world: thanks guys, merci les gars, gracias tios, danke, kiitos!! You cannot imagine how much this sport and you guys have changed my life.

Samantha

Curriculum Vitae

Samantha Pavón
+41-79-232-0160
samantha.pavon@a3.epfl.ch

Date of birth: September 5th 1980
Nationalities: Swiss and Spanish

PROFESSIONAL EXPERIENCE

- 2004 - present** **Swiss Federal Institute of Technology (EPFL), Lausanne, Switzerland**
Applied Thermodynamics and Turbo-machinery Laboratory (LTT)
Experimental physicist in the field of flow control with plasmas
Swiss National Science Foundation (NSF) experimental research project on:
Interaction between a surface dielectric barrier discharge and transonic air flows
- 2006 - 2007**
(3 weeks) **Mars Desert Research Station (MDRS), Utah Desert, United States**
Crew physicist and engineer
Mars analog studies
- 2002**
(1 month) **Swiss Federal Institute of Technology (EPFL), Lausanne, Switzerland**
Autonomous Systems Laboratory (ASL)
Engineering intern
Programming for robot sensors and actuators, hardware and software testing
- 2002**
(3 months) **European Space Operations Center (ESOC), Darmstadt, Germany**
Engineering intern
Mission Analysis for the XEUS mission (X-ray Evolving-Universe Spectroscopy)

EDUCATION

- 2004 - present** **Swiss Federal Institute of Technology (EPFL), Lausanne, Switzerland**
Applied Thermodynamics and Turbo-machinery Laboratory (LTT)
PhD student in Energy Sciences
- 1999 - 2004** **Swiss Federal Institute of Technology (EPFL), Lausanne, Switzerland**
Master in Engineering Physics, specialization in Plasma Physics and Engineering
- 2001 - 2002** **Carnegie Mellon University (CMU), Pittsburgh (PA), United States**
Exchange Student in Physics
-

PUBLICATIONS

Effects of surface dielectric barrier discharges on transonic flows around an airfoil

S. Pavón, B. Béguin, P. Ott and P. Leyland, J.-L. Dorier, Ch. Hollenstein

Accepted for the 47th AIAA Aerospace Sciences Meeting and Exhibit, Orlando (USA)

January 2009.

Long lifetime system for the generation of surface plasmas

Provisional US Patent n°61027044

S. Pavón, A. Sublet, J.-L. Dorier, C. Hollenstein, P. Ott, and P. Leyland

February 8th 2008.

Effects of high-speed airflows on a surface dielectric barrier discharge

S. Pavón, J.-L. Dorier, C. Hollenstein, P. Ott, and P. Leyland

Journal of Physics D : Applied Physics, 40(6):1733-1741, 2007.

The Spaceward Bound Field Training Curriculum

for Moon and Mars Analog Environments

J. C. Rask, J. Heldmann, H. Smith, M. Battler, K. Fristad, M. Allner, T. Clardy,

O. Clark, C. Taylor, R. Citron, B. Corbin, G. Negron, J. Skok, L. Taylor, F. Centinello,

A. Duncan, A. Fan, S. Pavón, W. Sutton, V. Drakonakis, C. Gilbert, S. Graves,

G. Guzik, R. Sahani and C. P. McKay

LEAG Workshop on Enabling Exploration, 2007.

Effects of transonic air flows on a dielectric barrier discharge

S. Pavón, J.-L. Dorier, C. Hollenstein, P. Ott and P. Leyland

Gordon Research Conference on Plasma Processing Science (GRC-PPS), 2006.

XEUS mission analysis and sky coverage

S. Pavón, G. Janin and M. Landgraf

MAO working paper n°446, 2002.
